Fakultät für Physik

Lehrstuhl für Physik (E18) – Univ.-Prof. Dr. St. Paul

Investigation of electric fields, losses and depolarization of ultra-cold neutrons for the new nEDM experiment at FRM II

Svetlana Chesnevskaya

Vollständiger Abdruck der von der Fakultät für Physik
der Technischen Universität München zur Erlangung des akademischen Grades eines
Doktors DER NATURWISSENSCHAFTEN
genehmigten Dissertation.

Vorsitzender: Univ.-Prof. Dr. B. Garbrecht

Prüfer der Dissertation:

1. Univ.-Prof. Dr. St. Paul
2. Univ.-Prof. Dr. L. Oberauer

Die Dissertation wurde am 01.07.15 bei der Technischen Universität München eingereicht und durch die Fakultät für Physik am 07.10.15 angenommen.

Abstract

The search for the existence of a nonzero neutron electric dipole moment (nEDM) has the potential to reveal new sources of **T** and **CP** violation and may have a significant impact on our understanding of the universe. At the TU München a next generation experiment to measure the EDM of the neutron is currently being set up. The goal of the new EDM experiment at TUM is to measure the electric dipole moment on an accuracy level of $5 \cdot 10^{-28}$ e·cm. This requires very good control of systematic effects which can mimic a false EDM effect on a level of $d_{false} < 1.5 \cdot 10^{-28}$ e·cm. Therefore, effects originating from the instability of the electric field, leakage currents, mechanical and electro-physical properties of the electrodes or deformations of the electrode due to mechanical and electrostatic forces need to be tested. Here, we discuss systematic effects produced by such phenomena, as well as ongoing investigations of solutions to various aspects of these problems, e.g. tests of novel electrode materials and the generation of electric fields. In the second part of the thesis, depolarization effects in ultracold neutron (UCN) guides are investigated. Such polarized neutrons are used in the nEDM experiment and the sensitivity of the experiment is dependent on the degree of UCN depolarization in the UCN guides and the nEDM spectrometer. Lowest depolarization per wall bounce for available UCN guides were found for NiMo (nickel molybdenum) alloys in the range of 10^{-5} or lower.

This work has shown that the electric field can be produced using different conductive plastics for a high-voltage electrode. Simulations of the electric field and systematic effects result in false effects one or two orders below the statistical uncertainties. Using glass and aluminum as neutron guides and different wall coatings for them, ultra-cold neutron losses and depolarization can be kept below the critical value to allow a measurement goal of $5 \cdot 10^{-28}$ e·cm.

Zusammenfassung

Die Suche nach einem endlichen elektrische Dipolmoment des Neutrons (nEDM) birgt das Potenzial, neue Quellen zur Verletzung der Zeitumkehrsymmetrie, **T**, und der kombinierten Ladungs - und Paritätssymmetrie, **CP**, zu entdecken. Eine solche Entdeckung hätte grossen Einfluss auf unser Verständnis des Universums. An der TU München wird eine neue Generation des Experiments zur Messung von nEDM vorbereitet und aufgebaut mit dem Ziel, eine stark verbesserte und weltweit beste Genauigkeit von $5 \cdot 10^{-28}$ e·cm zu erzielen. Dies erfordert ein genaues Vertändnis und Kontrolle sogenannter systematischer Effekte, die ein falsches nEDM-Signal simulieren könnten, auf einem Niveau $df \leq 1.5 \cdot 10^{-28}$ e·cm. Die Ursache solcher störender Effekte wie u.a. Instabilitäten der verwendeten elektrischen und magnetischen Felder im Experiment, Leckströme an den Hochspannungselektroden, mechanische und elektrische Eigenschaften dieser Elektroden oder deren Deformierung durch mechanische und elektrische Kräfte müssen genaustens untersucht werden. In der vorliegenden Arbeit werden im ersten und zweiten Teil solche systematischen Effekte behandelt und Lösungen zu ihrer Behebung aufgezeigt, wie z.B. Tests neuartiger Elektrodenmaterialien und die Erzeugung des elektrischen Feldes. Im dritten Teil der Arbeit werden die Wahrscheinlichkeiten für Verluste und Depolarisation von ultrakalten Neutronen (UCN) in speziellen Neutronenleitern untersucht. Polarisierte UCN werden im nEDM-Experiment verwendet und eine hoher Polarisationsgrad sowie minimale Depolarisierung sind für dieses Experiment essentiell. Mit Neutronenleitern aus Glas erzielt man die grösste Transmission. Beschichtet man diese Neutronenleiter mit paramagnetischen NiMo-Legierungen findet man eine sehr niedrige Depolarisationswahrscheinlichkeit pro Wandstoss von 10^{-5} oder weniger.

Diese Arbeit hat gezeigt, dass das elektrische Feld unter Verwendung verschiedener leitfähiger Kunststoffe für die Hochspannungselektrode erzeugt werden kann. Simulationen des elektrischen Feldes und der systematischen Effekte führen zu Falscheffekten ein oder zwei Größenordnungen unter den statistischen Unsicherheiten. Verwendung von Glas und Aluminium als Neutronenleiter und verschiedenen Wandbeschichtungen für diese, können die Verluste der ultrakalten Neutronen und die Depolarisation unter dem kritischen Wert gehalten werden, um eine Messung mit dem Ziel von $5 \cdot 10^{-28}$ e·cm ermöglichen.

Contents

I. Introduction

1. Search for the neutron electric dipole moment: theoretical background

Symmetry, or the principle of invariance under symmetry transformations, is one of the most important concepts in physics. Symmetries and conservation laws are a solid frame that holds the building of physical theory. But symmetry may not always be an immutable law of Nature. Some symmetries are exact, space-time transformation and gauge symmetries being such examples. In this work I will focus on the discrete space-time symmetries.

Parity transformation, **P**, changes the sign of the space coordinates **x**, **y** and **z**. Time reversal transformation, **T**, changes the sign of the time coordinate, **t**. Charge conjugation, **C**, transforms a particle into its anti-particle. These symmetries were believed to be exact in the fundamental physical theories. Parity was considered to be a good symmetry until 1956, Lee & Yang [1] discussed the possibility of parity non-conservation in weak interactions. They suggested some possible experiments of parity conservation. Parity violation was experimentally discovered in 1957 by Wu et al. [2] in the β-decay of Co^{60}. At the same time, Garwin, Lederman and Weinrich [3] and Friedman and Telegdi [4] also discovered parity violations in meson decays. Later, in 1964, Christenson, Cronin, Fitch and Turlay [5] discovered CP violation in neutral kaon decays. They first found that the long-lived neutral kaon state K_L could also decay to two pions with a CP= +1 with a branching ratio of $\sim 2 \cdot 10^{-3}$. The same CP violation mechanisms also occur in B_0 - $\overline{B_0}$ and is expected in the D_0 - $\overline{D_0}$ [6] systems.

Next experiments (Belle [7] experiment at the High Energy Accelerator Research Organization (KEK) and the BaBar [8] experiment at SLAC) have presented data for CP violation in the neutral B meson system. Known features in the Kaon, B-meson and in the D-meson system violate the combined operation of charge and parity symmetry can be fully explained by the complex phase in the Cabibbo–Kobayashi–Maskawa matrix (CKM) in the relativistic quantum field theory (RQFT) of the Standard Model (SM).

In local RQFT the three discrete symmetries P, T and C (and their violations) are not independent. Although P and CP symmetries are violated, the combined CPT transformation is a good symmetry: no violation of CPT has been observed so far [9, 10]. In the SM are two known possible sources [11] of CP violation. The first SM CP violation mechanism involves the Weak Interaction, the only interaction in which a quark can change its flavor and is only allowed to change by a unit amount of electron charge. There are four independent parameters, including three mixing angles, ($\boldsymbol{\theta_1}$; $\boldsymbol{\theta_2}$; $\boldsymbol{\theta_3}$)

and one complex phase, **δ** [12] for CKM, where $\boldsymbol{\theta_1}$ =13.05±0.05, $\boldsymbol{\theta_2}$=0.0201±0.011, $\boldsymbol{\theta_3}$=2.38±0.06, and **δ** =1.2±0.08. A nonzero complex phase **δ** will violate the CP symmetry by applying the CP transformation to the Weak Interaction Hamiltonian $H = \frac{4G}{\sqrt{2}} J^{\mu} J_{\mu}^{\dagger}$, where **G** is the weak coupling constant, $H_{CP} \neq H^{\dagger}$ if **δ** is non-zero and $\boldsymbol{J^{\mu}}$**-** charge-raising weak current. It is shown in [13].

Another possible source of CP violation in the SM is the θ term in the Lagrangian of Quantum ChromoDynamics (QCD), which describes the Strong Interaction. The generalized QCD Lagrangian has two terms, $L = L_{QCD} + L_{\theta}$ [14], where $\mathbf{L_{QCD}}$ describes the interaction among quarks and gluons which preserves the CP symmetry. The $\mathbf{L_{\theta}}$ term violates CP symmetry [15, 16]:

$$L_{\theta} = \theta \frac{g^2}{32\pi^2} G^{\alpha\mu\nu} \widetilde{G}_{\mu\nu}^{\alpha} , \qquad (1)$$

where $\widetilde{G}_{\mu\nu}^{\alpha} \equiv \frac{1}{2} \epsilon_{\mu\nu\rho\sigma} G^{\alpha\rho\sigma}$, $\epsilon_{\mu\nu\rho\sigma}$- the total antisymmetric tensor and $\epsilon^{\mu\nu\rho\sigma} = -\epsilon_{\mu\nu\rho\sigma}$, g is the strong coupling constant. The magnitude of the θ is unknown and can be only determined from the experiment, using predictions from models which relate physical quantities, such as the neutron EDM to this unknown parameter. It is an input to the SM and one expects that θ should be close to the order of one. From calculations [17, 18] the neutron EDM should be about 10^{-16}·θ e·cm. The current experimental limit of the neutron EDM is, however, 2.9 x 10^{-26} e·cm [19]. So, θ needs to be < 10^{-10}. This is termed the "Strong CP problem", when θ is so close to zero instead of being of order one as one may expect.

1.1. The nEDM as an indicator of discrete symmetry breaking

The experimental search for a neutron electric dipole moment has the potential to reveal new sources of time-reversal (**T**) and charge-conjugation-and-parity (**CP**) violation and to challenge calculations that propose extensions to the Standard Model.

The system, which is simple enough and well-understood, is the neutron. Though the neutron is a charge neutral particle, it can acquire a dipole moment if the positive charge and negative charge distribution of the involved quarks do not overlap with each other perfectly. In the rest frame of a non-degenerate quantum system with a non-zero spin, the direction of the spin $\hat{s}$ is the only vector to characterize the system. The "non-degenerate quantum system" means there is no degeneracy besides that due to 2s+1 possible orientations of the spin [20]. No other vectors can be selected since the system will be then degenerate, contrary to the property of the system. So the electric dipole moment $\vec{d}$

can only be along the spin $\hat{s}$ direction [21], $\vec{d}=d\hat{s}$. This applies to electrons, neutrons, protons, muons and other particles. If the neutron is placed in an external electric field $\vec{E}$, its Hamiltonian due to the interaction with electric field is $H=d_n\hat{s}\vec{E}$, where d_n is neutron electric dipole moment.

Name	Symbol	P	T
Time	**t**	+	-
Position	$\vec{r}$	-	+
Energy	**E**	+	+
Momentum	$\vec{p}$	-	-
Spin	$\vec{s}$	+	-
Electric field	$\vec{E}$	-	+
Magnetic field	$\vec{B}$	+	-

Table 1.1: Behavior of physical quantities under **P** and **T** transformation

According to the transformations in the Table 1.1, the Hamiltonian changes sign under both P and T transformation if d_n is non-zero. Assuming CPT is a good symmetry, CP is then also violated. Since the CP-violation discussed in the Standard Model is not sufficient to explain, e.g., the observed baryon asymmetry in the Universe (BAU), precision measurements of the nEDM present an opportunity for a direct violation of the T-symmetry and help identify new sources of T- and CP-violation to contribute for the explanation of the BAU. Thus we conclude that a nEDM is an indicator of breaking P- and T- symmetries in the sub-nuclear world. If the nEDM is found the sources and nature of the broken symmetry would not be easily revealed.

At present, the experimental upper limit of the neutron EDM is $2.9\cdot10^{-26}$ e·cm (90% C.L.)[19]. The Standard Model calculations have predicted d_n to be ~10^{-32}-10^{-31} e·cm [22].

2. Neutron electric dipole moment: experiments and techniques

James Chadwick discovered the neutron in 1932 (Nobel Prize in Physics in 1935). Since then, the study and measurement of the properties of neutrons were continued with huge interest. Purcell and Ramsey [23] pointed out, that it was possible to test the symmetry of parity by measuring the neutron EDM. The measurement of a neutron electric dipole moment is the most sensitive experimental test of the time reversal violation.

There are three methods proposed to measure the neutron EDM: neutron scattering [23], nuclear magnetic resonance (NMR) technique using neutron beams (1957-1977)[24], and NMR using bottled Ultra Cold Neutrons (UCNs) (after 1980) [25]. In neutron scattering, neutrons in a beam are scattered by the electrons in a solid lead target, which was chosen due to its large Z and its small absorption cross section for slow neutrons. The dipole moment is extracted assuming that the neutron-electron interaction is due to the nEDM. The observed n-e interaction strength would be due to the non-zero nEDM; an upper limit of $d_n < 3{\cdot}10^{-18}$ e·cm was extracted from the data. Early measurements of the neutron EDM were performed with beams of cold neutrons from reactors, but the relativistic transformation of the applied electric field into the neutron's rest frame produces an additional magnetic field. It's called $\vec{v}\times\vec{E}$ effect.

The best accuracy was achieved by the combination of nuclear resonance method and the use of UCN technique [26, 27].

2.1. The neutron EDM measurements with UCN

The measurement of the EDM is made with neutrons in a volume with uniform electric and magnetic fields $\vec{E}$ and $\vec{B}$, respectively. For a neutron in an electric field $\vec{E}$ and in a magnetic field $\vec{B}$, the field-dependent part of the Hamiltonian is

$$\mathrm{H} = -2(\mathrm{d_n}\vec{\mathrm{I}}\cdot\vec{\mathrm{E}} + \mu_\mathrm{n}\vec{\mathrm{I}}\cdot\vec{\mathrm{B}}), \qquad (1.1)$$

where $\mathrm{d_n}$ and μ_n are the electric dipole and magnetic moments of the neutron. Since $\vec{\mathrm{I}}$ is the only vector which defines the direction in the rest frame of the neutron, the EDM vector must point along $\vec{\mathrm{I}}$ and any component perpendicular to $\vec{\mathrm{I}}$ is unobservable. The Hamiltonian manifests parity (**P**) and time reversal (**T**) violation: under **P**, $\vec{\mathrm{E}} \rightarrow -\vec{\mathrm{E}}$, whereas $\vec{\mathrm{I}}$ and $\vec{\mathrm{B}}$ are unchanged; under **T** operation, $\vec{\mathrm{B}} \rightarrow -\vec{\mathrm{B}}$, and $\vec{\mathrm{I}} \rightarrow -\vec{\mathrm{I}}$, whereas $\vec{\mathrm{E}}$ is unchanged. Thus, if one applies the operators **P** or **T**, the Hamiltonian is altered, i.e. the electrostatic energy of the neutron stays the same

only if $d_n = 0$. Therefore $d_n \neq 0$ implies parity and time reversal violation:

$$\mathbf{P}H = -2(d_n\vec{I}\cdot(-\vec{E}) + \mu_n\vec{I}\cdot\vec{B}) \neq -2(d_n\vec{I}\cdot\vec{E} + \mu_n\vec{I}\cdot\vec{B}), \tag{1.2}$$

$$\mathbf{T}H = -2(d_n(-\vec{I})\cdot\vec{E} + \mu_n(-\vec{I})\cdot(-\vec{B})) \neq -2(d_n\vec{I}\cdot\vec{E} + \mu_n\vec{I}\cdot\vec{B}). \tag{1.3}$$

The experimental method to search for the EDM is to measure a change of the neutron-spin precession frequency in magnetic and electric fields in response to the change of the electric-field direction [23, 28]. If the applied constant electric field $\vec{E}$ is aligned with the magnetic field, we obtain for the spin precession frequency:

$$\nu_{\pm} = 2|\mu_n B \pm d_n E|/h \tag{1.4}$$

with h as Planck's constant, where the sign (−) stands for anti-parallel configuration of the magnetic and electric fields. The precession frequency difference between the two configurations (see Fig.1.1) is then

$$\Delta\nu = 4d_n E/h \tag{1.5}$$

with the electric dipole moment

$$d_n = h\Delta\nu/4E \tag{1.6}$$

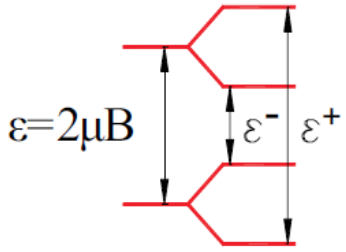

Figure 1.1: Schematic view of the neutron energy levels in a magnetic, and an electric field with different directions; ε: no electric field. For a non-zero neutron electric dipole moment $d_n > 0$: ε+: electric field parallel to the magnetic field; ε−: electric field anti-parallel to the magnetic field.

Progress in the EDM sensitivity was achieved by using UCNs. Y.B. Zeldovich [29] indicated that UCNs with kinetic energies lower than the optical potential of a wall material can be kept in a closed vessel for a long time, and F. L. Shapiro[30] proposed to use UCNs in searches for the neutron EDM, pointing out the considerable improvement of experimental accuracy achievable from an increase of the interaction time. Since UCNs stored in a bottle have a very small average velocity, $\vec{v}\times\vec{E}$ effects, are substantially reduced.

The technique to use stored UCNs in the search for the neutron EDM has been developed by two experimental groups working at the WWR-M reactor of the St. Petersburg Nuclear Physics Institute (PNPI) and at the Institute Laue-Langevin (ILL), Grenoble. At these Institutes, the best experimental EDM sensitivities have been obtained up today.

The current best nEDM upper limit of $d_n < 2.9 \cdot 10^{-26}$ e·cm (90% C. L.) was obtained at the ILL reactor at Grenoble.

2.2. Ramsey's method of separated oscillatory fields

N. Ramsey developed the separated oscillatory field method in 1949 (Nobel Prize in Physics in 1989) to measure the spin precession of a quantum mechanical system [31]. The basic principle is illustrated in Fig. 1.2:

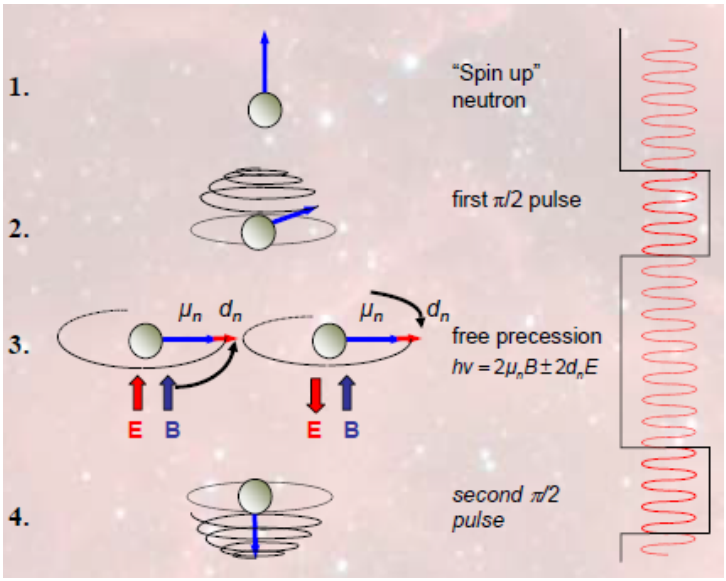

Figure 1.2.: Illustration of Ramsey's method of separated oscillatory fields.

The Ramsey cycle consists of four stages:

1) The neutrons are initially polarized along the main field axis.

2) A linear oscillatory field B_T, in which the neutron spins are precessed by π/2 and then oscillate at the neutron Larmor frequency, is applied perpendicular to the main field B_0:

$$B(t) = B_T \cos(2\pi\nu_L \cdot t) \qquad (1.8)$$

This oscillatory field is switched on and it rotates the spin at a given duration into the plane

perpendicular to the main field. (The frequency generator of B(t) is not switched off in order to keep its phase relation).

3) The neutrons precess now freely around the direction of B_0 for a time T (~140s). If nEDM is non-zero, the precession frequency in the combined magnetic and electric fields will differ from the Larmor frequency.

4) A second oscillating field pulse, phase coherent with the first pulse, further rotates the neutron spin by π/2. The accumulated phase is measured by counting the populations of the two resulting spin states after the second Ramsey pulse, N_{up} and N_{down}.

The experiment is operated on a batch cycle's principle, when cycles are conducted continuously, while the direction of E is reversed a few times per day. For example, the batch cycle's principle for the recent search on nEDM (old ILL experiment with a modernization and the new source of ultra-cold neutrons) at Paul Scherrer Institute (PSI) is:

1. Filling with polarized neutrons: about 40 s;
2. Carrying out the magnetic resonance;
3. Emptying of the experimental trap;
4. Spin analysis and detection to obtain N_{up} and N_{down}.

As it was written above, if ω is exactly equal to ω_0, the spin does a complete π flip. Otherwise, the spin acquires a phase shift during the free precession. It causes a characteristic resonance [32].

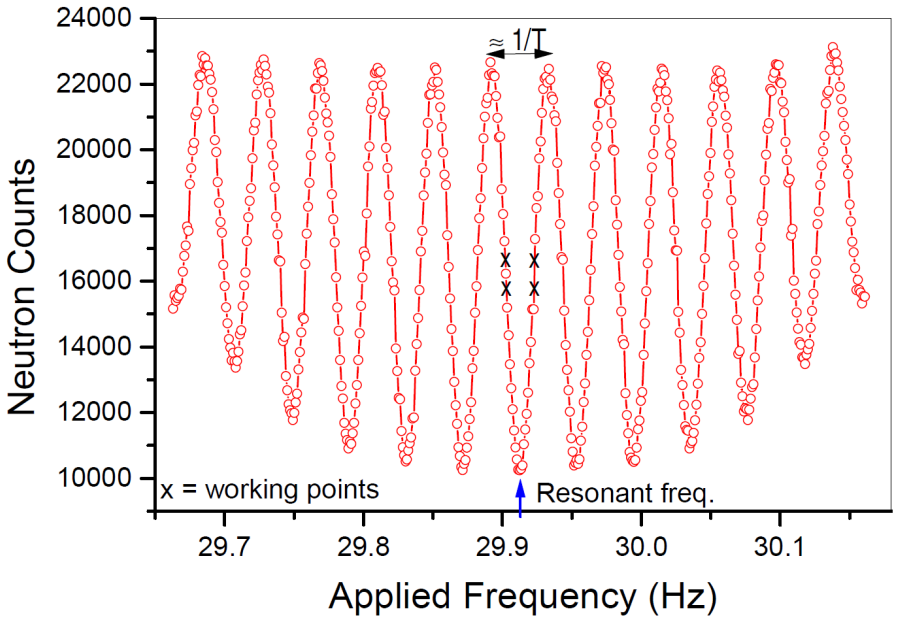

Figure 1.3: The resonance curve in the measurement the nEDM, the counting of neutrons as a function of the oscillating frequency of B(t).

In order to achieve the maximum sensitivity to such frequency shifts, the experiment operates halfway up the central valley in the regions marked by "×" on the curve. A small frequency shift produces a large change in the number of spin-up neutrons counted. The working points used to extract the resonance frequency obtained by fitting the central fringe. The neutron EDM can be calculated from the change in precession frequency between the two different directions of the electric field for perfectly constant magnetic field B. Using (1.6) and the data we can obtain d_n:

$$d_n = \frac{(N_{up,\uparrow\uparrow} - N_{down,\uparrow\uparrow} - N_{up,\uparrow\downarrow} + N_{down,\uparrow\downarrow})}{2\alpha ETN} \tag{1.9}$$

Here, α is the visibility of the central resonance fringe. It represents the efficiency of maintaining polarization throughout the process; N is the sum of the four neutron numbers: $N_{up,\uparrow\uparrow}$, $N_{down,\uparrow\uparrow}$, $N_{up,\uparrow\downarrow}$, $N_{down,\uparrow\downarrow}$.

The statistical uncertainty (the error due to counting statistics) of the nEDM experiment can be estimated in this way. For a known electric field, the uncertainty of d_n is

$$\delta d_n = \frac{h\delta\Delta\nu}{4E} \tag{1.10}$$

In order to minimize this error, we can generate as large an electric field as possible. From the uncertainty principle, $\Delta E \Delta t \geq \hbar$, we have

$$2\pi\hbar\delta\Delta\nu\Delta t \geq \hbar \tag{1.11}$$

The statistical error is inversely proportional to the square root of the sample size [33]. For our case this is the UCN number, N, then

$$\delta\Delta\nu \geq \frac{1}{2\pi T\sqrt{N}}, \tag{1.12}$$

where T is a time of free spin precession, N is the effective number of neutrons contributing in the measurement.

By multiplying h/4E on both sides of eq. (1.12), given a visibility α, the statistical error (sensitivity of the experiment) is

$$\sigma_{d_n} = \frac{\hbar}{2\alpha ET\sqrt{N}\sqrt{M}}, \tag{1.13}$$

where M is the number of measurements.

This equation can be applied assuming that the B_0 field has not changed over the four measurements.

2.3. History of neutron EDM experiments. Sussex-Rutherford-ILL experiment

Figure 1.4 shows the evolution of the measured upper limit on the neutron EDM as a function of year [34].

As it has been written, the neutron EDM's experimental upper limit is $d_n < 2.9 \cdot 10^{-26}$ e·cm (90% C. L.) [28]. The Standard Model calculations have predicted d_n to be ~10^{-32}- 10^{-31}e·cm (based at three loop level) [22, 35]. There are a lot of theories that predict the nEDM value to lie between 10^{-31}e·cm and 10^{-26}e·cm. The super-symmetry (SUSY) and most other possible extensions of the SM give rise to larger values of EDMs, because they arise already at one loop level [36].

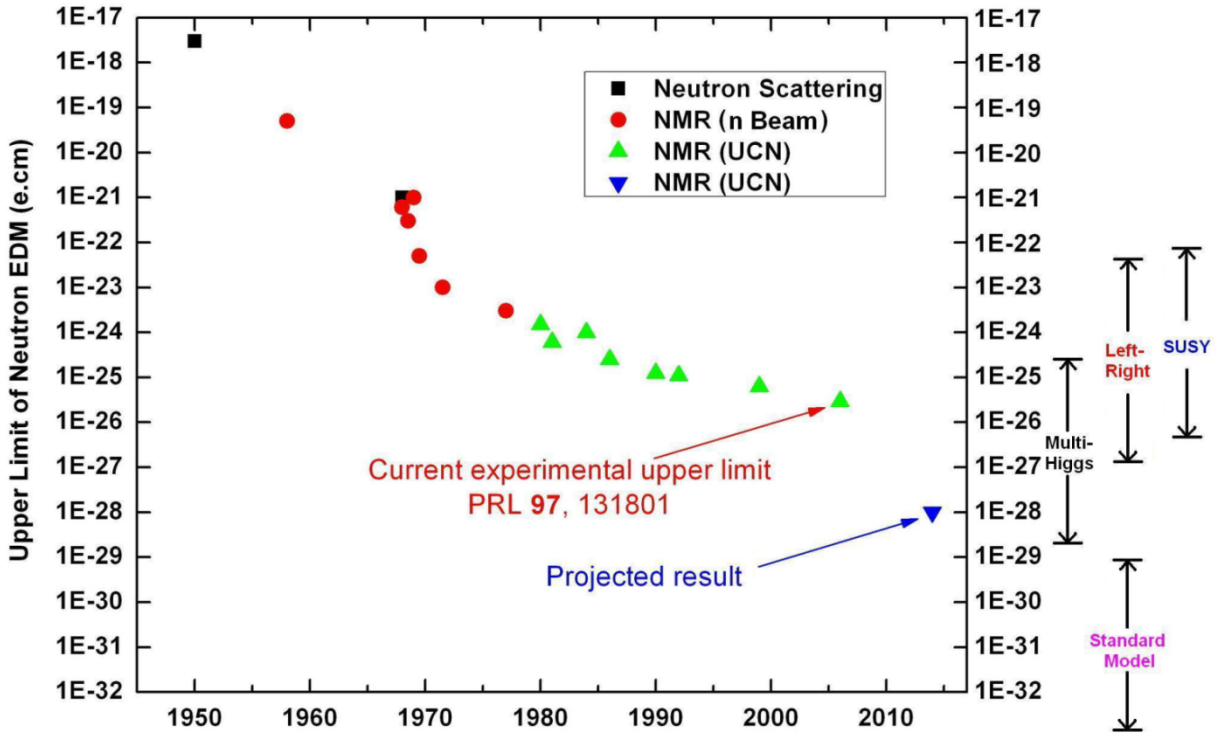

Figure 1.4: The nEDM experimental upper limit as a function of time. The experimental techniques are highlighted in the legend. Predicted ranges for the nEDM values from various theoretical approaches are shown to the right of the figure [37].

Currently, several collaborations worldwide try to measure EDMs with the next generation approaches to achieve an improvement of the sensitivity by almost 2 orders of magnitude to the 10^{-28}e·cm regime. An US community at the Spallation Neutron Source [38] is building a cryogenic experiment, based on the method for the production of UCN by down-scattering of cold neutrons in

superfluid liquid helium. Other groups try to improve existing technology and are working with trapped neutrons at room temperature (ILL [39] and PSI [40]).

Last results were achieved by the combination of nuclear resonance method and the use of UCN technique – experiments with trapped neutrons or storage experiments. All these measurements are much less accurate, than the measurements of atomic system [41, 42], but they have a strong impact on theory.

The latest and the most famous one is the RAL/Sussex/ILL experiment, later it has moved to PSI and it has been upgraded (see Fig.1.5).

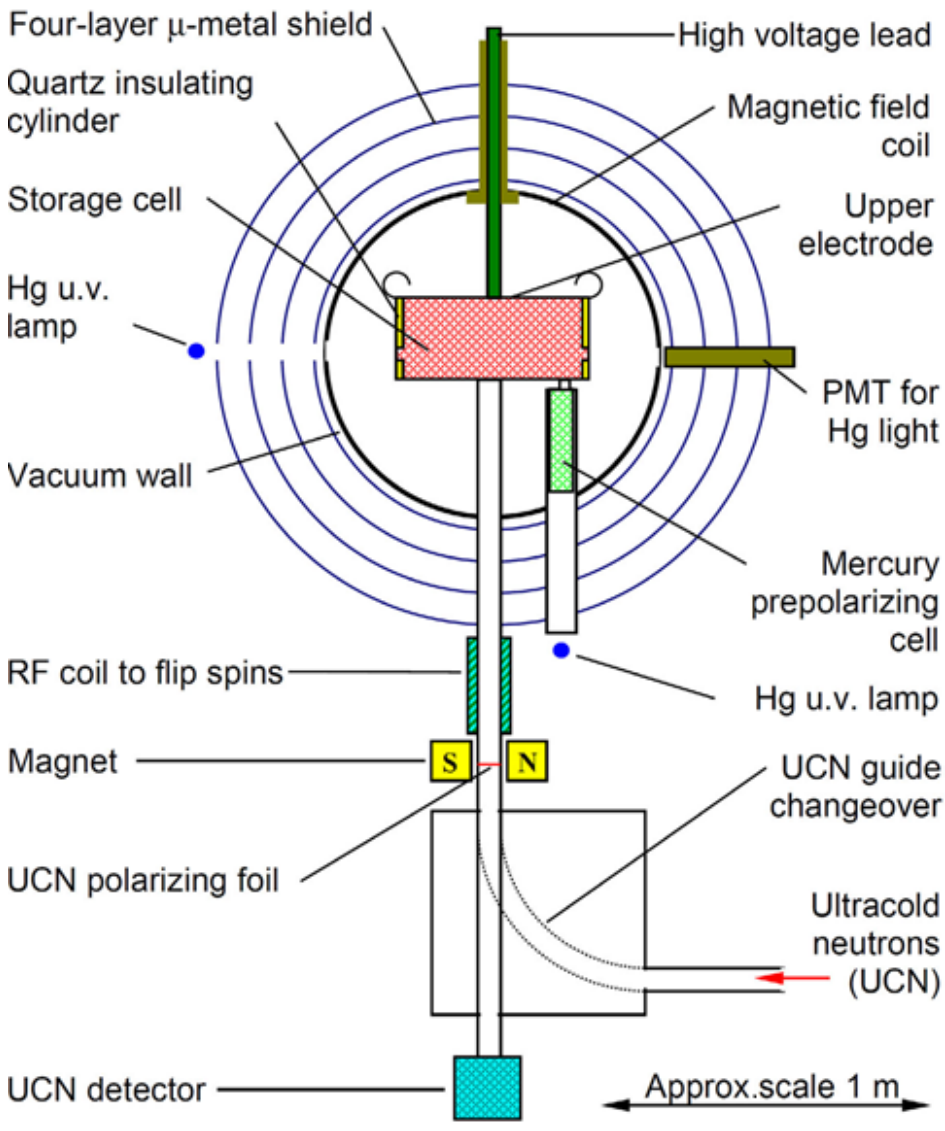

Figure 1.5: The Sussex-Rutherford-ILL apparatus for the search of the neutron EDM [43].

Figure 1.5 shows a schematic diagram of the room-temperature nEDM experiment at the ILL. The neutrons enter the neutron-guide from the UCN turbine and flow up to the polarizer foil (UCNs behave like a diffuse gas). Here is a division of the neutron flux. How does it work?

The potential energy V of a neutron in the magnetic field B is

$$V = -\vec{\mu}_n \cdot \vec{B}, \tag{1.14}$$

A 5 T magnetic field corresponds to about 300 neV UCN kinetic energy. In the inhomogeneous magnetic field B, a force F proportional to the potential gradient acts on the neutrons

$$F = \nabla(\vec{\mu}_n \cdot \vec{B}), \tag{1.15}$$

UCN in the presence of magnetic materials (here it's a polarizer foil), that polarize UCN beams, would experience total potential consisting of both magnetic and material optical potential, V_F.

$$V = V_F - \vec{\mu}_n \cdot \vec{B} = V_F - g \cdot \frac{e}{2m_p}\vec{I}, \tag{1.16}$$

Here g, g – the neutron g-factor, is equal to twice nuclear magneton – 3.82, e is the elementary charge, m_p is the proton mass, $\vec{I}$ – the neutron spin.

In according to eq. (1.16), the foil will have different potentials that depend on the orientation of the neutron spin $V_F \pm |\mu_n \cdot B|$. If the spin is oriented in the direction of the field within the foil, we call this orientation as "spin down", then $V = V_F + |\mu_n \cdot B|$. At $E_{kin.} < V_F + |\mu_n \cdot B|$ these neutrons will be reflected. Most of the neutrons with opposite spin orientation – "spin up" – can pass the foil. They reach the storage chamber at the center of the apparatus. Between the foil and the chamber an adiabatic spin flipper is situated, which is used at the end of the cycle, when the experimental trap is emptied. Then the polarizing foil will perform as an analyzer of the resulting neutron polarization after spin precession. Spin up neutrons are counted for 8 seconds, then the spin flipper is turned on and spin down neutrons can pass the foil for the next 20 seconds. At the end, the spin flipper is turned off and spin up neutrons are detected again, this time for 12 seconds. There counting periods are adjusted in order to avoid asymmetry between "spin up" and "spin down" counts for non-polarized neutrons.

The storage cell is located in a 1 μT vertical magnetic field; four layers of mu-metal were used to shield against external fields, including that of the Earth. They provide a radial shielding factor of about 10^4.

The storage cell consists of a hollow electrically insulating cylinder located between a HV electrode (top) and a ground (bottom) electrode. A high voltage of up to 180 kV (which translates to an electric field of 15 kV/cm) is applied to the top electrode. After each series of measurement cycles the high voltage polarity is reversed.

The filling time of the storage cell is about 20 seconds, after that the valve for neutrons is closed and the Ramsey cycle to the trapped neutrons is applied.

A ^{199}Hg magnetometer system is used to monitor of the B_0 stability. The ^{199}Hg vapor is produced by heating ^{199}HgO. This vapor is spin-polarized in the pre-polarizing cell by optical pumping from the light emitted by Hg discharge lamp, and it is fed into the storage chamber just after it is filled with UCN. The ^{199}Hg spin is also rotated into the precession plane by an RF pulse at the Hg Larmor frequency (~8 Hz for $B_0 = 1\mu T$) and they precess afterwards around the B_0-field. In an inhomogeneous magnetic field the field precession angle might not be the same for all UCN thus mimicking a false EDM effect.

Four layers of magnetic shield that performed from μ-metal (an effective permeability of 20000), is used to reduce the influence of external magnetic fields, nevertheless, strong external fields still can penetrate to the inside to some extent.

One of the main possibilities to reach a high sensitivity for EDM measurements is the homogeneity of the internal magnetic field.

3. The neutron electric dipole measurement at TU Munich

An advanced approach for a next generation of nEDM's measurement is the new experiment at the FRM II (Forschungsreaktor München). The goal is to reach a sensitivity of $5{\cdot}10^{-28}$ e·cm and a corresponding control of systematic effects of $\sigma_{d,\mathrm{syst}} < 2{\cdot}10^{-28}$ e·cm (1σ). The new measurement extends proven and already known technologies in order to achieve these goals.

The main possibilities to improve nEDM limit are:

1. A strong source of UCN;
2. An increase of the neutron polarization (see Chapter III);
3. Sufficient control of electric and magnetic fields;
4. Improved possibilities to test for systematic effects;

3.1. Principle layout

UCN are stored in two vertically aligned cylindrical vessels at room temperature and a vertical magnetic field B_0 (see Fig.1.5). The chambers are filled with a high density of UCN and simultaneously with a cohabitating magnetometer, consisting of ^{199}Hg vapor.

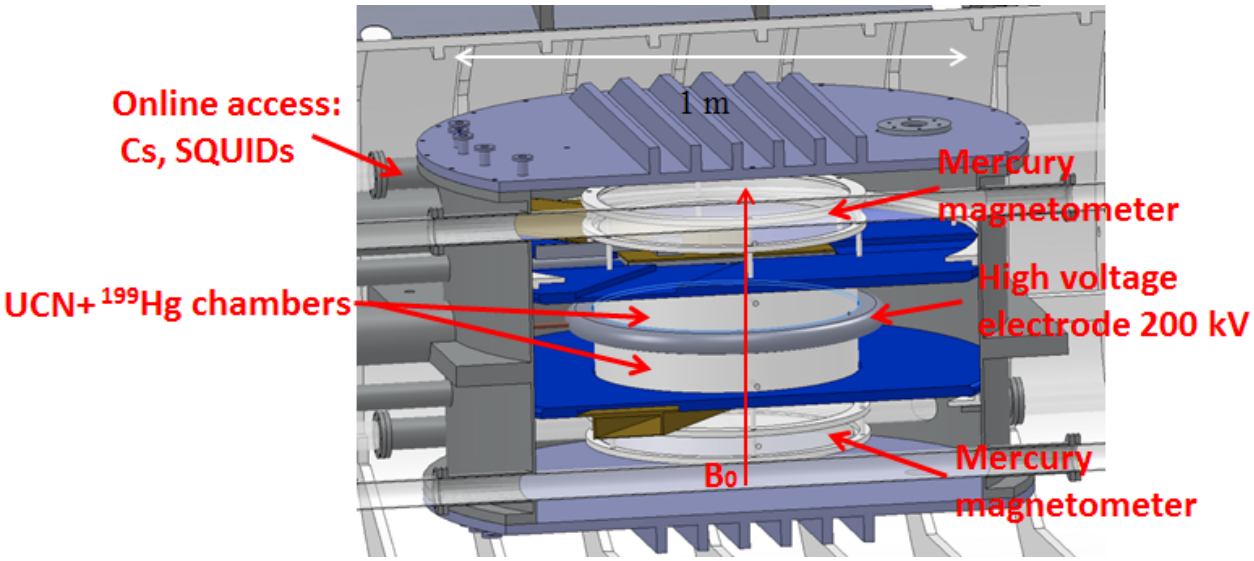

Figure 1.6: Double UCN chamber with co-magnetometers neutron EDM measurement setup. Ramsey experiment with UCN stored at room temperature.

A high voltage electrode is placed in between the cells. Above and below the arrangement, a ground electrode is placed. This provides measurements with an electric field parallel and anti-parallel to B_0 simultaneously. Cells with ^{199}Hg vapor on the top and bottom of the chambers are co-magnetometers. Thus, all 4 chambers are available for needs of magnetometry and for the determination of vertical gradients. A light-shift free laser based scheme for ^{199}Hg measurement reduces geometric phase effects (GPE). Plastic tubes that reach through the vacuum chamber are placed within close distance tangentially to the magnetometer cells in order to have access inside the experiment during the measurement. Any types of magnetic field sensor can be placed inside the tubes which is important for online mapping of the magnetic field and residual field distribution inside the volume.

Drifts of the homogeneous B_0-field cancel when the two Ramsey experiments are performed simultaneously in two chambers with inverted E-fields.

3.2. Ultra-cold neutron source

The source of UCN at the FRM II [44] will be placed in a tangential beam tube inside the reactor at the Technische Universität München in a thermal neutron flux of $1 \cdot 10^{14}$ s^{-1}. Solid deuterium is used as a super-thermal converter for the production of UCN. A beam line will be installed from specially prepared replica foil tubes with a relative transmission of > 0.99 per meter. The projected polarized UCN density is > 3000 cm^{-3}.

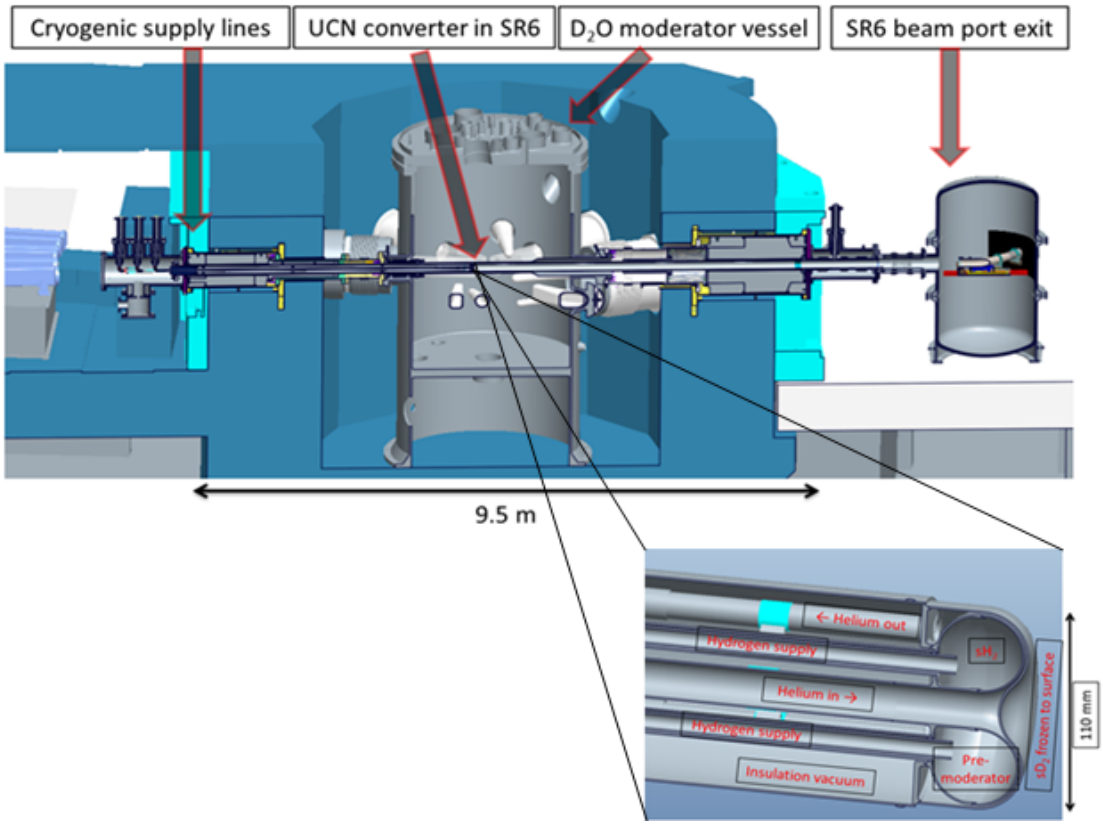

Figure 1.7: Strong new UCN source at the FRM II.

3.3. Vacuum chamber

The vacuum chamber has a cylindrical volume with its symmetry axis aligned along the B_0 field direction with large flanges on the top and bottom. The inner diameter of the chamber is 1060 mm, the height is 640 mm (see Fig. 1.8).

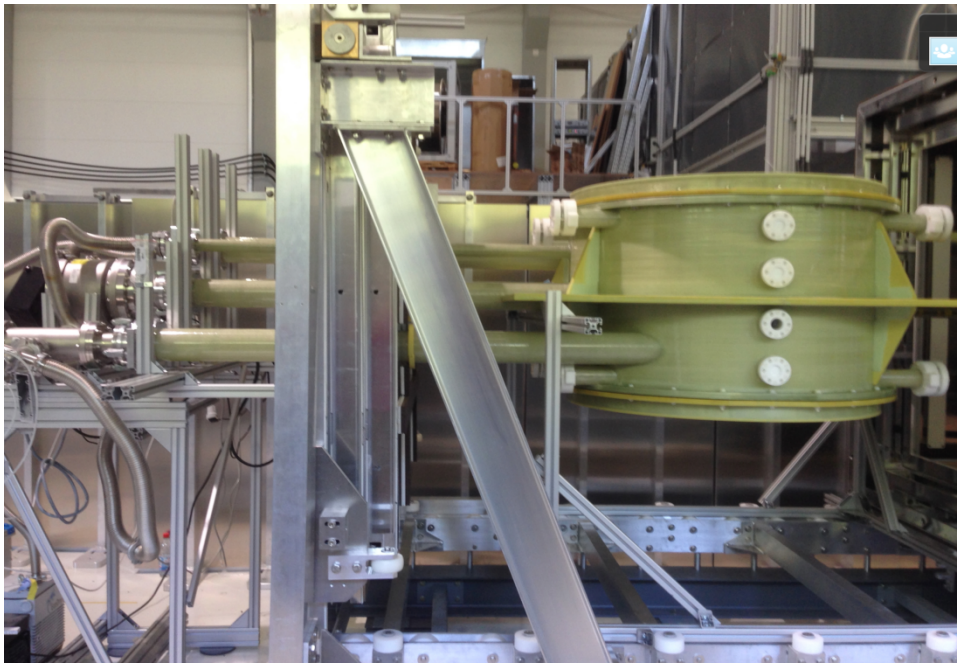

Figure 1.8: Vacuum chamber with feed-through for neutron guides, high voltage and actuators. All components are fabricated from glass fiber.

In order to avoid false signals due to geometric phase effects in magnetic fields caused by contaminations materials, the vacuum chamber must be non-magnetic. It must be also non-metallic in order to avoid Johnson noise which creates magnetic fields of the same order as limit of sensitivity of the experiment. Conductors that go through the shielding, e.g. the high voltage for the electric field, must have low electrical conductivity since it might create an antenna, which is a source of radio-frequency noise. A glass fiber composite shows high non-magnetic behavior and outgassing of less than 10^{-10}mbar·l·s^{-1}·cm^{-2}. It is suitable to achieve a vacuum 10^{-6}mbar in the chamber with pumping from outside the electro-magnetic shielding. The alignment of the chambers and the electric field must be matched to the magnetic field direction by 10^{-4}. The vacuum chamber, as well as the stack of

chambers, can be actively aligned relatively to the magnetic coil system with feedback of magnetic and interferometric means of adjustment and vibration monitoring. It was subsequently found an alternative to the vacuum as an insulator. With the help of the silicone gel, one can provide the insulation of the experimental chamber and full access around the chambers for magnetometers. Sections 4.3.1 and 5.3 in the Chapters 4, 5 describe in detail the tests and simulations concerning the use of silicone gel. Currently being considered two ways to isolate the experiment: vacuum and silicone gel.

3.4. Magnetic fields

One of the main sources of systematic errors is the non-uniformity and fluctuations of the magnetic field because the magnetic field determines the frequency of the neutron's spin precession – Larmor frequency. Next generation EDM measurements are extremely sensitive to magnetic fields as well as gradients. The magnetic field used for the EDM measurement must be homogeneous on a relative level of 10^{-4} over the volume of the EDM chambers and the magnetometer systems.

For a holding field of the Ramsey experiment of, e.g. B_0 = 1 μT, transverse field components must be smaller than 0.3 nT. At this level, false effects due to geometric phases of the Hg co-magnetometer already reach $d_{Hg,false} \sim 4 \cdot 10^{-27}$e·cm. Also geometric phases acquired by UCN become relevant on the level $d_{n,false} < 10^{-27}$e·cm.

An unmeasured change in average magnetic field between measurements yields a false value for an EDM:

$$\mathrm{d_{false}} = \frac{\mu \Delta B}{2E} \tag{1.17}$$

The unmeasured fluctuations between two Ramsey cycles must be less than about 10 fT for a sensitivity of 10^{-28}e·cm for 1 year nEDM measurements and statistically distributed magnetic field drifts. The drift between two measurements with inverted electric field in the double chamber approach is reduced to a drift of the vertical gradient only.

The magnetic environment in case of our nEDM experiment is controlled by a combination of several means: the floor is magnetically and vibrationally decoupled and built with low magnetism materials on an area of 6 × 9 m^2, covered by a temperature and humidity controlled clean-room environment. In order to compensate static and dynamic ambient fields and second order gradients, active 24 coil ambient field compensation is installed. Feedback is provided by 180 fluxgate magnetic field [45, 46].

Passive shielding is arranged by Mu-metal (two layers) and aluminum (1 layer) shells in a nested cuboid arrangement in order to reduce electromagnetic disturbances at different ranges of frequencies.

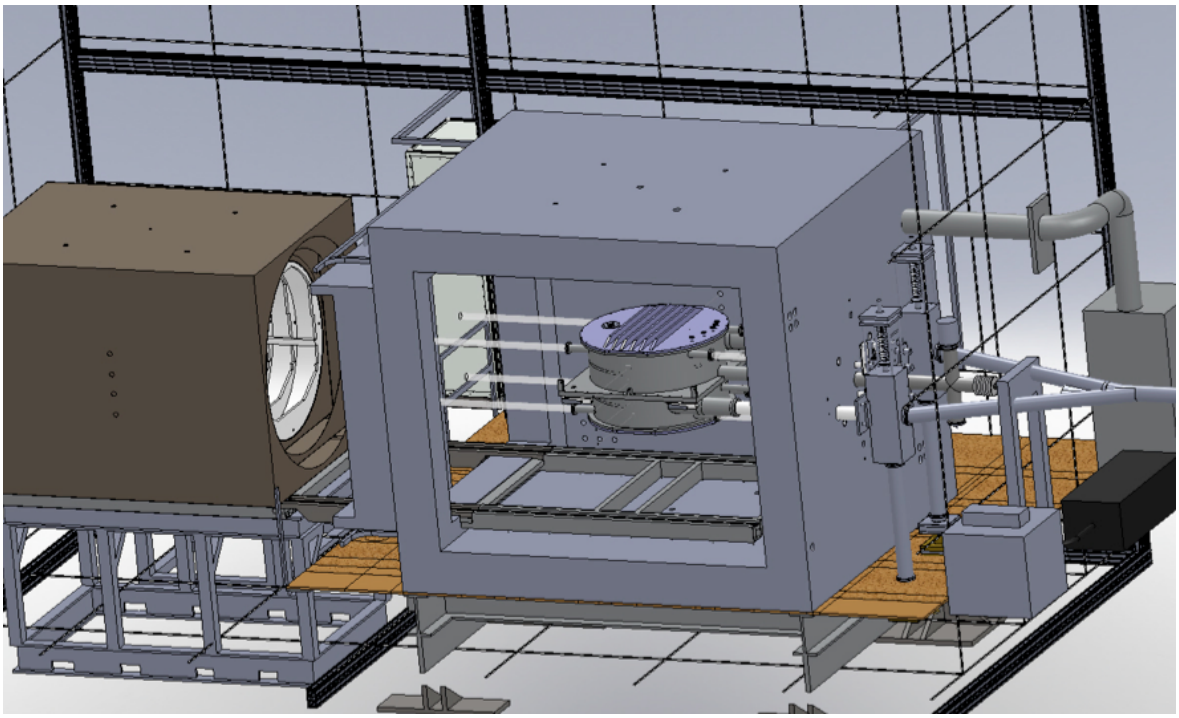

Figure 1.9: The shielded room with all integrated systems. Inner part can slide into the room on a rail system. A cylindrical Mu-metal shield with $\sim$ 1.5m diameter forms the innermost layer inside this cuboid assembly [45].

The inner magnetic shielding is a horizontal cylinder made of Mu-metal with a cosine-theta shaped coil aligned in the cylinder to produce a vertical magnetic field with detachable end caps. An optimized field configuration allows a perfect reduction of residual fields by demagnetization of cylindrical inner shield around the nEDM experiment volume.

3.5. ^{199}Hg magnetometry

Since the goal of the nEDM experiment is to achieve two orders of magnitude improvement in sensitivity over the current experimental upper limit, it requires excellent magnetometry in order to track the magnetic field's noise and drifts from measurement to measurement. The room temperature nEDM experiments use cohabiting magnetometers, i.e. mercury atoms, precessing in the storage chamber during the same time as the actual neutron EDM measurement. The ^{199}Hg magnetometer system was shortly described above for the Sussex-Rutherford-ILL experiment.

Figure 1.10 shows the principal drawing of the magnetometry for the new nEDM experiment.

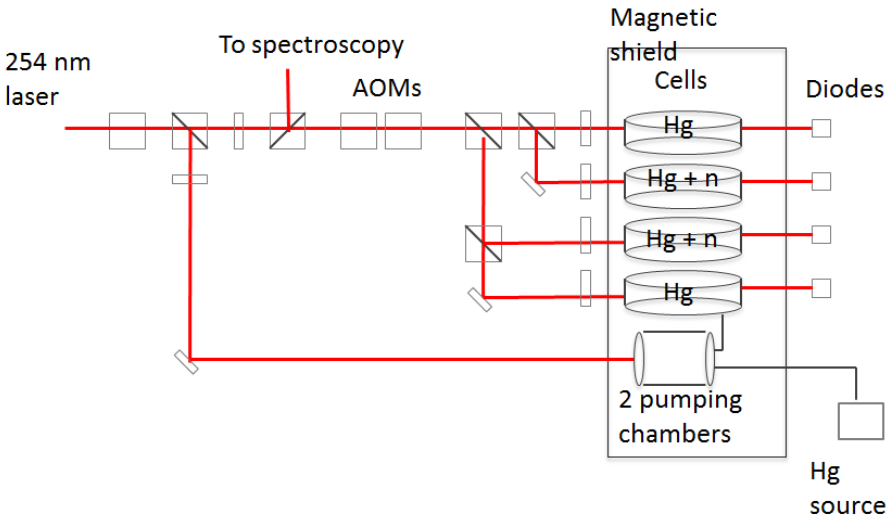

Figure 1.10: Magnetometry and co-magnetometry based on polarized 199Hg vapor with a laser based optical system [46].

Light from a source outside the shield penetrates through small holes in the shield, through the EDM chamber and again leaves the shield through holes and is detected outside the shield.

In the Ral-Sussex-ILL experiment the precession signal is read out via a transverse, circularly polarized beam which is absorbed in the chamber as a function of spin orientation of the Hg atoms. In the new experiment the same principle will be used. The alignment of the ^{199}Hg magnetometer can cause a so called light-shift effect, which directly translates in a false EDM measurement. The ^{199}Hg measurement relies on a light-shift free laser-based scheme [26] which also reduces geometric phase effects [27]. An additional and alternative magnetometry system is based on a novel approach by using ^{129}Xe to

optimize high voltage behavior and to study systematic effects. Free precessing ^{129}Xe nuclear spins are almost completely decoupled from the environment, so as a co-magnetometer ^{129}Xe is very suitable for precision field measurements (provides long-term stability). In Chapter 3.3 the measurement of high-voltage breakdown in the gaseous ^{129}Xe is described. These tests were conducted to determine the possibility of using xenon as the co-magnetometer.

3.6. Cs magnetometry

Cs magnetometry allows measuring of vertical gradients of the magnetic field and provides slow field stabilization. Scalar cesium magnetometers inserted into online access tubes of vacuum chamber (4 online access tubes for Cs magnetometer array, see Fig. 1.6) provide the tracking magnetic field, its gradients and glitches during nEDM measurement. It is expected to use up to 32 magnetometer heads in our experiment.

Cs magnetometers are scalar magnetometers, so they measure module of the magnetic field

$$\left|\overrightarrow{B_0}\right| = \sqrt{B_x^2 + B_y^2 + B_z^2}. \qquad (1.18)$$

If B_x and B_y components of the magnetic field are small compared to B_z component, the Cs magnetometers measure in principal only B_z component. The principal of the measurement based on the Faraday effect is shown in Fig. 1.11.

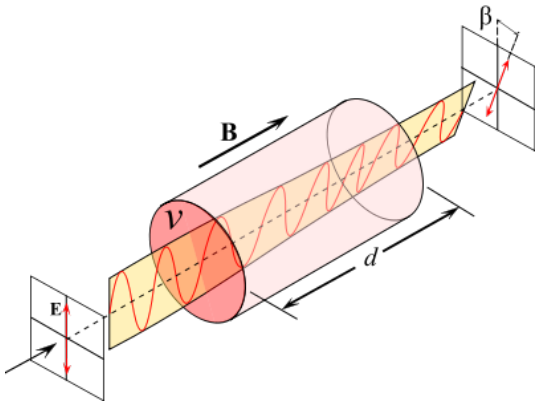

Figure 1.11: Faraday effect (Faraday rotation or magneto-optical phenomenon): The effect is the concept for measurements using cesium magnetometers. Here E is linearly polarized light, ν is the Verdet constant, d is longitudinal size of the isotropic medium, B is the magnetic field and β is the rotation angle of the polarization plane.

Rotation of the plane of light polarization of the incoming light is determined as

$$\beta = v \cdot B \cdot d \tag{1.19}$$

Figure 1.12 shows the test cell for Cs magnetometry, fixed in the holder, which was fabricated on a 3D printer [46].

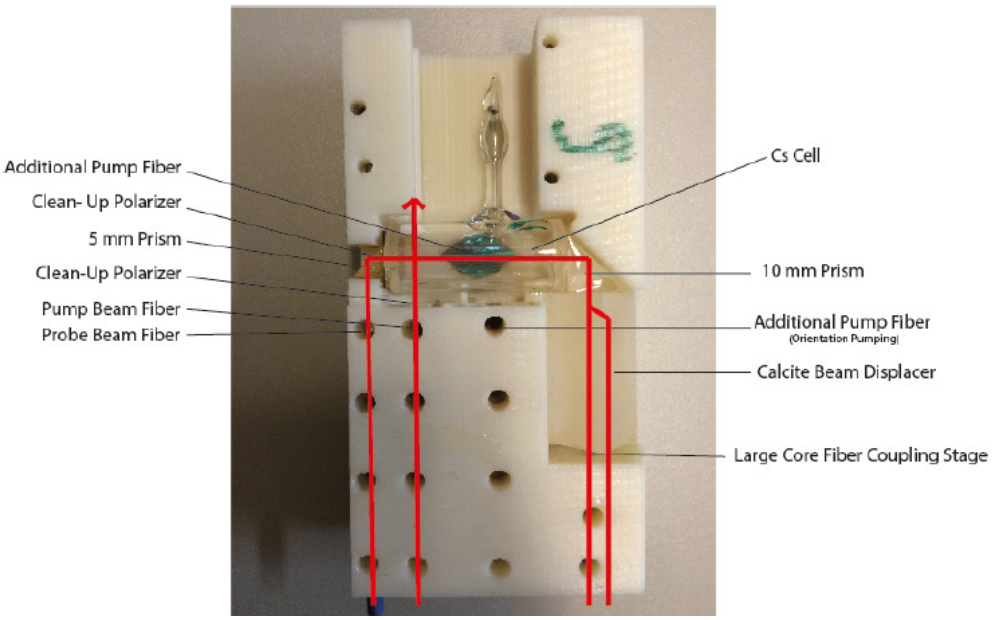

Figure 1.12: Cs cell in the holder. The red line shows the direction of propagation of the laser beam.

3.7. SQUID magnetometry

Superconducting Quantum Interference Devices (SQUID) are magnetic field sensors with the highest sensitivity and largest dynamic range known to date. A SQUID system will be used in the new neutron EDM experiment for additional magnetometry. They will be used for mapping of the fields inside the EDM experiment, tracking of field fluctuations while the experiment is running, and readout of polarized noble gases used for magnetometry. The typical SQUID magnetization measurement setup consists of a test sample, at a constant temperature, placed in a uniform field.

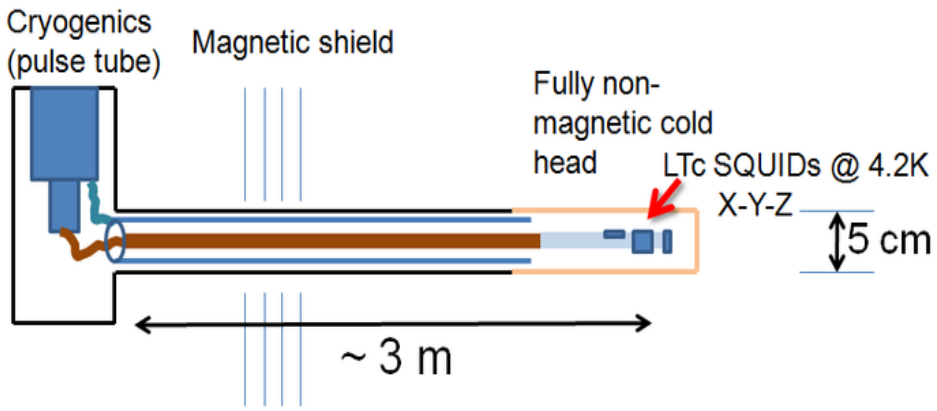

Figure 1.13: A concept of the SQUID system.

SQUIDs can be moved to any position in any tube of the experimental setup while the experiment is operating. This is a well suited tool that provides information on the level higher than 1 Hz. At DC level an accuracy of few pT can be expected. The cryostat contains several SQUID sensors: 3 are used for field measurements and additional sensors are used to monitor fluctuations of the vertical gradient at certain position during the measurements.

3.8. UCN optics

This section includes many components that provide the transport of the neutrons, their storage, and polarization as well as materials that are most appropriate to coat these components. The location of our experiment with respect to the reactor is shown in Figure 1.14.

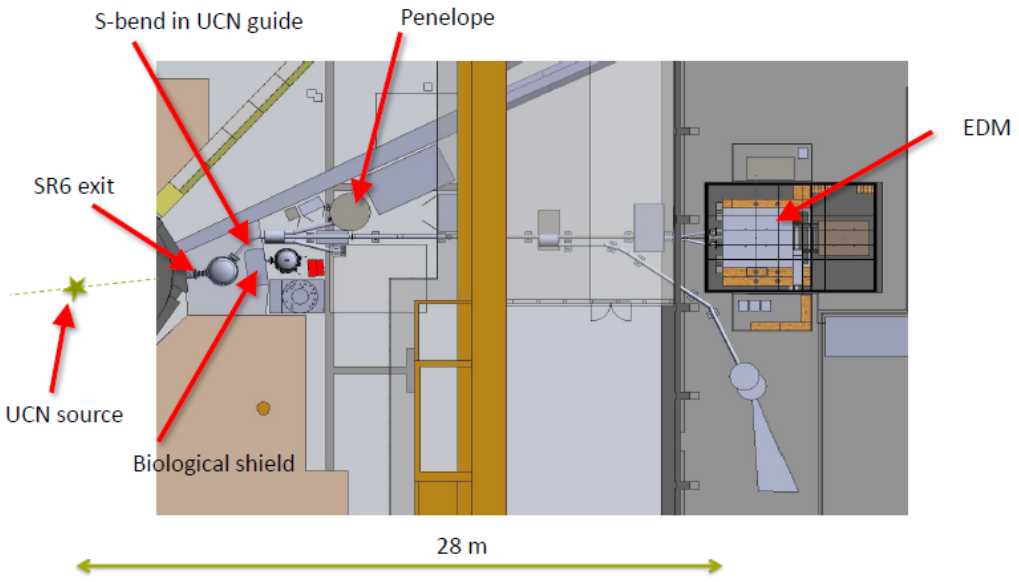

Figure 1.14: UCN guide system at the FRMII (Forschungsreaktor München). EDM is the placement of our experiment.

The UCN spectrum starts at around 100 neV due to the material optical potential of the deuterium UCN source, which is situated on the same height as the UCN's guide and the high voltage electrode. A neutron guide from FRM-II UCN source to the experiment is made from welded replica foils. This guide with 114 mm inner diameter leads UCN through the superconducting solenoid for UCN polarization. This superconducting solenoid is situated 4 meters in front of the experiment. A RF spin flipper can be deployed to adjust the energy spectrum of the polarized UCN by using the Zeeman splitting in the magnetic field. This tool can be used to investigate velocity dependent systematic effects by changing the average velocity of the UCN spectrum without an influence on any parameters in the nEDM experiment. Figures 1.15 and 1.16 UCN beam splitter and the UCN switch, which were tested at the ILL (Institute Laue-Langevin, Grenoble) in 2014 [46].

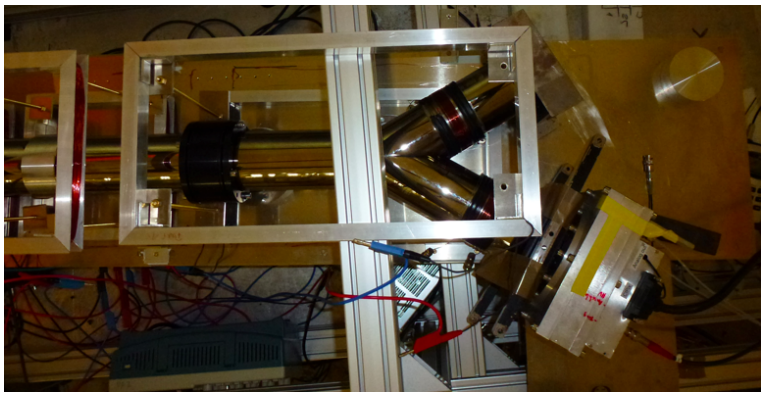

Figure 1.15: UCN beam splitter. The transmission is 60%. Polarization, adiabatic transport and spin detection were tested.

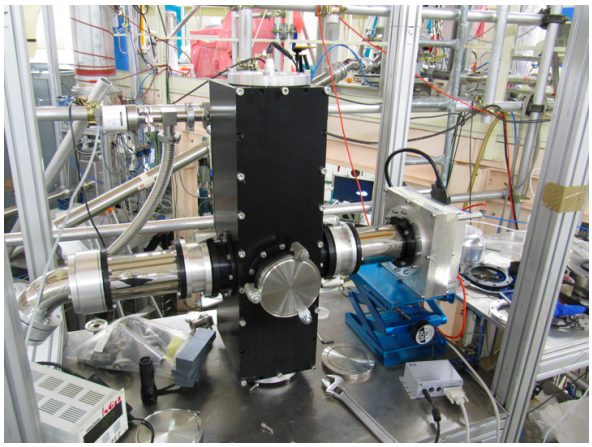

Figure 1.16: UCN switch installed in ILL for testing.

Figure 1.17 shows the nEDM spectrometer chamber with a new plug shutter.

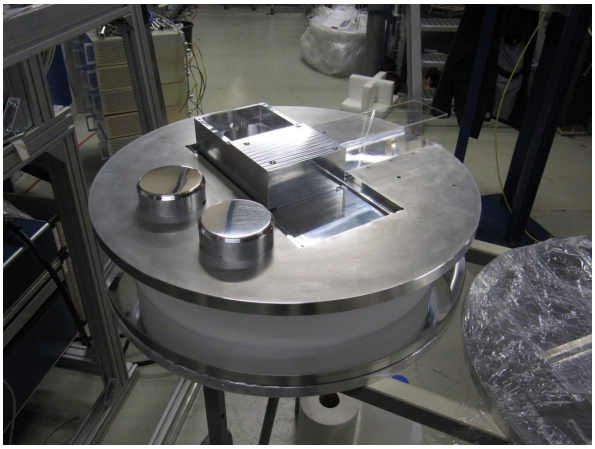

Figure 1.17: The nEDM chamber. The insulator ring is made of fused quartz, its inner surface will be coated with dPE (deuterated polyethylene). The shutter can be seen on the top cover.

Deuterated polyethylene was chosen because of its properties as the coating material for UCN storage and transport, such as:

i) High Fermi potential, V_F, it is 214±10 neV (see Section III, Chapter 2), and the wall loss coefficient η is $2 \cdot 10^{-4}$ per wall collision. It becomes possible to eliminate slits in UCN storage volumes.

ii) Deuterated polyethylene is a good alternative to BeO because of its high electrical resistivity.

iii) High ultra-violet resistance.

3.9. Extracting an EDM value

The double chamber construction with inverted electric field allows performing two Ramsey cycles in the same magnetic field B_0 simultaneously. Hence, it helps us to cancel drifts of the homogeneous magnetic field B_0 and to minimize the requirement for drift stability of the magnetic environment. However, fluctuations in the gradient (gradient noise) affect the nEDM measurement. To extract the order of magnetic gradients the procedure, which is used in precision gradiometry arrangements [47], will be described.

In Fig. 1.6 you can see four cells: the two of them are filled with n+^{199}Hg, other two are filled just with ^{199}Hg atoms. We can measure the vertical magnetic field gradient and its fluctuations by the cells in the center with applied electric field and by the magnetometer cells on top and bottom without applied electric fields together. Let's express the magnetic field as a Taylor series in order to determine the magnetic field gradients. The height from the center of the experiment to the height of the upper (+) and lower (-) chambers is h and the magnetometer chambers are at 3h:

$$\omega_{Hg,top/bottom} = \frac{\mu}{\hbar}\left(B_0 \pm 3h\frac{\partial B_0}{\partial z} \pm \frac{9}{2}h^2\frac{\partial^2 B_0}{\partial z^2} \pm \frac{9}{2}h^3\frac{\partial^3 B_0}{\partial z^3}\right), \quad (1.20)$$

$$\omega_{Hg,center,top/bottom} = \frac{\mu}{\hbar}\left(B_0 \pm h\frac{\partial B_0}{\partial z} \pm \frac{1}{2}h^2\frac{\partial^2 B_0}{\partial z^2} \pm \frac{1}{6}h^3\frac{\partial^3 B_0}{\partial z^3}\right) \quad (1.21)$$

It allows extracting the gradients from four stacked ^{199}Hg cells with an accuracy of < 10 fT. The analysis of the measurement is based on the Sussex-RAL-ILL experiment with a double magnetometer [36, 48]. When an electric field is applied, the reading of the Hg frequency will differ depending on the alignment of electric field relatively to the direction of magnetic field B:

$$\omega_{Hg,center,top/bottom} = \frac{\mu}{\hbar} B_{Hg} + \frac{1}{\hbar} E\left(d_{Hg} + d_{Hg,false}\right), \tag{1.22}$$

where $d_{Hg} < 3.1^{-29}$e·cm [49] and $d_{Hg,false}$ – signals that mimic EDM due to effects of particles that move through the electric and the magnetic fields.

In the end of the nEDM measurement, the frequency of the neutron $\omega_{n,\frac{t}{b}}$, extracted from the simultaneous Ramsey measurements on top and bottom cells are compared to $\omega_{Hg,center,\frac{t}{b}}$ and the signal $d_{n,false}$ originating from systematic effects.

As the average velocities of UCN and ^{199}Hg differ significantly, the average center of gravity for UCN is Δh~2.5mm lower than for mercury. Then UCN and ^{199}Hg will see different average magnetic field B (a vertical gradient changes the ratio R of the UCN and mercury spin precession frequencies). So for mercury atoms we have:

$$B_{avg,Hg} = B_0 + \frac{\partial B_z}{\partial z} h/2 \tag{1.23}$$

and for neutrons

$$B_{avg,n} = B_0 + \frac{\partial B_z}{\partial z}\left(\frac{h}{2} - \Delta h\right). \tag{1.24}$$

Each measurement cycle forms the ratio of the neutron to mercury Larmor frequency R = $\frac{\nu_n}{\nu_{Hg}}$, and we obtain

$$R = \frac{\gamma_n}{\gamma_{Hg}}\left(1 - \frac{\frac{\partial B_z}{\partial z}\Delta h}{B_0 + \frac{\partial B_z}{\partial z} h/2}\right). \tag{1.25}$$

Alignment of electric and magnetic field plays an important role, because it is also a source of systematic error. To account for the influence of alignment one usually extracts the EDM as a function of the ratio of precession frequencies for different alignments of B- and E-fields:

$$R^{\uparrow\uparrow} = \left|\frac{\gamma_n}{\gamma_{Hg}}\right| - \frac{2d_{meas}}{\hbar\omega_{Hg}} E + \Delta h \frac{\frac{\partial B_z}{\partial z}}{|B|} \left|\frac{\gamma_n}{\gamma_{Hg}}\right|, \tag{1.26}$$

where the sign change for the respective alignments of B- and E-fields relative to each other. γ_n and γ_{Hg} are gyromagnetic ratios of the neutron and mercury atom. Here

d_{meas} is

$$d_{meas} = d_n + d_{n,false} + \left|\frac{\gamma_n}{\gamma_{Hg}}\right| (d_{Hg} + d_{Hg,false}). \quad (1.27)$$

Taking into the account transverse magnetic field components that appear from two conspiring effects (see in the chapter below): radial component caused by the vertical gradient, B_{0xy}, and fields caused by the motion of the particles in the electric field, B_v, get the deviation from the Larmor frequency that called as the Ramsey-Bloch-Siegert shift:

$$\partial\omega \propto \frac{\partial B_z}{\partial z} r \cdot \frac{\vec{v}\times\vec{E}}{c^2}. \quad (1.28)$$

The two chambers construction for nEDM experiment allows measurements with E-parallel and E-antiparallel to B simultaneously. The analysis R versus d_{meas} can be done for $R^{BE} = R^{\uparrow\uparrow},\ R^{\uparrow\downarrow}$ to obtain the set of curves with a linear behavior around the region of zero gradients and a defined slope that is inverse for the inverse B and E alignment. This slope originates from systematics that scales with the sign of magnetic field B_0:

$$d_{meas} = d_n \pm \alpha(R_\alpha - 1) \quad (1.29)$$

The sign depends on the polarity of B_0. The intersection at the position of zero the gradient only shifted by an EDM and higher order corrections. The result must correspond to measured combinations of $R^{BE} = R^{\uparrow\uparrow},\ R^{\uparrow\downarrow}$.

II. Systematic effects from electric field stability

In this Chapter the systematic uncertainties of the neutron EDM experiment are discussed. All systematic effects can be classified as [48]:

1. Directly related to the magnetic field. Mainly any drifts and fluctuations of gradients, as well as leakage currents;
2. Particle motion related effects. They appear from the *B* and *E* inhomogeneities, for example, geometric phases of the Hg atoms and the neutrons;
3. Mechanical effects, like vibrations, alignment of electrodes or laser beams, symmetry of the chamber and shutters.

The geometric phase effect is the leading source of systematic error in the room-temperature experiment, and will be discussed later.

The reason for systematic effects lies in the coupling of the magnetic moment to magnetic fields.

$$d_n^{meas.} = d_n + d_{n,f} = d_n + \frac{\mu_n}{2E}\Delta B = d_n + \frac{\hbar\gamma_n}{4E}\Delta B. \quad (2)$$

Then $d_{n,f}$=$-2 \cdot 10^{-12} e \cdot cm \frac{\Delta B}{1T}$ for our electric field E=150 kV/12 cm.

An excerpt of systematic effects for the previous generation of the experiments is shown in the table 1 [36]:

Effect	**Shift[10^{-27} e·cm]**	**σ [10^{-27} e·cm]**
Door cavity dipole	-5.60	2.00
Other dipole fields	0.00	6.00
Quadrupole difference	-1.30	2.00
v x E translational	0.00	0.03
v x E rotational	0.00	1.00
Second order v x E	0.00	0.02
Hg light shift (geom. phase)	3.50	0.80
Hg light shift (direct)	0.00	0.20
Uncompensated B-drift	0.00	2.40
Hg atom EDM	-0.40	0.30
Electric forces	0.00	0.40
Leakage currents	0.00	0.10
Ac fields	0.00	0.01
TOTAL	**-3.80**	**7.19**

Table 1: Systematic effects and their influence on the current nEDM sensitivity in units of 10^{-27} e·cm.

i) The first three items are the most critical and they are related to the quality of the magnetic field. Neutrons are moving on different paths in the measurement cell, so any spatial non-uniformity and temporal instability will increase the uncertainty in the neutron frequency measurement. The way to minimize these effects is the development of a highly homogeneous magnetic environment.

ii) A rotational $\vec{v} \times \vec{E}$ effect is due to motional magnetic fields in an electric field. Light-induced shifts in the Hg resonant frequency affects the result in two ways: 1. By shifting the measured frequency that changes the correction of the geometric-phase; 2. The frequency shift will reflect the correlation of the light's amplitude with the electric field in some way. So it produces a signal directly.

iii) Uncompensated B-field drifts due to fields induced by the high voltage. The ^{199}Hg has been re-measured in 2009 [41]. It is negligible and does not contribute any more.

iv) Mechanical deformation of an electrode due to electrostatic forces.

v) The most probable reason of false EDM effects are leakage currents caused by the high voltage in the traps with electric fields. Leakage currents change their sign upon reversal of the electric field and the resulting magnetic field change will be the reason of the shift in the neutron spin precession.

In order to systematize the issues of systematics due to the electric field can be grouped as follows:

1. Stability and uniformity of electrostatic field.
2. Leakage currents.
3. Mechanical and electro-physical properties of the electrodes.
4. Alignment of the electrodes in the magnetic field.
5. Electric forces cause deformations of the electrode.
6. Gradients in the electric field and alignment of the tilt of the electrodes in the fields.
7. Currents caused by HV fluctuations and asymmetries in conductivity of the electrodes and contact positions of the electrodes.

In the following discussion these effects and their impact will be considered.

1. Direct and indirect systematic effects

1.1. Geometric phase effect

The most critical for the next generation of the room-temperature EDM experiment is the geometric phase effect that arises from a joint action of the two effects: the $\vec{v}$ x $\vec{E}$ effect and a vertical gradient in the magnetic field. It is also called "the motional field effect". This systematic effect is indirect.

This problem for particles in traps was first highlighted by Pendlebury et al. [50]. It is basically the Berry phase [51] in the experiment, which is a pure geometric effect. The result of this interaction is a frequency shift proportional to the external electric field, just like an EDM signal. To describe the geometric phase effect, which has been observed in ILL nEDM experiment [52] a general analytical approach based on the relationship between the systematic frequency shift and the velocity autocorrelation function of the stored particles has been developed [46]. The principle of the geometric phase effect is described below.

In a cylindrical storage cell, assume there is a radial magnetic field due to a magnetic field gradient in the z direction

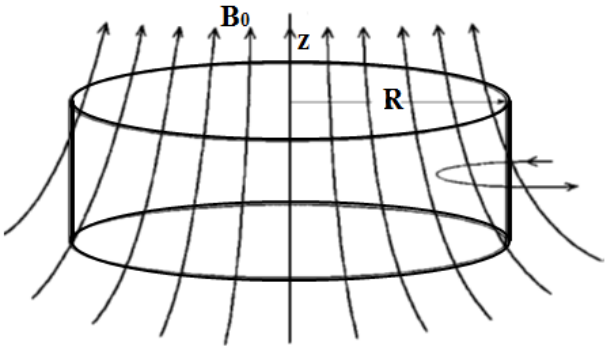

Figure 2.1: The distorted magnetic field, which is the result of applying a positive gradient $\frac{\partial B_{0z}}{\partial z}$ to the holding magnetic field B_0.

A slightly trumpet-shaped field, which is the case of an azimuthally symmetric field with a vertical gradient ∂B/∂z, was taken for the simplification (see Fig.2.1). Since $\boldsymbol{\nabla} \cdot \vec{\boldsymbol{B}} = \frac{\partial B_x}{\partial x} + \frac{\partial B_y}{\partial y} + \frac{\partial B_z}{\partial z} = 0$ and we know about cylindrical symmetry, then $\frac{\partial B_x}{\partial x} = \frac{\partial B_y}{\partial y} = \left|\frac{1}{2}\frac{\partial B_z}{\partial z}\right|$. From the Laplace equation we can get with use the cylindrical coordinate system a radial magnetic field component $B_r = \frac{r}{2}\frac{\partial B_{0z}}{\partial z}$ (see App.1).

The motion of UCN in the electric field will create the additional motional magnetic field

$$\vec{B}_v = \frac{\vec{v}\times\vec{E}}{c^2}, \tag{2.1}$$

where $v = \omega_r r$ is the neutron velocity in the lab frame.

As a result of these two effects we get a transverse magnetic field component B_{xy}, i.e. a radial magnetic field:

$$B_{xy} = \frac{\vec{r}}{2}\frac{\partial B_{0z}}{\partial z} \pm \frac{\vec{v}\times\vec{E}}{c^2}, \tag{2.2}$$

where the first term is the magnetic field due to the gradient, the sign "$\pm$" refers to the rotation direction of the neutron in the electric field.

We can roughly imagine the motion of neutrons in the experimental chamber as the diametrical straight-line movement in the XY-plane and a moving on the nearly circular orbits (the Garland orbits). The orbits of the particles will be roughly circular due to specular reflection around the cell (see Fig. 2.2).

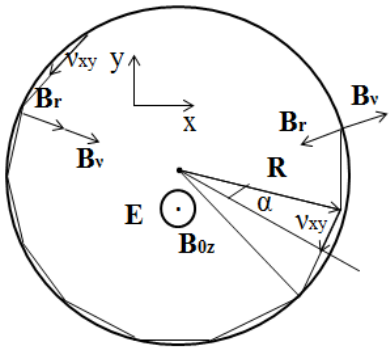

Figure 2.2: A cross section view of the cylindrical cell. A particle is undergoing specular reflections. B_{0z} and $\vec{E}$ are perpendicular to the paper. The orbit is characterized by the angle α.

If τ_c is the time between collisions, then the inverse value is the wall collision rate, $1/\tau_c$. A cyclic frequency at the incident angle α relative to the surface is $\omega_r = \frac{2\alpha}{\tau_c}$. From Ramsey calculation for a neutral particle with spin and magnetic moment precessing steadily with an angular velocity we obtain ω_L=ω_0=$-\gamma B_{0z}$ in a constant magnetic field B_{0z}.

Then the precession frequency of the neutron ω_L rotating with the frequency $\omega_r$in its rest frame will be

$$\omega_L = \sqrt{(\omega_0 + \omega_r)^2 + (\omega_{xy})^2}\,, \tag{2.3}$$

where $\omega_0 = \gamma_n B_0$ is the Larmor frequency of the neutron in the magnetic field B_0, $\omega_{xy}=\gamma_n B_{xy}$.
In the lab frame the precession frequency of the neutron will be shifted [53]

$$\Delta\omega = \omega_L - \omega_0 = \sqrt{(\omega_0 - \omega_r)^2 + \omega_{xy}^2} - (\omega_0 - \omega_r) \approx \frac{\omega_{xy}^2}{2(\omega_0 - \omega_r)}, \tag{2.4}$$

This shift is called the Ramsey-Bloch-Siegert shift [54-56].
By using (2.2) we can get ω_{xy}^2:

$$\omega_{xy}^2 = (\frac{\vec{r}}{2}\frac{\partial B_{0z}}{\partial z})^2 + (\frac{\vec{v}\times\vec{E}}{c^2})^2 + 2\frac{\vec{r}}{2}\frac{\partial B_{0z}}{\partial z}\cdot\frac{\vec{v}\times\vec{E}}{c^2}, \tag{2.5}$$

The third term in Eq. (2.5) depends linearly on the velocity of the particle and is leading to a false EDM signal. The first term describes the influence of the fields B_r on the resonance frequency. It is the source of the indirect false effects. The second term will be a serious problem if the electric field strength is not equal in both measurements. Beside of this second term increases the main magnetic field and leads to a false EDM signal.

If we the boundary between the ranges $|\omega_r| < |\omega_0|$ and $|\omega_r| > |\omega_0|$, then they will correspond to the adiabatic and non-adiabatic case.

For the typical nEDM experiment with trapped UCN and mercury atoms the description of the adiabatic case fits to UCN, while the non-adiabatic is for mercury atoms. From the Pendelbury analysis [50] we have two different false effects. After averaging over the volume they found that for an isotropic distribution of velocities and a uniform distribution in space the result for UCN is:

$$d_{f,n} = -\frac{J\hbar}{2}\left(\frac{\langle(\partial B_{0z})/\partial z\rangle_V}{(B_{0z}^2)}\right)\ \frac{v_{xy}^2}{c^2}\left[1 - \frac{\omega_r^{*2}}{\omega_0^2}\right]^{-1}, \tag{2.6}$$

where $\omega_r^{*2} = \frac{\pi^2}{6}(\frac{v_{xy}}{R})^2$, J is the total spin angular momentum of the neutron.
In the case of general fields and trap (straight perpendicular walls with parallel electrodes) we can re-write Eq. (2.6) as:

$$d_{f,n} = -\frac{J\hbar}{2}\left(\frac{\langle B_{0xyn}\rangle A_S}{(B_{0z}^2)V}\right)\ \frac{v_{xy}^2}{c^2}\left[1 - \frac{\omega_r^{*2}}{\omega_0^2}\right]^{-1}, \tag{2.7}$$

where $\langle B_{0xyn}\rangle A_s$ is the net magnetic flux passing through the side walls.

For the high-velocity limit (mercury atoms) one obtains

$$d_{f,Hg} = -\frac{J\hbar}{4}\left(\frac{(\partial B_{0z})}{\partial z}\right)\ \frac{\gamma_{Hg}^2\, R^2}{c^2}\ \left[1-\frac{\omega_0^2}{\omega_r^{\dagger 2}}\right]^{-1}, \tag{2.8}$$

where $\omega_r^{\dagger 2} = 0.65(\frac{v_{xy}}{R})^2$.

The false effect for mercury atoms depends on the radius of the trap and a gradient. Harris and Pendlebury later showed [52] an impossibility to replace this gradient in case of a dipole field.

Finally, the resulting false effect can be found as (see App. 2):

$$d_{f,n,Hg} = \left|\frac{\gamma_n}{\gamma_{Hg}}\right| \cdot d_{f,Hg}. \tag{2.9}$$

We will continue this discussion with the description of measurement of the geometric phase effect at PSI in 2011 below (see Chapter 2).

1.2. Potential sources of direct systematics

We can calculate approximately the false effects, associated with the electric field that can be expected in our experiment.

1. First order $\vec{v}\times\vec{E}$ effects.

The UCN moving through an electric field results in an additional magnetic field according to the principles of special relativity. We can estimate the magnetic field that is generated in the neutron rest frame when a neutron moves in an electric field (see (2.1)). The electric field in our experiment is E=150 kV/12 cm. For the neutron with the straight line path across the diameter of the trap we can write a rotational frequency of the magnetic field B_{xy} rotating in the xy-plane:

$$\omega_r = \frac{\pi v_{xy}}{2R}, \tag{2.10}$$

where R is the radius of the trap. The isotropic distribution of the velocities for the ensemble of trapped UCN [46] is

$$\bar{v}_{xy}^2 = \bar{v}_x^2 + \bar{v}_y^2 = \frac{2}{3}\bar{v}^2, \tag{2.11}$$

where $\bar{v}$ ≈5 m/s.

Then we can calculate the additional magnetic field $B_v = \frac{|v_{xy}||E|}{c^2}$ ≈56.7 pT.

i) Non-parallelism of the electric and the magnetic fields.

If the electric and the magnetic fields are not exactly parallel, i.e. the angle theta is not equal to zero (see Fig. 2.3), an additional component to the main magnetic field B_0 appears.

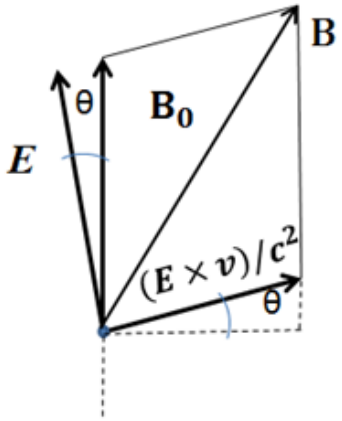

Figure 2.3: Vector diagram of the non-parallel electric and magnetic fields, and the additional component B of the motional magnetic field.

This $(\vec{v}\times\vec{E})$ – effect is also called "translational" effect due to the fact that we consider the motion of the ensemble of neutrons (changes the energy spectrum of the UCN), the velocity of which is determined by the displacement of its center of mass during the period of free precession of neutrons. In the ensemble dominated by collisions of neutrons with each other, that is why the center is shifted only to a distance of about 1 mm for 150 s of the precession. In the simulations of the electric field with the different shapes of the high voltage electrode (see section 4.1 and Appendix 4) the average angle θ was about 2° on the non-uniformities of the shape. For the additional magnetic field we can write

$$\Delta B = 2 sin\varphi \frac{(\bar{E}\times\bar{v})}{c^2}. \quad (2.12)$$

This results in a false EDM signal

$d_{f,n} = -\frac{\hbar}{4E}\cdot\Delta\omega = -\frac{\hbar}{4E}\gamma_n\cdot\Delta B \approx -2\cdot 10^{-12}$e·cm· ΔB/1T≈ $1.3\cdot 10^{-29}$e · cm, E=150 kV/12cm.

ii) $\vec{v}\times\vec{E}$ rotational.

Another effect connected with the motion of the neutron ensemble in the non-parallel electric and magnetic fields is a rotational effect. Neutrons begin to rotate when they fill the chamber from the neutron guide. After several cycles, depending on the smoothness of the chamber, this rotation gradually suppressed due to diffuse scattering at the chamber walls. Typical decay times for such ordered rotational motion is about 1 s. After the filling the trap is closed. Even at the precession of the neutrons during the 150 s this effect will be damped significantly, i.e. 1 s/150 s ≈ 0.007 at the end of the precession. The false effect even at the initial velocity of the ordered motion v= 1 m/s will be about $d_{f,n} = \pm 1 \cdot 10^{-28}$e · cm [57].

iii) Electrostatic forces.

Electrostatic forces deforming the electrode and the insulator ring can cause systematic effects, because there will appear a tilt between the electric and magnetic field, which will create (v×E) effect. In the case of the potential U = 200 kV, with the capacity for our chamber C ≈ 15 pF, appears an electrostatic force F:

$$F = \varepsilon_0 S(\frac{U}{d})^2 \approx 5\ N, \tag{2.13}$$

where S is the electrode area, S ≈ 0.2 m^2, d=12 cm, ε_0 is the electric constant (vacuum permittivity), ε_0=8.85·10^{-12} F/m.

The influence of electrostatic forces has been measured at PSI [58]. They used a laser beam to measure the relative tilt with and without weight, which was re-calculated from electrostatic force. It was found that the electrostatic field of 10 kV/cm (equivalent mass is about 100 gr) leads to the tilt angle θ=0.0±0.02 [mrad]. The false effect due to this tilt we can estimate as (v×E) net effect:

$$d_{f,n} < 7 \cdot 10^{-33}\text{e} \cdot \text{cm}.$$

This effect is tiny even when compared with other false effects due to the electric field and thus can be neglected.

2. Quadratic $\vec{v}\times\vec{E}$ effect (second order).

This effect is compensated in our experiment with a double-chamber installation. No additional frequency occurs because of the quadratic nature of this effect. Both our traps will be fed by the same power supply, so we don't wait the false effect from the difference in the magnitudes of the electric field there.

The resulting magnetic field which the UCN see when moving in the experimental chamber with the holding constant magnetic field B_0 and with the electric field E is:

$$B = \sqrt{B_0^2 + B_v^2} \approx B_0 + \frac{B_v^2}{2B_0}. \quad (2.14)$$

The main magnetic field is equal B_0=1 μT. Then, the quadratic term comes out as $B\text{-}B_0 \approx 1.6$ fT. If we suppose the electric field is not exactly equal, for example, the difference is 10%, the false effect will be $d_{f,n} = -\frac{\hbar}{4E} \cdot \Delta\omega = -\frac{\hbar}{4E}\, \gamma_n \cdot \Delta B \approx 3\cdot 10^{-29}$ e·cm.

2. Measurement of the geometric phase false mercury nEDM at PSI

A false EDM due to the shift in the ^{199}Hg precession frequency can be determined as a function of the applied vertical magnetic field gradient and the strength of the electric field. As a member of the experimental team at PSI in May 2011[59] I joined the measurement of the geometric phase originating from precession frequency shift of mercury and to the calculation of corrections for systematics related to the geometric phase.

During the run, several 100 cycles of the measurement were performed, when a certain magnetic field was set and a certain gradient was applied. In order to calculate the difference between the precession frequencies for parallel and anti-parallel direction of the electric field to B_0 a high voltage of 100 kV for both polarities was applied. Every 20 cycles, the direction of the electric field was changed.

In order to make the effect visible, the vertical gradient has to be large. For this run, the trim coils were set in order to produce a gradient of 0-4 nT/cm (4 nT/cm-gradient creates a frequency shift ~ 3 pT)

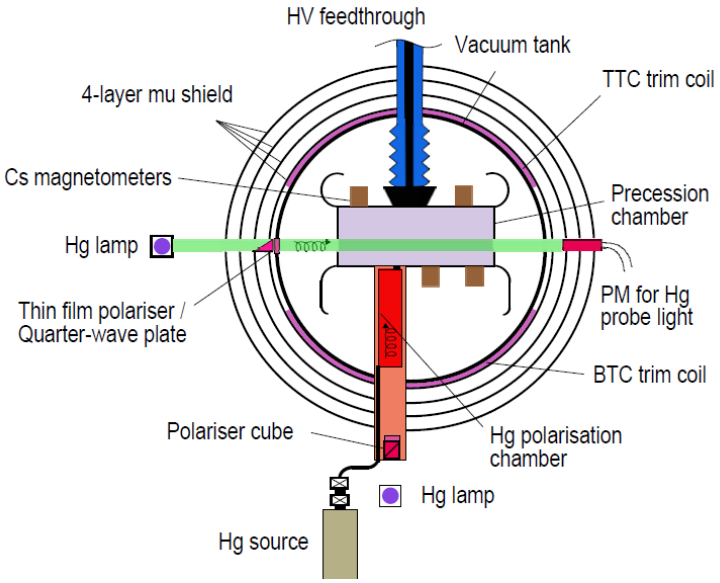

Figure 2.4: The main parts of old ILL-experimental apparatus in PSI used for the measurement of the Hg geometric phase.

Cs-magnetometers were set up on the top electrode and below the bottom electrode to measure the local magnetic fields (see Fig. 2.4). They allow determination of magnetic field gradients. For the geometric phase measurement, a small polarizer cube with integrated quarter wave-plate is put on the lower end of the Hg polarization system.

Usually each measurement for a certain value of the current was performed during one day (about 650 cycles) or half a day (about 350 cycles), trying to get an equal number of cycles for the two directions of the electric field. The current on a TTC (Top Trim Coil) and BTC (Bottom Trim Coil) was changed in the limits (-25 mA ;+ 25 mA) to 0 through 6-7 mA in order to get different gradients. After that, the direction of the static magnetic field was inversed (up and down). The typical error from the gradient stability of a cycle was 50-100 pT/cm, thus the drifts of gradients were negligible for the average gradient of one run.

One of the examples of a frequency distribution is shown in Figure 2.5. The residuals of the fit are the shift in frequency. They correspond to the geometric phase. Regular residuals from our frequencies can be found and an average of a frequency shift can be calculated. The distribution for each polarity gives a mean value and an error for both directions of the electric field.

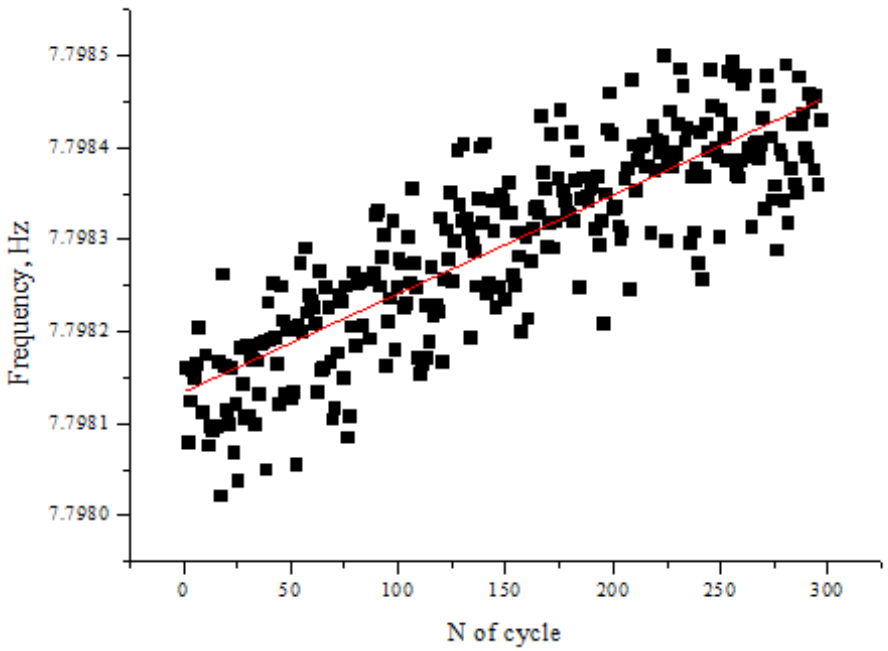

Figure 2.5: Distribution of frequency at the electric field of 8.3 kV/cm, at the gradient of 3 nT/cm.

As a result, the two frequency shifts for positive and negative HV can be transformed to a false EDM for every applied gradient and for both B_0-directions. In Figure 2.6 you can see the intermediate result of such calculations.

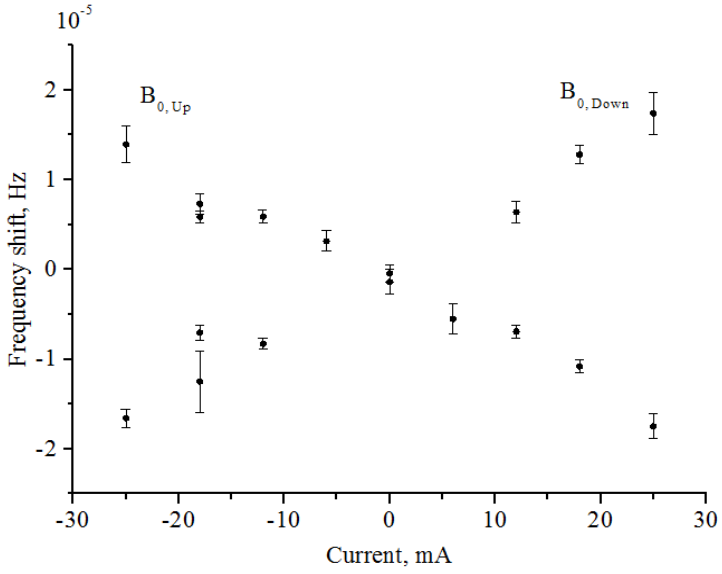

Figure 2.6: The dependence of the frequency shifts on the applied current in TTC and in BTC with opposite sign.

To get the average gradient two methods were used:

i) the field maps of TTC and BTC (see Fig. 2.7)

ii) the data from Cs-magnetometers (see Fig. 2.8)

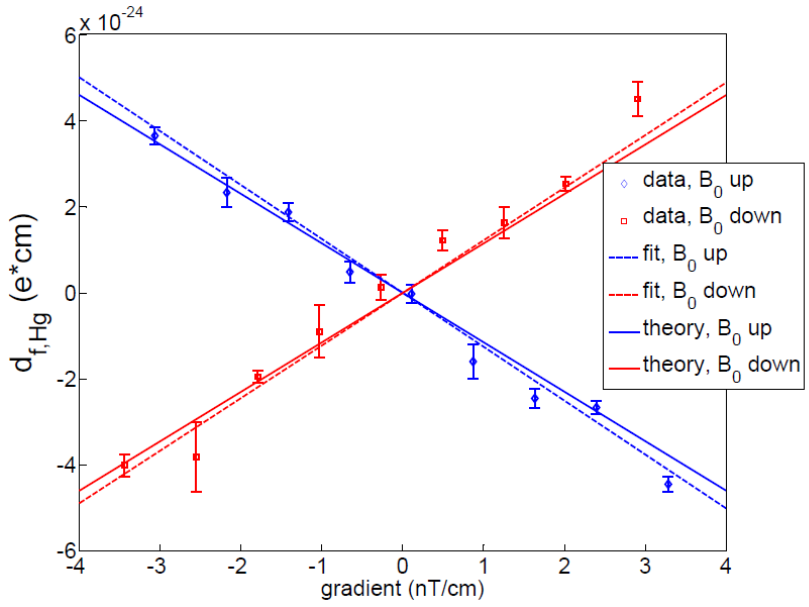

Figure 2.7: False Hg EDM when the gradients are average values over the precession chamber and are calculated from the fluxgate magnetometer maps of TTC and BTC.

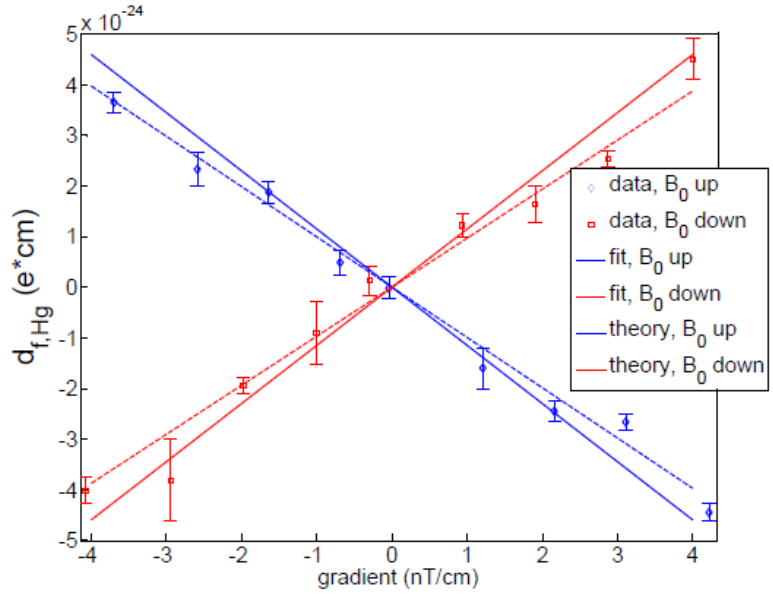

Figure 2.8: False mercury EDM when the gradient is determined using the Cs magnetometers. The solid lines are theoretical.

Finally, the average false mercury EDM is calculated from the absolute values of a straight-line fits for B_0 up and down [59]:

$$\frac{d_{false,Hg}}{\langle \partial B_{0z}/\partial z \rangle} = (1.24 \pm 0.04) \cdot 10^{-27} ecm\ (pT/cm) \tag{2.15}$$

The average false nEDM obtained from the Cs magnetometers is

$$\frac{d_{false,Hg}}{\langle \partial B_{0z}/\partial z \rangle} = (9.82 \pm 0.29) \cdot 10^{-28} ecm\ (pT/cm). \tag{2.16}$$

The theoretical result calculated from Eq. (2.8) is

$$\frac{d_{false,Hg}}{\langle \partial B_{0z}/\partial z \rangle} = (1.16 \pm 0.04) \cdot 10^{-27} ecm\ (pT/cm). \tag{2.17}$$

The results obtained by the two methods are slightly different. A possible reason could be that the center of mass of the Cs-magnetometers is not leveled, thus the gradient will not be vertical.

3. Electric field and its stability in the new nEDM experiment

The electric field stability is the one of the most important conditions for the next generation experiments for such a small value of the neutron EDM. The motion of the neutrons through the electric field affects the stability of the static magnetic field by the additional motional magnetic field, the "v×E" – effect (see Table 1). The new experiment is designed and will be constructed so as to ensure the suppression or reduction of systematic effects that result from instability of the electric field. In Figure 2.9 is shown a draft of the future chambers and components of the high-voltage system.

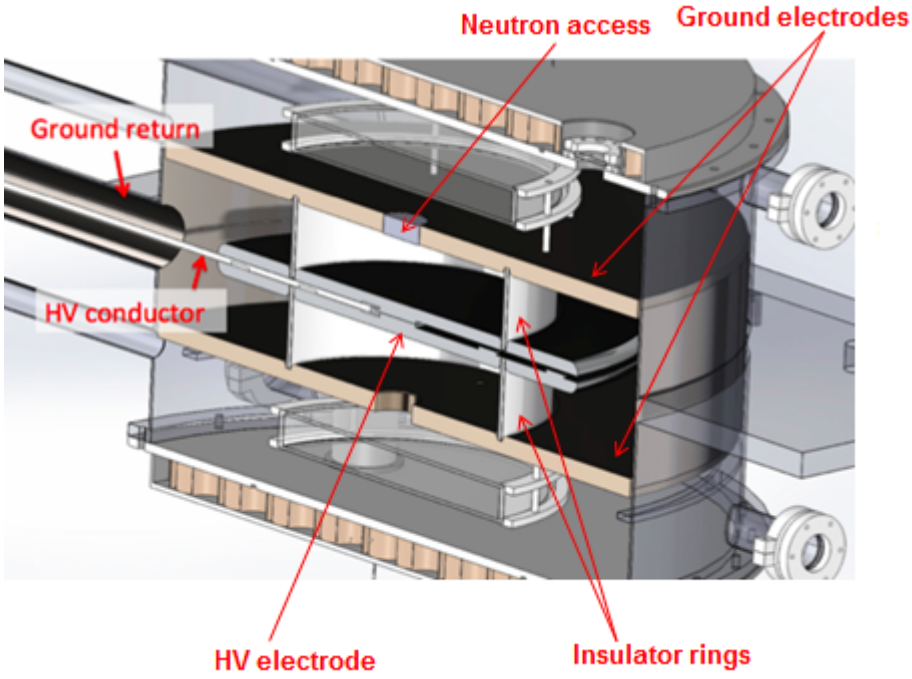

Figure 2.9: The double chamber layout for the new nEDM experiment at FRM II.

The main components are: the high voltage electrode, the ground electrodes, the high voltage conductor, the insulator rings and the grounding. All components of the experimental setup will be non-metallic, because the disadvantages of the metals are, e.g., Johnson's noise, thermal currents, radio-frequency noise – the main reason for additional magnetic fields and, as a result, for the geometric phases.

Coming closer to the direct discussion of the performed work, it should be noted that the sequence of the description is defined by the real process of the investigations and the preparation. Therefore I start from a selection of the material for the electrodes.

3.1. High voltage electrode: Research and Development.

The investigations of the materials for the high voltage electrode play a main role, because the experiment is very sensitive to the instability of the electric field. Therefore, there are many requirements for the materials of the electrode. For example, it should be conductive, but non-metallic. Also important are flexural and tensile strengths, thermal plasticity, and the possibility to machine the material. These tasks were only the first stage of the research.

In the previous generation of nEDM experiments the high voltage electrode was metallic. Metals usually have a very high conductance and at same time it is a source of Johnson-Nyquist noise (thermal noise), these materials are magnetizable.

Thermal, or Johnson-Nyquist, noise is present in any kind of conductor and depends only on the conductor's resistance and temperature. This "white" noise is not correlated with the direction of the electric field, and therefore it will not be the source of false nEDM. However, this noise can limit the sensitivity of the magnetometers.

$$i^2 = 4k_B T\Delta f/R, \tag{2.18}$$

where i is the noise current, k_B is Boltzmann's constant, Tis the absolute temperature of the resistor, Δf is the bandwidth over which the noise is measured, R is the resistor value.

By decreasing the thickness of the electrode we can suppress this noise, but the mechanical stability will also decrease.

3.1.1. Plastic electrode

Magnetic impurities will be the source of systematic effects like B-field drift. It can be suppressed by using non-metallic and non-magnetic materials. One idea was to build a high voltage electrode made from conductive plastic. But plastics have some disadvantages compared to metal.

All plastics are insulators. In order to make them conductive the conductive materials must be implemented and the conductivity will depend on its concentration. However, increasing the conductivity can degrade mechanical and physical properties of plastic.

Furthermore, plastic electrodes, being conductive, can be destroyed depending on their electrical resistance and breakdown voltage in the presence of local voltage changes. Usually the resistance of conductive plastics lies between the limits 1 Ohm and 1000 Ohm and compared to metals it is 5-8 orders of magnitude higher. There are very few plastics with suitable properties. Most of conductive plastics do not have sufficient heat resistance and mechanical rigidity: the melting point must be higher than 200°C and the tensile modulus should be close to the tensile modulus of aluminum (70 GPa).

Based on these conditions, several types of different plastics have been found and tested. Ultimately, there remained three samples of plastics:

i) Ticona VECTRA A230 LCP (Liquid Crystal Polymer), 30% Specialty (30% carbon fiber reinforced);
ii) Ticona VECTRA B230, LCP, 30% Specialty(30% carbon fiber reinforced);
iii) RTP 285 D TFE 15, Nylon 6/12 (PA), (30% carbon fiber reinforced), PTFE Lubricated.

They are shown in Figure 2.10. Their properties are listed in Table 2.

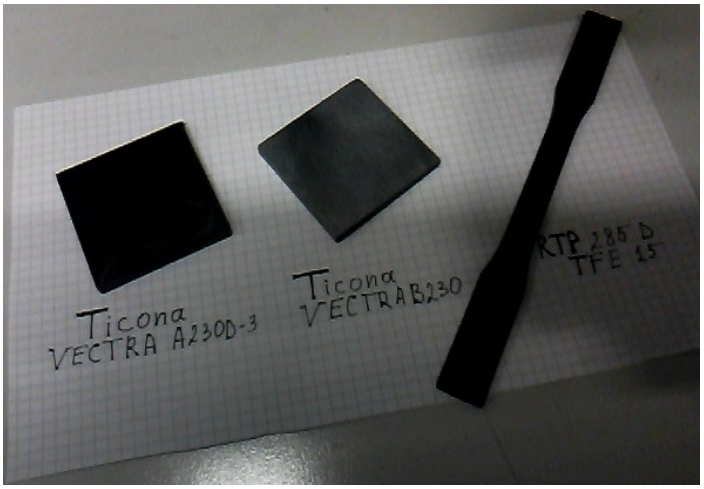

Figure 2.10: Three samples of conductive plastics, suitable as the material for high-voltage electrode based on mechanical and physical requirements.

Product name	Description	Processing method	Tensile modulus (MPa)	Flexural modulus, (MPa)	Surface resistivity, (Ohms)	Volume resistivity, (Ohm-cm)	Melting point, ℃
RTP 285 D TFE 15 Nylon 6/12 (PA) Carbon Fiber – PTFE	PTFE	Injection molding	20000	17900	<=10000	<=100	249-285
Ticona VECTRA A230, LCP, 30% Specialty	LCP	Injection molding	23500	23000	100	1000	280
Ticona VECTRA B230, LCP, 30% Specialty	LCP	Injection molding	32200	32800	100	1	280

Table 2: Three selected samples and their properties.

Before describing the various tests conducted with these plastics, we briefly present the test setup and mention the improvements (see Fig.2.11) which we need for the investigation of the material conductivities.

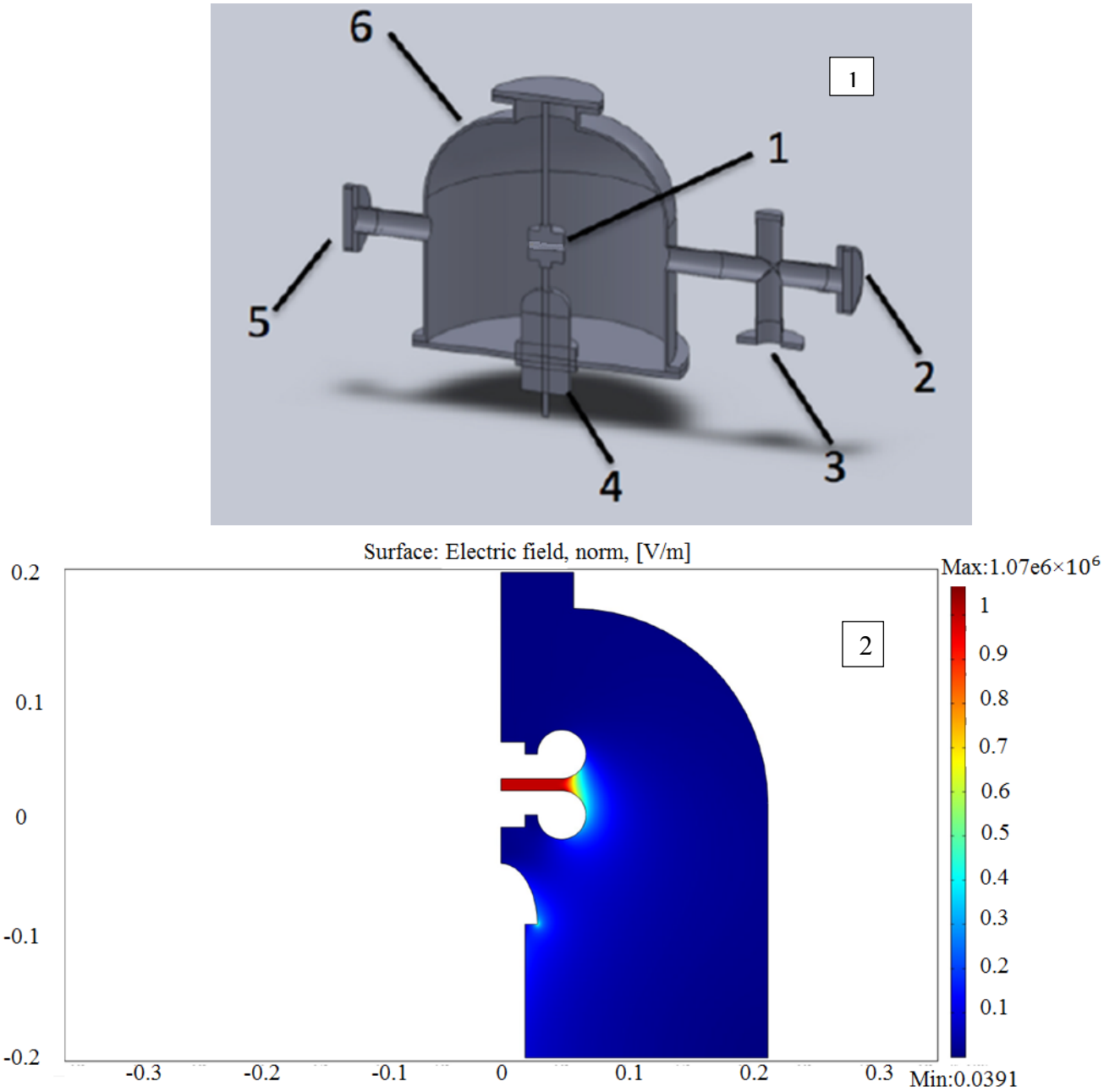

Figure 2.11: 1. Test setup: 1) Plate capacitor, where the upper electrode is ground, and the lower electrode is high voltage; 2) Window; 3) Connection for Turbo-Vacuum Pump; 4) High voltage inlet; 5) Windows; 6) Vacuum vessel, 2. COMSOL simulation of the electric field distribution inside the experimental vacuum chamber. The height of the chamber is 400 mm, the inner diameter is 500 mm. The electric field in the maximum is 10 kV/cm.

The volume of the vacuum chamber is about 50 liters. The electric field occurs between two aluminum electrodes. The electrodes are donut-shaped, the surface of their base is with a radius of 10 cm (the

electrodes are in parallel in this region to ensure a homogeneous field) and are formed with a radius of curvature of 2 cm to a donut. A 10 mm hole is located at the upper side of the electrode for the attachment of the electrodes at the two flanges of the vacuum vessel by means of a threaded rod. The chamber was evacuated usually for tests to a pressure of about 10^{-6} mbar. As you can see in Figure 2.11.2 the electric field strength decreases with the increasing of the distance between the electrodes. The electric field is most homogeneous in the inter-electrode region. This shape of the electrodes is the most optimal (more information about the shape of the electrodes see in Chapter 5).

In the vacuum chamber on the ground electrode sensory scales – miniature sensor [60] - were installed in order to measure the electric field between the electrodes [61]. The entire construction is shown in Figure 2.12:

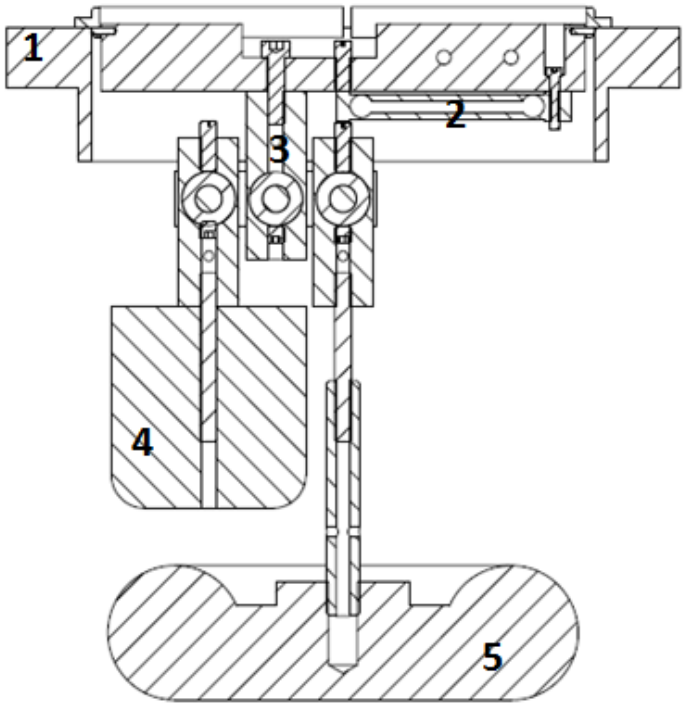

Figure 2.12: 1. The cover of the vacuum chamber; 2. Miniature sensor-balance; 3. Arms of the balance; 4. Counterweight; 5. Ground electrode.

The measurement of the attractive electrostatic forces between the electrodes allows determining the electric field strength. For two electrodes separated by a distance d forms a capacitor with capacitance C, the electrostatic force is.

$$F = qE = CUE = \frac{1}{2}\varepsilon_0 \cdot S \cdot (\frac{U}{d})^2, \quad (2.19)$$

where E=1/2(U/d) is the electric field of one plate of the capacitor, U is the applied voltage, q – charge of the other plate of the capacitor, C= $\varepsilon_0\varepsilon$ S/d, S – surface area, ε_0- electric constant, ε – permittivity.

The electrostatic force measured in the experiment can be translated to the electric field. On the next two plots the calibration curve for these measurements and one of the examples of the measurement interpretation are shown.

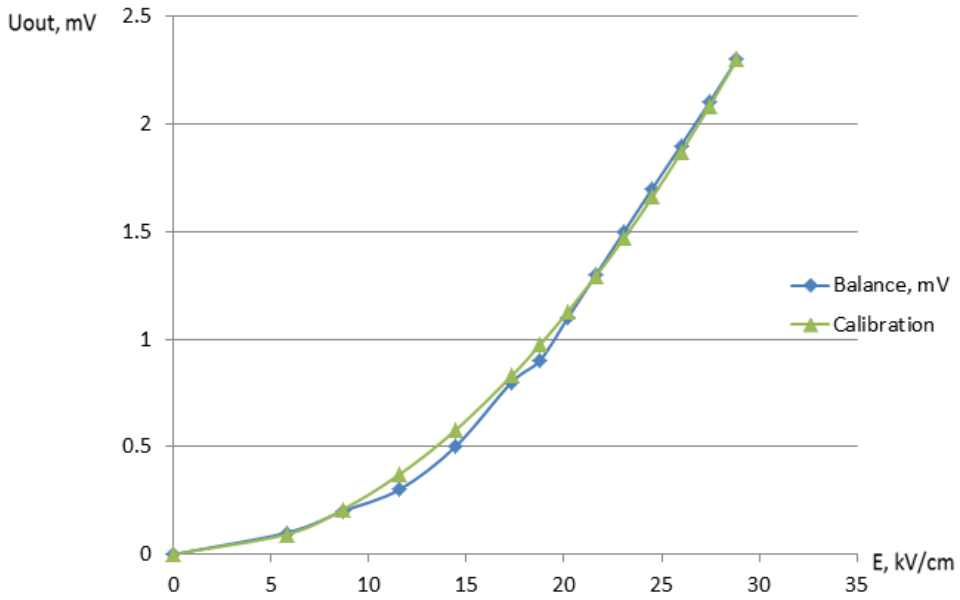

Figure 2.13: The calibration curve expresses the relation between the voltages from high voltage source. Here, the electric field is E and the corresponding measured values are called as U_{out} (voltmeter). Statistical error is 0.1 mV.

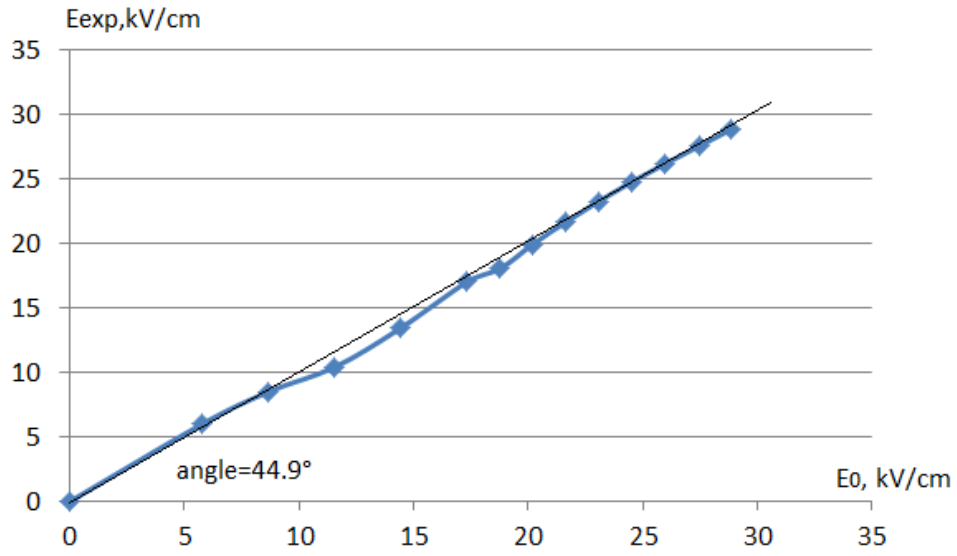

Figure 2.14: Result of the electric field calculation. E_{exp} is the measured and calculated electric field, E_0 is applied electric field (HV source), d= 35 mm is the distance between electrodes. The black line is to guide the eye for the linear correspondence between the applied and the measured electric fields.

In Figures 2.13 and 2.14 the sagging of measured electric field arises from the friction between mechanical parts of the balance. This method to measure the electric field works, but inaccuracies may occur later because of the mechanical construction. Besides, we want to avoid any metallic parts and constructions in the experiment. However, this method fits for the first tests and in this way the tests on the conductivity of the chosen materials for the high voltage electrode were performed.

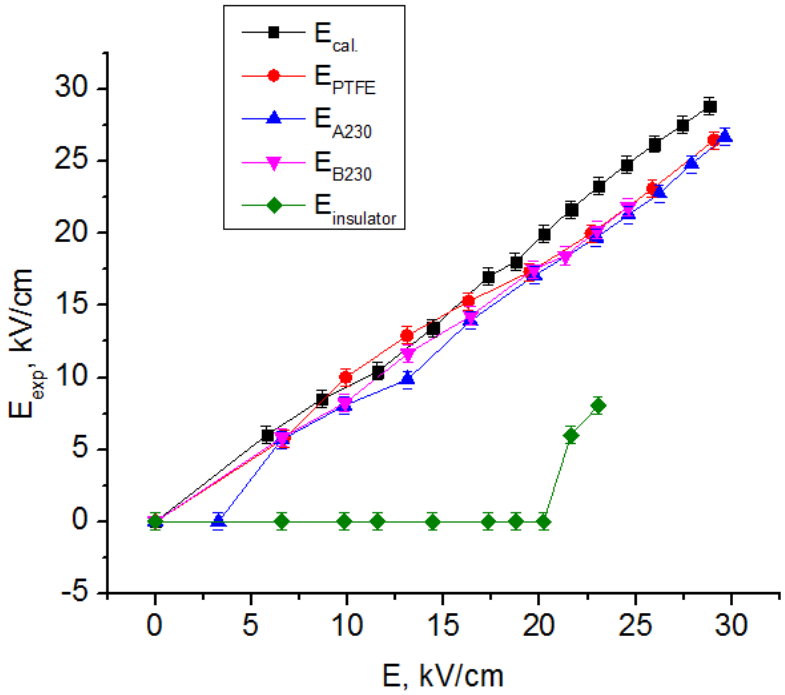

Figure 2.15: Direct electric force measurement (surface charge tests). The results of the electric field calculation for the three conductive plastics and for Teflon plate are presented. The black squares show a calibration. E_{exp} is the measured and calculated electric field, E is applied electric field.

All three types of conductive plastic plates are compared to a Teflon insulator (see Figure 2.15). The investigation of these materials on electrical conductivity shows good results. The electrical resistance of the conductor must be small enough to maintain the high voltage against leakage currents, but large enough in order to suppress RF noise (see Eq. (2.18)).

Besides the measurements of the electric field we also tested the outgassing of the different plastic materials in vacuum at pressure P = (10^{-7}-10^{-6}) mbar. Checking of these plastics with the mass-spectrometer shows very nice results (see Fig. 2.16).

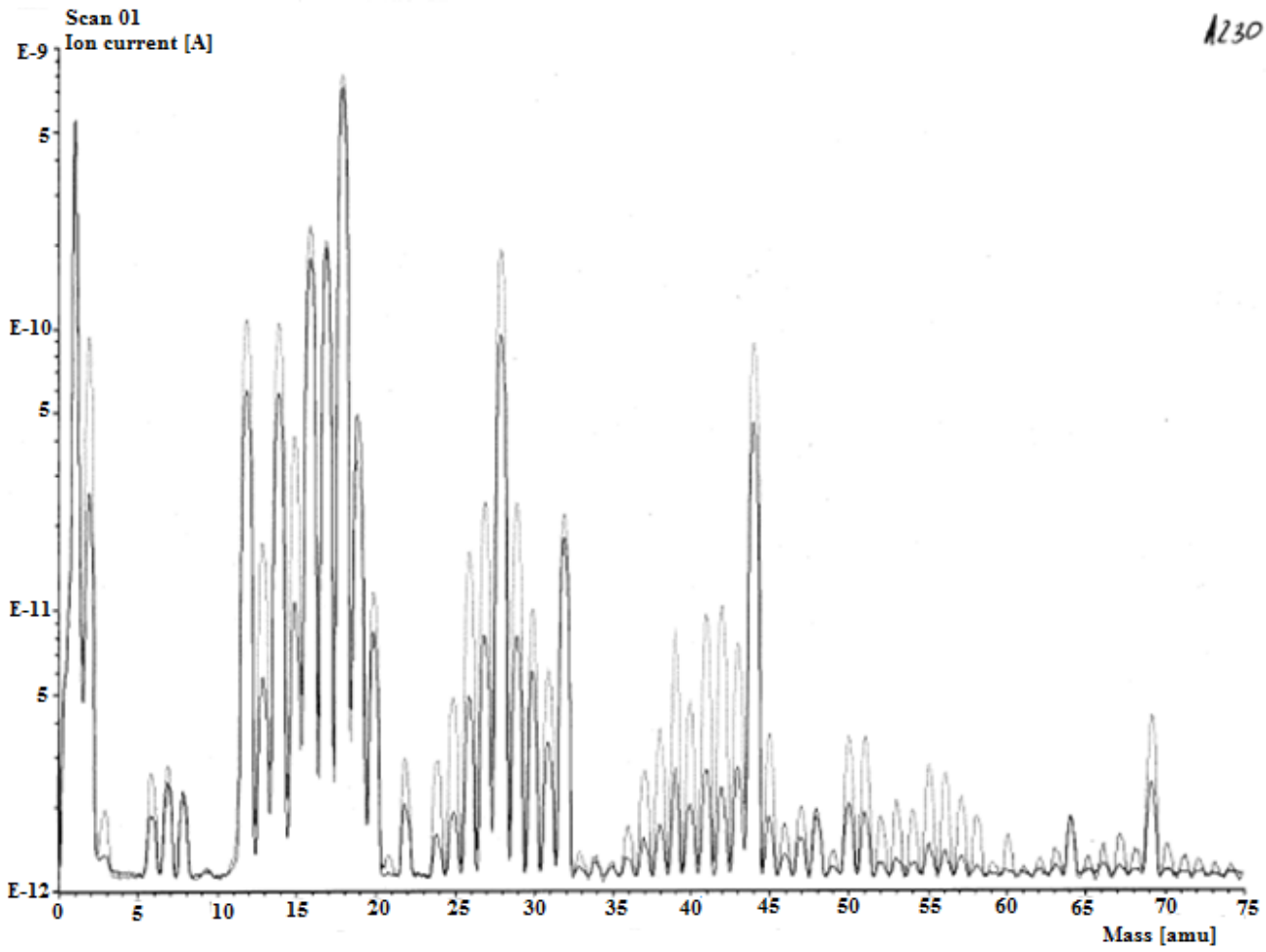

Figure 2.16: Outgassing from the sample "Ticona A230". Background is shown in the light-gray tone; the spectrum with the sample (in the dark gray tone) compared to background is lower due to the difference in the time of evacuating. The vacuum chamber was evacuated on several hours longer compared to the time for evacuating at the background measurement.

The working vacuum of future nEDM-experiment will be 10^{-6} mbar and it was confirmed that all tested plastics can be operated in such a vacuum.

In conclusion, these plastics can be used as high voltage electrode material.

The reason why we decided to stop working with plastics was the result of checking the samples on demagnetization. These tests were performed in PTB (Physikalisch-Technische Bundesanstalt (Berlin)).

The measurement of demagnetization is based on the Josephson Effect. It is an example of a macroscopic quantum phenomenon. The current flows indefinitely long, without any applied voltage, across a device which consists of two superconductors coupled by a thin insulating barrier.

The sample moves back and forward in the uniform field. On the both ends of a sample, coils are located. Crossing through the measurement coils induces a current. This current generates a magnetic field in the SQUID, which, in turn, is a measure of the sample magnetization [45].

The samples were fixed with adhesive tape and a spot was magnetized with a Neodym magnet. It produced a local magnetization, when moved below the SQUIDs. After degaussing the residual magnetization of the sample was 10-20 pT pp (peak-to-peak). However, we need less than 3 pT pp. It appeared the idea to use a material such as glass or ceramic. This was due to the requirements of the mechanical rigidity of the HV electrode (see Chapter 5, Section 5.2). In order to ensure the conductivity for the glass electrode, it is necessary to use, e.g., salt water as a conductor. That is, the high-voltage electrode will be a vessel with salt water. More on this see Section 3.1.2.

3.1.2. Glass electrode

By using the electric conductivity of salt water, we can make an electrode from a non-conductive material, such as glass, for example. This method has been used successfully earlier [61].

In order to understand whether it is possible to use a glass electrode filled with saltwater as a high voltage electrode, several tests on the measurement of the electric field were performed.

The glass electrode (see Fig.2.17) has been made from a borosilicate glass tube, having a very low coefficient of thermal expansion (~3×10^{-6} /°C at 20°C).

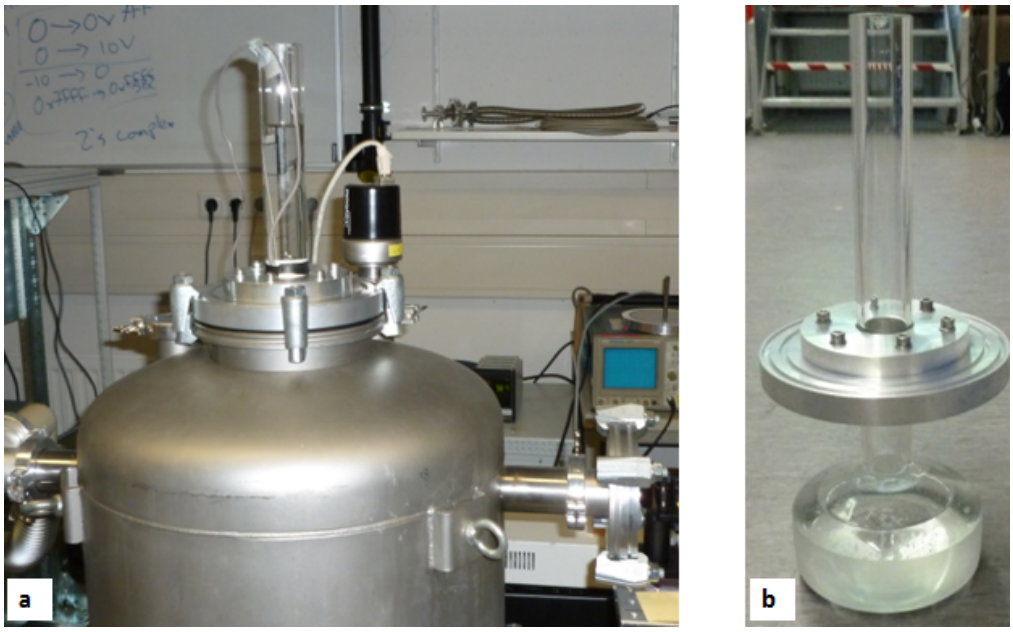

Figure 2.17: a) Vacuum chamber with installed glass electrode; b) Glass electrode.

The electric field was measured using the Pockels effect (see Chapter 3.2.3). Also, leakage currents have been measured at various concentrations of salt in the water that fills the volume of the electrode (see Figure 2.18).

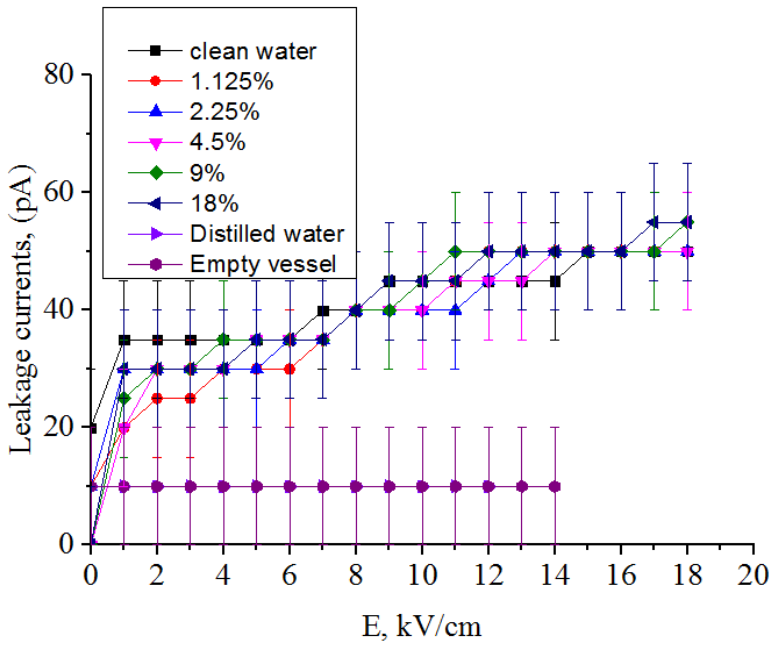

Figure 2.18: Measurement of the leakage currents at the different concentration of salt in water is checking the electrical conductivity. The sensitivity of the voltmeter is limited by 0.1 mV that is why the statistical error is large relatively to the leakage currents values.

Leakage currents confirm the presence of the electric field between the electrodes. Electrons flowed on the exterior surface of the glass electrode to the water and then follow through the wire to the device for the measurement. The procedure of measurement of leakage currents will be described separately below in the Chapter 4.2.

By changing the concentration of the salt in the water we wanted to make sure that in a rough approximation there is practically no difference for the different salt concentrations. When the vessel was filled with distilled water, there is no the electric field, as well as, when the vessel is empty.

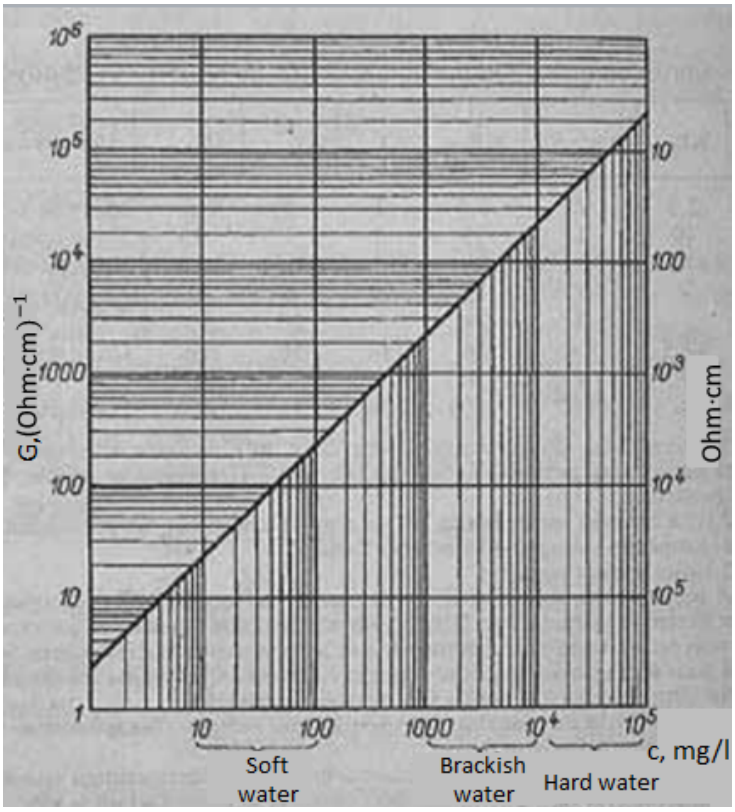

Figure 2.19: The dependence of the resistivity / conductivity of the dissolved NaCl at 20 ° C [62].

The main result is that the electric field does not depend on the salt concentration between 1.125% and 18% and that there is no the electric field for the distilled water or air in the electrode. In fact, the electrical resistivity (or conductivity) of the used distilled water was 10^6Ohm·cm (10^{-6} siemens/cm). The resistivity of the solution with 1% salt in the water (salt concentration is c=3600 mg/l) was 0.2 to 1 kOhm. It depends from the solution temperature; in the solution with 10% salt in the water (c=36 g/l) the resistivity is 20 to 100) Ohm. The concentrations of salt that are higher will be difficult to discriminate between the resistances. In the Chapter 3.2.3, the measurement of the electric field using the Pockels effect in case of the glass electrode will be shown.

In conclusion to this chapter, i.e. must be mentioned that we stopped to further use borosilicate glass cylinders filled with salty water as material for our HV electrode. The conductivity of the glass electrode can be ensured by the coating of a conductive material. The decision on the use of the quartz glass electrodes has become final. Such electrode is much easier to operate. It is important to choose the optimal parameters for this electrode, to ensure stability and uniformity of the electric field inside a neutron chamber.

3.2. Pockels effect and measurement of the electric field.

In the previous chapter we considered the possibility of measuring the electric field in the experiment by using the measurement of the electrostatic force between the electrodes. This method, however, has several disadvantages, e.g., mechanical construction is not stable, and parts of the construction must be placed outside the chamber in order not to disturb the experiment. One of the methods of the electric field measurement and control of its stability is measuring of the Pockels effect in an anisotropic crystal.

The Pockels effect (after Friedrich Carl Alwin Pockels who studied the effect in 1893), or Pockels electro-optic effect, produces birefringence in an optical medium induced by a constant or varying electric field [63, 64]. It is distinguished from the Kerr effect by the fact that the birefringence is proportional to the electric field, whereas in the Kerr effect it is quadratic to the field. The Pockels effect occurs only in crystals that lack inversion symmetry, such as lithium niobate or gallium arsenide and in other non-centrosymmetric media such as electric field poled polymers or glasses.

The lithium niobate crystal is an uniaxial crystal, i.e. its optical properties have rotational symmetry with respect to a single direction, called the optical axis of the crystal. $LiNbO_3$is a trigonal system, their optical indicatrix is ellipsoid having two eigenvalues and an axis of rotation parallel to the axis of symmetry of the highest order.

In isotropic media the vector of electric induction, D, is connected with the vector of electric field, E, of the light wave by the formula [65]:

$$\overrightarrow{D} = \varepsilon \cdot \vec{E}, \tag{2.20}$$

where ε is scalar (permittivity), depending on the frequency (frequency dispersion ω) and on the wave vector $\overrightarrow{K}$ (spatial dispersion). In anisotropic media the permittivity is a tensor (with eigenvalues), depending on the direction. Thus the vector E does not necessarily coincide with vector D. This tensor ε is a tensor of order 2. It converts one vector to another, which is not parallel to the first vector.

As shown in the Appendix 3, there are 2 solutions of the Eq. (A.7, A.8) in the case of lithium niobate:

i) n_o is the refraction coefficient for ordinary wave.

ii) n_e is the refraction coefficient for extraordinary wave, $n_e < n_o$.

That is lithium niobate is a negative crystal, and the indicatrix is an ellipsoid of rotation around the main axis of symmetry (see Figure 2.20).

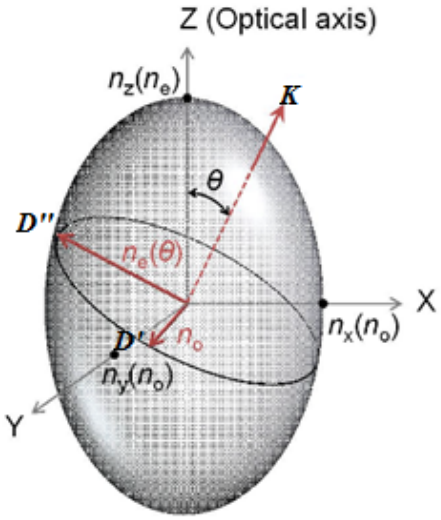

Figure 2.20: Optical indicatrix of an uniaxial crystal – ellipsoid of rotation – describes birefringence. Two solutions of the Fresnel's equation give two coefficients of refraction: n_o and n_e, where n_e depends on the θ. The wave vectors $\overrightarrow{K}$, $\vec{D}'$, $\vec{D}''$ are the directions of oscillations of polarized waves.

If the z axis is directed along the main axis of symmetry, the equation of the indicatrix $\frac{x^2}{n_{x^2}^2}+\frac{y^2}{n_{y^2}^2}+\frac{z^2}{n_{z^2}^2}=1$ moves to:

$$\frac{x^2}{n_o^2}+\frac{y^2}{n_o^2}+\frac{z^2}{n_e^2}=1 \tag{2.21}$$

Without an electric field E we can rewrite the equation of the indicatrix as

$$a_1x^2+a_2y^2+a_3z^2=1, \tag{2.22}$$

where a_1, a_2, a_3 are the main dielectric impermeability of the crystal in the absence of the electric field.

As a result of applying the electric field, rotation and deformation of the optical indicatrix occur. In a rectangular coordinate system, Eq. (2.22) has the form of the indicatrix [66]:

$$a_{11}x^2+a_{22}y^2+a_{33}z^2+2a_{23}yz+2a_{13}zx+2a_{12}xy=1 \tag{2.23}$$

where a_{ij} are the new polarization constants. The tensor $[a_{ij}]$ is the inverse of the permittivity tensor $[\varepsilon_{ij}]$.

The relationship between changes in the polarization constants and the electric field is given by

$$\Delta\vec{a}_{ij}=r_{ijk}\vec{E}_{\mathrm{k}}+R_{ijk}\,\vec{E}_{\mathrm{k}}\,\vec{E}_{\mathrm{l}} \tag{2.24}$$

The linear electro-optic effect (Pockels effect) is described by the equation

$$\Delta\vec{a}_{ij}=r_{ijk}\vec{E}_{\mathrm{k}},\ (\mathrm{i,\ j,\ k=1,\ 2,\ 3}) \tag{2.25}$$

where r_{ijk} are the coefficients forming the tensor of the linear electro-optic effect; $\vec{E}_{\mathrm{k}}$ is the electric field strength.

Due to the symmetry of the tensor of polarization constants Eq. (2.25) is written in matrix notation as

$$\Delta\vec{a}_{i}=r_{ij}\vec{E}_{\mathrm{k}},\ (\mathrm{i,=1,\ 2,\ldots,6;\ j=1,\ 2,\ 3}) \tag{2.26}$$

The phase difference Δφ between the ordinary and extraordinary waves, acquired during the passage through the crystal of length l, can be expressed by using Eq. (A.9) as

$$\Delta\varphi=\frac{2\pi}{\lambda}\cdot l\cdot(n'-n''), \tag{2.27}$$

where λ is the wavelength of the incident light.

Assuming that n_e and n_o differ slightly, for small angles ($\sin\theta\approx\theta$) we obtain

$$n''=n_o-(n_o-n_e)\cdot\theta^2 \tag{2.28}$$

Then the phase difference (phase retardation) for them will be

$$\delta=\frac{2\pi}{\lambda}\cdot l\cdot(n_o-n_e)\cdot\theta^2 \tag{2.29}$$

Imagine now that we put the crystal in a constant electric field E directed along the X-axis and perpendicular to the optic axis Z.

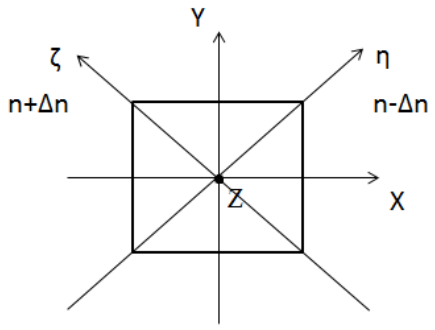

Figure 2.21: The emergence of new main directions when imposed to an electric field – Pockels effect (the transverse Pockels effect is shown).

For any polarization in the absence of an external electric field the refractive index is equal to n_o. The symmetry properties of the crystal and its electro-optic tensor are such that in the result of the linear electro-optical effect in a plane (X, Y) arise two main directions ζ and η at the angle 45 ° to the axes X and Y with the refractive indexes (n-Δn) and (n+Δn), i.e. “slow” and “fast” axes. Here Δn=A·E, A depends on the type of crystal (this coefficient will be considered in the Chapter 3.2.2). Imagine a simple scheme for describing of the Pockels effect when the light is polarized vertically at the input and the analyzer is placed at the output so that through this analyzer can pass just horizontal polarization.

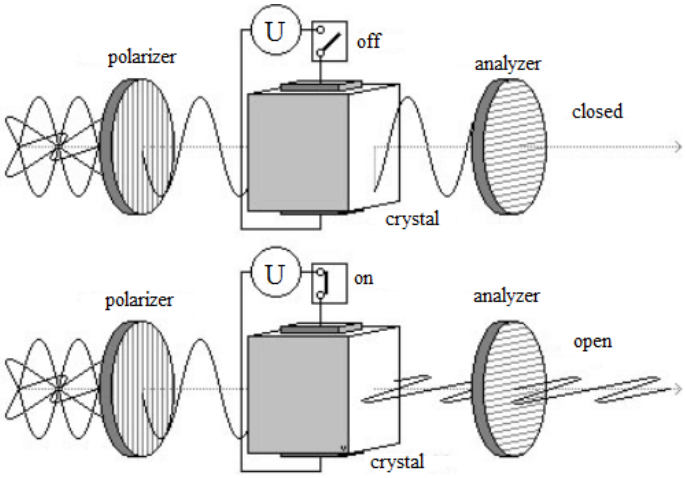

Figure 2.22: Simple scheme for describing of the Pockels effect (transverse): natural light after passing through the polarizer becomes polarized vertically. If the electric field is off, then polarization of the light passing through the crystal is preserved; when the electric field is on, it rotates the polarization, which is proportional to the applied voltage, and in the first case, when the analyzer is rotated by 90 °, the light cannot pass through. In the second case, when the light becomes polarized horizontally and therefore passes through the analyzer.

Expansion of the initial light vector $E = E_0 e^{i(\omega t - kz)}$ along the ζ and η gives us: $E_\zeta = E_\eta = E_0/\sqrt{2}$. While passing through the crystal a phase difference between the vectors E_ξ and E_η appears:

$$\delta = \frac{2\pi l}{\lambda} 2\Delta n = \frac{4\pi l}{\lambda} AE = \frac{4\pi}{\lambda}\frac{l}{d} AU, \qquad (2.30)$$

where U=E·d, d is the size of the crystal in the transverse direction, δ is the phase retardation, λ is the wavelength of the light, l is the length of the crystal.

The applied electric field and the light beam directions can be parallel or perpendicular to each other. These two cases are called longitudinal effect and transverse effect.

In the case of the longitudinal effect the product of (E·l) is equal to external voltage U, applied to the crystal. In the case of the transverse effect U = E·d, where d is size of the crystal along the electric field lines. When we use transverse disposition of the light and the voltage, the effect depends on the geometry of the element (d / l). Further, we discuss the transverse effect, because it was measured in the test.

The resultant field after leaving the crystal is the sum of the projections E_ζ, E_η on the X-axis:

$$E = \frac{E_0}{2} e^{i(\omega t - kl)} \left(e^{\frac{i\delta}{2}} - e^{\frac{-i\delta}{2}} \right) = E = E_0 e^{i(\omega t - kl)} \sin\left(\frac{\delta}{2}\right). \quad (2.31)$$

The light intensity then is

$$I_{out} \sim E E^* = E_0^2 sin^2\left(\frac{\delta}{2}\right). \quad (2.32)$$

We can rewrite this expression as

$$I = I^2 \cdot sin^2\left(\frac{\pi}{2} \frac{U}{U_{\lambda/2}}\right), \quad (2.33)$$

where $U_{\lambda/2}$ (or U_π) is the half-wave voltage. This is the figure of merit for electro-optic modulators, the voltage needed to produce a phase shift of 180°.

With using Eq. (2.30-2.33) we obtain for the half-wave voltage for the LiNbO3 crystal

$$U_{\lambda/2} = \frac{\lambda}{4A} \frac{d}{l} = \frac{\lambda}{n_e^3 r_{33} - n_0^3 r_{31}} \frac{d}{l}, \quad (2.34)$$

where l is the size of the crystal in the direction of light propagation, n_e and n_o are the refractive indexes, r_{13}, r_{33} are the coefficients of the matrix r_{ij} in the Eq. (2.26) (see in the Table 3 below), and for the quartz crystal

$$U_{\lambda/2} = \frac{\lambda}{4A} \frac{d}{l} = \frac{\lambda}{n_0^3 r_{41}} \frac{d}{l}, \quad (2.35)$$

where n_0 is the refractive index, n_0 = (1.54-1.55), r_{41} is the coefficient of the matrix r_{ij} (see in the Table 4 below). Hence, $U_{\lambda/2}$ depends on the material properties, on the wavelength λ, and on the ration d/l.

This half-wave voltage used to describe the transverse Pockels-effect.

For the longitudinal electro-optical effect we have

$$U_{\lambda/2}=\frac{\lambda}{2n_0^3 r_{11}}, \text{ and intensity } I = I^2 \cdot cos^2\left(\frac{\pi}{2}\frac{U}{U_{\lambda/2}}\right). \quad (2.36)$$

This half-wave voltage are hundreds of volts for transverse effect, and a few kilovolts for longitudinal Pockels-effect.

3.2.1. The experimental setup for the measurement of the Pockels effect.

The experimental setup is shown in Figure 2.23:

Figure 2.23: Test setup and equipment for measurements of the transverse Pockels effect: 1. Vacuum vessel; 2. Pressure sensor; 3. Optics for the input beam; 4. Optics for the output beam; 5. High voltage source; 6. Oscilloscope; 7. Laser controller.

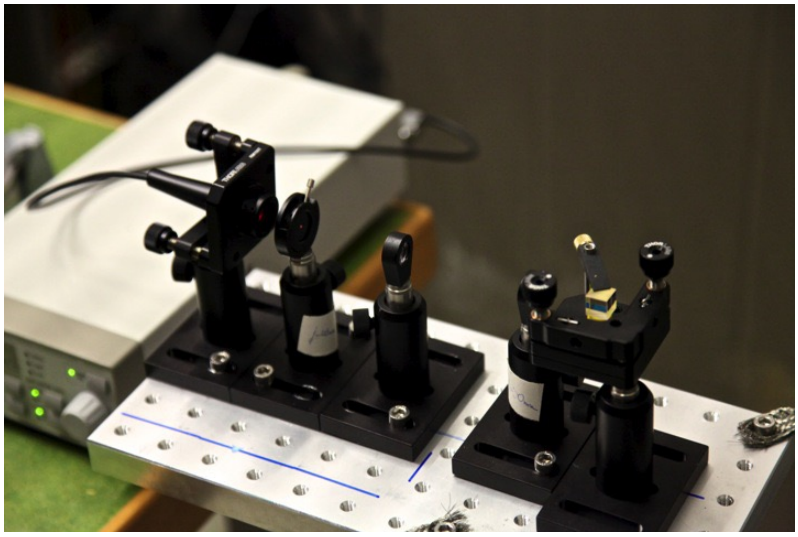

Figure 2.24: Optical components are shown in the part, which is installed in front of the vacuum vessel, comprising the laser diode, an aperture, two biconvex lenses, and a linearly polarizing beam splitter.

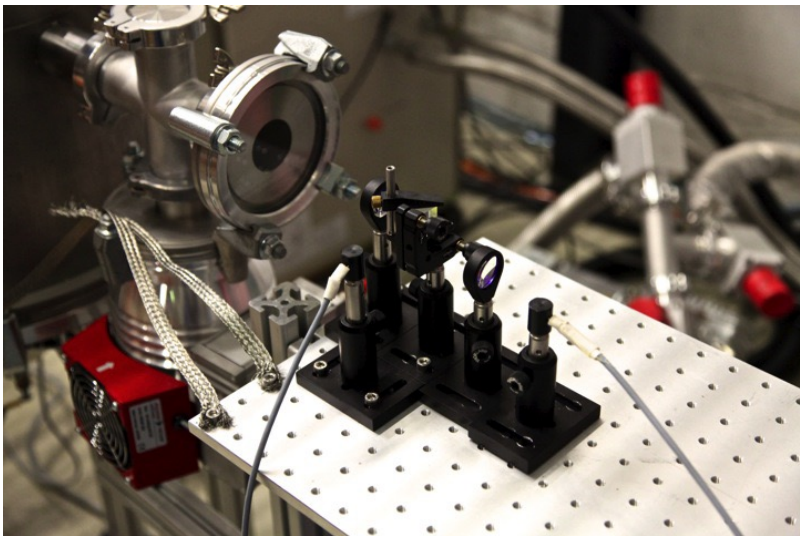

Figure 2.25: Optical components here are shown after transmission through the vacuum chamber consisting of biconvex lens, linearly polarizing beam splitter, a bi-convex lens for curbing the beam divergence, and two photodiodes for detection.

A sketch of the test setup is shown in Figure 2.26.

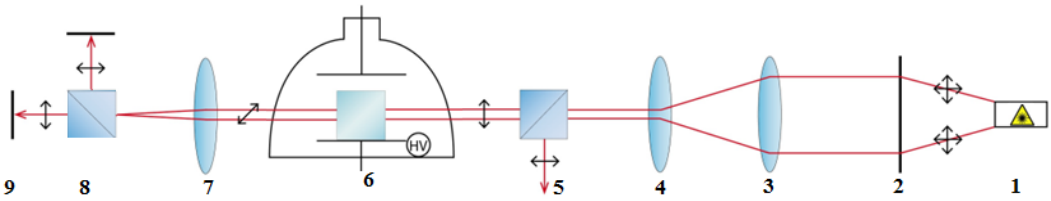

Figure 2.26: 1. Laser diode; 2. Diaphragm; 3. Lens to adjust the beam width; 4. Lens to adjust the beam width; 5. Polarizing beam splitter; 6. Vacuum vessel with built-in high voltage electrodes, the electro-optical crystal is situated between the electrodes; 7. Lens for focusing; 8. Polarizing beam splitter; 9. Photodiodes.

A linearly polarized laser beam of wavelength 670 nm goes through a diaphragm (2), where it is collimated. The collimated light is focused on the polarizer by a pair of lenses (3), (4). After the beam meets a polarizing beam splitter (5) which splits the incident beam into two orthogonal linear polarized beams. Part of the beam goes through a sight window into the vacuum chamber to the electro-optic crystal that is located between two high voltage electrodes made of aluminum (6). The vacuum was in the range of 10^{-6} mbar. Applying a voltage to the two electrodes will change the polarization of the laser beam by the resulting electric field. The laser beam goes then again on a lens (7) and is focused before it gets on a second linearly polarizing beam splitter (8). The laser beam splits again by the beam splitter into two mutually perpendicular linearly polarized beams, whose intensity is to be subsequently detected by means of photo-diodes (9) and by an associated oscilloscope.

3.2.2. Electro-optic crystals

As it was mentioned before, measurements of the electric field (transverse Pockels effect) in a quartz crystal and in a lithium niobate crystal, $LiNbO_3$, were performed. Here, we give a brief overview about these crystals.

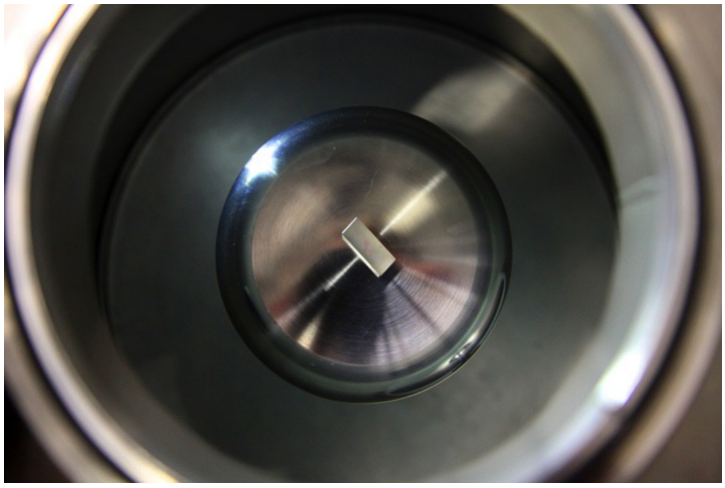

Figure 2.27: On the photo, the lower electrode connected to the high voltage power supply is shown. The $LiNbO_3$-crystal (10mm×5 mm×10 mm) is located in the beam path of the laser.

$LiNbO_3$	
Transparency range	420-5200 nm
Refractive index at 1064 nm	n_o=2.156, n_e=2.232
Electro-optic coefficients	r_{22}=6.8 pm/V, r_{31}=10 pm/V, r_{33}=32 pm/V, r_{51}=28pm/V

TRIGONAL

Group 3m	0	$-r_{22}$	r_{13}
	0	r_{22}	r_{13}
	0	0	r_{33}
	0	r_{51}	0
	r_{51}	0	0
	$-r_{22}$	0	0

Table 3: Optical parameters for the $LiNbO_3$ crystal.

The location of the crystal in the experiment is the same as in Figure 2.21, but the electric field is directed along y-axis. The significant elements for the $LiNbO_3$ crystal are r_{22} and r_{51}.

Figure 2.28: The quartz crystal cube (with the side of 20 mm), which was used for the measurement.

Quartz crystal	
Transparency range	180-3500 nm (also > 40 μm)
Refractive index at 600 nm	n_o=1.5442, n_e=1.5533
Electro-optic coefficients [69]	r_{41}=1.4 pm/V, r_{11}=0.59 pm/V

TRIGONAL

Group 32	r_{11}	0	0
	$-r_{11}$	0	0
	0	0	0
	r_{41}	0	0
	0	$-r_{41}$	0
	0	$-r_{11}$	0

Table 4: Optical parameters for the quartz crystal.

The significant elements for the quartz crystal are r_{11} and r_{41}. We can easily see that the coefficients differ roughly by an order of magnitude. But the difficulty of measurements with quartz arose mainly from the deformations in this quartz cube that affect the intensity of the output beam. The reason that quartz was investigated is the ability of the crystal to operate in a strong electric field. The electric field in our experiment is planned to be 15 kV/cm. The dielectric strength of quartz crystalline is up to 1.5 MV/cm, whereas for lithium niobate this value is about 3 kV/cm (see App. 4.1).

3.2.3. Results

The measured data are the intensities of the laser radiation, which has passed through the crystal. The outgoing intensity is described by the Eq. (3.14). The signal was measured 3 times in sequence. Measurements are performed for the $LiNbO_3$ crystal and for the quartz crystal.

In Figures (2.29-2.32) are shown the results of these measurements:

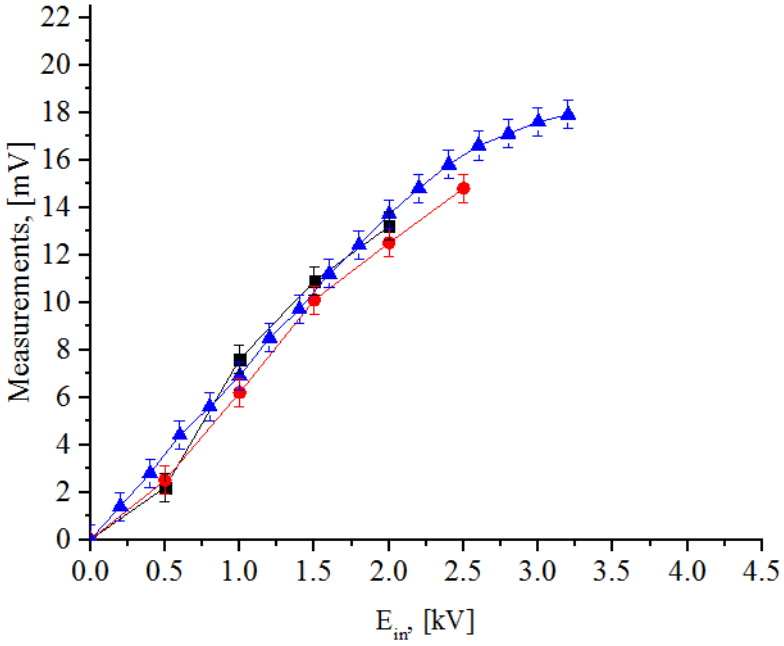

Figure 2.29: The example of measurement of the outgoing intensity (LiNbO3). The three consecutive measured signals in different colors are shown. Statistical error is 0.1mV for all the measurements. The measurements were performed for electric field up to 3.5 kV because of the risk of destruction of the crystal. “Red” and “Black” measurements are finished earlier because of high voltage breakdown.

In Figure 2.30, one can see the calculated electric field, E_{out}, compared to the electric field from the high voltage power supply.

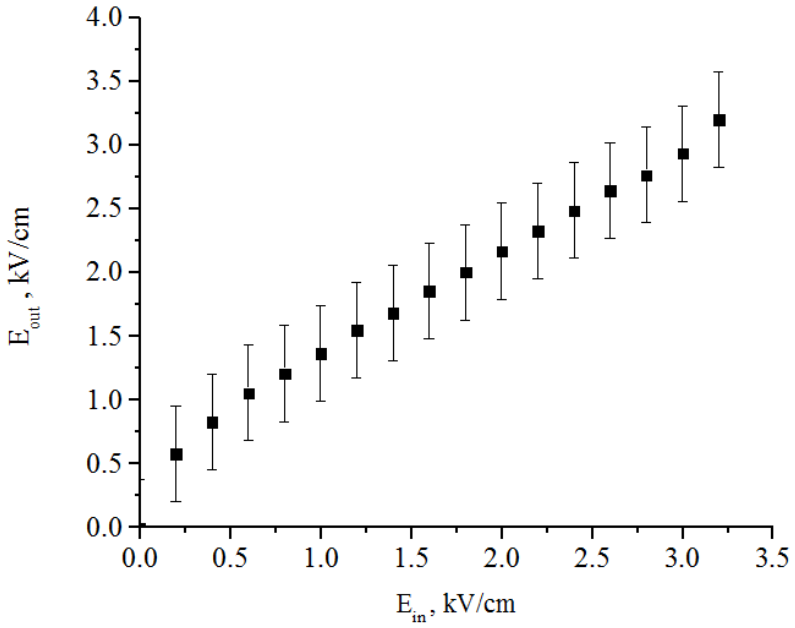

Figure 2.30: The LiNbO3 crystal: One example of a comparison of the calculated electric field, E_{out}, with the applied electric field, E_{in}. It corresponds to the blue curve in Figure 2.29.

The calculations show a discrepancy of measured and applied electric fields (200-300 V) in the measurements of up to 2 kV. It is due to the inaccuracy of focusing, due to the presence of external noise (light).

The calculated $U_{\lambda/2}$ for the $LiNbO_3$ crystal is about 5 kV (E=5 kV/cm) at λ=670 nm and $U_{\lambda/2} \approx 64$ kV (E=32 kV/cm) for the quartz crystal (see Eq. (2.34-2.35)). When half-wave voltage is applied to a crystal, the intensity of the exiting radiation will reach its maximum value. We can see that in the case of the LiNbO3 crystal the maximum of the intensity is situated in the region 3.2 kV, but unfortunately, we could not to check it properly due to sparks between the electrodes and because of the risk of crystal destruction. The measurement of the Pockels effect on the quartz crystal is shown here for the glass electrode with salt water. The procedure for the measurements remained the same, only we replaced the metal electrode with a glass electrode filled with salt water. The measured values are shown in Figure 2.31.

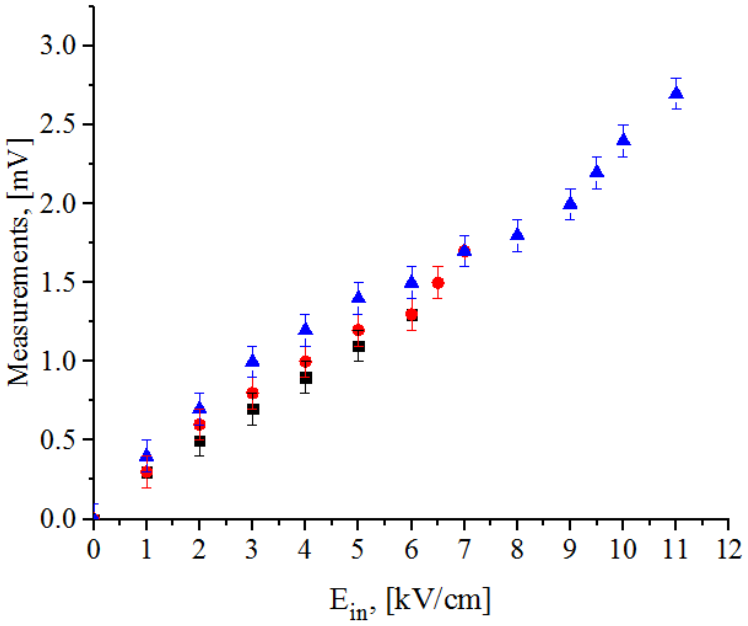

Figure 2.31: The example of measurement of the outgoing intensity (quartz crystal). The three consecutive measured signals in different colors are shown. The distance between the electrodes is equal to the size of the quartz cube, i.e. 2 cm.

Stopping of the measurements is associated with the multiple high voltage breakdowns in the working gap. Numerous high-voltage breakdowns are due to the presence of not rounded edges and micro-peaks on the surface of the cube. In addition, quartz becomes polarized, which prevented further measurements due to a respective offset.

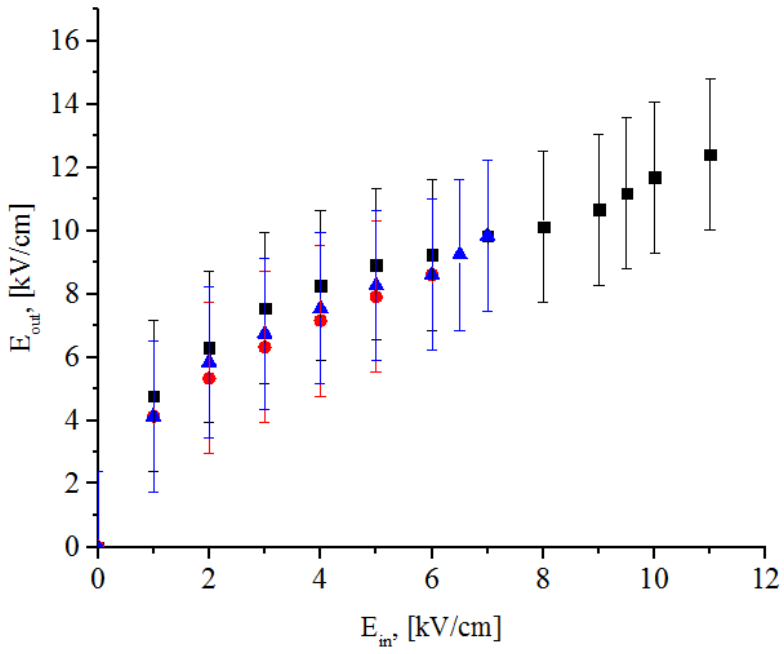

Figure 2.32: The quartz cube: the calculated electric field, E_{out}, vs the applied electric field, E_{in}. The results are obtained from the conversion of the measured intensities by the Eq. (2.32).

During the measuring of the Pockels effect with the quartz cube we reached a field strength E = 11 kV/cm. Half-wave voltage calculations give a value almost three times more, i.e. E = 32 kV/cm, so the differences in the measured values relatively of the applied electric field are about 2 kV at the beginning and up to 8-9 kV/cm. Besides, the measurement might be distorted by the residual polarization of the crystal as well as deformation of the structure within the quartz cube. The measurements were repeated and they confirm the presence of the electric field effect on the polarization of the crystal. In conclusion, this method can be applied for the control and measurement of the electric field in our main experiment.

3.3. Investigation of high voltage breakdown in gases: ^{129}Xe.

An unstable electric field can be the reason for voltage breakdowns between electrodes. The experimental electric field is always non-uniform. Therefore, strictly speaking, breakdown in gas cannot be found as a quotient of dividing the potential difference by the distance between the electrodes. It is even possible when the shape of the electrodes provides excellent field homogeneity. With an increase of the potential difference, the density of the space charges increase which distorts the electric field. In some places the field is weakened, in other it is increased. With sufficient potential difference in some places voltage reaches a value sufficient to impact ionization, which can lead to a breakdown [67].

A goal of our measurements was to determine the breakdown voltage of ^{129}Xe which could be applied as co-magnetometers (a mixture of helium and xenon) in the nEDM-experiment, in high vacuum region. Also, the electric breakdowns in air and in helium were measured.

High vacuum region with respect to voltage of breakdown in various gases is almost unexplored area. That is why practical interest presents to study the electrical breakdown in various inert gases at a very low pressure. In experiments on the search for the electric dipole moment of the neutron uniformity and stability of the electric field play a crucial role in the accuracy of nEDM measurement.

The mechanisms of electrical breakdown in gases are studied for a long time. De La Rue and Muller first discovered the dependence of the breakdown voltage U from the product of the gas pressure p and the distance between the electrodes d [68]. Paschen investigated ignition DC discharge between spherical electrodes, changing the distance d between them. He showed that the breakdown voltage U depends only on the product p·d. This law is commonly known as Paschen's law [69] (see Fig. 2.33).

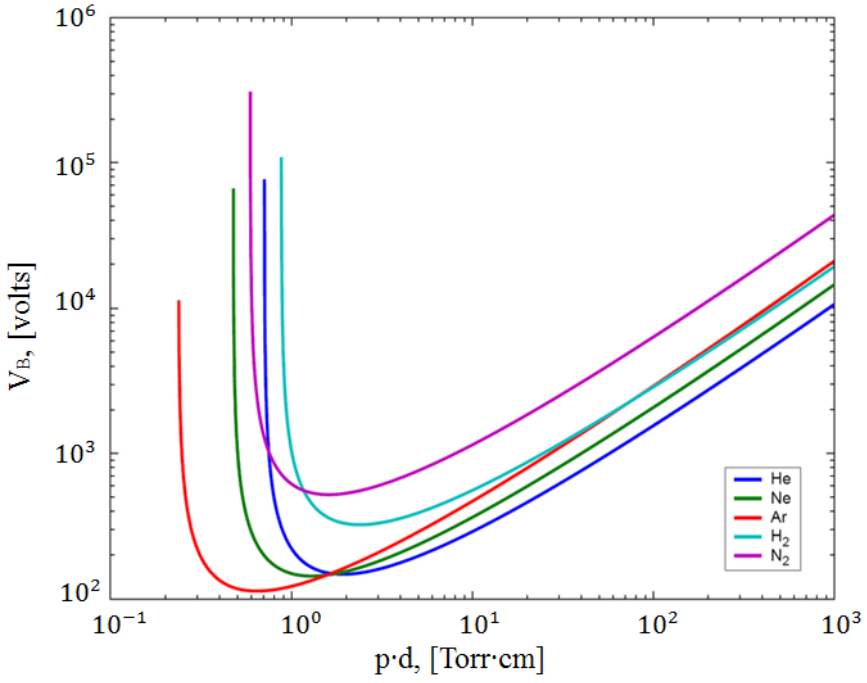

Figure 2.33: Paschen curves for helium, neon, argon, hydrogen, and nitrogen. Paschen's law means that the ignition curves U(p), measured for different distances between the electrodes d, must overlap each other, if they are constructed as a function U(p·d).

Later, various researchers observed deviations from the law [70, 71]. But these measurements have been performed at very low vacuum or at the atmospheric pressure.

The voltage breakdown in the inert gas ^{129}Xe in the discharge chamber with varying distances between the electrodes in a DC electric field was investigated in this work. We used a test chamber, in which the voltages could be tested on voltage breakdown over varying distances and Xenon gas pressures. The Xenon, tested over different pressures, should breakdown easily at a low pressure, while maintaining a high resistance near high vacuum (10^{-5}mbar-10^{-4}mbar).

We performed tests with xenon at pressures between $1.7{\cdot}10^{-5}$mbar and 0.035 mbar. In Figure 2.34 you can see the test setup and equipment for the study of the breakdown in xenon, which is fed into a vacuum chamber through a needle valve from the container.

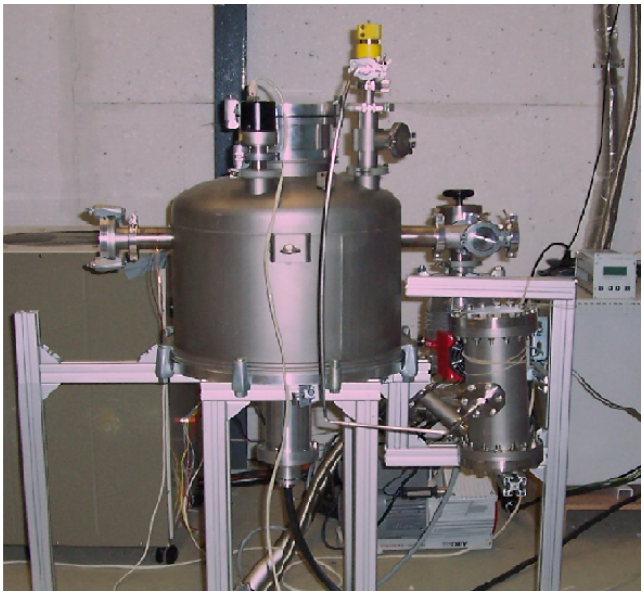

Figure 2.34: Test equipment: 1) Vacuum chamber (vessel V=50 l); 2) Gas cylinder with ^{129}Xe (V=3 l); 3) Vacuum sensor.

Prior to gas inlet, the vacuum was P=$2\cdot10^{-5}$mbar. In the tests we used a HV-supply, which exploits 230V ±10% to provide 150 kV at 2 mA. The HV source was connected to the vacuum chamber through a HV inlet. The HV electrode was fixed on the inlet. The ground electrode was screwed into the lid of the vacuum chamber.

Procedure:

1. The electrodes were placed at a fixed distance. During the measurements the vacuum pumps were continuously running. The pumping speed was S ≈ 20 l/s. We can adjust the pressure in the vacuum chamber through the needle valve. This valve was connected to a gas cylinder with the ^{129}Xe. Hence, xenon is pumped during the measurements.

2. We should "train" the electric field in the vacuum. When everything was properly working the valve was carefully opened and the ^{129}Xe is released into the chamber slowly until the pressure, at which we want to measure the breakdown voltage was reached.

3. Starting at 0 V, we slowly raised the voltage until a current is detected. The breakdown was also visible as a flash through the vacuum chamber window. We recorded the pressure and voltage

simultaneously. All values of pressures were corrected for xenon gas. The measurements were repeated 5 times.

4. Now we go to the next pressure and so on – from the highest to the lowest.
5. Items 1 to 4 were repeated at four different distances between the electrodes.
6. The measurements of the breakdown voltages were repeated in the same way for air and for helium.

The vacuum region of our interest in these measurements is between 10^{-5}mbar and 10^{-3}mbar. Here, it corresponds to $\sim 10^{-4}\text{mbar} \cdot \text{cm} - 10^{-2}\text{mbar} \cdot \text{cm}$. The results are introduced in Figures 2.35-2.37.

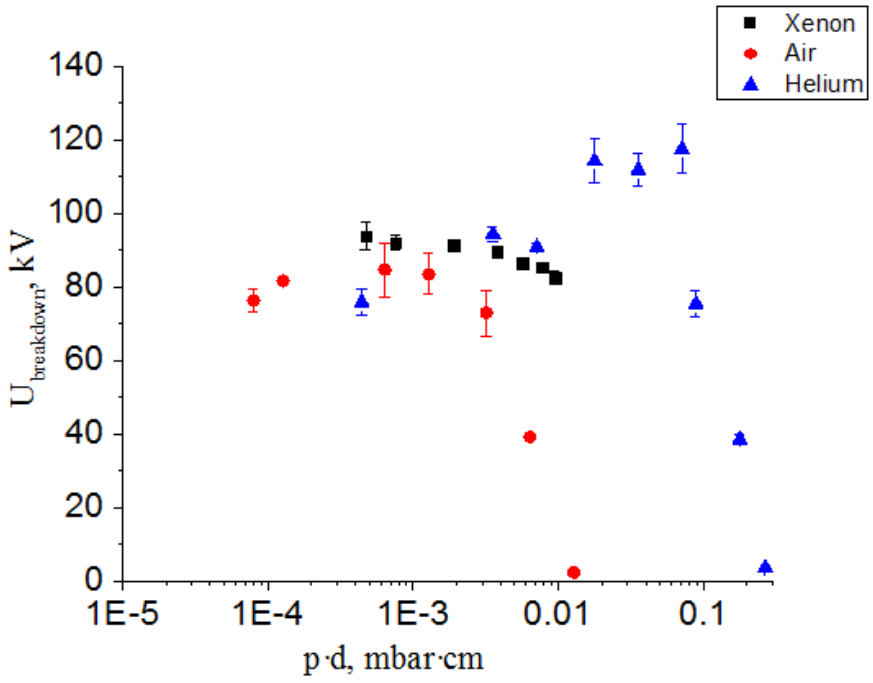

Figure 2.35: Electric breakdown voltage for different gases at a distance 1.6 cm between the electrodes.

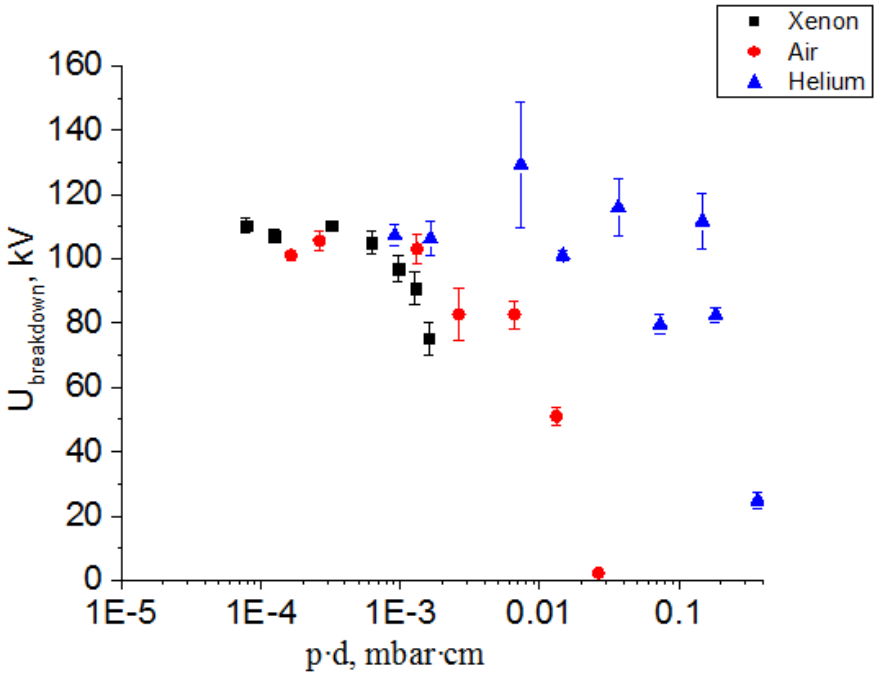

Figure 2.36: Electric breakdown voltage for different gases at a distance 3.3 cm between the electrodes.

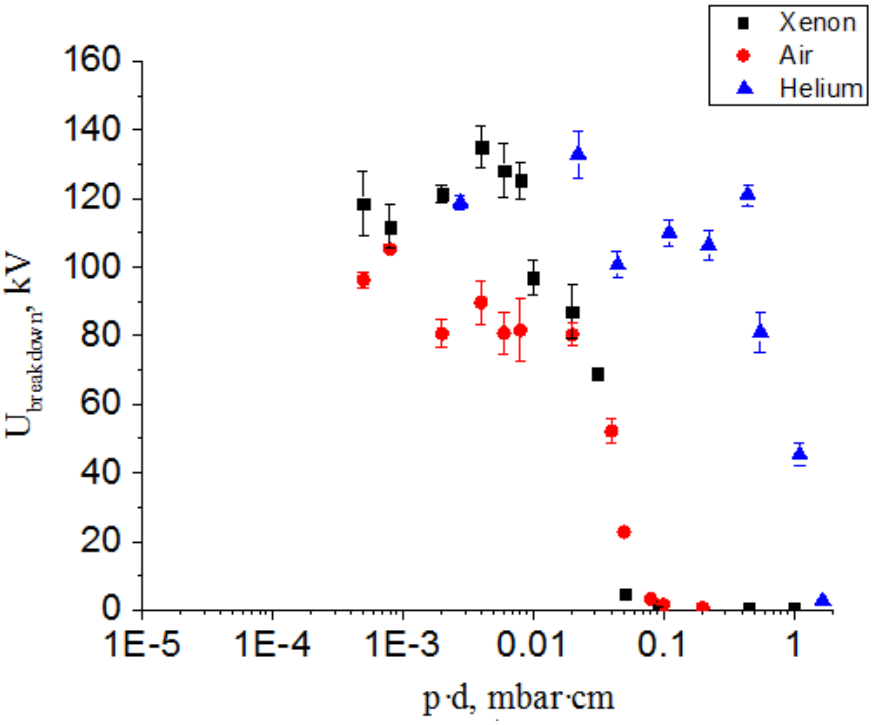

Figure 2.37: Electric breakdown voltage for different gases at a distance 10 cm between the electrodes.

We can see that the distributions of the voltage breakdowns are independent of the gas at the pressure below10^{-3}mbar·cm. In the extreme case, when the pressure of the gas is a few10^{-5}mbars, all tested gases reach the vacuum breakdown value. But we need the more accurate measurements. Different gases fill a whole volume of the vacuum chamber (see Fig. 2.11, Chapter 3.1.1) in this experiment. It is difficult to point out the localization of sparks exactly. A new vacuum chamber was constructed in order to perform precise measurements including the measurement of breakdown voltage in gases (see Fig. 2.38).

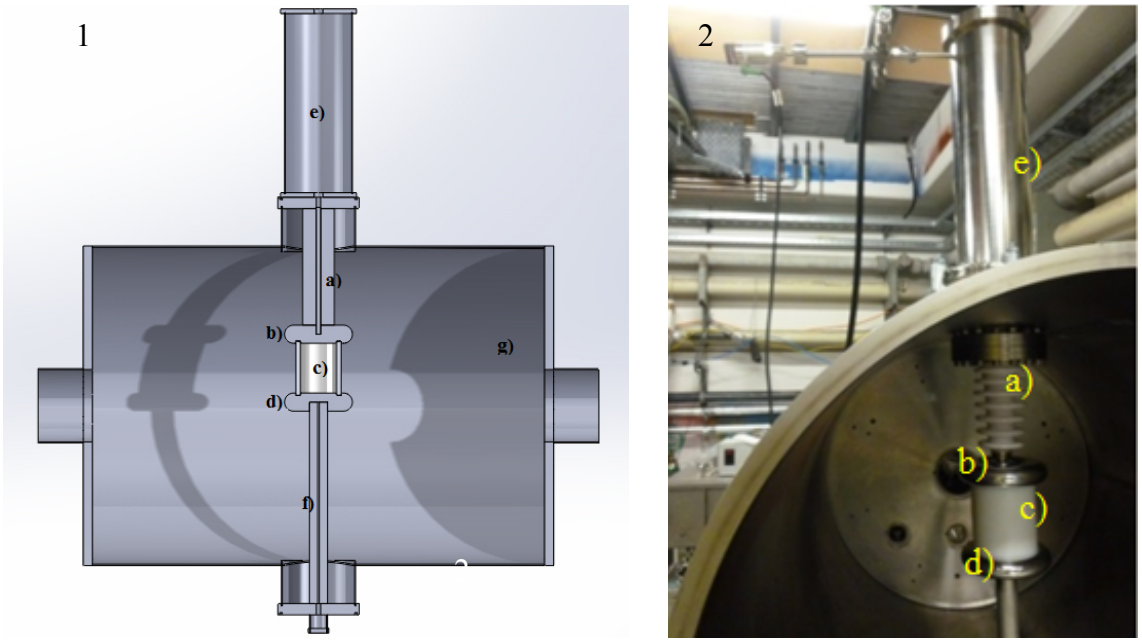

Figure 2.38: 1. Simple model of the new test setup (SolidWorks simulation); 2. The new test setup with the: HV inlet (a), high-voltage electrode (b), insulator ring (c), ground electrode (d) and with the chamber for SF6 (e). Small chamber is pumped out through the tube (f). The small vacuum chamber and high-voltage equipment are located in a large vacuum chamber (g).

The experimental setup consists of two vacuum chambers. The small chamber is placed in the large one and it is used for the voltage breakdown test. The plastic insulator ring (c) is placed between the electrodes (the distance is 10 cm). A new measurement of the voltage breakdown in this test setup has been performed. Four different gases were filled into the small chamber with the use of a needle valve. A fixed pressure was set, and the voltage was slowly changed until a breakdown occurred. Prior to gas inlet, the vacuum was P=$6 \cdot 10^{-6}$mbar. The system was operated in a flow-through mode with the

turbo pump running up to a pressure of about 10^{-5} mbar. The maximum voltage that could be reached, U, is 110 kV for this high-voltage feedthrough. The remote control/readout was used in order to avoid possible ionizing radiation in the plastic chamber. This measurement is particularly interesting in that an insulator was placed between the electrodes. The results are introduced in Figure 2.39.

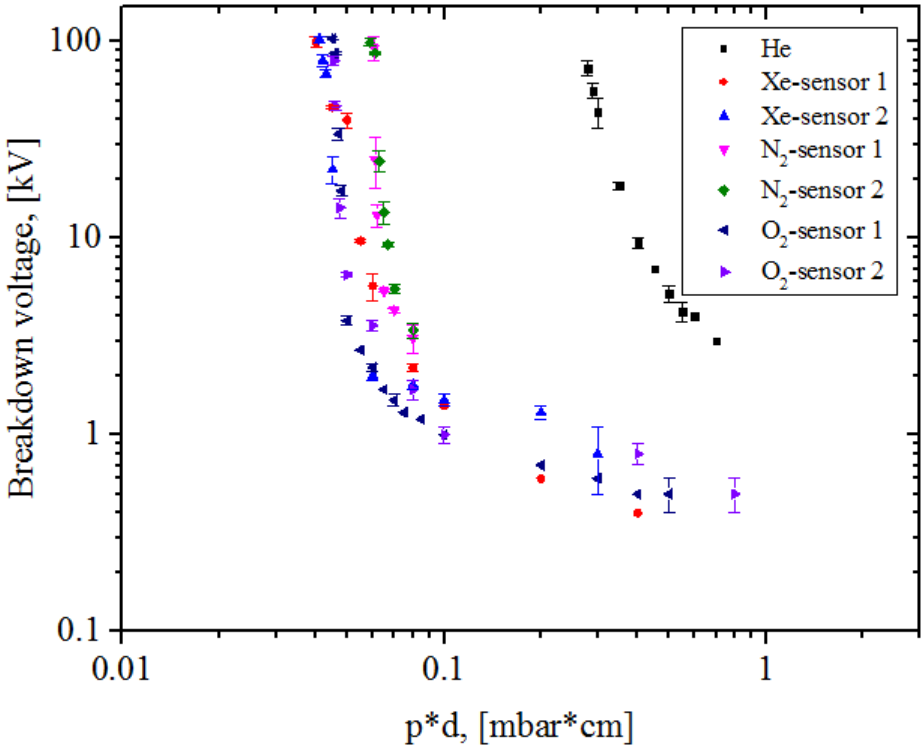

Figure 2.39: Electric breakdown voltage for different gases in the small chamber at a distance 10 cm between the electrodes.

These results are in agreement within tolerances with the measured voltages of breakdown in different gases at PSI [58] in 2013. Differences in measurements up to factor of 2 are associated with different types of pressure sensors: 2 gas-dependent sensors (TUM) and 2 gas-independent sensors (PSI). Furthermore, one more reason of the shift is that different insulators between the electrodes have been used (plastic (TUM) and quartz glass (PSI)).

4. Leakage currents.

4.1. Simulation of leakage currents for the nEDM experiments.

One of the most probable sources of false EDM effects (direct systematic effect) in the experimental search for nEDM are leakage currents arising on surfaces of insulators in traps and caused by the high voltage. They are connected with imperfections of these surfaces (such as microcracks or inhomogeneous surface conductance) and depend on the contact between the electrodes and the insulators. The directions of these currents are associated with the direction of the electric field in the experiment. If these leakage currents have a circumferential component, then they will produce a magnetic field that will add linearly to the uniform magnetic field, and thus affect the precession of the neutron spin. The measured cell leakage currents are typically less than 0.5 pA. In the worst case it would produce an error equivalent to an EDM of about $d_{false} \sim 10^{-29}$ e·cm [72]. We can simulate many different paths for leakage currents, but the real routes are not known, it is possible only to measure the current. In Figure 2.40 you can see a schematic representation of a possible path of the leakage current.

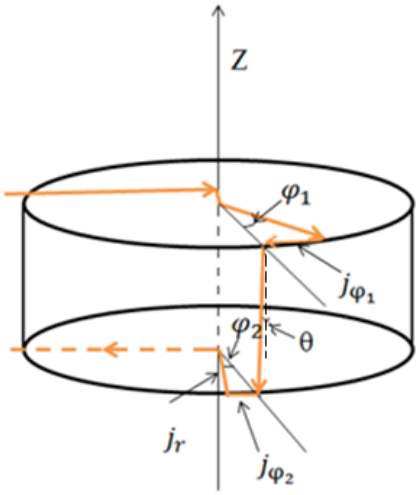

Figure 2.40: The geometrical characterization of leakage currents.

Here, it is assumed that two high voltage wires are connected to the centers of the electrodes on the top and bottom of the cell. A leakage current can originate from the first contact point and flows radially toward the edge of the chamber, where the electrode and the insulator ring are connected (φ-

component). This current may circularly move until it reaches a point where the breakdown will happen. In another scenario it can move along the surface of the insulator, choosing the path of least resistance, and then just go back to the lower conductor.

A leakage current can be decomposed by components in a cylindrical coordinate system in terms of j_z, j_r, and j_φ. Most harmful to the systematic effects is the j_φ current component. It creates a magnetic field in the direction of the magnetic holding field inside the chamber and it remains outside the chamber in the opposite direction. It cannot be compensated. The larger the angle θ, the greater the influence of this component on the error. A j_r component affects the average spin precession frequency of the neutrons because the UCN density distribution is not homogeneous in the vertical plane. A j_z component of the current does not affect the error, because it creates a magnetic field perpendicular to the main magnetic field B_0. Hence, no changes in precession frequency can occur.

In Figures 2.41- 2.43, one can see COMSOL simulations of three different paths of leakage current flowing along the surface of the insulator.

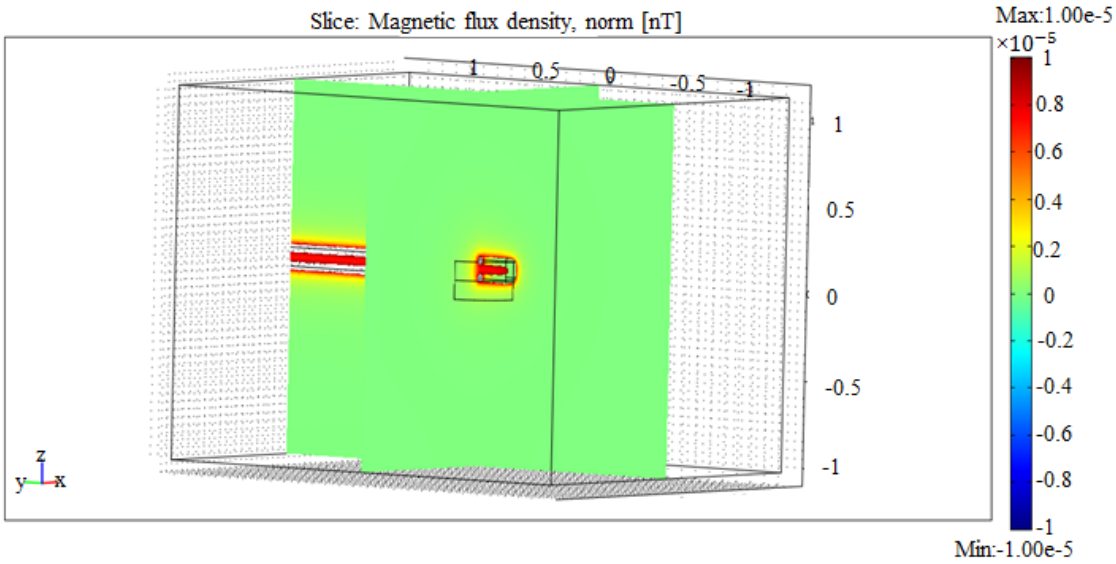

Figure 2.41: COMSOL simulation of a magnetic flux density for I_{leak}=1nA in the case of a simple straight leakage current.

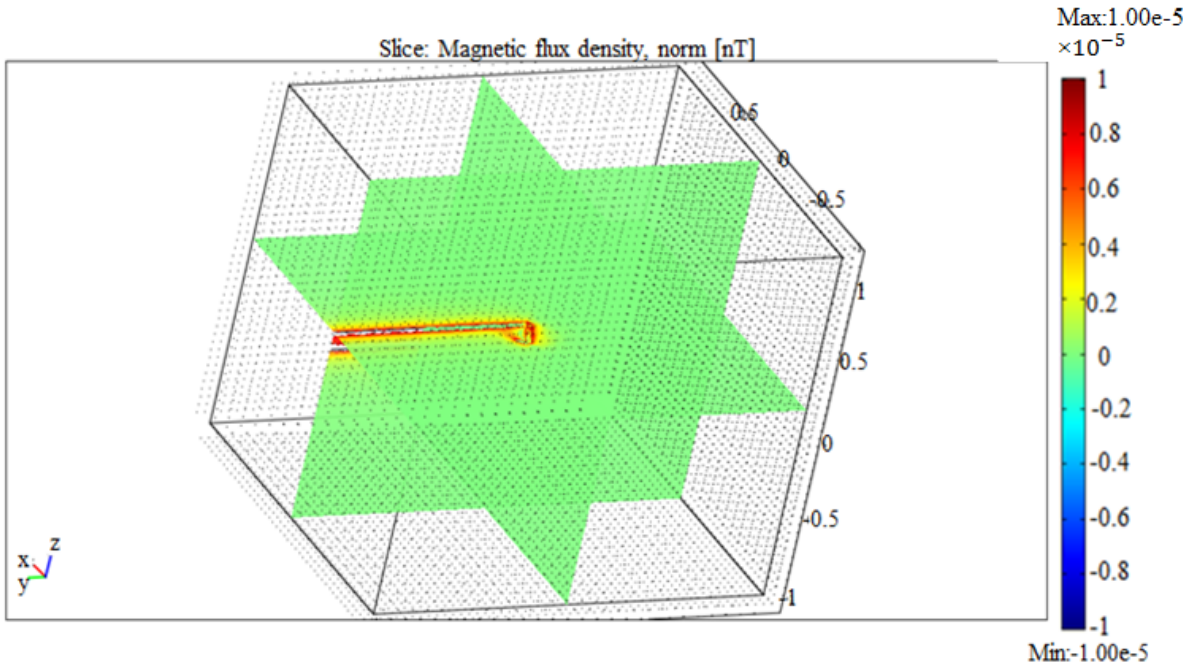

Figure 2.42: COMSOL simulation of a magnetic flux density for I_{leak}=1nA in the case of straight leakage current, which can reach the other electrode along the side surface (straight+arc).

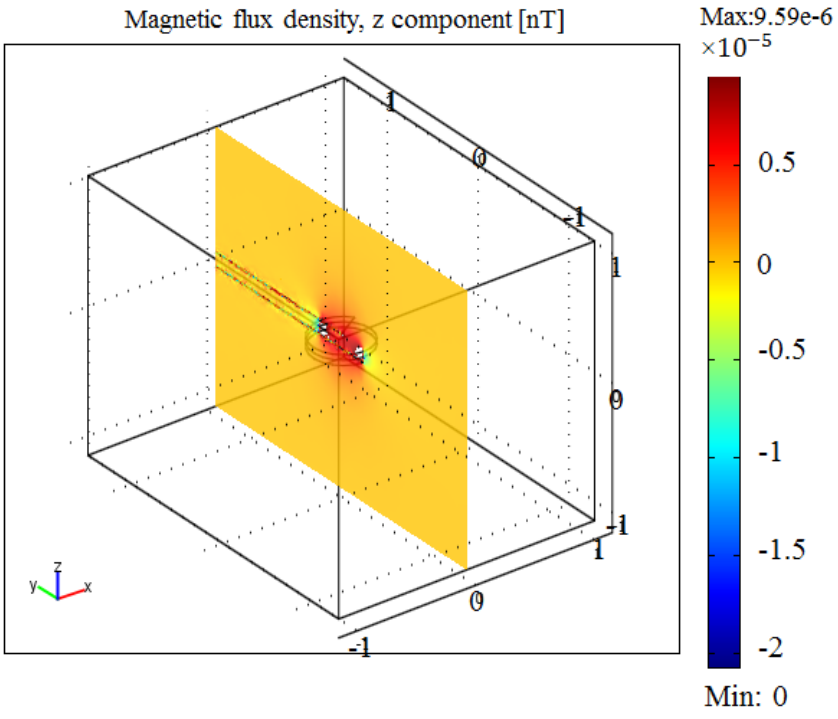

Figure 2.43: COMSOL simulation of a magnetic flux density for I_{leak}=1nA, when the current flows in a spiral counterclockwise about the Z-axis along the surface of the insulator ring.

As seen here, the leakage current in I_{leak}=1nA of various configurations gives rise to a magnetic field of up to 10^{-15} T. In the new nEDM experiment the magnitude of the main magnetic field is 1 μT that is 8 orders of magnitude higher. The UCN will precess with frequency

$$\omega_n = \gamma_n B_n = \gamma_n \cdot \sqrt{(B_x + B_y + B_z)^2}, \tag{2.37}$$

where γ_n is the neutron gyromagnetic ratio, γ_n= 1.83·10^8 Hz/T,

whereas mercury atoms precess at a frequency

$$\omega_{Hg} = \gamma_{Hg} B_{Hg} = \gamma_{Hg} \cdot \sqrt{{B_x}^2 + {B_y}^2 + {B_z}^2}, \tag{2.38}$$

where $\left|\frac{\gamma_n}{\gamma_{Hg}}\right| \approx 3.84$.

This will result in a false EDM [36]

$$d_{f,n} = -\frac{\hbar}{4E} \cdot \omega_n = -\frac{\hbar}{4E}\, \gamma_n \cdot \overline{\Delta B_E}, \tag{2.39}$$

In our experiment the electric field is E=150 kV/12 cm=1.25 MV/m.

In Table 5, one can see the average values of the projections of the magnetic field created by the leakage current, the magnetic fields experienced by the neutrons and mercury atoms, $\overline{B_n}$and $\overline{B_{Hg}}$. The average volume gradient $\overline{G_z}$ was also calculated and is presented in the table.

$$\overline{G_z} = \sum_{i \neq j}^{\forall x_i = x_j, y_i = y_j} \frac{B_{z_i} - B_{z_j}}{z_i - z_j}, \tag{2.40}$$

Finally, the false effects $d_{n,f}$ are extracted.

Sample	$\overline{B_x}$, aT	$\overline{B_y}$, aT	$\overline{B_z}$, aT	$\overline{B_n}$, aT	$\overline{B_{Hg}}$, aT	$\overline{G_z}$, aT	$d_{n,f}$ without Hg comagnetomer, e·cm	$d_{n,f}$ with Hg comagnetomer, e·cm
1. Straight, I = 1nA	2360	16	165	2970	3290	7700	$3.3\cdot10^{-28}$	$6.8\cdot10^{-28}$
2. Straight+arc, I = 10pA	5.5	1.94	8.9	28.8	28.6	37.7	$17.8\cdot10^{-30}$	$0.62\cdot10^{-30}$
3. Spiral, I = 10pA	12.2	4.93	51.6	105.4	110.2	53	$10.3\cdot10^{-29}$	$1.02\cdot10^{-29}$

Table 5: Calculation of the false effects for the sampled configurations of the leakage currents.

The magnetic field change B_z would result in a false EDM of the neutron (see Eq. (2.12)) of up to $d_{n,f} = 3.3\cdot10^{-28}$e·cm for the straight current without the Hg co-magnetometer. An uncorrected field $\Delta B_E = \Delta B + \Delta h G_z$ (a typical center-of-mass offset of $\Delta h = 0.3$ cm) will be created only by the difference $\Delta B = B_{UCN} - B_{Hg}$ and the average gradient G_z in combination with the center of mass offset Δh between Hg and UCN due to the correction with the Hg co-magnetometer. It will result in a systematic effect $d_{n,f}=6.8\cdot10^{-28}$ecm. By using the Hg co-magnetometer we obtain a large difference in these effects for the second configuration of the leakage current.

The inclination angle θ (see Fig. 2.40) can be limited by ±15°. It is based on the experience of the PNPI group on leakage currents measurement [73]. They simulated (Monte Carlo simulations) 72 possibilities (the HV breakdown points) on a circular line between the HV electrode and the insulator ring: the inclination angle within a Gaussian distribution of θ= ± 15 °and the angle φ within a Gaussian distribution of ±2.5°. The simulation was performed for 13 experimental cells, the mean of the leakage currents $\bar{I}_{leak}$ was chosen to be 1 nA. The average false effect that they have received for the complete spectrometer is $d_{n,f} = 2\cdot10^{-28}$e·cm. A similar simulation of the same leakage current with COMSOL (see Fig. 2.44) gives $d_{n,f} \approx 9\cdot10^{-28}$e·cm.

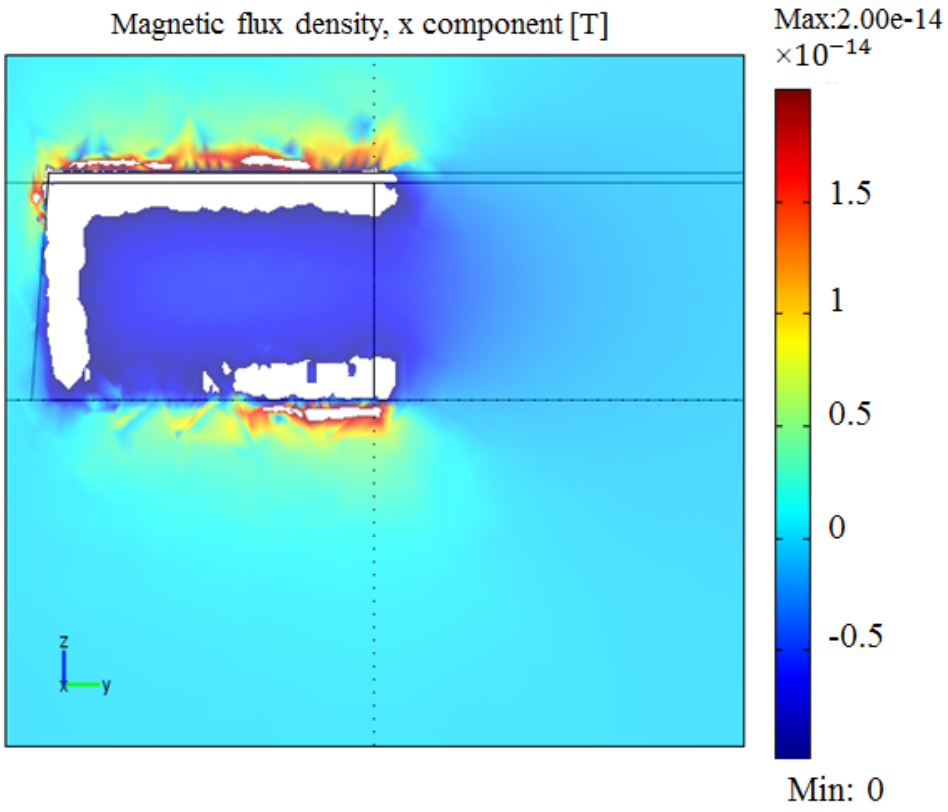

Figure 2.44: COMSOL simulation of the leakage currents based on studies of their paths of the PNPI group. Here, the x-component of the magnetic field, B_x, is taken in the plane YZ.

They concluded that the width of the distribution of the leakage currents for one single trap is four times wider than for the complete spectrometer. This is the reason why we find the false effect 4.5 times higher in the single simulation with COMSOL. This is an excellent confirmation of using a multi-chamber setup (in our case a double-chamber) for minimizing systematic errors.

4.2. Measurement of leakage currents.

In this chapter, the measurements of the leakage currents are discussed. Any interference in the experiment will affect the result of the measurement. Usually the leakage currents are registered on the contact of the ground electrode, whereto they flow over the insulator. Since the leakage currents are very small, i.e. they are limited to tens of nA in the old experiments, then in order to register them, it is necessary to use high resistances. This allows us to get a signal in the range of millivolts. In Figure 2.45 a scheme of the test setup and an example of such a converter of small currents to voltage has shown.

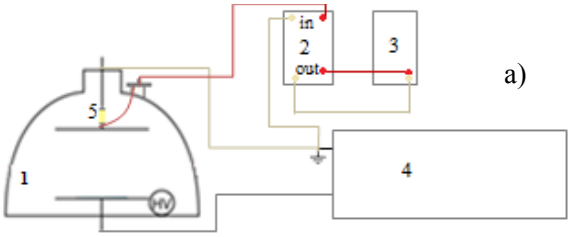

a)

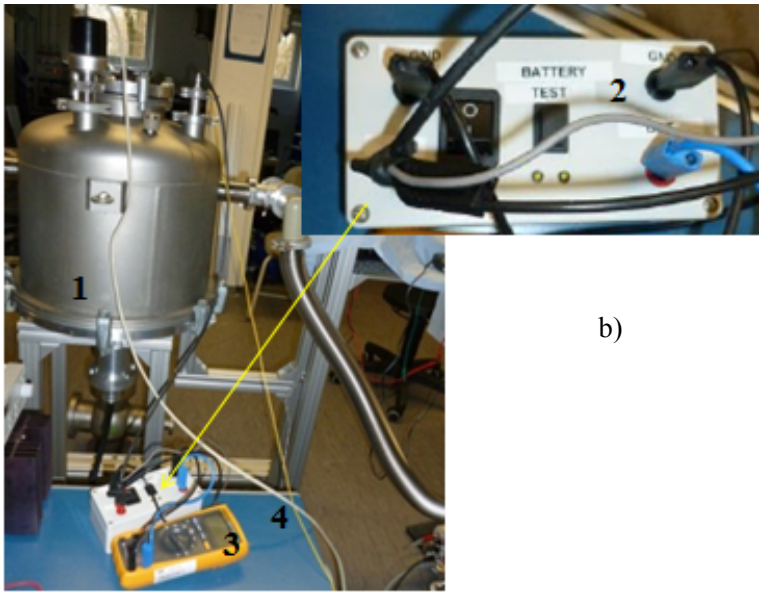

b)

Figure 2.45: Measurements of leakage currents in the experimental chamber: a) Scheme of the test setup, b) The test setup: 1. Vacuum chamber; 2. “Current-to-voltage” converter; 3. Multimeter; 4. The high-voltage power supply; 5. Teflon rod.

The resistance in the device can be replaced to raise or to lower limits of measurements. For example, the resistance R=100 MOhms allows to measure the leakage currents in the limits of 1 pA - 50 nA. But

the restrictions are imposed on the sensitivity of the convertor because of the external interference from the other operating equipment. The device was tested between 1 pA to 1 nA. Later, a new setup was assembled that works on the same principle but the influence of extraneous signals is eliminated. All metal wiring is replaced to optical fibers. This converter was tested on breakdowns created intentionally by sparks in the electrode gap. After these artificial breakdowns, no irregularities of the converter were observed. In Figures 2.46-2.47 you can see the results of the first measurements of the leakage currents in the test setup as the function of the applied voltage.

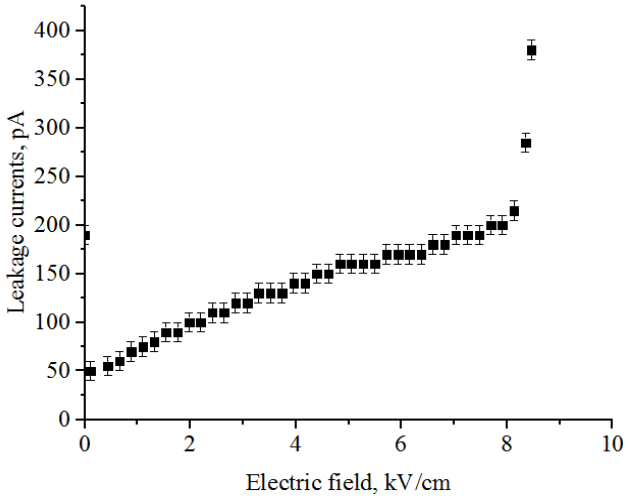

Figure 2.46: Measured leakage currents versus the applied electric field for a distance, D, between the electrodes of D=9 cm. The statistical error was 0.1 mV, which corresponds to 10 pA.

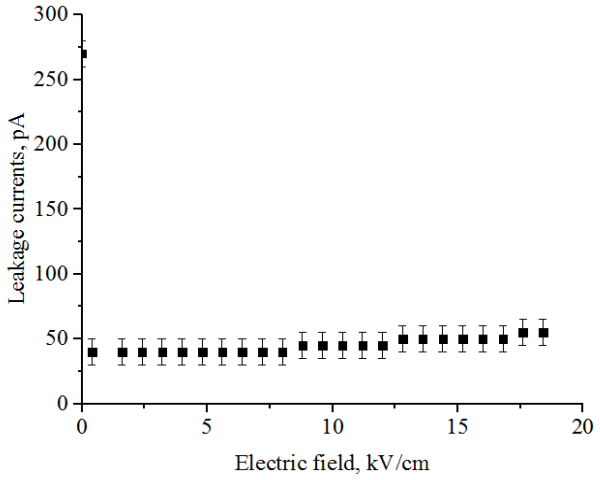

Figure 2.47: Measured leakage currents versus the applied electric field for a distance, D, between the electrodes D=2.5 cm.

Figure 2.48: The ground electrode with a fixed insulator (Teflon rod).

The leakage currents flowed over the surface of a Teflon rod, which was fixed on the ground electrode. The vacuum for the tests was $5 \cdot 10^{-5}$mbar. The first point is not zero due to different capacities which discharged when current started to flow. The leakage currents grow very rapidly at large distances between the electrodes (see Fig. 2.46). In this case we observe the influence of high-voltage effects. In Figure 2.47, we can see a steady slow increase in current by increasing the voltage applied to the electrodes. As a result of these tests, the device is able to measure very low currents. But we need to measure leakage currents flowing across the surface of the insulator ring. As mentioned in the Chapter 3.3, the new test setup (see Fig. 2.38) is better suited for our measurements because it simulates the future experiment. We have several insulator rings made from plastic and quartz glass which can be installed between the electrodes. These measurements were not performed due to the suspension of work on the accelerator where this setup is placed.

4.3. Investigation of the resistivity of insulating materials by measuring the leakage currents.

4.3.1. SilGel®612.

The possibility of using of silicone gel as an insulating material instead of vacuum was investigated. We measured the leakage currents on the insulator to determine its resistivity.

In Figure 2.49 is shown a two-component silicone rubber.

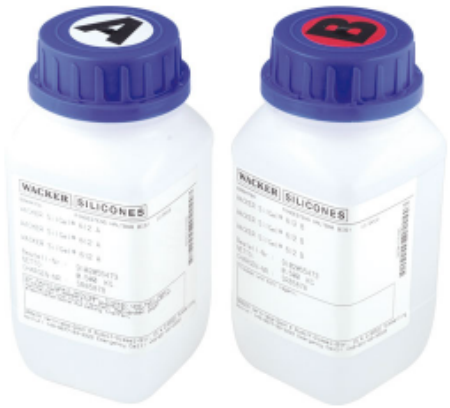

Figure 2.49: WACKER SilGel®612 is a pourable, addition-curing, two-component silicone rubber that vulcanizes at room temperature to a very soft silicone gel.

Property	Test method	Unit	Value
Color			Clear
Density at 23 °C	ISO 2781	[g/cm³]	0.97
Penetration (150 g hollow cone)	DIN ISO 2137	[mm/10]	300
Dielectric strength	IEC 243	[kV/mm]	23
Volume resistivity	IEC 93	[Ωcm]	10^{16}
Dielectric constant	VDE 0303 T4 / 50 Hz	[ε_r]	2.7
Dissipation factor	VDE 0303 T4 / 50 Hz	[tan δ]	10×10^{-4}
Tracking resistance	DIN IEC 112	[CTI]	> 600
Surface resistivity	DIN IEC 93	[Ω]	10^{14}
Refractive index	n_D^{25}		1.404

Cured for 30 min at 150 °C in circulating air oven.

Table 6: SilGel®612: Physical and mechanical properties.

The manufacturers offer two methods of preparation of the two-component silicone rubber:

i) Mixing the components in a ratio of 1:1 (A: B);

ii) Mixing in proportions of 1.5:1.

The first attempt to mix components A and B in a ratio of 1:1 was unsuccessful, because the viscosity of the resulting silicone rubber was insufficient for use (see Table 6). It did not keep its shape and was sticky.

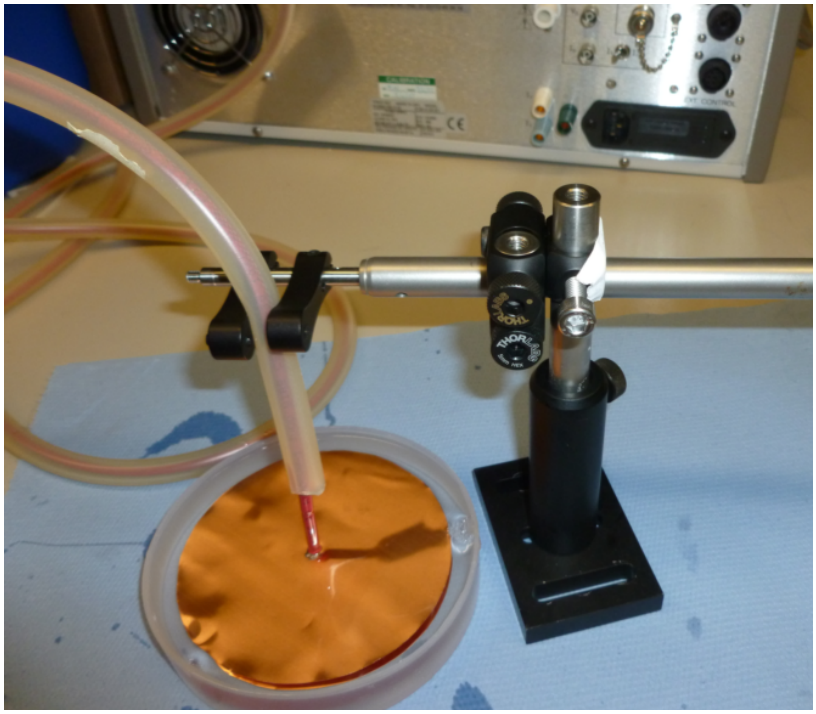

Figure 2.50: Unsuccessful attempt: silicone rubber is too viscous and sticky. Plates-electrodes made of thin copper almost float in the mixture.

Component B serves to change the viscosity. Thus, we made the mix stiffer by decreasing the amount of component B. The mixture was then prepared with a ratio of 1.5:1. The dependence of the curing time from temperature (thickness 1 cm) is as follows:

i) At 23°C the curing time is 8 hours;

ii) At 100°C it is 15 minutes;

iii) At 150°C it is 5 minutes.

In Figure 2.51, one can see the scheme of the test setup (a) and the experimental setup with a cylinder of silicone rubber in which the copper plate electrodes are located.

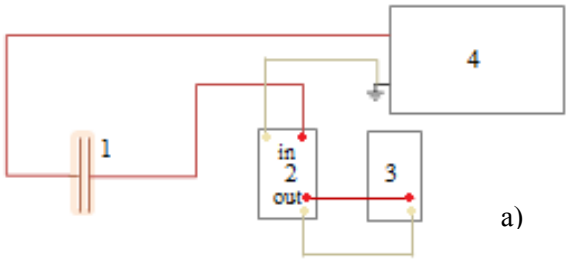

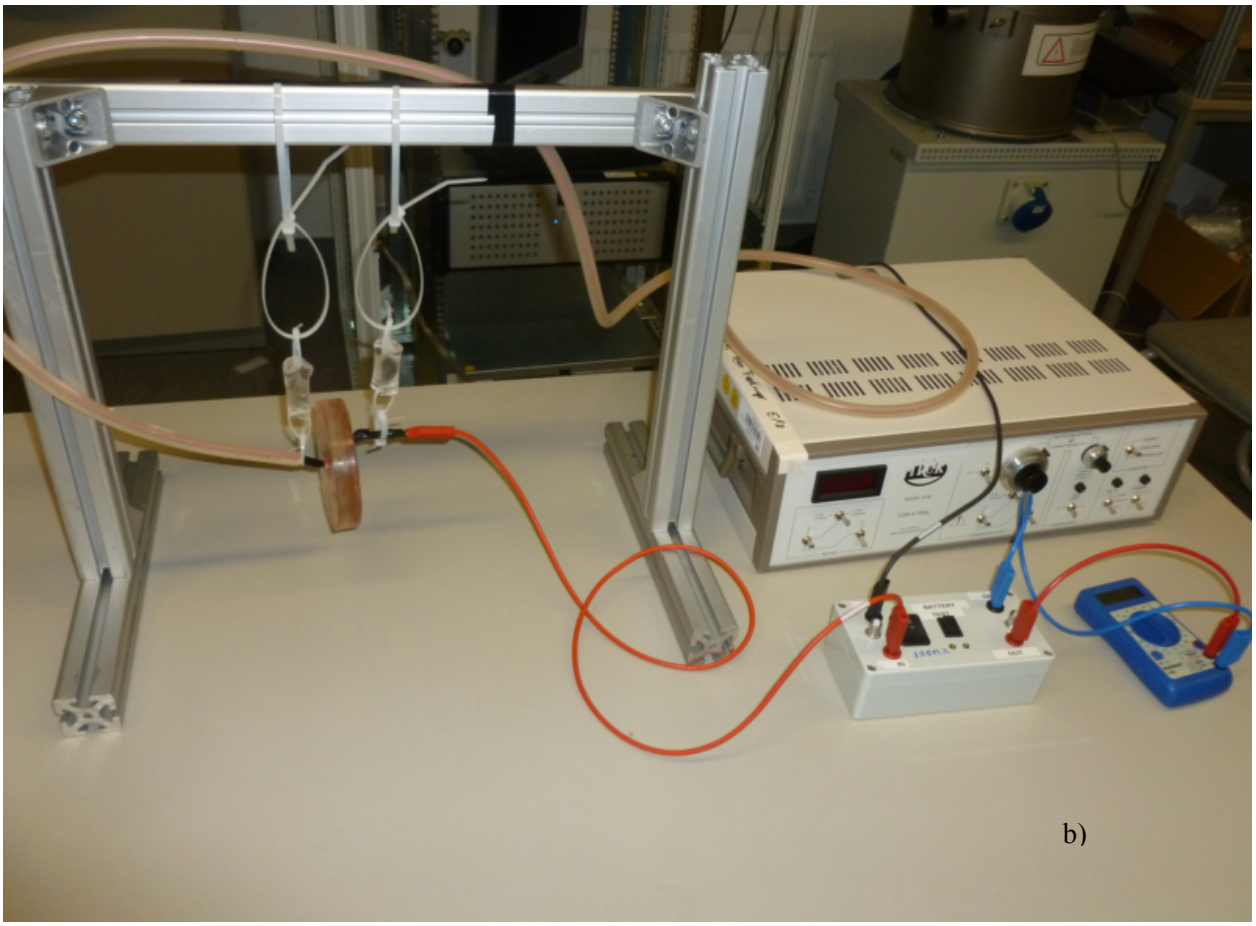

Figure 2.51: a) The scheme of the test setup: 1. Copper electrodes within the silicone rubber cylinder; 2. “Current-to-voltage” converter; 3. Multimeter; 4. The high-voltage power supply; b)The experimental setup. Leakage currents are converted in the current-to-voltage convertor, and measured with a voltmeter.

A high voltage power supply (0 -10 kV) was used as a voltage source. Picoampere currents are measured on the contact of the ground electrode. This silicone rubber should have a volume resistivity of 10^{16} Ohm·cm. From the calculations related to resistivity, the geometric sizes of the cylinder were selected such as: diameter of the electrodes, d = 10 cm, the distance between copper electrodes,

h = 1 cm. The sensitivity of the converter depends on the resistance through which the leakage currents pass. Suitable sensitivity corresponds to the resistance R = 1 GOhm. This is reflected in the range of measurements as follows: I = 0.1 pA, ... 1 nA → U = 0.1mV, ... 1V. The repeated results of the measurement (see Figure 2.52) are consistent with each other and changes of a voltage on the voltmeter were within 1 mV. The measured mean of the resistance is (1.07±0.77)· 10^{16} Ohm·cm. Thus, the resistance of silicone rubber on the level of 10^{16} Ohm·cm is confirmed.

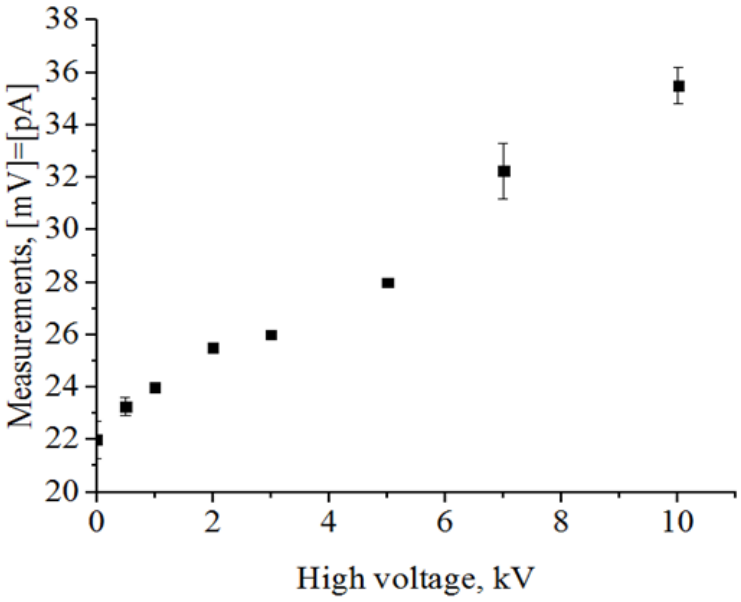

Figure 2.52: The measurement of leakage currents in the SilGel612. The measurements correspond to tens of picoampere (1 mV=1 pA), which in terms of the false nEDM effect is, $\bar{d}_{\text{false}} \approx 10^{-29}$e·cm.

More information about the use of silicone gel as an insulator is presented in Chapter 5.3.

4.3.2. Resistivity measurements of polyethylene films.

To measure the resistance of deuterated polyethylene films, tests with clean polyethylene films were performed. Firstly, we have tested a polyethylene film usually used for package of food and secondly a film of pure polyethylene. The measurements were repeated performed three times for each of the samples. In Figure 2.53, one can see an example of the measurements for pure polyethylene. The mean of the resistivity for pure polyethylene is $(2.84\pm2.03)\cdot10^{17}$ Ohm·cm. In the same manner the leakage currents were measured for a film of polyethylene for food. The mean of the resistivity in this case is about $4.5\cdot10^{16}$ Ohm·cm. This difference is probably attributable to the impurity on the film and with the other polymers, included to the composition. But we can say that the method works, and we can use it in future measurements.

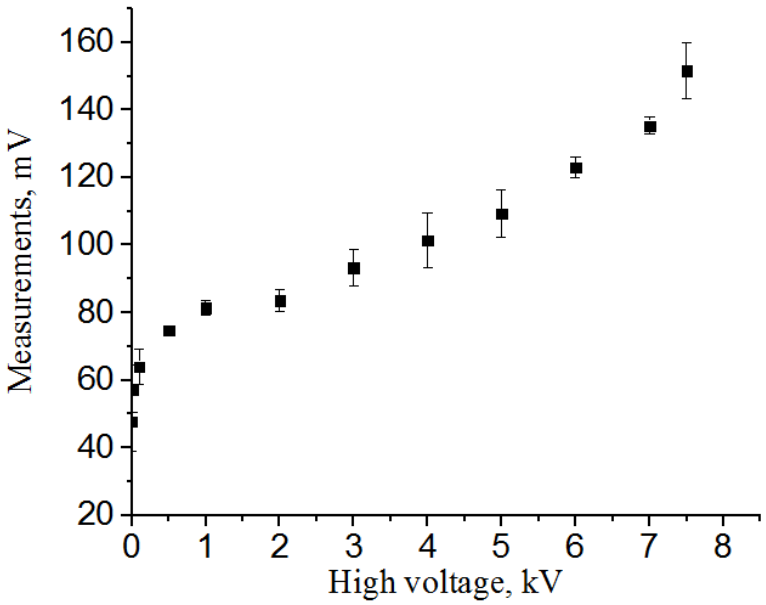

Figure 2.53: The measurement of the leakage currents on the pure polyethylene: measurements with the voltmeter vs the high voltages from the power supplies.

5. Design of the high-voltage electrode and simulations of the electric field distribution.

If the neutron EDM exists, one should see its direct interaction with the electric field (see. Eq. (1.1)). All methods of search for the EDM are based on detection of effects that are caused by this interaction, depending on the direction of the neutron spin with respect to the applied electric field. By setting the electric field in the magnetic field direction or against it, we will reduce or increase the angular velocity of precession of neutrons (see Eq. (1.4)).

As it is known, the ideal uniform field can only be obtained between flat electrodes of infinite size. At the edges of planar electrodes of finite size, there is the so-called edge effect, i.e., bending the electric field lines. To obtain the field, which is close to a uniform, often rounded electrodes are used. The potential distribution and the dependence of the field on the coordinates of the specific form of the electrodes can be determined by a conformal transformation, which allows translating the shape or area from one plane of complex variable to another, keeping equal the angles and the likeness in the infinitesimal elements. Using the transformations [74], one can find the shape of the electrodes, which in the best way provides a uniform field (capacitor of Rogowski [75, 76]). In Figure 2.54, the electrostatic field is shown, calculated from the condition that at all points the field strength is not higher than in the middle part of the capacitor.

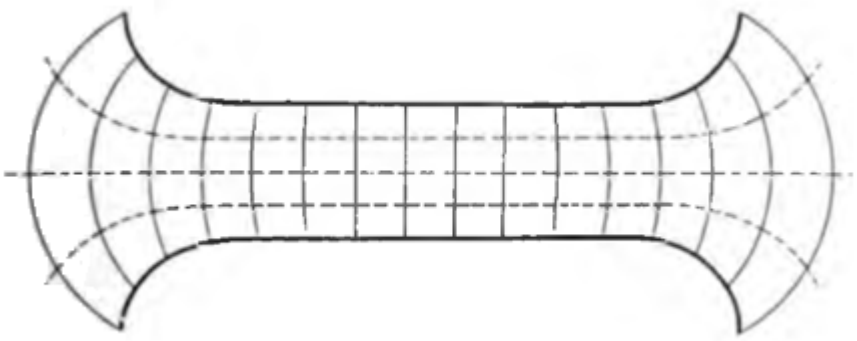

Figure 2.54: The electrostatic field lines (solid) and lines of equal potential (dashed) in a Rogowski capacitor.

It is obvious that the field strength is maximal in the middle of the capacitor. There the electric field will be very close to uniform and its strength equal to U/d, where d is the distance between the electrodes, if the linear dimensions of the plates are sufficiently large compared with the distance d. Therefore, the construction of components for the nEDM experiment is very similar than that for a uniform electric field. The only difference is that in the nEDM experiment, we have the neutron spin precession chamber as the heart of the experiment around which the electrodes have to be arranged.

5.1. Simulations of the electric field.

In Figure 2.55, one can see the electric field distribution inside the new experimental chamber (see Fig. 2.38). In both cases (the old and the one test setup), the shape of the electrodes is the same, and corresponds to the criterion of the maximum homogeneity of the electric field in the space between the electrodes.

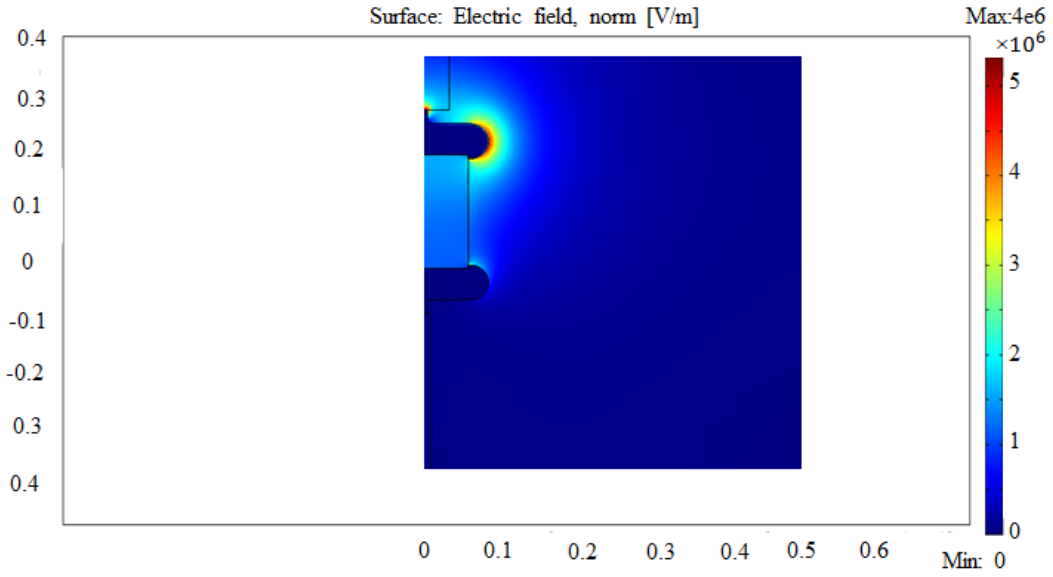

Figure 2.55: New test setup: COMSOL simulation of the electric field distribution inside the new experimental vacuum chamber.

One can easily see how the electric field varies at the bends of the electrodes. With this arrangement, we firstly find the optimal shape of the electrodes and secondly reduce the influence of irregularities related to the needs of the experiment, such as the high-voltage breakdowns between the quartz ring

and the electrodes, leakages due to a wrong size of the O-rings, degradation resistance of the inner coating of the insulator ring due to the sparks. As a result, the limit on the false effects arising from inhomogeneities of the electric field is in the order of a few 10^{-29} e·cm, see Table 7. In order to understand how the distribution of the electric field lines will affect the magnitude of the false effect, the electrodes were modeled with different sizes [61]. It is important to understand how the uniformity of the electric field changes inside the chamber as a function of the distance between the edge of the electrode and the insulator ring.

In Figures 2.56-2.57, one can see COMSOL simulations of the electric field distribution inside the neutron and vacuum chambers depending on the size of the high voltage electrode.

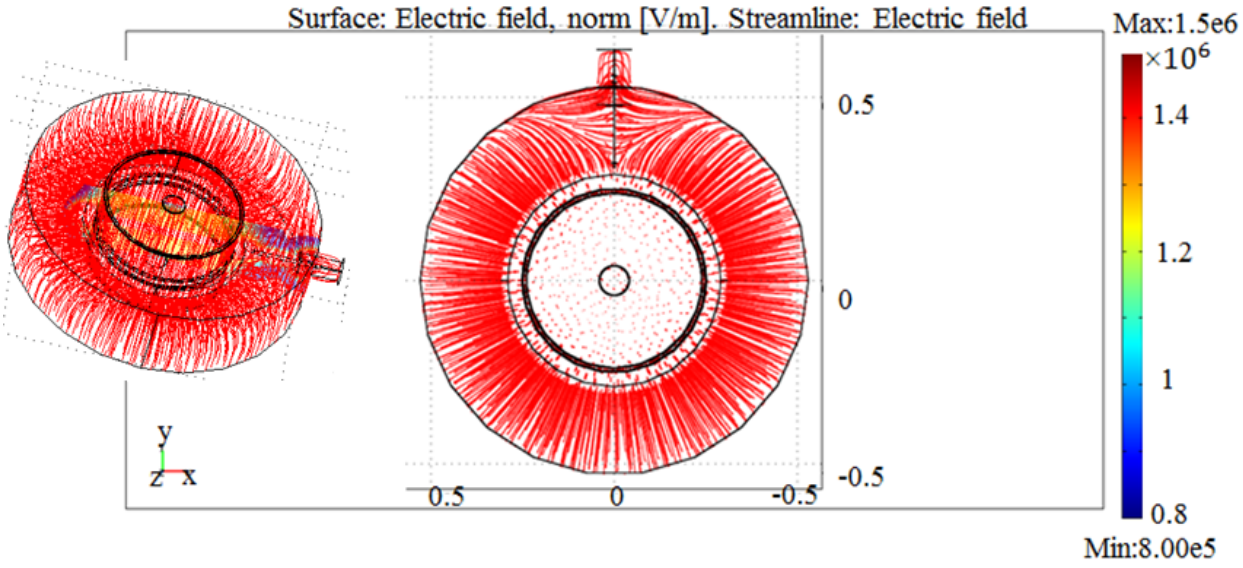

Figure 2.56: COMSOL simulation of the electric field distribution (streamlines and surface in the origin) inside the experimental and vacuum chambers is presented in the XY plane and in three-dimensional form for ease of visualization. The diameter, d, of the insulator ring is d=500 mm. This ring is shown by the double solid circle in black. The diameter, D, of the electrode is D=580 mm. Yellow coloration of the slice at the auxiliary picture on the left side indicates the presence of the electric field E = 150 kV / 12 cm = 12.5 kV/cm.

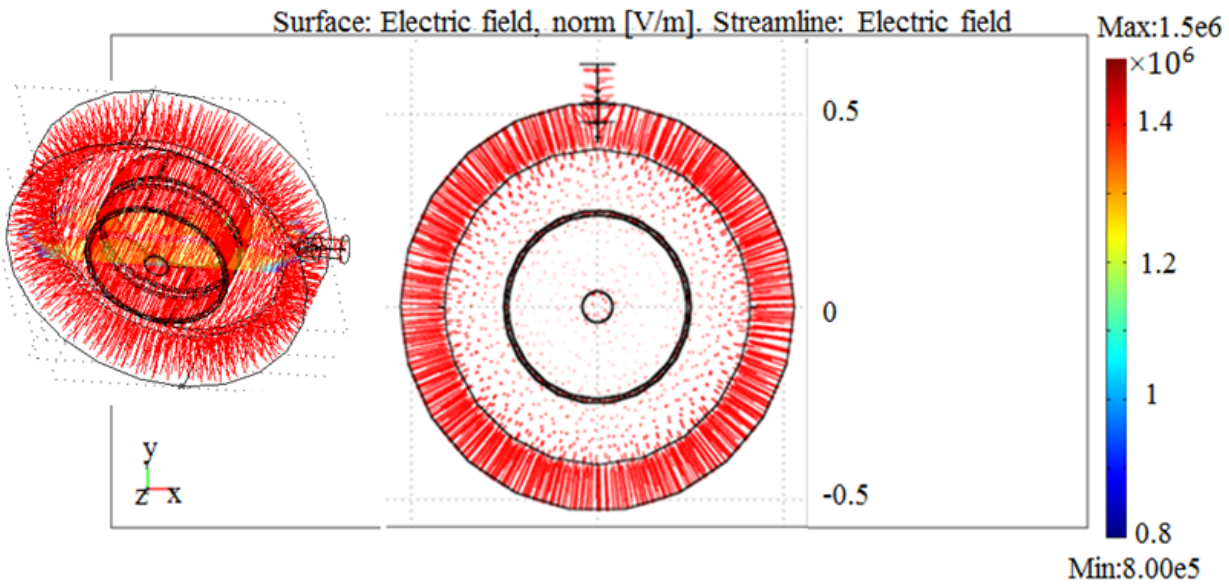

Figure 2.57: COMSOL simulation of the same type, but the diameter, D, of the electrode is D = 800 mm. The diameter, d, of the insulator ring is d=500 mm. This ring is shown by the double solid circle in black.

For convenience, we call the electrodes “small” and “large”. If one calculates the electric field distribution over angle and magnitude, one can see significant differences for the small and large electrode. Geometric dimensions for them are: the diameter of the vacuum chamber is 1060 mm; 2 neutron chambers with a diameter of 500 mm and a height of 120 mm are placed inside the vacuum chamber; the thickness of a circular high-voltage electrode is of 20 mm. Voltage is supplied by a feedthrough connected to the high voltage electrode. Top and bottom of the vacuum chamber are grounding electrodes. In the area bounded by an insulating ring, are visible red dots. This means that the electric field lines are visually straight, e.g., the electric field is homogeneous inside the neutron chambers.

The Figures 2.58 – 2.60 show the distribution of the angular deviation of the electric field from straight lines in the upper chamber at fixed z-heights. In COMSOL, there are no differences between the simulations of the electric field in the upper and in the lower chamber. Since the model and the parameters are the same, so just the electric field is inverted.

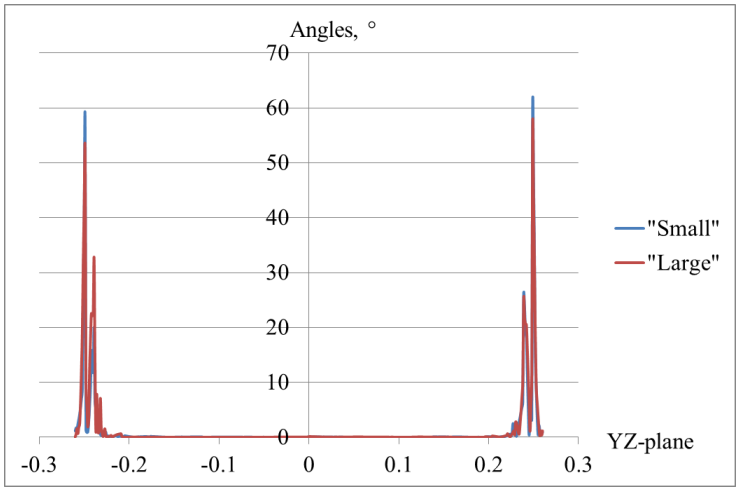

Figure 2.58: Distribution of the angular deviations of the electric field from straight lines in the chambers. Here, the distance from the HV electrode is 20 mm.

The peaks on both sides at the edges of the chamber are distortions of the electric field originating from the insulator ring. The deviations appear and grow with increasing distance from the HV electrode, i.e., chamber height.

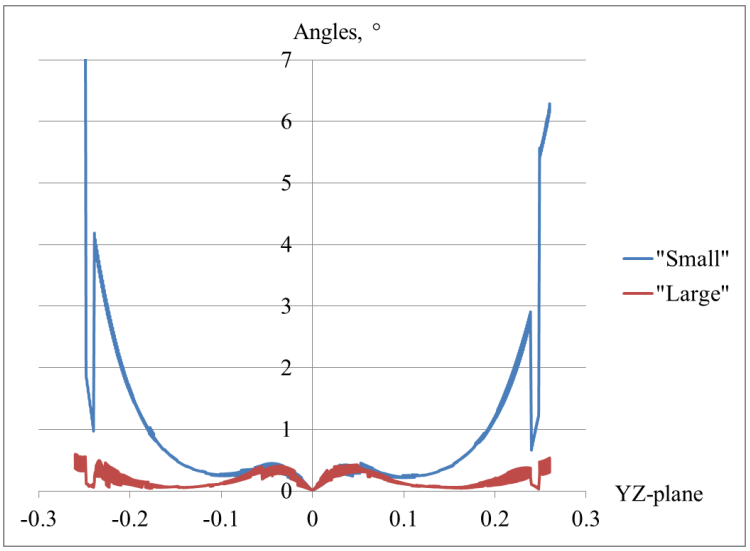

Figure 2.59: Distribution of the angular deviations of the electric field from the straight lines in the neutron chambers in the middle of the chamber (z = 75 mm).

There is an obvious deviation of the electric field lines from straightness due to the influence of the hole on top of the chamber for the neutron guide. Field lines are also curved everywhere inside due to

small distance to the edges of the electrode. But as you can see, distortions on the "small" electrode are stronger.

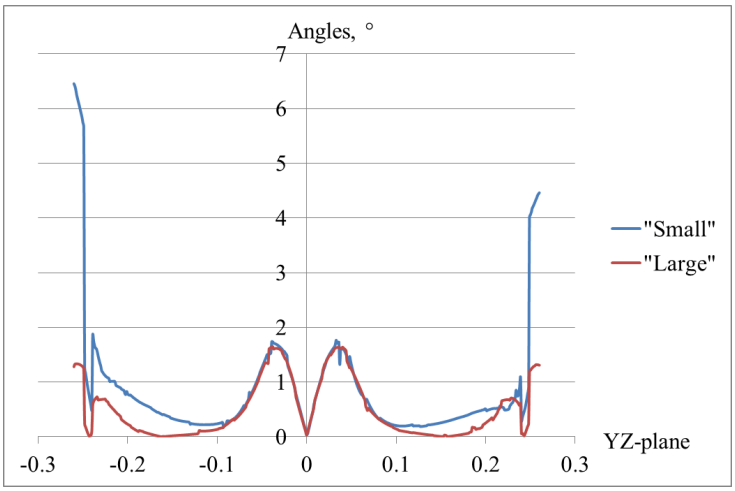

Figure 2.60: Distribution of the angular deviations of the electric field from the straight lines in the neutron chambers near the top, i.e. z = 110 mm.

At this level, deviations originating from the hole for the neutron guide are dominating. In Chapter 2.1, the impact of non-parallel electric and magnetic fields are described. An additional electric field ΔB (see Eq. (2.11)) distorts the main magnetic field B_0. The calculations of the deviation angles averaged over the volume give the next values for the additional magnetic field and for the false effect in case of the "small" and the "large" electrodes. The velocity of the center of mass is chosen $\bar{v}$=1mm/150 s.

HV electrode	$\bar{\theta}$, °	ΔB, T	$d_{n,\,f}$, e·cm
“Small”	0.76	2.46×10^{-18}	0.5×10^{-29}
“Large”	0.52	1.68×10^{-18}	0.34×10^{-29}

Table 7: The calculated values of the additional magnetic field and the false effects based on the average angle deviation .

Near the hole for the neutron guide the deviation angle almost reaches 2 °, which translates into a false effect $d_{n,\,f} \approx 10^{-29}$e·cm. One can say that a significant difference in the magnitude of false effects in the

case of "large" and "small" electrodes is not present. But for a such tiny nEDM value, the apparatus must be designed to avoid all contributions from such effects.

If we consider the deviations over the magnitude of the electric field, we see a similar effect of distortions from the neutron guide hole and for the insulator ring. This is demonstrated in Figure 2.61.

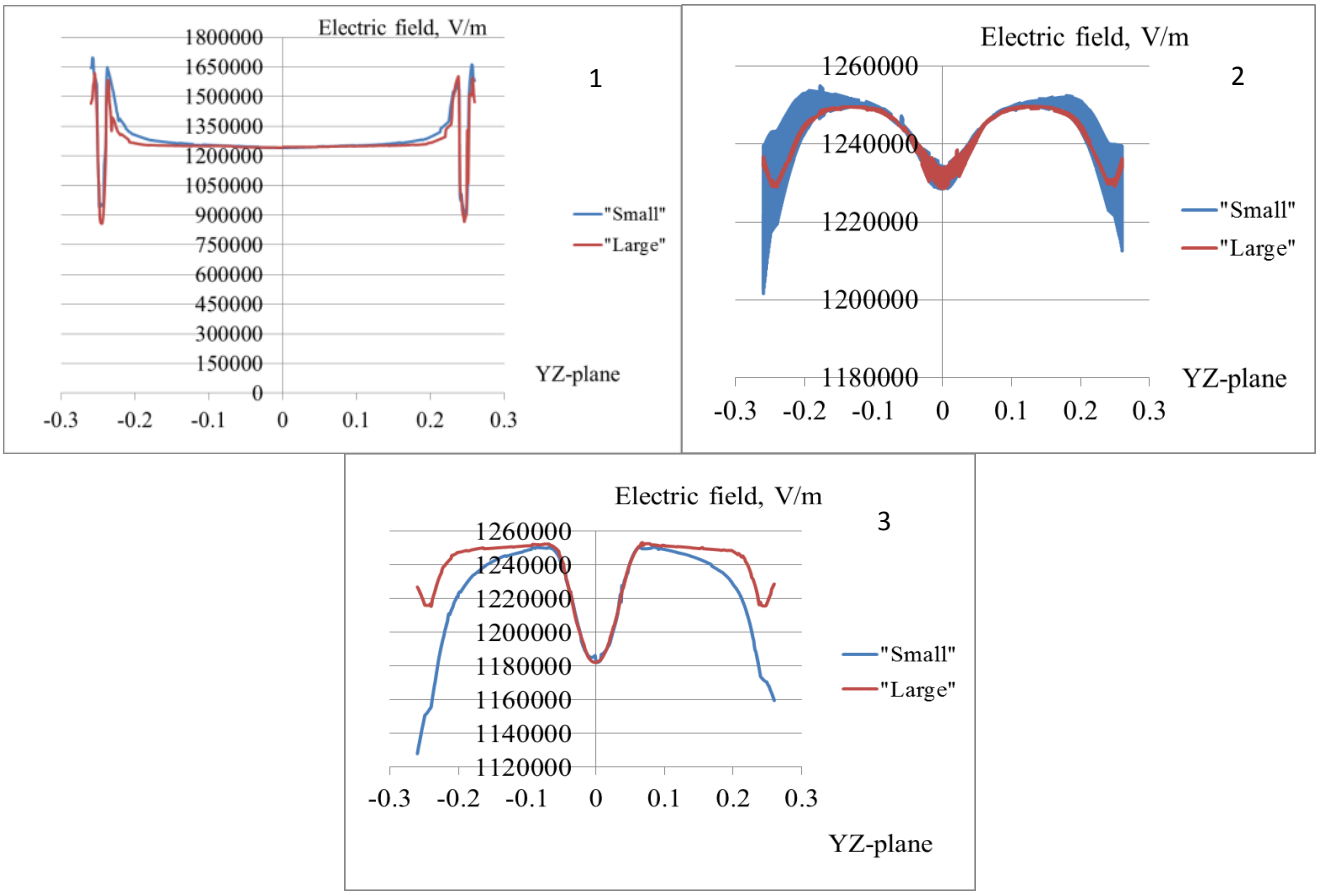

Figure 2.61: The distribution of the deviations over the magnitude of the electric field component Ez at different levels of z: 1) at the 20 mm; 2) at the 70-80 mm; 3) at the 110 mm.

One can see that in the region of the hole the difference in the magnitude of the electric field reaches 0.7 kV/cm, this is about 5.6%. In the middle of the chamber, this difference is about 2%.

As it was shown previously, the electric field is distorted by many irregularities on the chamber and the electrode surfaces. Further analysis is associated with a more thorough study of the local effects

associated with the size of the electrodes, its holes and grooves. All this distorts the field and can lead to voltage breakdowns.

The size of the hole for the neutron guide depends on the diameter of the tubes. In order to avoid small vacuum leaks in the chamber ($P = 10^{-6}$mbar in the neutrons chambers) it was decided to use O-rings in the contact point between the electrode and the insulator ring. This affords cutting of grooves on the electrode's plate. In Figure 2.62, a two-dimensional model of the experiment (axial symmetry) is shown.

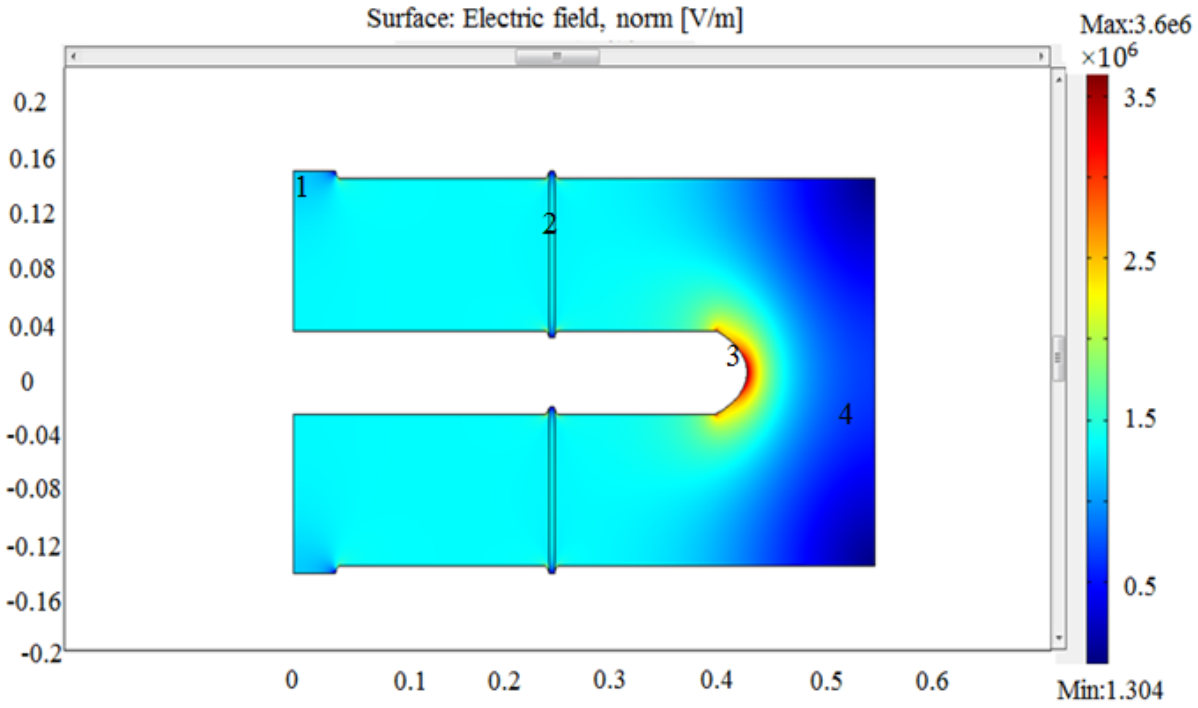

Figure 2.62: 2D model of the electric field distribution in the experiment: 1. The hole for the neutron guide; 2. The insulator ring; 3. The edge of the electrode; 4. The vacuum chamber. The diameter of the holes, d, is 80 mm, the thickness of the wall is 10 mm, the depths of the grooves were taken 5 mm and 8 mm.

The electric field inside the neutron chamber bounded by an insulating ring is uniform. Field distortion can be seen near the holes and in the grooves region.The distance between the edge of the electrode and the wall of the vacuum chamber was choosen larger than 100 mm in order to avoid voltage breakdowns. It can be smaller and still stable even at a pressure in the vacuum chamber of $P=10^{-4}$mbar in the presence of helium.

From local analysis, one can see the difference in the magnitude of the distortion. For example, we compare the effect of the groove depth at different heights of the chamber, see Figures 2.63-2.65.

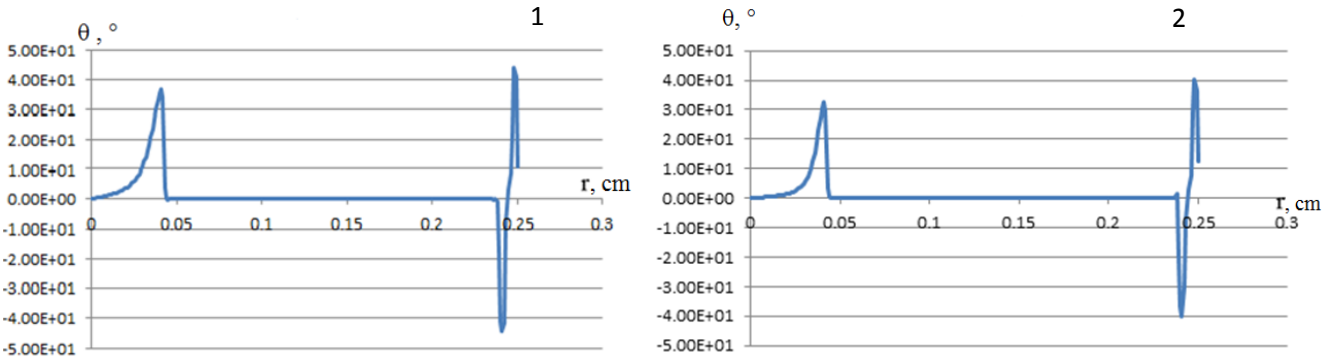

Figure 2.63: Calculated angular distribution of the electric field inside the neutron chamber at the top of the upper chamber: 1) The depth of the groove is 8 mm; 2) The depth of the groove is 5 mm.

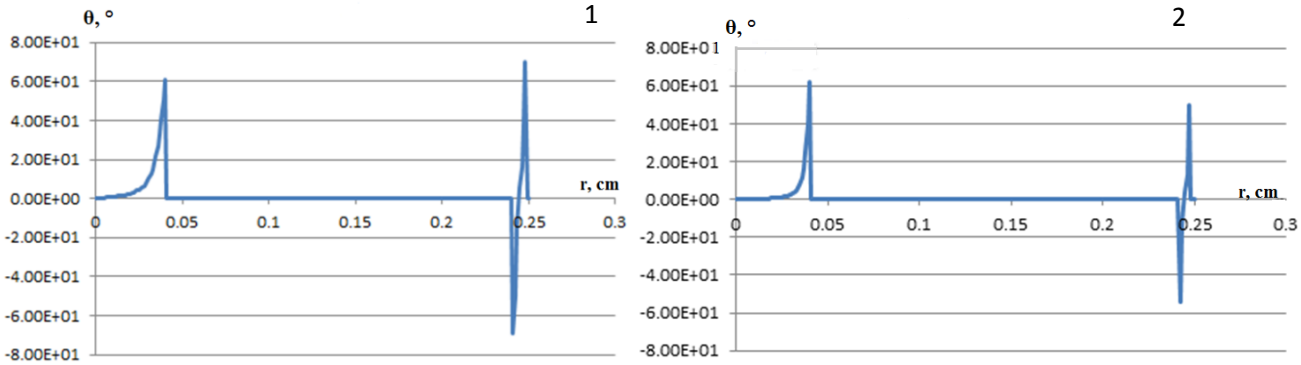

Figure 2.64: Calculated angular distribution of the electric field inside the neutron chamber at a height of 3 mm inside of the groove on the ground electrode: 1) At the 8 mm of the depth; 2) At the 5 mm of the depth.

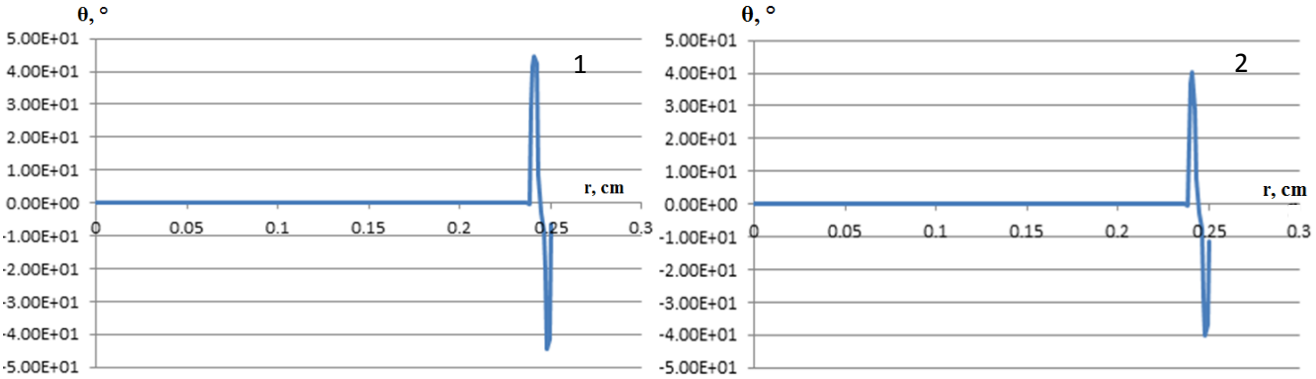

Figure 2.65: Calculated angular distribution of the electric field inside the neutron chamber at the bottom of the neutron chamber: 1) At the 8 mm of the depth; 2) At the 5 mm of the depth.

The differences of the angular distributions are significantly visible, even at small height differences of a few millimeters. The calculation of a corresponding false effect is four orders of magnitude smaller than our expected sensitivity.

A more detailed analysis of effects from surface irregularities distorting the electric field was performed. It was also connected with the choice of optimal sizes of the electrode, which is made of quartz glass coated with a conductive material (see Section 3.2.1.). In order to ensure the uniform distribution of the electric field across the electrode and for of convenient handling, the HV electrode was made from two ring-like parts with a gap between the plates. In Figure 2.66, one of the numerous models of the high voltage electrode is shown (see App. 4.1) which takes into account possible distortions of the field from

i) the electrode edges,
ii) the grooves for O-ring,
iii) the hole for the neutron guide,
iv) the large size of the electrode and the corresponding material,
v) the voltage breakdowns between the HV electrode edges and the vacuum chamber,
vi) the weight of the electrode, and
vii) the possibility of mounting the high voltage cable between the two parts of the electrode.

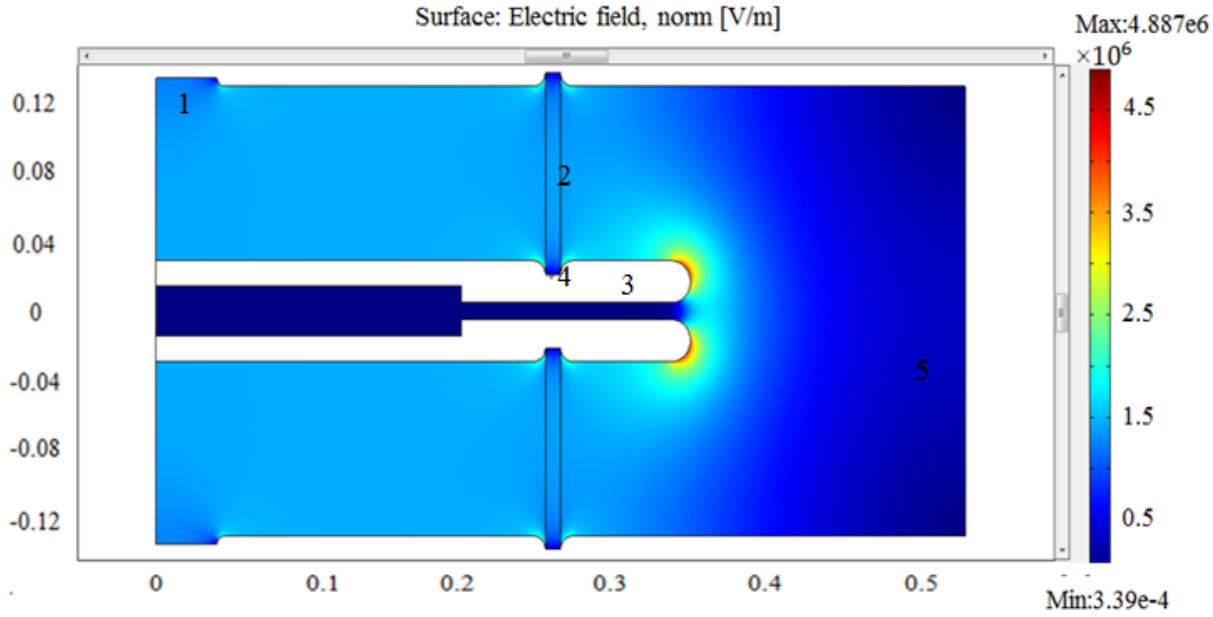

Figure 2.66: COMSOL simulation for one optimal HV electrode design: 1. The hole for the neutron guide; 2. The insulator ring; 3. One plate of the HV electrode; 4. The groove for the insulator ring; 5. The vacuum chamber. The width of the grooves is the same as the width of the wall, r=10 mm; the roundness of the corners on the groove is 10 mm; the sizes for O-ring are 2 mm×1.5 mm (will be explained later in App. 4.1).

The groove is shown only on the upper plate in order to compare the influence visually. The size of the electrode is chosen to less than 70 mm due to the difficulties in producing of larger ones. Cutout in the body of the electrode serves to reduce its weight and in order to provide easy handling between the two electrodes.

In addition, it is important to choose the right size for the groove of the O-ring, because there is

i) the risk of warping of the insulator ring which can lead to chipping of the edges,

ii) a breach of the vacuum isolation,

iii) electrical breakdowns and damaging of the high voltage electrode.

The results of the simulation for skewing of the wall are shown in App. 4.1.

In order to create a uniform electric field inside the neutron chambers, we need to make the HV electrode large, i.e. the larger the diameter of the electrode outside of the neutron chamber, the more

uniform the electric field inside the experiment. The distribution of the field outside the neutron chambers depends on remoteness of the wall of the vacuum chamber from the edge. The field distribution at the edges of the electrode depends on the degree of rounding, as it was shown in the analysis of the shape of the electrodes in Appendix 4.1. Additional analysis of the shape of the electrode edges is shown in Appendix 4.2.

5.2. Simulation of mechanical deformations.

The investigation of mechanical deformations of the HV and ground electrodes is important even if these deformations are in the order of micrometers. Because of the presence of the electric field, motional magnetic fields arise which affect the measurement of the nEDM. Therefore, the mechanical stiffness of the electrodes is critical. The choice of electrode material is for ceramic materials or glasses (fused quartz in our case), with a thickness of about 3 cm. In Figure 2.67, the mechanical deformation of the electrodes with a thickness of 25 mm is shown. It is less than 0.2 μm in the critical region.

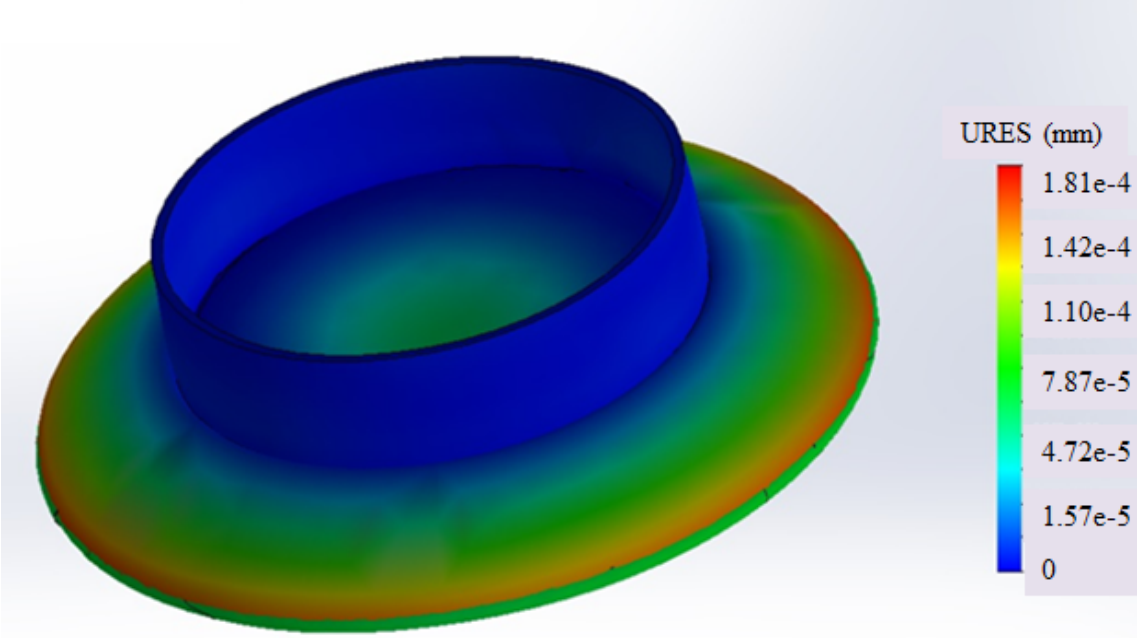

Figure 2.67: SolidWorks simulation of the mechanical deformations (the resultant displacement) for the electrodes made from fused quartz at a voltage of 200 kV and under their own weight. The thickness of the electrode is 25 mm, the weight is about 35 kg. An insulator ring made of fused quartz is shown in blue.

Here, we compare a quartz glass electrode with an aluminum one, a material often used as electrode material in previous experiments, see Fig. 2.68.

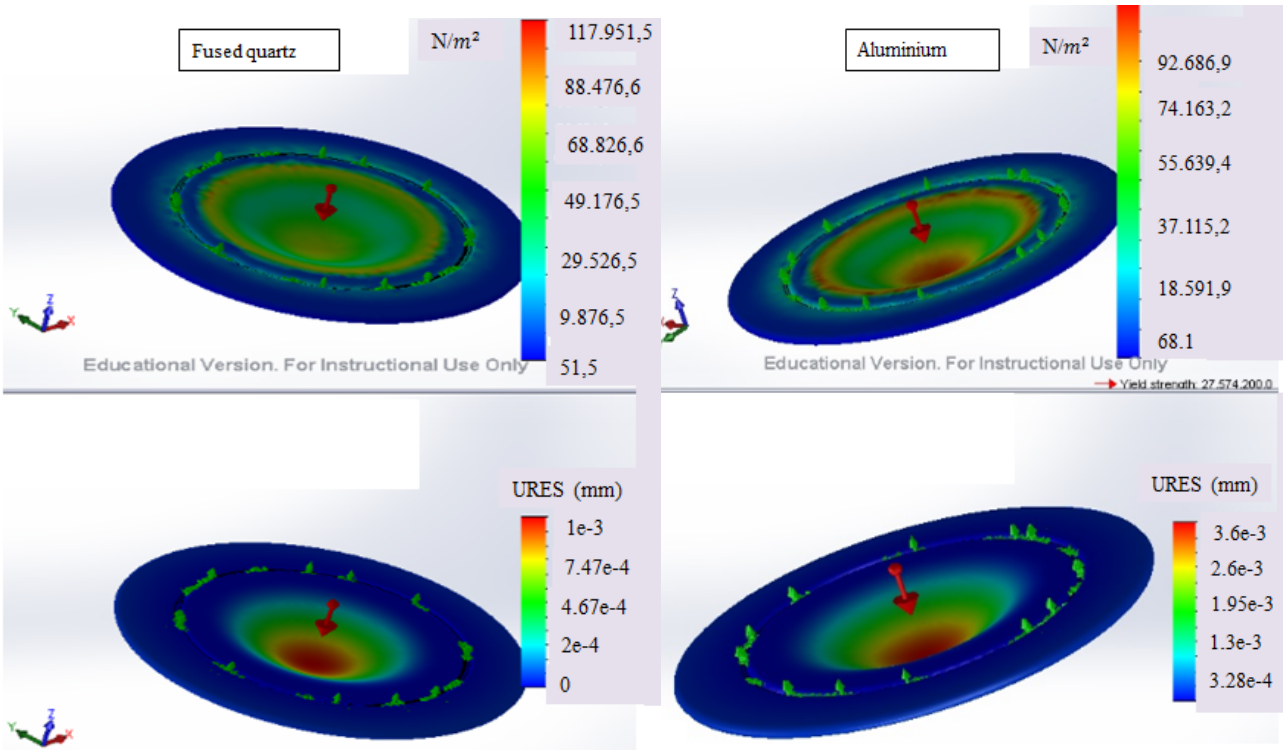

Figure 2.68: SolidWorks simulations: deformation for an electrode made of fused quartz and for an aluminum electrode. The upper plot show tensile strengths in N/m^2, the lower ones show the resultant displacement in millimeters (URES).

The tensile strength of the quartz glass is 50 MN/m^2 (MPa), whereas for aluminum it is 80 MN/m^2 (MPa). For this simulation, the model is chosen with a cutout on the bottom of the electrode in order to facilitate its handling. The diameter of the cut is 400 mm, its depth is 15 mm and the thickness of the electrode is 20 mm. Different models were analyzed. The displacement for all the models is approximately 3-3.5 times larger in case of the aluminum electrode compared to the quartz glass one. The mechanical tension on the aluminum electrode is also slightly larger. In Figure 2.69, an example of the analysis of the cutout is shown with the thickness of the quartz glass electrode and the aluminum one are 30 mm each.

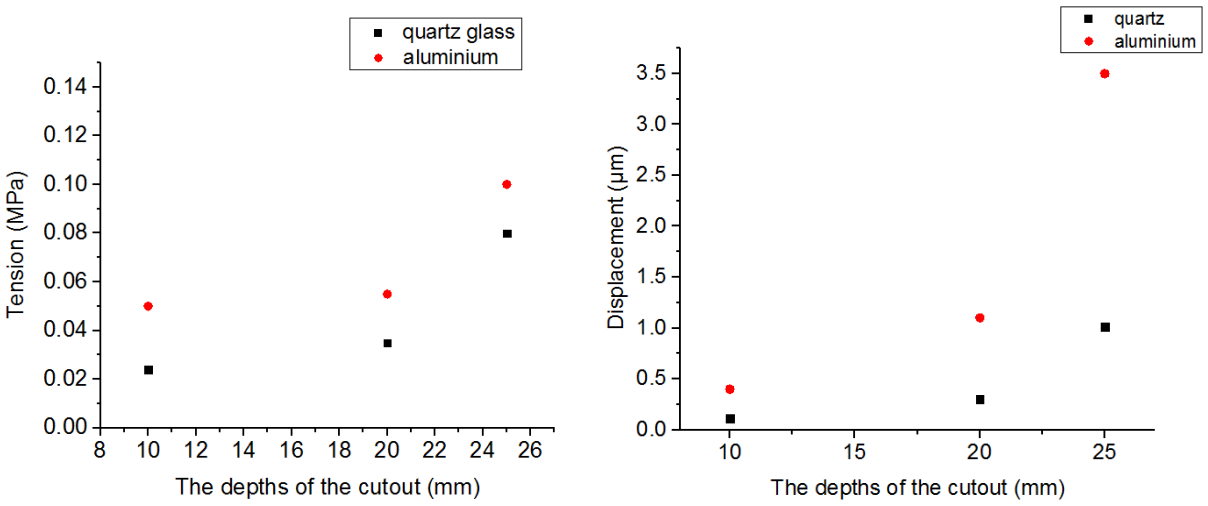

Figure 2.69: Comparison of mechanical deformation for models made of fused quartz and of aluminum alloy.

We can clearly see, the aluminum electrode is deformed stronger than the quartz glass one.

The production of large quartz electrode is a complex process and expensive. Primarily, we considered the electrodes with a diameter larger than 800 mm. It turned out, however, that such large diameters are not easily available and electrodes up to a diameter of 700 mm could be found only. In order to reduce the costs of the electrodes, we calculated the corresponding parameters for a composite electrode where one part is at larger radius than the neutron chamber and is made, e.g., of aluminum (see Figure 2.70).

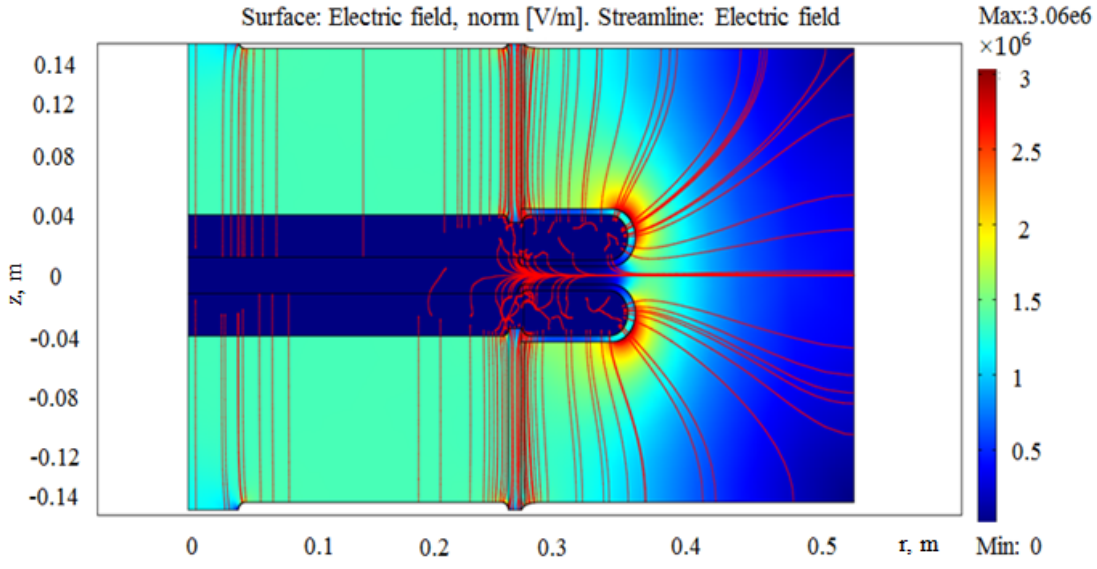

Figure 2.70: COMSOL simulation of the electric field distribution (streamlines and surface) in case of the composite electrode. The part located outside the neutron chamber (r=0.27 cm-0.35 cm) is made of other material.

We use silicone gel to cover the outside parts of electrodes for their insulation (see Chapters 4.3.1, 5.3).

Next, we investigate the deformation of the composite electrode. We assume that its external parts are made of aluminum (see Fig. 2.71).

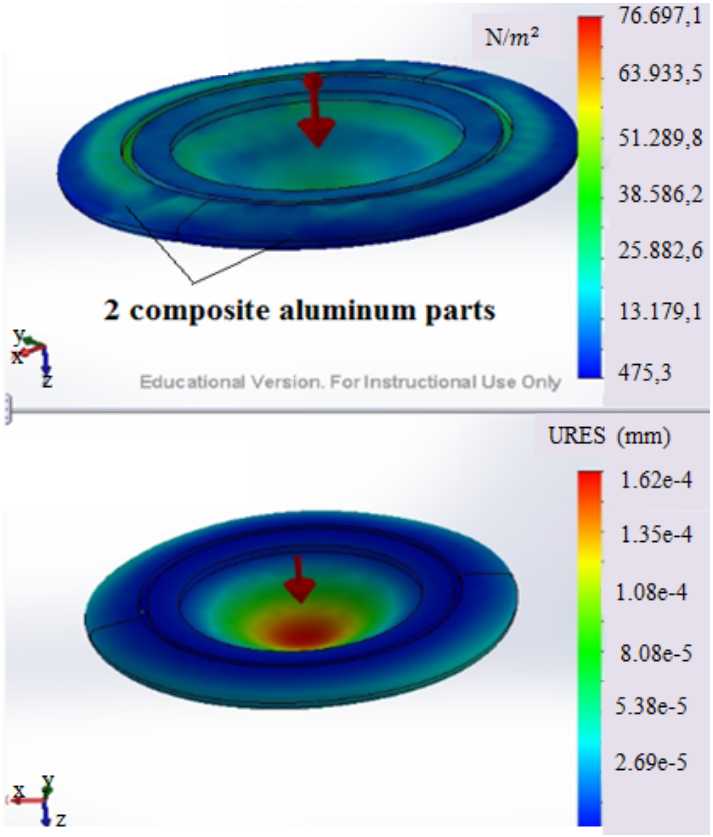

Figure 2.71: SolidWorks simulation of the mechanical deformation in the case of the composite electrode. URES is the resultant displacement.

We can see that the displacement is of the same order as it was before, i.e. about 0.2 μm and the mechanical tension of the electrode is practically the same. As the result, we are no longer limited by the difficulties and costs of the manufacturing now.

5.3. Silicone gel instead of vacuum.

In Chapter 4.3.1, we mentioned the possibility of using silicone gel as insulator instead of vacuum outside the neutron spin precession chamber. To do so, the volume resistivity of this material was measured (see Chapter 4.3.1). In the previous section, models of the high voltage electrode coated with silicone gel and the respective electric field distribution are shown. With an insulating material instead of vacuum, one can avoid several difficulties in the HV electrode design and it becomes more practical for handling etc. In addition, there are many useful benefits from the direct access to the experimental chamber, such us,

i) we can work without vacuum in the large vacuum chamber. As the result, the problem with the distance between the edges of the high-voltage electrodes and the walls of the vacuum chamber and the resulting voltage breakdowns in the vacuum chamber is cancelled.
ii) it facilitates to install the monitoring equipment in the immediate vicinity of the experiment.
iii) With this solution, the electrode may consist of two parts. The outer part may be even made from a different, i.e., more convenient and cheaper material. This will solve the problem of manufacturing a large electrode. In turn, the outer part can be designed such that we can change its shape in order to adapt it optimally to the experimental.

It should be pointed out that it is possible to change the design of the ground electrode in order to ensure homogeneity of the electric field in the neutron chamber for both cases, i.e., with and without. However, in the case with vacuum, the grounding electrode have to be longer or a different shape for better handling and installation.

In order to determine the most optimal shape of the electrodes, now without vacuum that is with silicone gel, several models were simulated, see App. 5. By varying the electrode shapes and the handling system, we obtain the following conclusions:

i) the main part of the HV electrode will be short. It allows us to optimize the total shape by additional outer shapes.
ii) the grounding may be performed in two different ways:
    1) with different shapes as described above, see Fig. A.5.4(4), App. 5, or
    2) with an additional ground electrode installed around the outer part of the HV electrode.

This is, firstly, to avoid a high electric field in the region of constriction of the HV electrode and ground electrode, and, secondly, to divert eventual leakage currents from the HV electrode concentrically through the insulating silicone gel layer.

5.4. The final design of the electrode.

In order to develop the design of an electrode, we have to create a model and simulate its performance. This was done with SolidWorks simulation, a 3D CAD package. Before this, one has to determine the placement of all electrodes (two high voltage electrodes and two ground electrodes) in the experimental chamber relative to each other and their mutual fixing. We also decided how to connect an electrical power supply to the HV electrodes.

In the design, one has to take care about some limitations of our experimental chambers such as:

i) Our vacuum chamber has some holes for a laser beam for optical pumped magnetometers and for neutron guides, see Fig. 1.8-1.10. Structural elements of the experimental chambers must be adapted for them.
ii) Structural elements of the experimental chambers must be well fixed to prevent from displacements or deformations and to ensure their horizontal and vertical alignment.
iii) All structural parts should be non-magnetic.
iv) Parts must be stacked so as to avoid a change in the HV electrode potential and exclude the possibility of high voltage breakdown.

Based on these requirements, structural parts of the experimental chambers have been modeled. In Figure 2.72, a double chamber experimental setup is shown consisting of the electrodes, insulating rings and fixators. In Figures 2.73-2.75, parts of the high-voltage construction are shown.

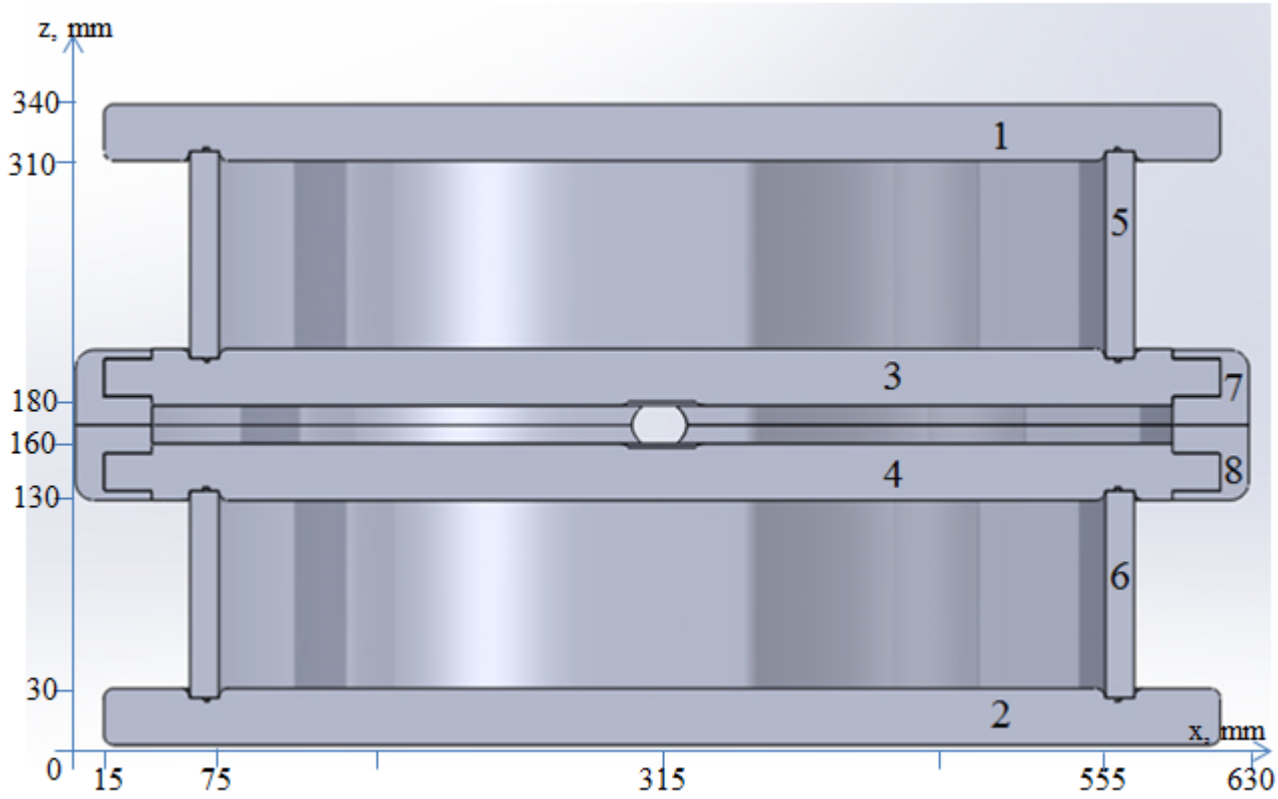

Figure 2.72: UCN double chamber (SolidWorks simulation): 1, 2. Ground electrodes (quartz glass coated with NiMo); 3, 4. High-voltage electrodes (quartz glass); 5, 6. Insulator rings (quartz glass); 7, 8. Clamps for fixation (aluminum).

Figure 2.73: High-voltage electrode (SolidWorks simulation): 1. Groove for insulator ring. A second groove inside this groove is for an O-ring; 2. Flat part of the electrode, designed to provide a uniform electric field within the neutron chamber; 3. Circular recess for the high-voltage connector; 4. The outer part of the high-voltage electrode with slots for clamps for fixation. The thickness of the HV electrode is 30 mm, the diameter is 600 mm. The drawing of the high-voltage electrode is shown in Fig. A.6.1, see App. 6.

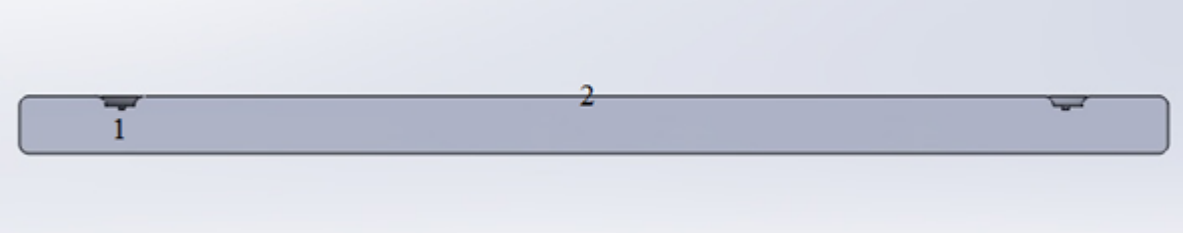

Figure 2.74: Ground electrode (SolidWorks simulation): 1. Groove for insulator ring. A second groove inside this groove is for an O-ring; 2. Flat part of the electrode, designed to provide a uniform electric field within the neutron chamber. The thickness of the ground electrode is 30 mm, the diameter is 600 mm.

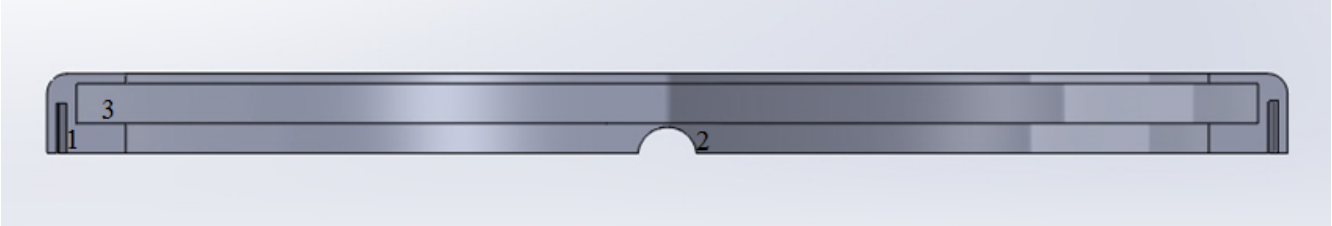

Figure 2.75: Part of the clamps for fixation (SolidWorks simulation): 1. Groove for fastening the two clamps together; 2. Hole for the high-voltage rod; 3. Groove for fixing the high-voltage electrode on a circumference.

All the high-voltage elements can be put together safely. These clamps for fixation can be replaced by others which might have different outer shape in order to change grounding. In Figure 2.76, the electric field distribution in the double chamber setup is shown.

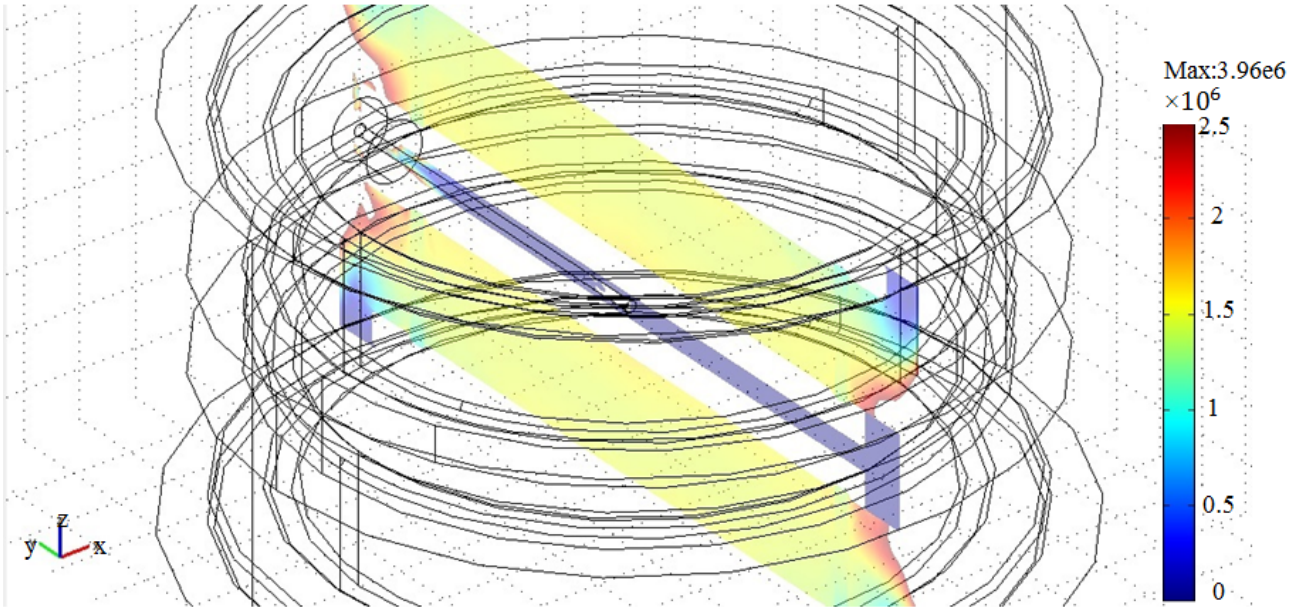

Figure 2.76: COMSOL simulation of the electric field distribution in the UCN double chamber. The electric field inside the neutron chambers is uniform.

In order to check up a design of this construction on high-voltage breakdown, a model has been prepared (see Fig. 2.77).

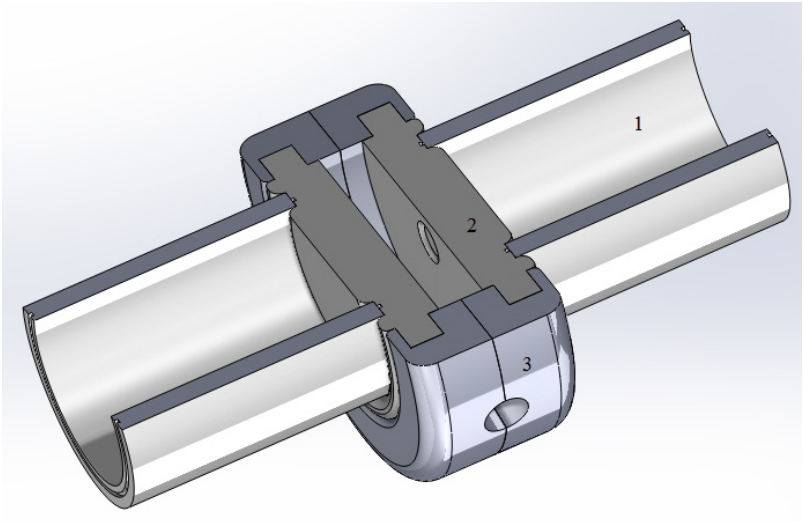

Figure 2.77: Model of the UCN double chamber without ground electrodes (SolidWorks simulation): 1. Insulator ring (quartz glass); 2. High-voltage electrode (quartz glass coated with NiMo); 3. Clamps for fixation (aluminum).

This model will be inserted into a new vacuum chamber, see Fig. 2.78.

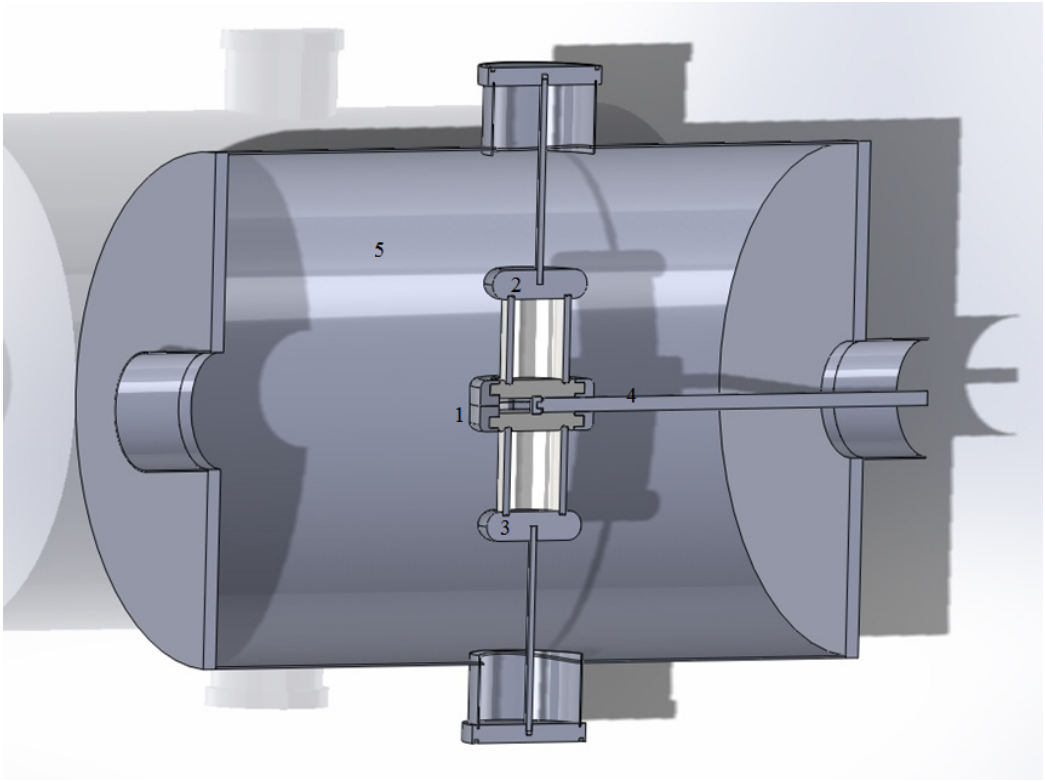

Figure 2.78: Test setup (SolidWorks simulation): 1. Model of the double UCN chamber; 2-3. Ground electrodes; 4. The schematic view of a high-voltage inlet with a connector; 5. Vacuum chamber.

This test setup is shown in Figure 2.79. A photo of the installation was taken during the “training” test for the high-voltage equipment. A chamber (3) on the top of the vacuum chamber (2) has been placed for installing the electronic equipment. It is filled with SF-6 gas in order to prevent high-voltage breakdowns. A high-voltage cable passes into the chamber with SF-6 and is connected to the high-voltage inlet.

Figure 2.79: Test setup during the “training” of the high-voltage equipment: 1. High-voltage source (U=0-150 kV); 2. Vacuum chamber; 3. The chamber for the electronic equipment.

The measurement of the breakdown voltage in the different gases in this test setup has been performed (see Chapter 3.3). Unfortunately, all planned measurements were not performed due to the suspension of work on the accelerator where this setup is placed.

III. UCN depolarization and loss probabilities

1. General considerations

As mentioned in Part I above, a non-zero neutron electric dipole moment, nEDM, does not conserve both parity, P, and time reversal, T, symmetries [77,78] and, because of the CPT theorem also not the combined charge and parity symmetry, CP. In order to explain the observed baryon asymmetry in the Universe, additional CP violation beyond that established in the Standard Model of Particle Physics is necessary [79]. The nEDM is amongst the most sensitive probes for such additional sources of CP non-conservation. Our collaboration is involved in setting up new nEDM experiments [80, 81]; the apparatus are upgrades of the Rutherford-Sussex-ILL experiment.

The sensitivity of a nEDM experiment, σ_{d_n}, is given by Eq. (1.13). There, α is the visibility of the central resonance fringe [36, 53]

$$\alpha = \frac{N_{\uparrow max} - N_{\uparrow min}}{N_{\uparrow max} + N_{\uparrow min}} \tag{3.1}$$

with similar values for $N_{\downarrow}$ where the arrow, e.g. ↓, indicates the polarization orientation of the neutrons before the spin precession. The parameter α is polarization dependent: the higher the neutron polarization, the bigger the visibility parameter and, hence, the better the experimental sensitivity, σ_{d_n}.

Besides many tools for the suppression of systematic uncertainties in the new experiment in preparation [80], there are mainly three parameters to reduce the overall sensitivity of the measurement, cf. Eq. (1.13):

i) the total number of neutrons which is planned to be increased by more than an order of magnitude by the construction of new intense sources of ultracold neutrons (UCN) [82, 83] based on a very cold moderator/converter using solid deuterium (sD_2) [84–97] at a temperature around 5 K,

ii) an increase of the electric field, E, and

iii) the neutron polarization which is increased to ~100 % by means of a superconductive solenoid with a magnetic field of 5 T,

In order to minimize the influence of the high (5 T) magnetic field of the neutron polarizer on the spin precession procedure in the nEDM experiment, this neutron polarizer must be placed at some distance (~2→5 m) from the neutron spin precession chamber. The neutron guides from the neutron polarizer to the neutron spin precession chamber must hence be selected for minimal neutron

depolarization and losses. That is, the neutron guides have to fulfill the following criteria for optimal polarized neutron transport:

1. Minimal surface roughness to avoid non-specular reflections.

This was achieved by using glass tubes with a roughness at the inner surface of less than 2 nm.

2. High material optical potential.

It was demonstrated recently that the velocity distribution of neutrons from a solid deuterium converter is proportional to the square of the neutron velocity, v_n^2, or proportional to the neutron kinetic energy, E_n [94,96]. The total number of neutrons transportable in UCN guides, e.g., the integral over the velocity distribution, is thus proportional to v_n^3 or $E_n^{3/2}$ with the maximum of $E_n = V_f$, V_f the material optical potential of the UCN guide. The glass tubes were internally coated with 500 nm of the materials under investigation, see Table 8 [98].

Coating (Tube material)	V_0, neV
Ni/Mo 82/18 (Glass)	212
Ni/Mo 85/15 (Glass, PET, Stainless steel)	217
Ni/Mo 88/12 (Glass)	222
Ni 100 (Glass)	245
Ni/V 93/7 (Glass)	224
Cu (Glass)	170
dPS	161

Table 8: Measured values of the optical potential, V_0, for various coatings on different tube materials (tube length is 1m, the inner diameter is 70 mm).

3. Minimal loss probability per wall loss collision.
4. Minimal depolarization probability per wall collision.

Items1 has been investigated in Ref. [98]; items 3 and 4 are the objectives of the present experiment and paper.

2. UCN losses and depolarization from surfaces.

In the new nEDM experiment [80], the neutron spin precession chamber must be coated with a high-resistivity and non-magnetic material of high material optical potential. In principal, BeO fulfills best these properties. The drawbacks, however, are (i) its high toxicity, (ii) the lack of available coating facilities and (iii) its depolarization of the mercury co-magnetometer vapor. Other candidate coatings are deuterated polystyrene (dPS) and deuterated polyethylene (dPE). Their material optical potentials, V_f, and other material parameters have been determined recently [99], V_f(dPS) = (161±10) neV, V_f(dPE) = (214±10) neV. The UCN loss probability per wall bounce at room temperature for dPS is $\eta = (3 \pm 1) \cdot 10^{-4}$ [99], i.e., very similar to those of commonly used UCN storage materials, e.g., diamond-like carbon or beryllium [100][1]. In the new experiment [80] one has chosen dPS as a first option; coating the neutron spin precession chamber with dPE would further enhance the storable UCN density, the coating techniques for dPE, however, are still under development.

For the transport of UCN in neutron guides, the highest material optical potential was found for ^{58}Ni (335 neV). Since nickel is ferromagnetic, polarized neutrons will be rapidly depolarized. The way out is nickel molybdenum alloys [101-103] with a material optical potential of about 315 neV for, e.g., ^{58}Ni/Mo 85/15 with weight percentages of 85 % Ni and 15 % Mo. The choice of the UCN guide wall material should, however, be adapted to the maximal available neutron energy from the respective UCN source. At PSI, the new UCN source is based on the spallation principle [83] for neutron production with a 600 MeV proton beam on a lead spallation target [104]. Neutrons are thermalized in pure heavy water and further cooled and down-scattered in solid deuterium at 5 K. Energy and velocity spectra of UCN leaving a solid deuterium moderator have been measured recently [94, 96]. Because of the material optical potential of solid deuterium, $V_f \sim 105$ neV, neutrons leaving it are accelerated and the velocity spectrum of UCN from a solid deuterium moderator starts at about 4.75 m/s. Neutrons leaving the solid deuterium moderator vertically are slowed down by gravity in a 1.2 m vertical neutron guide. This shifts the UCN spectrum to lower energies and more UCN are therefore storable in the storage volume above the vertical neutron guide. The storage volume is 2.4 m high with a volume of 1.6 m^3 and must be coated with a material of high optical potential and low loss probability per wall bounce. Nickel alloys, as used for neutron guides, are not very well suited for long UCN storage times because of their relatively high loss probability, see below. Practicable materials for UCN storage are beryllium and diamond-like carbon with optical potentials around 250 neV [100, 105–110] and low

[1] The UCN loss probability for dPE could not be measured so far.

[2] Storage of very slow neutrons in magnetic fields was first discussed by Vladimirski [116]. First experiments were

loss probabilities per wall bounce. As mentioned above, beryllium coatings have their drawbacks. Therefore, at PSI, the UCN storage volume has been coated with diamond-like carbon with a material optical potential of about 230 neV. As a consequence, UCN guides at PSI do not need the maximal material optical potential coating with ^{58}Ni and may be coated with alloys of natural nickel and molybdenum thereby avoiding the extremely expensive costs of the pure isotope ^{58}Ni.

The correlation between the material optical potential and UCN losses is beautifully described in Refs. [111, 112]. Here, we present a short outline in order to make the paper self-contained, see also Ref. [100, 106].

The material optical potential, sometimes also termed Fermi potential, is complex, $V_f = V - iW$, where V and W depend on the nuclear properties of the surface atoms:

$$V = \frac{2\pi\hbar^2}{m} \cdot N \cdot b, \quad W = \frac{\hbar}{2} \cdot N \cdot \sigma_{loss} \cdot v, \tag{3.2}$$

Here, m denotes the neutron mass, N the scattering center density, b the bound coherent nuclear scattering length, σ_{loss} the loss cross section per atom of the surface material and v the neutron velocity. For neutrons reflecting at a material surface the real part of the potential, V, sets the critical velocity, $v_c = \sqrt{2V/m}$, for total reflection and the imaginary part, W, determines the reflection loss [112]. The loss rate, $1/\tau_\mu$, originating from wall interactions for UCN of one specific kinetic energy, E, i.e., without the influence of external fields, is given by

$$\frac{1}{\tau_\mu} = \mu(\theta, E) \cdot \nu(E), \tag{3.3}$$

where $\mu(\theta, E_\perp)$ is the wall-loss probability per bounce, θ is the angle of incident and $\nu(E)$ is the frequency of wall collisions, which depends on the geometrical buckling of the storage volume.

For $W \ll V$, which is valid for almost all materials useful for UCN guides and storage volumes, the reflection coefficient, R, can be calculated from

$$|R|^2 = 1 - \mu(\theta, E) = 1 - 2\eta\left(\frac{E_\perp}{V - E_\perp}\right)^{1/2}, \tag{3.4}$$

where

$$\eta = \frac{W}{V} = \frac{(\sigma_{loss} \cdot m \cdot v)}{(4\pi\hbar \cdot b)}\,. \tag{3.5}$$

Here, $E_\perp$ is the kinetic energy from the radial velocity component in the direction perpendicular to the surface, $E_\perp = E \cdot cos^2\theta$. Since σ is proportional to $\frac{1}{v}$, the parameter η is independent of neutron energy. From Eq. (3.4) we obtain

$$\eta = \frac{\mu(E_\perp)}{2} \cdot \left(\frac{V - E_\perp}{E_\perp}\right)^{1/2}. \qquad (3.6)$$

The loss coefficients η of commonly used materials for UCN storage and UCN guides calculated from Eq. (3.2) are plotted in Fig. 3.1, see also Refs. [111, 112].

Depolarization of UCN has been described in Refs. [100, 106, 113, 114]. This effect proves that UCN reflection on surfaces is not completely coherent. Its explanation is so far hypothetical and might originate from, e.g., impurities on the surfaces.

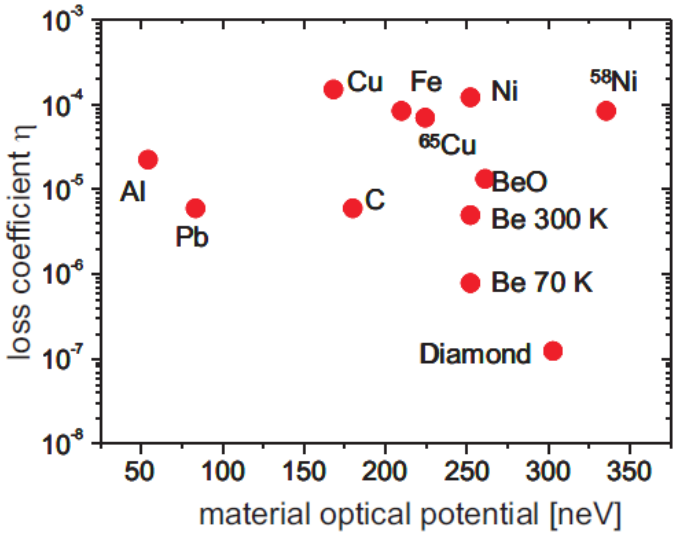

Figure 3.1: Loss coefficients η versus the material optical potential V (see Eq. (3.2)) of commonly used materials for UCN storage (high potential plus low losses) and UCN guides. The material optical potential of diamond-like carbon (DLC) is between that of diamond and that of carbon depending on the graphite/diamond ratio of the crystal structure. The data have been calculated from Eq. (3.2), see also Refs. [97, 98].

3. Experimental setup

The experimental apparatus shown in Fig. 3.2 is described in detail in Ref. [115]. First experimental results on diamond-like carbon and beryllium have been published earlier [100, 106]. The experimental apparatus consists of cylindrical sample tubes of 1.5 m length, which are placed in a bore through the center of the iron yokes and poles of an H-type split coil magnet. The cylindrical sample tubes have an outer diameter of 80 mm and an inner diameter of 70 mm coated with the materials under investigation.

The upper 90 cm of the tube serve as a storage volume, which can be closed by a rapidly (~2 s) switchable magnetic field of 1.5 T in the air gap (17, Fig. 3.2) of the H-type split-coil magnet (7,8, Fig. 3.2). This midplane of the magnet air gap defines our coordinate system with the height z in the cylindrical tube and the radius r, with r = 0 in the center of the bore.

In the magnetic field, the spins of the neutrons are orientated adiabatically parallel or antiparallel to the magnetic field direction and one spin component of the originally unpolarized UCN can be stored above the air gap[2]. The upper end of the storage volume is confined by gravity: the maximum magnetic field of 1.52 T corresponds to a storable UCN energy of $E_B = |1.91\mu_N B| = 90$ neV with μ_N the nuclear magneton. This energy, in turn, corresponds to a maximum reachable height of the UCN versus gravity of 92 cm with the gravitational potential per height of 102 neV/m. Higher energy UCN are absorbed by a gadolinium coated metal plate at the upper end of the storage volume (15, Fig. 3.2), or can penetrate the magnetic field barrier and leave the storage volume at its lower end. Radially, the UCN are confined by the material optical potential of the inner cylindrical sample tube surface. This storage principle avoids mechanical slits in the storage volume which are difficult to control and which would be a serious cause of UCN loss and hence would lead to a lower storage time constant simulating higher loss probabilities per wall bounce. The measurements of storage times with this apparatus allow for extraction of UCN losses on material walls and, simultaneously, the precise determination of depolarization effects, see below.

[2] Storage of very slow neutrons in magnetic fields was first discussed by Vladimirski [116]. First experiments were performed by Abov et al. [117].

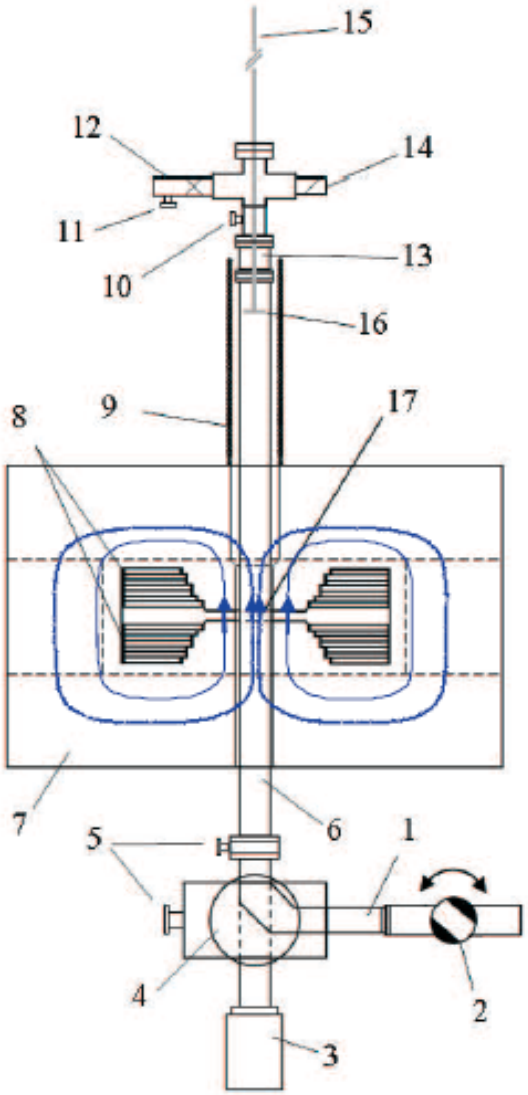

Figure 3.2: Experimental apparatus for the investigation of materials for the storage of ultracold neutrons: 1. UCN guide from the ILL turbine; 2. Beam-line shutter; 3. UCN detector; 4. UCN switch between UCN guide from turbine/sample and sample/UCN detector; 5. Vacuum pumping ports; 6. Vertical UCN guide (sample) below magnetic field region; 7. Magnet yoke; 8. Magnet coils; 9. Holding field coils; 10. Vacuum port to prepump; 11. Vacuum port to prepump; 12. Vacuum pump (turbo); 13. Extension vacuum tube; 14. Vacuum sensor; 15. UCN absorber with variable height; 16. Vertical UCN guide (sample) above magnetic field region (storage volume); 17. Magnetic field lines at I=300 A in the air gap of the split coil magnet. Solid lines: B=2.7 T in the 30 mm air gap. Dotted lines: B=1.5 T in the center of the bore for the vertical neutron guide (z=0, r=0).

3.1. Preparation of samples

We used samples where the materials under investigation were sputtered directly on the inner side of glass tubes. These tubes were produced by Schott AG, Mainz, Germany. There length was 1.5 m and there outer and inner diameters are 80 mm and 70 mm, respectively. In order to remove contaminations from the glass surface, the tubes were cleaned in a Mucasol[3] bath at a temperature of ~ 50◦C and rinsed with demineralized water. After this wet cleaning, the tubes were heated up in vacuum for 12 h to about 150 ◦C. Still hot, the tubes were transferred to the sputter chamber which was pumped down to a vacuum of 10^{-7} mbar. The glass tubes were then coated with a layer of typically 500 nm.

4. Data taking

The experiment was performed at the beam line PF2/EDM [118, 119] of the Institute Laue-Langevin, ILL, in Grenoble, France and at the new UCN source at the Paul Scherrer Institute in Villigen, Switzerland [83]. Ultracold neutrons from the UCN turbine [120] or the PSI-UCN-West beam enter the experimental apparatus from the right through an UCN guide (1, Fig. 3.2) and a rotatable shutter (2, Fig. 3.2) in open position. With the UCN switch (4, Fig. 3.2) in filling position, UCN are deflected into the vertical neutron guide (6 and 16, Fig. 3.2).

After 20 s of filling, equilibrium neutron density in the sample storage volume is reached and the magnetic field in the air gap is switched on for the storage of UCN. The field is raised within ~2 s to 90 % of the maximum electric current, i.e., 1.45 T corresponding to 87 neV UCN kinetic energy at z = 0. Then, the mechanical neutron switch (4, Fig. 3.2) is moved from the filling position to the emptying position thereby blocking the UCN from the turbine. The beam line shutter (2, Fig. 3.2) is closed for improved background suppression.

After switching on the magnetic field, the stored UCN spectrum is “cleaned" over a time of 100 s. It was found by Monte-Carlo calculations using GEANT4UCN [121] and by experiment that during this time, all UCN with energies higher than 87 neV have either been absorbed at the top of the storage volume (absorber position z = 90 cm) or have penetrated the magnetic field and fallen into the neutron counter (3, Fig. 3.2) where they have been absorbed and detected.

Neutrons with the magnetic moment antiparallel to the magnetic dipole field and energies below 87 neV at z = 0 are reflected into the upward direction and are trapped in the storage volume. Because of this reflective behavior they are called low-field seekers, LFS.

[3] http://www.sigmaaldrich.com/catalog/product/sigma/z637181?lang=fr&region=CH

There are quite some UCN which are in the region of the magnetic field while the field is ramped rapidly. Low-field seekers are accelerated out of the magnetic field, e.g. into the storage volume. They experience a gain in total energy and can be stored if their kinetic energy after this acceleration is below 87 neV at the origin of the coordinate system. Those with their spins parallel to the magnetic field are decelerated and trapped in the magnetic field region if their kinetic energy is on average ∼17 neV immediately after the magnetic field is switched on. Some UCN, however, may have energies up to 89 neV. These neutrons are termed high field seekers, HFS. The phenomenon of trapping UCN with two different spin directions in the same apparatus was subject of another investigation and was published earlier [122].

After the spectral cleaning time of 100 s, the magnetic field is raised to 100 %, i.e., 1.52 T and the remaining UCN are stored over times chosen to reach from 20 s to 370 s. The LFS neutrons which have been depolarized during these storage times, e.g., by an interaction with the sample surface atoms during a wall bounce, can penetrate the magnetic field and are registered in the neutron detector. After storage, the magnetic field is rapidly switched off ($t < 2$ s) and the remaining UCN are detected over an emptying time of 45 s. Figure 3.3 shows the detector counts over time from filling (detector closed), spectral cleaning, storage and emptying.

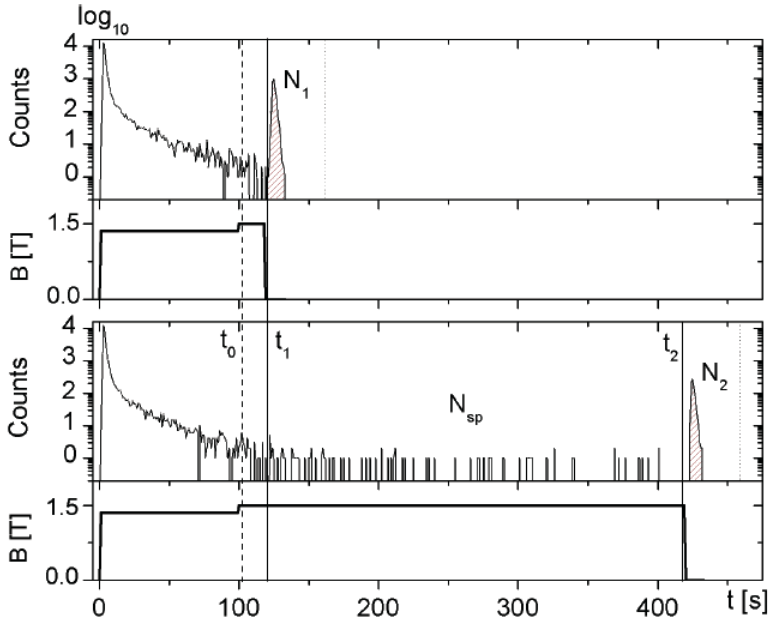

Figure 3.3: Detector counts for the sequences ‘filling’ (−20 - 0 s), ‘cleaning’ (0 - 100 s), ‘holding’, and ‘emptying’ for different holding times t_i, $t_1 - t_0 = 20$ s (top) and $t_2 - t_0 = 320$ s (bottom); N_1, N_2 and N_{sp} are the neutron counts at t_1, t_2, and the spin flipped neutrons, respectively. The magnetic field B at z = 0, r = 0 as a function of time is also shown.

5. Data analysis

With the procedure shown in Fig. 3.3 the wall loss μ and depolarization β probabilities of UCN interacting with the surface material of the sample tube can be determined simultaneously. The storage time constant of the storage volume under investigation, τ_{st}, is determined from the UCN counts, N_1 and N_2, after holding times t_1 and t_2.

It depends on

i) the lifetime of the free neutron, τ_n,

ii) the wall loss time constant, τ_μ, which is the inverse of the average loss rate, cf. Eq. 3.3, and

iii) the time constant τ_β originating from losses through spin flips during the holding times.

In total,

$$\frac{1}{\tau_{st}} = \frac{\ln\left(\frac{N_1}{N_2}\right)}{t_2 - t_1} = \frac{1}{\tau_n} + \frac{1}{\tau_\mu} + \frac{1}{\tau_\beta}, \tag{3.7}$$

The ratio of time constants τ_{st} and τ_β is inversely proportional to the measured count rates:

$$\frac{\tau_{st}}{\tau_\beta} = \frac{N_{sp}}{N_0 - N_1}, \tag{3.8}$$

With this, the spin flip time constant, τ_β, can be determined directly from the spin flip counts, N_{sp}, see Fig. 3.3,

$$\frac{1}{\tau_\beta} = \beta \cdot \nu(E) = \frac{N_{sp}}{N_0 - N_1} \cdot \frac{1}{\tau_{st}}, \tag{3.9}$$

The UCN energy distribution in the apparatus (see Fig. 3.2), was measured by varying the height of the absorber (15, Fig. 3.2). The maximal storable UCN energy is then defined by the absorber height. Figure 3.4 shows the UCN counts as a function of the UCN absorber height. Between z~30 cm and z~10 cm, the UCN counts are constant at a level of about 7 % of the total counts and decrease to zero at zero height position. This means that there are no UCN in the storage volume between z~10 cm and z~30 cm, as one can easily see from the differential energy spectrum, Fig. 3.4. This finding is confirmed by the potential energy distribution of UCN in the apparatus, see Fig. 3.5. The calculation is based on magnetic field measurements along the vertical axis of the apparatus and two-dimensional rotation-symmetric field distribution calculations using the code POISSON SUPERFISH [123]. The

neutrons in the high magnetic field region below z = 20 cm could be identified as HFS trapped during the rapid ramping of the field [122].

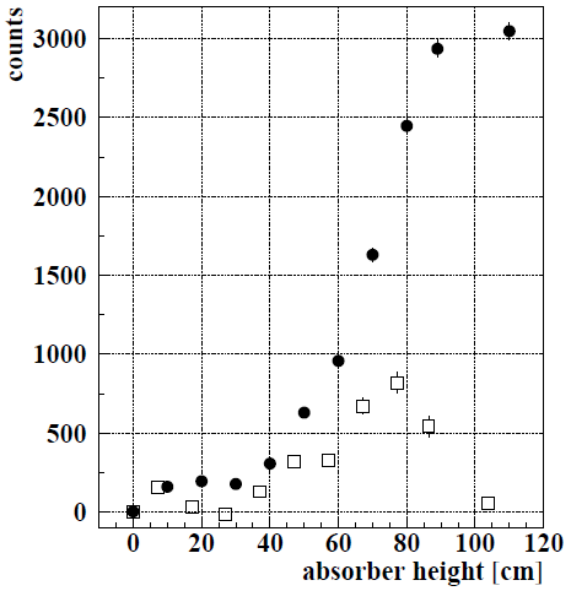

Figure 3.4: Ultracold neutron counts as a function of the absorber height z after 20 s filling, 100 s spectral cleaning, and 20 s holding time. Black dots: integral UCN energy spectrum; open squares: differential UCN energy spectrum. The differential spectrum was obtained by the count rate differences at z (i) and z (i−1), where z (i−1) = z (i) − 10 cm. The z position for the differential spectrum is then the weighted mean, z (i−1) + 10/√2 cm.

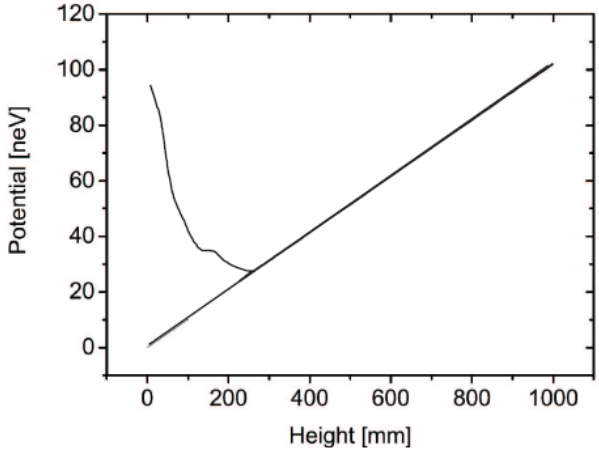

Figure 3.5: The potential energy in the storage volume during UCN storage as a function of the height. At small heights, the potential is mainly determined from the magnetic field in the air gap of the magnet. The kink around 150 mm originates from saturation effects in the iron where the bore diameter increases from 81 mm to 121 mm. The gravitational potential energy rises linearly with height and dominates at larger heights (see App. 7.1).

5.1. Determination of the wall collision frequency ν(E)

For the determination of both the wall loss and depolarization probabilities per wall bounce one needs to know the bouncing frequency ν(E) of the UCN at the sample walls, cf. Eqs. (3.3) and (3.9). This has been determined by two different methods:

i) Applying kinetic gas theory and

ii) Monte Carlo calculations.

The results are shown in App. 7.

5.2. Data and background

An example for the raw data for our sample NiMo-82/18 is shown in Fig. 3.6 for different absorber positions. The data for absorber 20 cm and 30 cm agree with each other. As can be seen from Fig. 3.4, these data are solely high field seeking UCN (HFS). Since these particles have a higher wall bouncing frequency, see Fig. 3.7 they represent an unwanted background for the analysis of the low field seeking UCN (LFS). Besides HFS, the data at absorber position 20 cm and 30 cm contain also background events common to all absorber heights. So, for the analysis of the LFS, the data at 30 cm and/or 20 cm absorber positions have to be subtracted from the data taken at higher absorber positions. In the analysis of the HFS, i.e. for absorber positions of 30 cm or less, a background measured at 0 cm absorber position was subtracted.

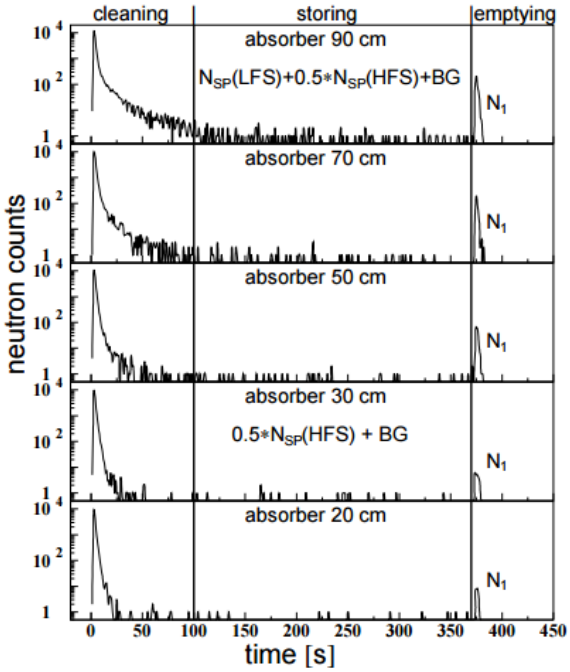

Figure 3.6: Neutron spectra at different absorber positions, 90 cm, 70 cm, 50 cm, 30 cm, and 20 cm.

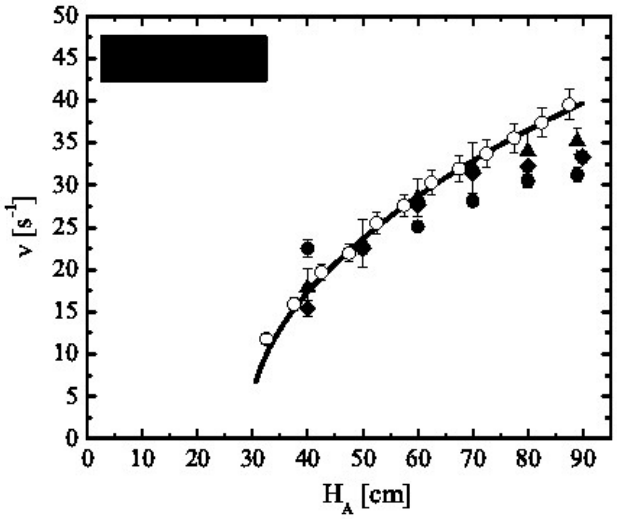

Figure 3.7: Bounce rates of UCN as a function of their kinetic energy. The black line is calculated from kinetic gas theory. Black circles, open circles, triangles, and diamonds are from different Monte Carlo calculations. The rectangle in the upper left corner is the Monte Carlo calculation for high field seeking ultracold neutrons, HFS.

5.3. The storage time constant τ_{st}

Data after background subtraction are presented in Fig. 3.8.

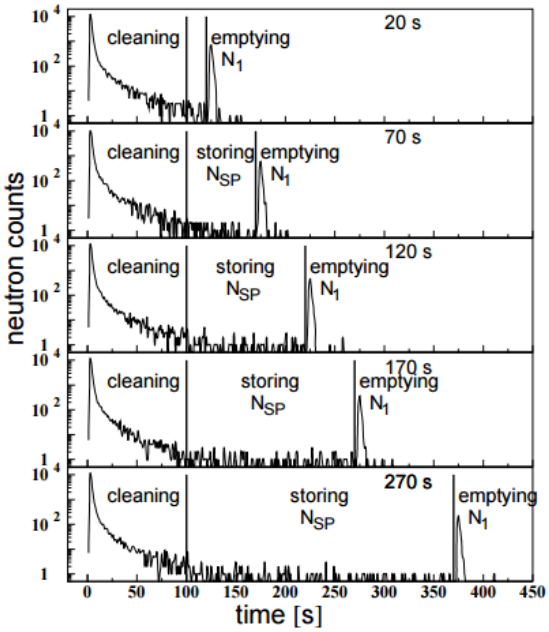

Figure 3.8: Neutron spectra for different storage times between 20 s and 270 s. The sample is NiMo-82/18. The absorber height is 90 cm. N_{SP}: spin-flipped UCN during storing; N_1: UCN in the read-out peak after storage.

Here, the sample is NiMo-82/18, the absorber position is 90 cm, and the storage times vary from 20 s to 270 s. The counts in the read-out peak after storage, N_1, are used to determine the storage time constant, τ_{st}. The storage time constant, τ_{st}, is needed to evaluate the depolarization and loss probabilities per wall bounce, β and μ, respectively, cf. Eqs. (3.8) and (3.9).

The storage time constant τ_{st} was obtained by fitting an exponential function with two free parameters, N_0, the number of UCN at time 0 s, and τ_{st}, the storage time constant, to the five (or seven) N_1 values.

$$N_0 = N_1 \cdot e^{-\frac{t}{\tau}} \tag{3.10}$$

The results are shown in Fig. 3.9. The χ^2 values per degree of freedom (reduced χ^2) of the fits were 2.2, 3.0, 1.2, 1.1, and 1.2, respectively for the five absorber positions[4]. In order to obtain a reduced χ^2 of 1.0 and to account for unknown systematic uncertainties, we increased the uncertainties of the N_1 data by a factor of χ [124]. The storage time constants for the sample NiMo-82/18 as a function of absorber position are shown in Fig. 3.10.

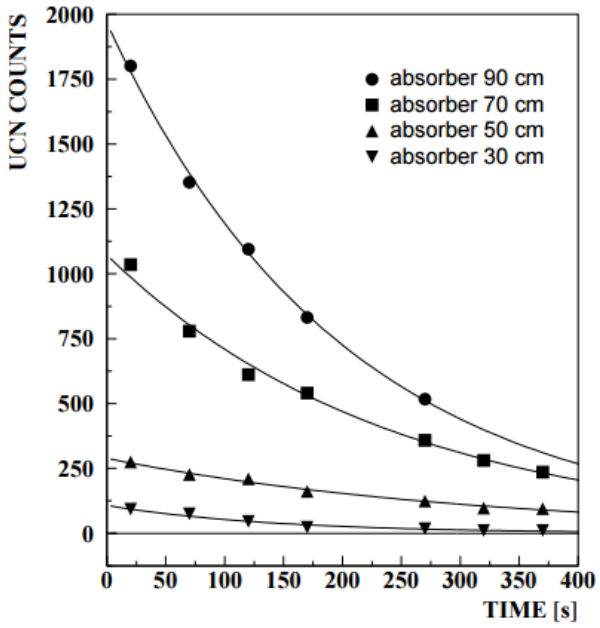

Figure 3.9: Determination of the storage time constants for NiMo-82/18 for different absorber positions. The storage time constants are obtained from the N_1 values after different storage times ranging from 20 s to 370 s. The background originating from HFS and ambient events were subtracted. At absorber position 20 cm and 30 cm, there are only HFS events and background, cf. Figs. 3.4 and 3.6. Here, the background, measured with absorber position 0 cm, was subtracted.

[4] The data at 20 cm are indistinguishable from those at 30 cm and are not shown in Fig. 3.9.

There is a clear tendency: for smaller kinetic energies, i.e., for smaller wall bouncing frequencies, the τ values are higher, as expected. For the HFS, the bouncing frequencies are higher: because of their small kinetic energy (E_{kin}(av) ~ 17 neV), they are reflected by the material optical wall potential only to a very short distance before they are pulled back again towards the sample wall due to the large magnetic field gradient, $d\vec{B}_{\perp}/dr \approx$(0.58 T)/(0.035 m) = 16.6 T/m, in the region of the air gap of the H-type split coil magnet. The results are summarized together with the depolarization and loss probabilities in Table 9 below.

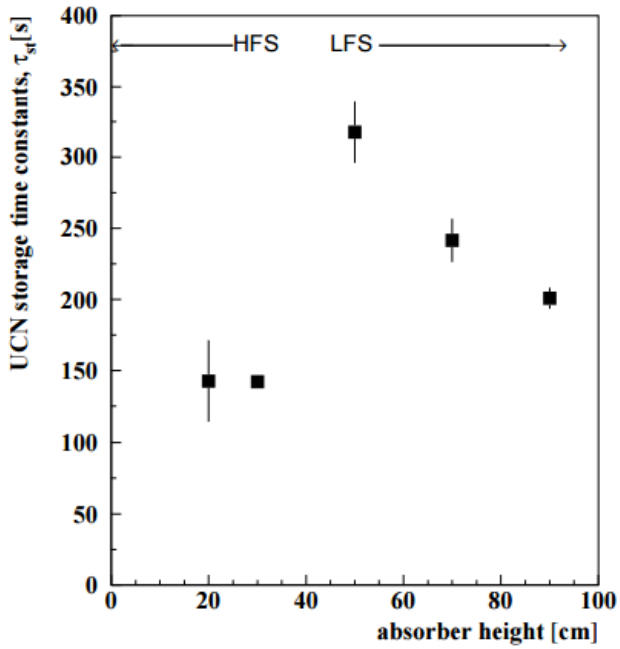

Figure 3.10: Storage time constants for NiMo-82/18 for different absorber positions.

Sample	Type	h_a [cm]	V [neV]	τ_{st} [s^{-1}]	β [10^{-5}]	μ [10^{-4}]	η [10^{-4}]	η=W/V [10^{-4}]
NiMo82/18	LFS	90		200.8±7.4	0.98±0.05	0.8±0.05	2.5±0.5	
NiMo82/18	LFS	70		241.5±15.3	0.98±0.06	0.81±0.07	2.0±0.4	
NiMo82/18	LFS	50	212	317.5±21.5	1.00±0.15	0.75±0.06	2.1±0.5	1.3
NiMo82/18	HFS	30		142.2±4.0	0.8±0.2	1.27±0.07	3.4±0.7	
NiMo82/18	HFS	20		142.7±28.7	0.2±0.8	1.31±0.28	3.6±2.6	
NiMo88/12	LFS	90		266.1±11.2	0.69±0.1	0.68±0.12	1.74±0.31	
NiMo88/12	LFS	70	222	295.6±14.2	0.74±0.11	0.63±0.11	1.54±0.27	1.2
NiMo88/12	LFS	50		317.9±9.3	1.04±0.21	0.79±0.18	2.19±0.5	
NiMo88/12	HFS	30		188.1±8.8	0.78±0.11	0.9±0.13	2.38±0.4	
Ni/Mo85/15-Alu	LFS	90		269.9±2.9	0.81±0.1	0.66±0.11	1.65±0.28	
Ni/Mo85/15-Alu	LFS	50	217	387.6±44.7	1.61±0.33	0.48±0.12	1.28±0.32	1.2
Ni/Mo85/15-Alu	HFS	20		115±1.6	-	-	-	
Ni/Mo85/15-Glass	LFS	90		202.3±9	0.53±0.08	1.04±0.19	2.6±0.48	
Ni/Mo85/15-Glass	HFS	20	217	90.4±43.6	0.64±0.54	2.25±2.19	2.96±2.88	1.2
Ni 100	HFS	10	245	169.9±4.9	-	-	-	1.2
Ni/Mo91/9	LFS	90	227	150±26.6	-	-	-	1.2
Ni/Mo94/6	LFS	90	232	191.9±7.4	-	-	-	1.2
Ni/V93/7	LFS	90		171.1±27.7	-	-	-	
Ni/V93/7	LFS	70		145.9±6.1	-	-	-	
Ni/V93/7	LFS	50	224	106.1±39.6	-	-	-	1.3
Ni/V93/7	HFS	30		155.9±9.9	1.12±0.18	1.12±0.18	2.97±0.48	
Cu 100	LFS	90		233.1±1.2	0.32±0.04	0.87±0.14	1.94±0.31	
Cu 100	LFS	70		254.4±14	0.53±0.09	0.82±0.17	1.74±0.36	
Cu 100	LFS	50	170	336±30.9	0.78±0.16	0.74±0.18	1.78±0.31	1.6
Cu 100	HFS	30		157.6±1.2	0.22±0.05	0.88±0.2	2.02±0.46	
dPS	LFS	90		251±18.2	0.13±0.02	0.8±0.16	1.73±0.35	
dPS	LFS	70		309.5±3.3	0.52±0.07	0.6±0.1	1.24±0.21	
dPS	LFS	50	161	345±19.1	0.89±0.16	0.69±0.14	1.61±0.33	~0.0016
dPS	HFS	30		140.7±8.4	0.39±0.08	1.35±0.3	3.01±0.67	

Table 9: Summary of results for storage time constants τ_{st}, depolarization probability per wall bounce β, loss probability per wall bounce μ and loss parameter η; h_a is the absorber position.

6. Results

6.1. The depolarization probability β

The depolarization probability per wall bounce β is derived from Eq. 3.10:

$$\beta = \frac{N_{sp}}{(N_0 - N_1)\cdot\tau_{st}\cdot\nu} \tag{3.11}$$

Here, N_{sp} is the number of spin-flipped UCN during storage, N_0 is the number of UCN at the beginning of the UCN storage and N_1 at the end of the storage, respectively: N_0 is obtained from the fit, cf. Sec. 5.3 and N_1 from the read-out peak after emptying, cf. Figs. 3.6, 3.8. For absorber positions 90 cm ≤ h_a < 30 cm, the count rate during storage, N_{sp} at 20 or 30 cm has to be subtracted in order to obtain the pure spin flips for LFS and without background. For absorber positions h_a > 30 cm, the background for N_{sp} obtained at h_a = 0 cm was subtracted. The β parameters as a function of absorber position for the sample NiMo-82/18 are shown in Fig. 3.11. The results of all samples are displayed in Table 9.

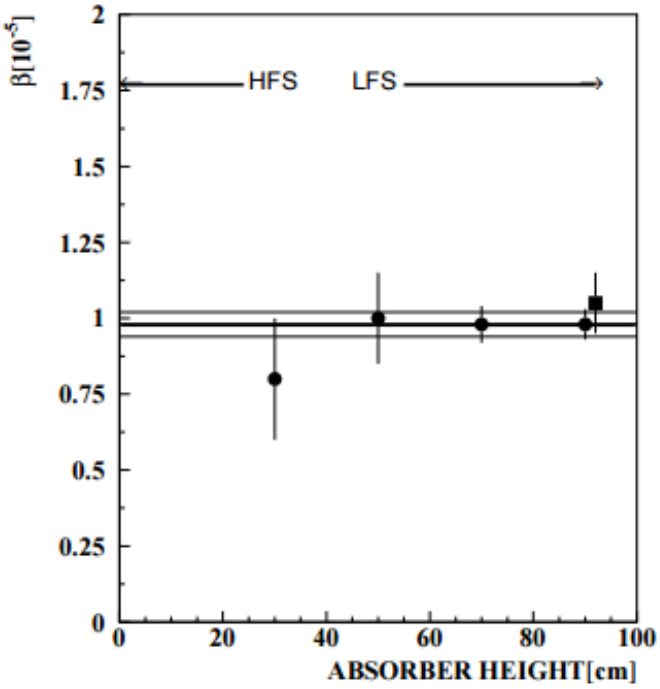

Figure 3.11: Depolarization probability β for NiMo-82/18 and for different absorber positions. Black circles: data taken at the ILL, black square: data taken at PSI.

6.2. The wall loss probability

The wall loss probability per bounce μ is derived from Eqs. (3.3), (3.7):

$$\mu = \frac{1}{\tau_{st} \cdot v(E)} - \frac{1}{\tau_n \cdot v(E)} - \beta. \qquad (3.12)$$

For the neutron lifetime we use τ_n = (880.3 ± 1.1) s [124]. The μ values are not altered significantly by a neutron lifetime change of several seconds [125-127]. The μ parameters as a function of absorber position for the sample NiMo-82/18 are shown in Fig. 3.12. The results of all samples are displayed in Table 9.

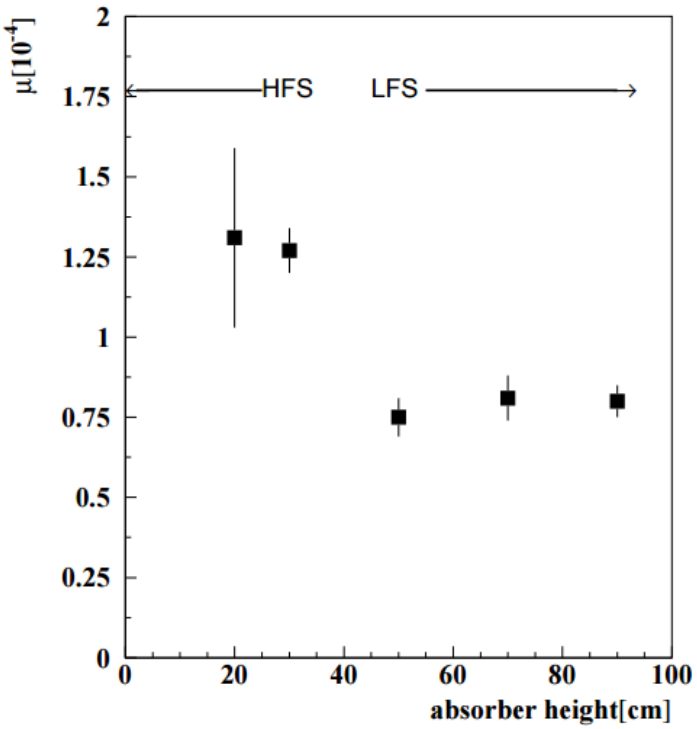

Figure 3.12: Wall loss probability μ for NiMo-82/18 and for different absorber positions.

6.3. The wall loss parameter η

As mentioned above, the wall loss coefficient, η, is the ratio of the imaginary part, W, to the real part, V, of the material optical potential. Experimentally, we can deduce η from the average losses over angle, μ(E,θ) given by Eq. (3.6). This equation holds for monoenergetic UCN with energy E. In our apparatus we have, however, a UCN energy distribution between 0 and 90 neV. To solve this problem, we firstly performed a Monte Carlo calculation to determine the velocity distribution $v_\perp$ of UCN, i.e., perpendicular to the sample surface. The results for absorber positions 90 cm and 20 cm are shown in Fig. 3.13. We obtain the energy distribution $E_\perp$ as function of absorber height from the $v_\perp$ distribution by

$$\frac{dN}{dE_\perp} = \frac{dN}{v_\perp} \cdot \frac{v_\perp}{E_\perp}. \tag{3.13}$$

Here, $E_\perp = \frac{m}{2} \cdot {v_\perp}^2$ =5.22· ${v_\perp}^2$; m=940 MeV/c^2 the rest mass of the neutron. Hence Eq. (3.13) yields

$$\frac{dN}{dE_\perp} = \frac{1}{10.44} \cdot \frac{1}{v}. \tag{3.14}$$

The $E_\perp$ distributions for absorber positions 90 cm and 20 cm are shown in Fig. 3.14. Since the material optical potential V of all our samples is lower than the maximal $E_\perp$ value, the Monte Carlo simulations are valid for all samples under investigation.

Our measured value μ for the loss probability per wall bounce is then

$$\mu = \frac{\sum g_i \cdot \mu_i(E)}{\sum g_i}. \tag{3.15}$$

Here, g_i is the value from the $E_\perp$ distribution, cf. Fig. 3.14, and

$$\mu_i(E) = 2\eta\left(\frac{E_{\perp,i}}{V - E_{\perp,i}}\right)^{1/2}. \tag{3.16}$$

We make the substitution

$$A_i = \left(\frac{E_{\perp,i}}{V - E_{\perp,i}}\right)^{1/2}. \tag{3.17}$$

Then, η is

$$\eta = \frac{\mu}{2} \cdot \frac{\sum g_i}{\sum (g_i \cdot A_i)} \tag{3.18}$$

The results for NiMo-82/18 are displayed in Fig. 3.15. The results for all samples are listed in Table 9.

The experimental data are in all cases up to a factor ~2 higher than expected from W/V. In the case of dPS, where one expects an extremely low loss factor W/V = 0.0016 $\cdot 10^{-4}$, the difference is even

three orders of magnitude. This difference, earlier termed anomalous losses, is attributed to impurities, surface contaminations or tiny, microscopic holes in the coating [128-130]. The data also show that there is no dependence on energy as expected.

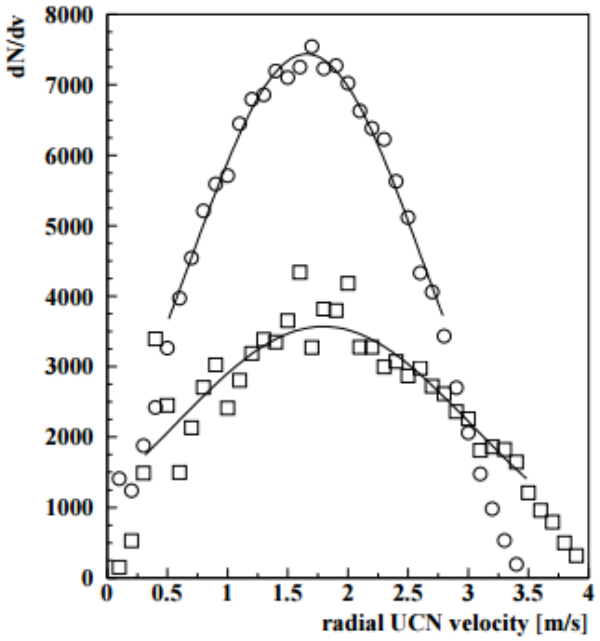

Figure 3.13: Radial velocity distribution $dN/dv_{\perp}$. Open circles: absorber height 90 cm, LFS. Open squares: absorber height 20 cm, HFS. The solid lines in the figure are Gaussian distributions fitted to the central values in order to guide the eye.

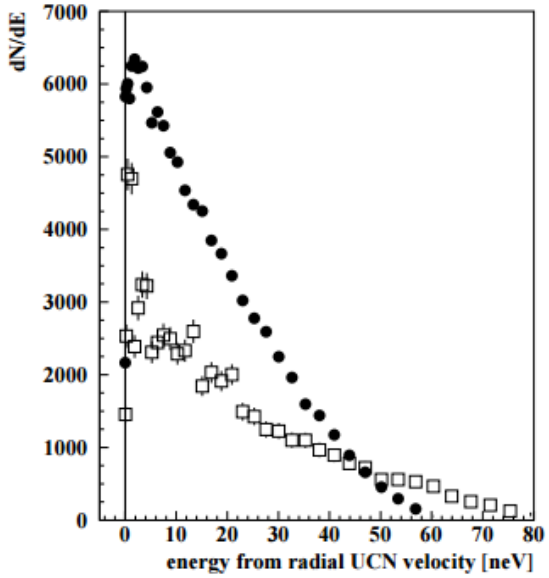

Figure 3.14: Energy distribution $dN/dE_{\perp}$ obtained from the radial UCN velocity distribution $dN/dv_{\perp}$. Open circles: absorber height 90 cm, LFS. Open squares: absorber height 20 cm, HFS.

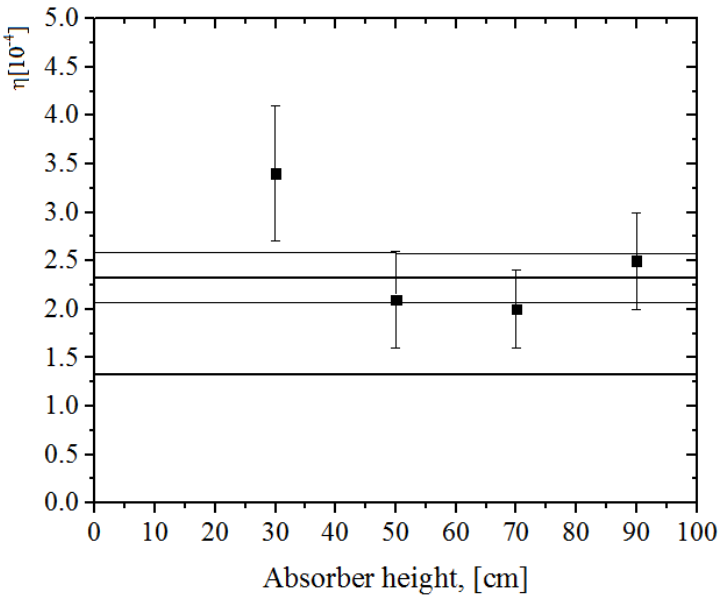

Figure 3.15: Energy loss parameter η over absorber height for NiMo-82/18. A constant was fitted to the data, ($\bar{\eta}$ = 2.3±0.25)· 10^{-4} . At 1.3 ·10^{-4} we show the expected value from W/V.

7. Conclusions

Nickel molybdenum alloys are often used for the transport of polarized as well as unpolarized ultracold neutrons. We have investigated the wall loss and depolarization probability per wall bounce with the alloys (i) NiMo-82/18, (ii) NiMo-85/15, (iii) NiMo-88/12, (iv) NiMo-91/9, NiMo-94/6, Ni-100, and NiV-93/7. With a Nickel content of more than 88 weight percentages, depolarization of the LFS happened spontaneously and only the HFS could have been stored in the region of the high magnetic field (1.52 T) in the vicinity of the air gap of the H-type split-coil magnet. The number of storable HFS UCN was only ∼7 % of the storable LFS in the samples at paramagnetic sample surface conditions.

For the three paramagnetic NiMo samples, i.e. NiMo-82/18, 85/15 and 88/12 we see no energy dependence for the β and η parameters, see App.7.2, 7.3. The η parameters over molybdenum content of the samples are shown in Fig. 3.14. There, also no variation over the molybdenum content is visible: the data agree well with their mean value of $(2.1\pm 0.3)\cdot 10^{-4}$, about a factor 1.5 higher than expected from W/V.

The β values of these three alloys over molybdenum content are shown in Fig. 3.15. Fitted to a constant value, the χ^2/dof is 12.5, that is, there is no real correlation. The reason for this is unknown and might originate from the sputtering process. The total values for these three NiMo alloys, however, are small and suitable for the transport of polarized UCN without noticeable polarization losses. The β and η values of NiMo-85/15 on an aluminum substrate are in agreement with those from glass. The transmission, however, was found in an earlier experiment to be substantially lower [98].

For the dPS sample, the results were satisfactory for the use in a UCN spin precession chamber of the experiment to determine the neutron electric dipole moment. The same hold for copper as a nonmagnetic UCN guide, however with a somewhat lower material optical potential compared to the NiMo alloys.

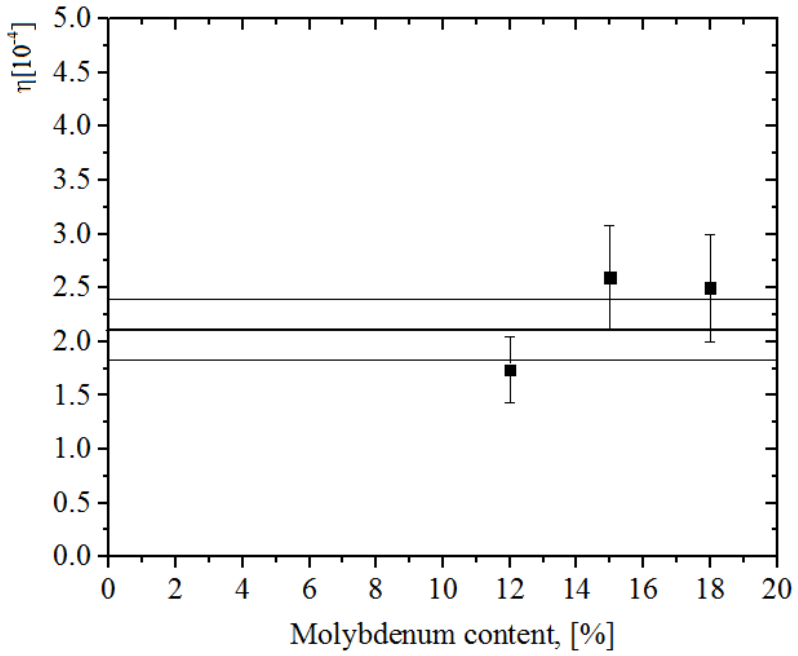

Figure 3.14: Energy loss parameter η over molybdenum content of the sample coating. A constant was fitted to the data, ($\eta_{all} = 2.1 \pm 0.29$) · 10^{-4}. The χ^2 per degree of freedom (dof) was 1.5. The uncertainties of the single values have been increased by a factor of $\chi = 1.22$ as explained above.

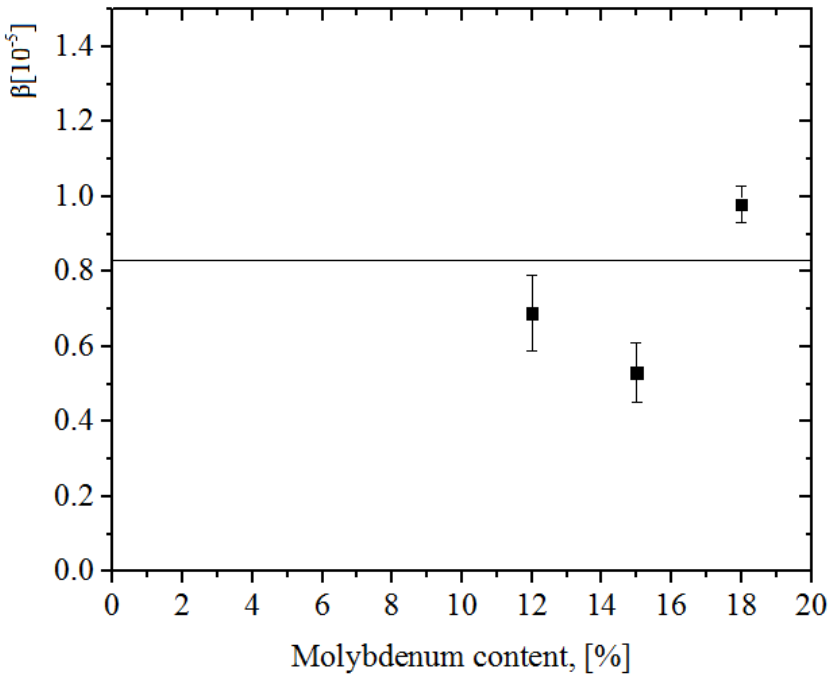

Figure 3.15: Depolarization parameter β over molybdenum content of the sample coating. A constant was fitted to the data, ($\beta_{all} = 0.83 \pm 0.14$) · 10^{-5}. The χ^2 per degree of freedom (dof) was, however, rather poor, 12.5, so that no correlation could be stated.

Conclusions

In this dissertation, we investigated new materials for the design of electrodes in a nEDM experiment, in particular conductive plastics. We designed and constructed a test setup for the measurements of electric fields. Firstly, the electrostatic force between a high voltage electrode and ground was measured by a balance weight connected to sensitive readout electronics. Secondly, we measured the electro-optical effect in crystals placed in the electric field. This last method via Pockels effect is instantaneous and does not influence or disturb the sensitive nEDM experiment; it will be used in the future. Besides, a variety of methods for high-voltage breakdowns suppression was performed at distances between the electrodes up to 10 cm: (i) in vacuum of a few 10−5 mbar, (ii) in different gases at low pressures, and (iii) with silicone rubber as an insulator. This latter method allows placement of equipment for the measurement and control of the very low and constant magnetic field in the nEDM experiment very close to the experimental chambers. The resistance of the silicon rubber was measured with a picoamperemeter calibrated carefully for the measurements of very low leakage currents. In a set of simulations, the final design of the shapes and sizes of the high voltage electrodes was developed and used for manufacture. In the last part of the dissertation, data for the construction of UCN guides and UCN spin precession chambers were analyzed. The result is, that nickel alloys with molybdenum content between 18 and 12 weight percentages were equally well suited for an optimal transport of UCN with respect to low loss and depolarization probabilities. Lower molybdenum contents lead to rapid UCN depolarization. Also nickel alloy with 7 weight percentage of vanadium lead to instantaneous UCN depolarization. For neutron guides, copper had the lowest depolarization probability for the samples under investigation. The losses were similar to that of the nickel alloys. The drawback here is its lower material optical potential compared to the nickel alloys and should be used only for UCN energies up to 167 neV. Similar small depolarization was found for dPS ($V_f = 161$ neV) which makes this material very suitable for the inner coating of a high resistivity spin precession chamber in a nEDM experiment.

The possibility to use different conductive plastics for a high-voltage electrode has been investigated. Our electrode will be made from quartz glass coated with NiMo. All the systematic effects that are related to the electric field were shown to be one or two orders below the statistical uncertainties. Analysis of different coatings on glass and aluminum shows the possibility to achive a measurement goal of $5 \cdot 10^{-28}$ e·cm.

Appendix

1. Geometric phase effect

In a cylindrical coordinate system, $\vec{B} = (B_x, B_y, B_z)$ becomes $\vec{B} = (B_r, B_\varphi, B_z)$.

Since div$\vec{B}$=0, we have

$$\frac{1}{r}\left(\frac{\partial}{\partial r}(r \cdot B_r)\right) + \frac{1}{r} \cdot \frac{\partial B_\varphi}{\partial \varphi} + \frac{\partial B_z}{\partial z} = 0.$$

The second term in the equation is 0, that is:

$$\frac{1}{r}\left(\frac{\partial}{\partial r}(r \cdot B_r)\right) = -\frac{\partial B_z}{\partial z},\ \frac{\partial}{\partial r}(r \cdot B_r) = -r\frac{\partial B_z}{\partial z}.$$

Assuming a constant gradient in z-direction, we obtain the magnetic field in the xy-plane:

$$B_r = -\frac{r}{2}\frac{\partial B_z}{\partial z} \tag{A.1}$$

2. Corrections for the measured nEDM

According Eq. (1.4) we can evaluate the nEDM. ^{199}Hg atoms as co-magnetometer allow correction of the neutron precession frequency. The nEDM can be extracted by using the geometric phase effect [19]. Taking the ratio of neutron and mercury frequencies using Eq. (1.5-1.6) and assuming that magnetic field B does not change, we have:

$$\frac{\nu_n}{\nu_{Hg}} = \frac{|2h(\mu_n B \pm d_n E)|}{h\nu_{Hg}} = \left|\frac{\gamma_n}{\gamma_{Hg}}\right| + \frac{2(d_n + \left|\frac{\gamma_n}{\gamma_{Hg}}\right| d_{Hg})E}{h\nu_{Hg}} \tag{A.2}$$

That is, $d_{meas} = d_n + \left|\frac{\gamma_n}{\gamma_{Hg}}\right| d_{f,Hg}$ contains a non-negligible contribution of $d_{f,Hg}$,

where $d_{f,n,Hg} = \left|\frac{\gamma_n}{\gamma_{Hg}}\right| \cdot d_{f,Hg}$.

3. Propagation of a plane electromagnetic wave in an anisotropic medium

For a plane electromagnetic wave in an anisotropic medium we have

$$\vec{E} = \vec{A}\exp\left[-i\left(\omega t - \vec{K}\vec{r}\right)\right], \tag{A.3}$$

where $\vec{K}$ is the wave vector.

If this medium is non-magnetic (μ=1), $\vec{B}=\vec{H}$, then for $\vec{D}$ (the vector of electric induction) and $\vec{H}$ (vector of magnetic field strength) Maxwell's equations will be:

$$rot\vec{H} = \frac{1}{c}\frac{\partial\vec{D}}{\partial t},\ div\vec{H} = 0,\ rot\vec{E} = -\frac{1}{c}\frac{\partial\vec{H}}{\partial t},\ div\vec{D} = 0 \tag{A.4}$$

If the wave is plane, then

$$rot\vec{H} = -i\left[\vec{H}\vec{K}\right],\ \vec{K} = \frac{\omega n}{c}\vec{N},$$

where $\vec{N}$ is wave normal, n is refraction coefficient, and

$$rot\vec{E} = -i\left[\vec{E}\vec{K}\right],\ \frac{\partial\vec{D}}{\partial t} = \frac{\partial(\vec{A}\exp\left[-i\left(\omega t - \vec{K}\vec{r}\right)\right])}{\partial t} = -i\omega\vec{D},$$

$$\frac{\partial\vec{H}}{\partial t} = -i\omega\vec{H}$$

becomes

$$\vec{D} = n\left[\vec{H}\vec{N}\right],\ -\vec{H} = n\left[\vec{E}\vec{N}\right] \tag{A.5}$$

The vectors $\vec{D}$ and $\vec{H}$ lie in the plane of wave front, $\vec{H}$ coincides with the direction of the magnetic induction $\vec{B} = \mu\vec{H}$. The vector $\vec{E}$ does not coincide with $\vec{D}$ in an anisotropic medium and forms with it a certain angle α. The vector $\vec{S}$, characterizing the direction of the energy flux in the wave, is coplanar to the vectors $\vec{E}$, $\vec{D}$, $\vec{K}$, and forms with the vector $\vec{K}$ the angle α, called the vector of Umov-Pointing: $\vec{S} = \frac{c}{4\pi}\left[\vec{E}\vec{H}\right]$.

.

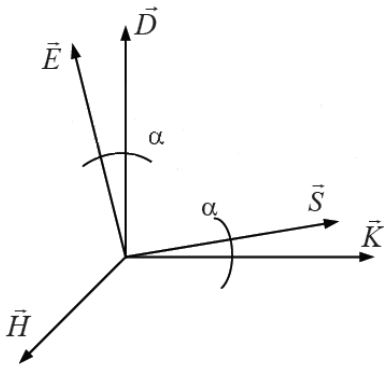

Figure A.3.1: Location of the vectors $\vec{D}$ and $\vec{E}$ in an anisotropic medium. The vectors $\vec{E}$, $\vec{D}$, $\vec{K}$, $\vec{S}$ are coplanar.

By using algebraic properties of the vector product $\left[\vec{a}\left[\vec{b}\vec{c}\right]\right] = \vec{b}(\vec{a}\vec{c}) - \vec{c}(\vec{a}\vec{b})$, we obtain $\vec{D} = n\left[\vec{H}\vec{N}\right] = n\left[-n\left[\vec{E}\vec{N}\right]\vec{N}\right] = -n^2\left[\left[\vec{E}\vec{N}\right]\vec{N}\right] = n^2\left[\vec{N}\left[\vec{E}\vec{N}\right]\right] = n^2\left\{\vec{E} - \vec{N}\left(\vec{E}\vec{N}\right)\right\}$. Then components of the vector $\vec{D}$:

$$D_x = n^2\left\{\frac{D_x}{\varepsilon_x} - N_x\left(\vec{E}\vec{N}\right)\right\},\ D_y = n^2\left\{\frac{D_y}{\varepsilon_y} - N_y\left(\vec{E}\vec{N}\right)\right\},\ D_z = n^2\left\{\frac{D_z}{\varepsilon_z} - N_z\left(\vec{E}\vec{N}\right)\right\},\ =>,$$

$D_x\left(\frac{1}{n^2} - \frac{1}{\varepsilon_x}\right) = -N_x\left(\vec{E}\vec{N}\right)$, so on.

$\vec{D} \perp \vec{N}$ ($\vec{S} \perp \vec{E}$), then $\vec{D}\vec{N} = D_xN_x + D_yN_y + D_zN_z = 0$. Rewrite this expression:

$$\frac{N_x^2}{\frac{1}{n^2} - \frac{1}{\varepsilon_x}} + \frac{N_y^2}{\frac{1}{n^2} - \frac{1}{\varepsilon_y}} + \frac{N_z^2}{\frac{1}{n^2} - \frac{1}{\varepsilon_z}} = 0. \qquad \text{(A.6)}$$

Let us set the main velocities along the main axes and along the normal:

$V_x = \frac{c}{\sqrt{\varepsilon_x}}$, $V_y = \frac{c}{\sqrt{\varepsilon_y}}$, $V_z = \frac{c}{\sqrt{\varepsilon_z}}$, $V_n = \frac{c}{n}$, then we obtain

$$\frac{N_x^2}{V_n^2 - V_x^2} + \frac{N_y^2}{V_n^2 - V_y^2} + \frac{N_z^2}{V_n^2 - V_z^2} = 0 \qquad \text{(A.7)}$$

is Fresnel's equation of wave normals.

Fresnel's equation of wave normals gives the dependence of V_n from the normal direction, given by N_x, N_y, N_z, and of the properties of the crystal, given the main permittivities ε_x, ε_y, ε_z or the main velocities V_x, V_y, V_z [65].

This equation has two positive solutions V_n' and V_n'', because it is quadratic with respect to $V_n^2 (n^2)$. Hence, for each direction of the normal there have two different velocities. This means that in an anisotropic medium at the same time two waves propagate with different velocities, corresponding mutually in perpendicular directions of oscillations of the electric induction vector D: $\vec{D}'$ and $\vec{D}''$, and $\vec{D}'' \perp \vec{N}$.

In $LiNbO_3$ crystal one crystallographic direction stands out. If we take z-axes, then $\varepsilon_x = \varepsilon_y \neq \varepsilon_z$, and $V_x = V_y = V_0$, $V_z = V_e$ - the main velocities. Rewrite the equation (A.7)

$$\left(V_n^2 - V_0^2\right)\left[\left(V_n^2 - V_e^2\right)\left(N_x^2 + N_y^2\right) + \left(V_n^2 - V_0^2\right)N_z^2\right] = 0 \qquad \text{(A.8)}$$

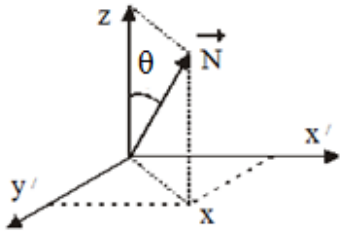

Figure A.3.2: The x-axis lies in the plane z$\vec{N}$ (main plane).

If the vector N forms an angle θ with the crystallographic axis z, then $N_z = \cos\theta$ and $N_x^2 + N_y^2 = 1 - N_z^2 = \sin^2\theta$. So one can find the roots of the equation (A.8): $V_n'^2 = V_o^2$, $V_n''^2 = V_o^2 \cos^2\phi + V_e^2 \sin^2\theta$, from which we get

$$n' = \frac{c}{V_n'} = \frac{c}{V_o} = n_o,\ n'' = \frac{c}{V_n''} = \frac{c}{\sqrt{V_o^2\cos^2\theta + V_e^2\sin^2\theta}} = \frac{n_o n_e}{\sqrt{n_o^2\sin^2\theta + n_e^2\cos^2\theta}} = n_e. \qquad \text{(A.9)}$$

The surface of normal has two cavities: a sphere of radius $V_n' = V_o$ and a surface of rotation of 4-th order – ellipsoid (ovoid shape). Therefore each direction of the normal N corresponds to 2 waves: o is ordinary, e is extraordinary and depends on the direction of $\vec{N}$ with respect to the symmetry axis z.

4. COMSOL simulations of the electric field distribution for different models of the high voltage electrode.

4.1. Study of the electric field distortions

Five most different examples were selected from a variety of simulated shapes:

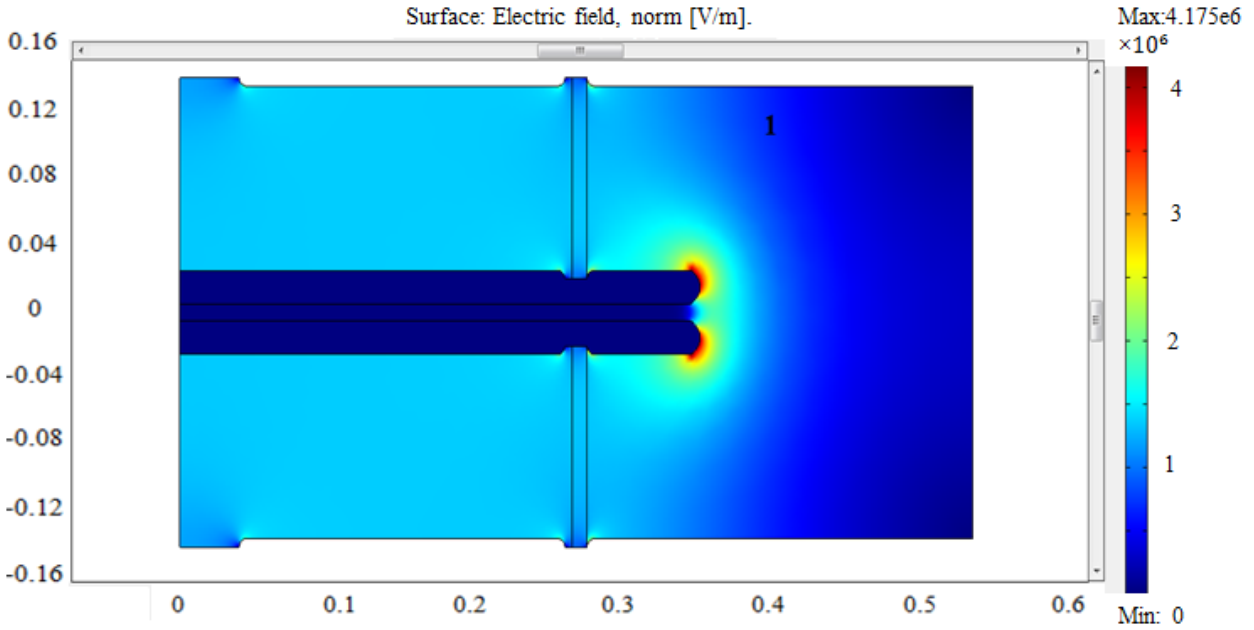

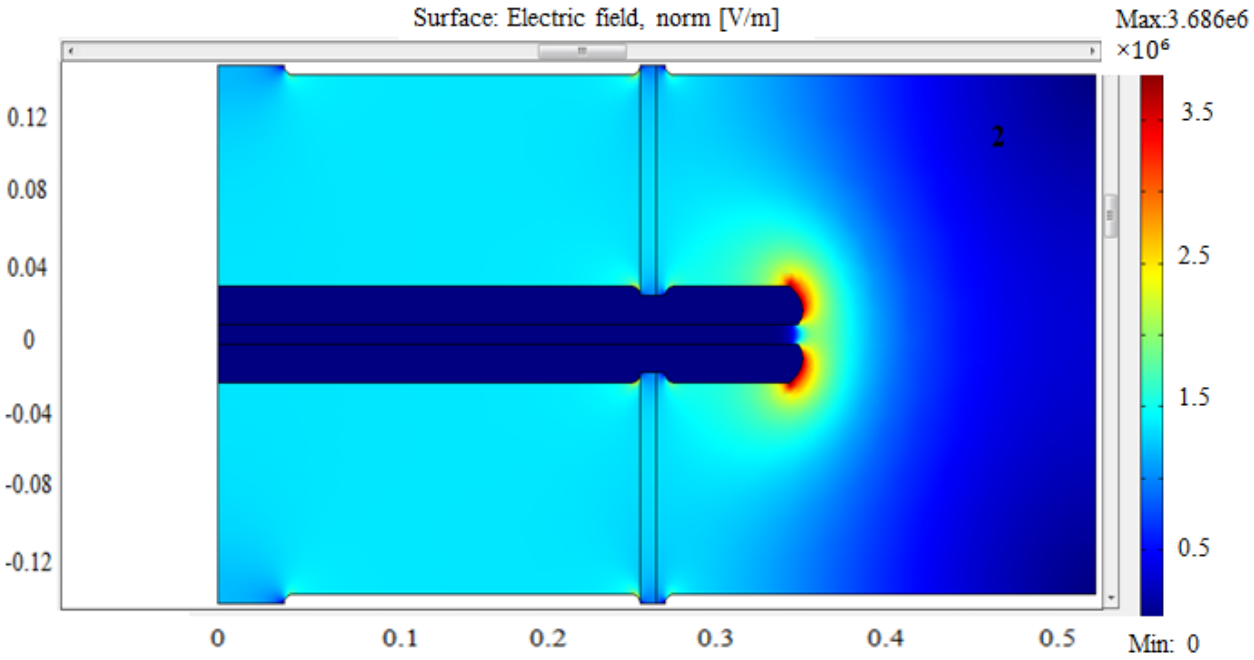

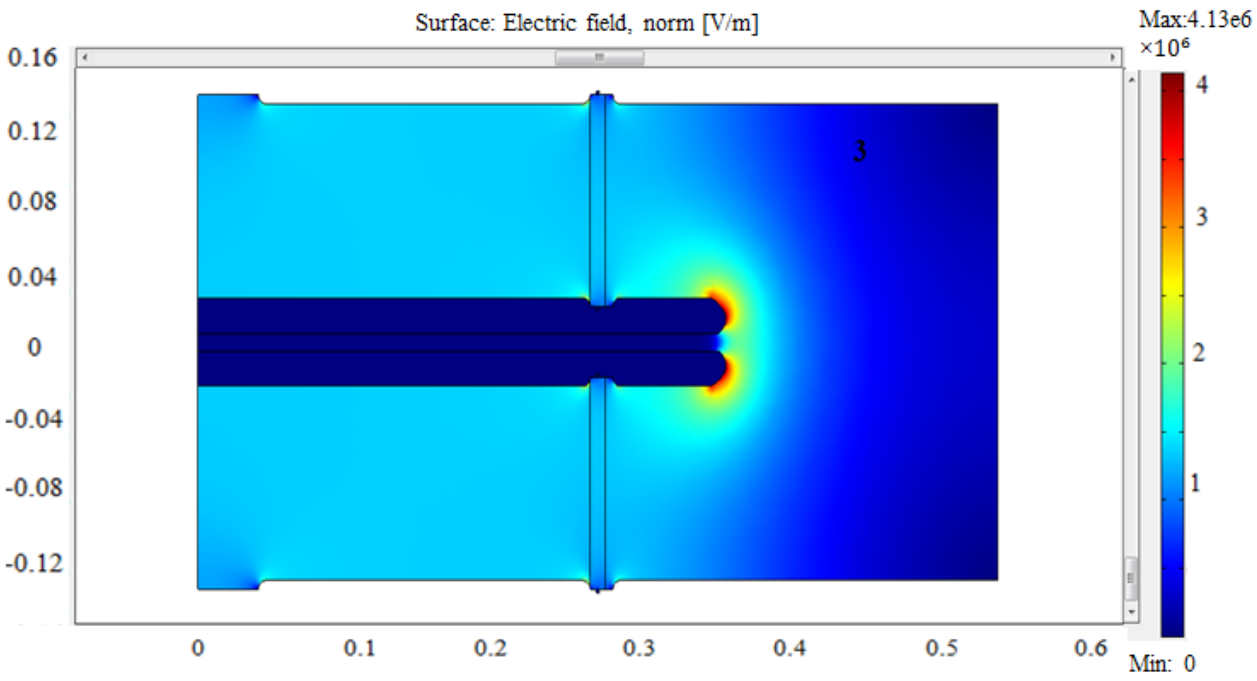
Surface: Electric field, norm [V/m]
Max:4.13e6
×10⁶
4
3
2
1
Min: 0
0.16
0.12
0.08
0.04
0
-0.04
-0.08
-0.12
0
0.1
0.2
0.3
0.4
0.5
0.6
3

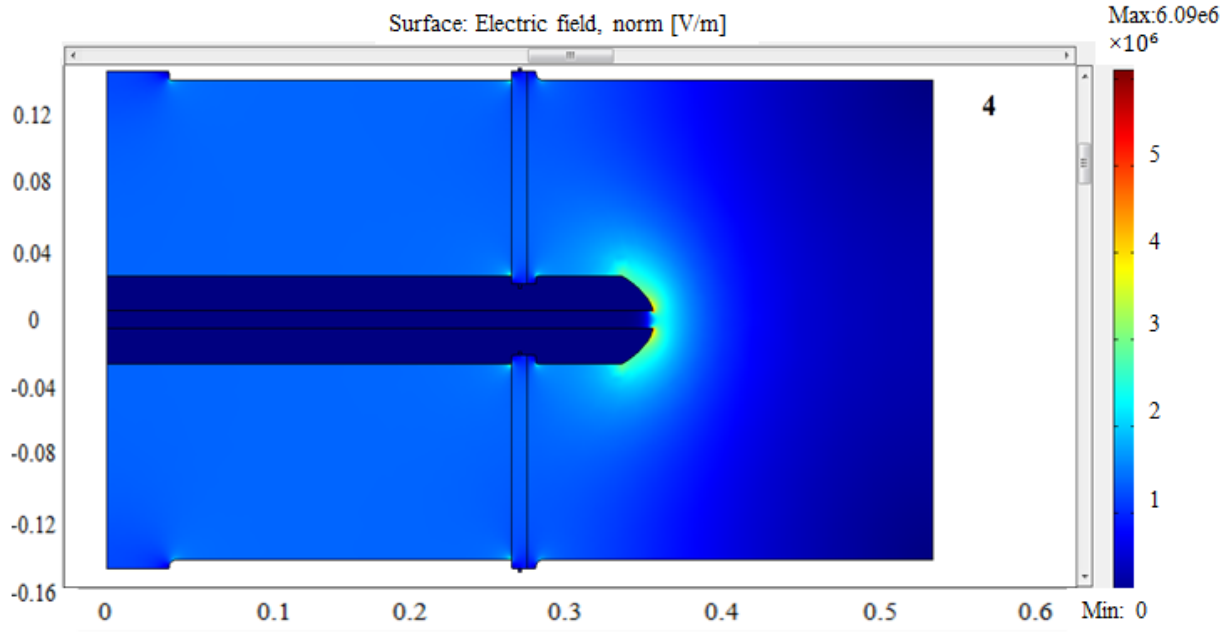
Surface: Electric field, norm [V/m]
Max:6.09e6
×10⁶
5
4
3
2
1
Min: 0
0.12
0.08
0.04
0
-0.04
-0.08
-0.12
-0.16
0
0.1
0.2
0.3
0.4
0.5
0.6
4

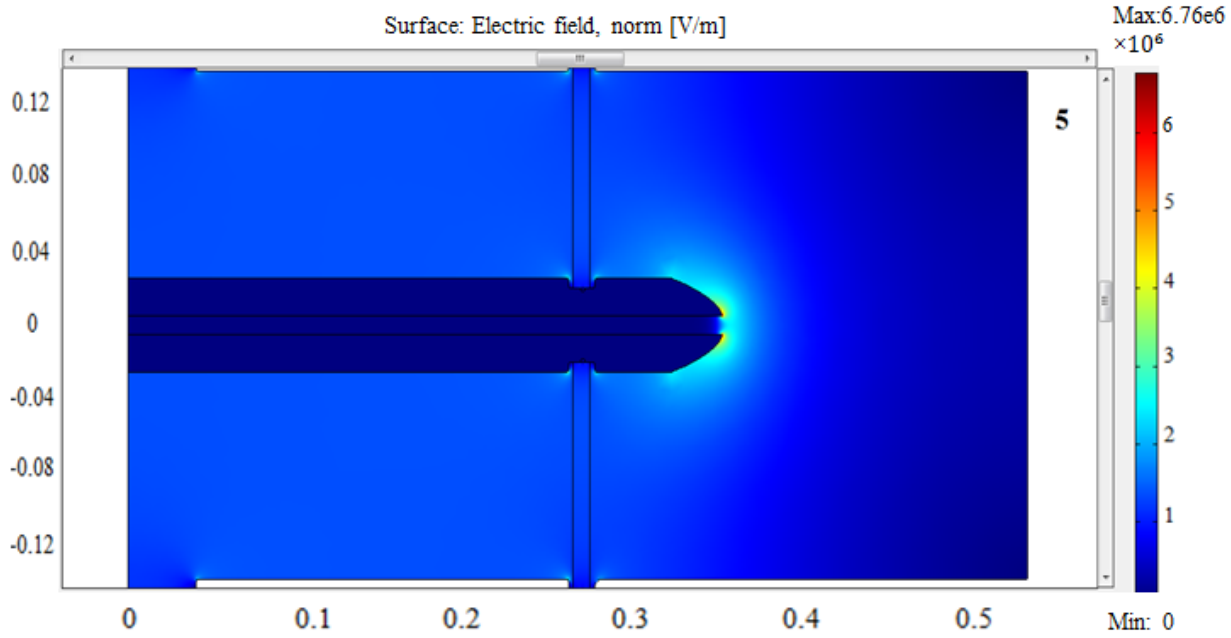

Figures A.(4.1-4.5): 2D COMSOL simulations (axial symmetry) of the HV electrode with the possible distortions of the electric field.

It was supposed to broaden the grooves for the insulator rings up to 15 mm in order to avoid chipping at various manipulations. But the opportunity to apply the equipment designed to micrometer accuracy, is eliminated the need for a wide channel.

To study the influence of geometrical effects on the magnitude of the false signal five regions have been investigated:

1. The region of the neutron guide: z = (0.125 - 0.14) m, r = (0 - 0.07) m;
2. The region of the groove (top) for an insulator ring: z = (0.125 - 0.14) m, r = (0.25-0.262) m;
3. Outside the insulator ring (vacuum chamber at the pressure P = 10^{-4}mbar): z = (0.02-0.07) m, r = (0.272-0.45) m;
4. The region of the groove (bottom): z = (0.02-0.04) m, r = (0.25-0.262) m;
5. The average over the volume of the neutron chamber.

One can see the examples of the results in the next two figures.

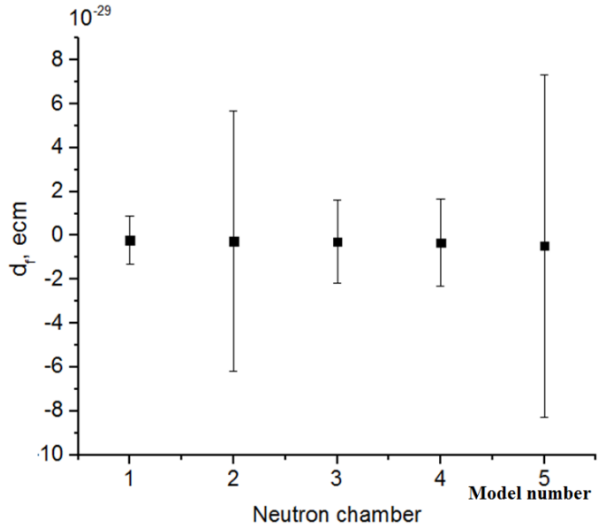

Figure A.4.6: The false effect is calculated for the fifth region. The spread of values in magnitude is $d_{f,n} \approx (0.2 - 0.5) \cdot 10^{-29}\text{e} \cdot \text{cm}$.

On this step we found that the edges of the electrode that are disposed in the vacuum chamber, give a lower false effect in the case of rounded top and bottom edges. Since the neutrons are absent there and the distance between the edges and the walls of the vacuum chamber is 18 cm (<10 cm is dangerous) it does not matter so much. Our simulations show the complete absence of the electric field near the walls of the vacuum chamber.

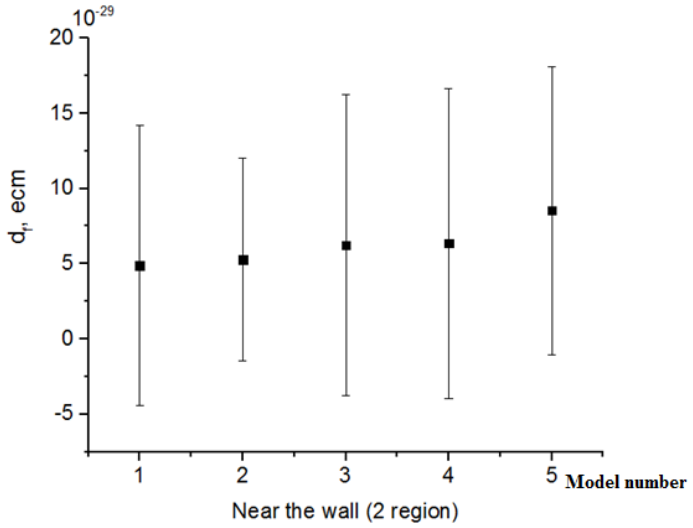

Figure A.4.7: The false effect is calculated for the second region. Here the false effect is distributed as $d_{f,n} \approx (4.9 - 8.5) \cdot 10^{-29}\text{e} \cdot \text{cm}$. Uncertainties of the calculations are large due to the narrow localization of the effect compared to the region of investigation.

In the next figure you can see one of the worst examples of curvature of the neck hole for the neutron guide.

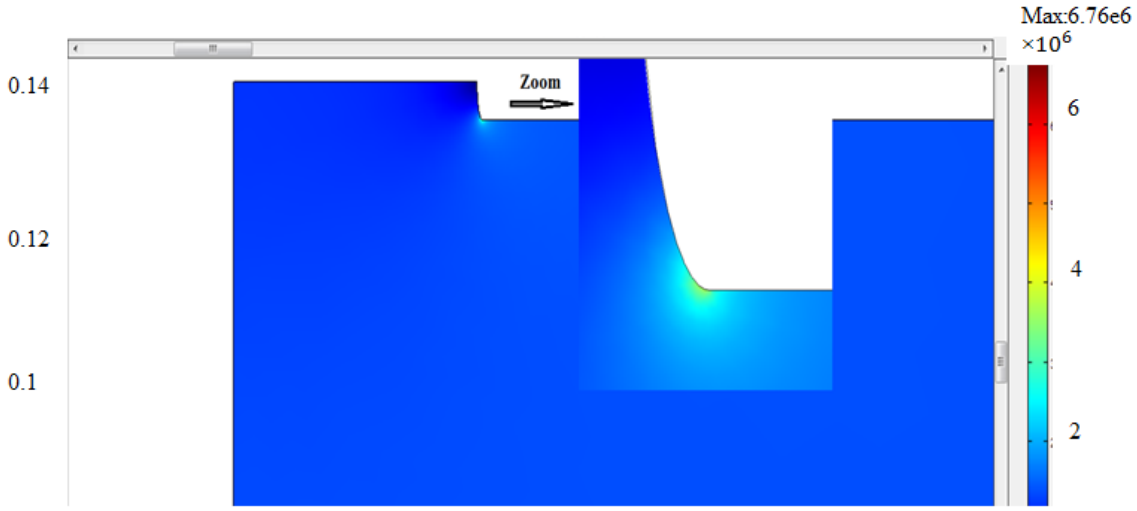

Figure A.4.8: COMSOL simulation for the rounding of the hole of the neutron guide. Here, a Bézier curve of the 2 order was used in order to smooth out the right angle just a little.

The calculation of the local false effect gives a value $d_{f,n} \approx 0.8 \cdot 10^{-29}\text{e} \cdot \text{cm}$.

1. The region of the groove. O-ring.

The influence of the O-ring is very small (for all models $d_{f,n} \approx 10^{-31}\text{e} \cdot \text{cm}$), and its location on the upper or lower side of the insulator ring also does not matter (vacuum insulation does matter). The main attention is given to only the design of this ring. The thickness of the O-ring and of the groove under it 2 mm×1.5 mm is assumed to be sufficient.

In Figure A.4.9 the region of the groove with the O-ring is shown.

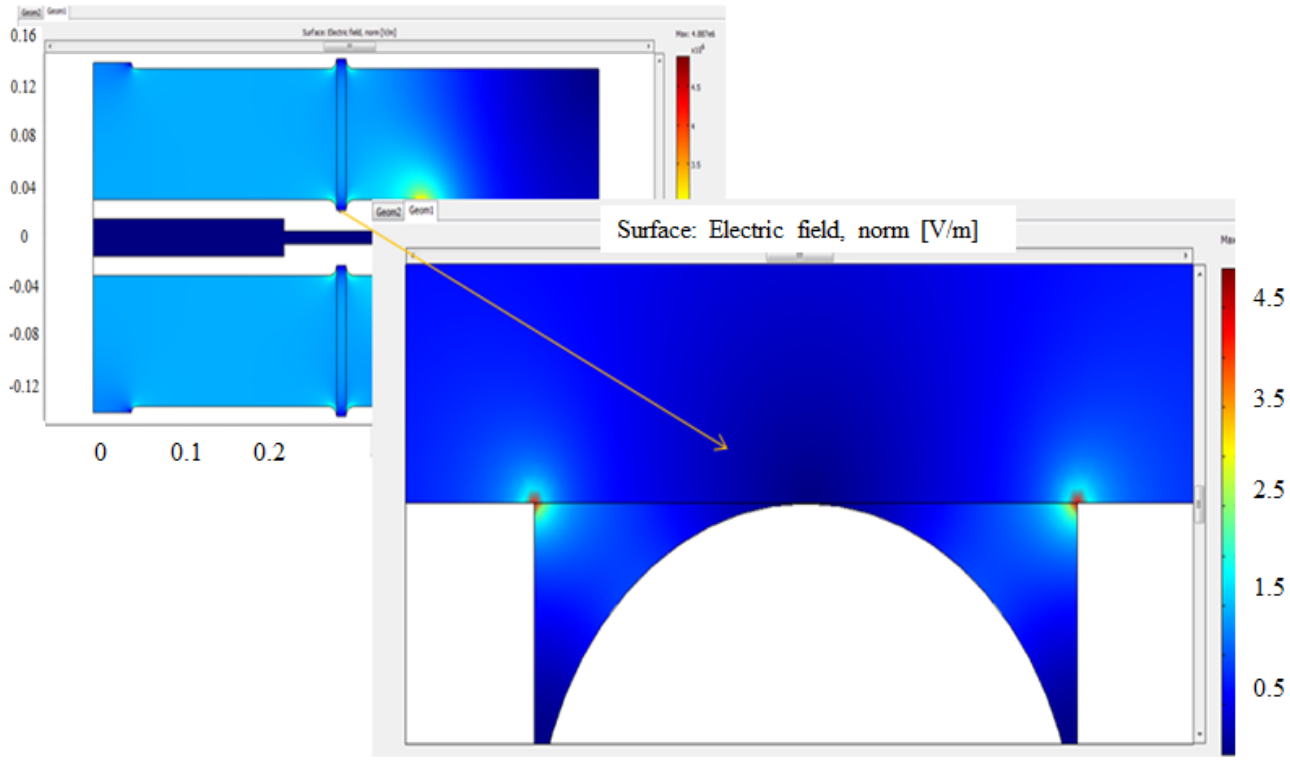

Figure A.4.9: COMSOL simulation of the electric field distribution in the groove.

E-field distortion on the groove for the O-ring is at a level of 30-45 kV/cm. But this will not damage the electrode or the insulator ring because they are made from quartz glass. The dielectric strength of the fused quartz is 250–400 kV/cm at 20 °C [74]. A misaligned wall of the insulator ring (see Fig. A.4.10) causes an increased field at the place of touch and can be a source of sparks and also can violate the vacuum insulation. Therefore it is necessary to choose the O-ring correctly. The thickness of the wall of the insulator ring is 10 mm. The diameter of 2 mm for the O-ring is optimal. The rule is [61]: if the diameter of O-ring will be 2 mm, the cross-section of the groove should be at 90% of the O-ring cross section square, it is about $S_{groove} \approx 2\ mm \times 1.5\ mm = 3\ mm^2$.

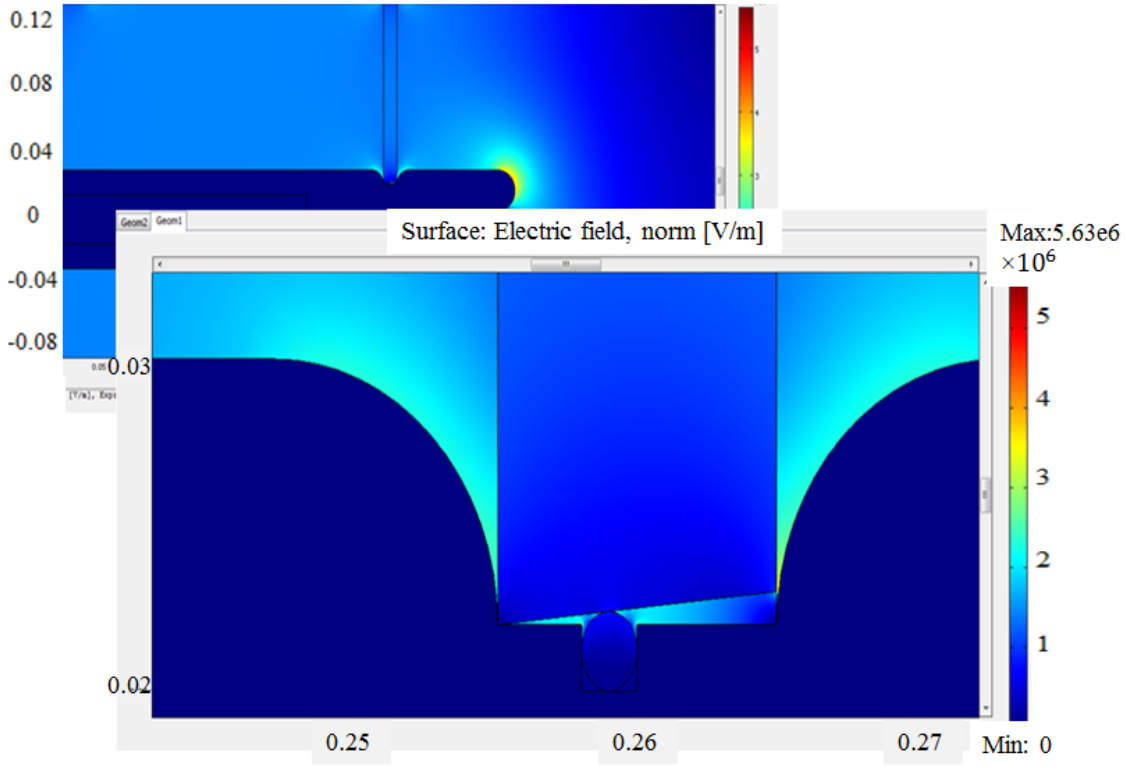

Figure A.4.10: COMSOL simulation of the skewed wall of the insulator ring.

4.2. Distance between the HV electrodes, their thickness (radius of edge rounding).

Furthermore we studied the effect of the thickness of the electrodes and the distance between them on the weakening of the field outside the electrode in the vacuum chamber (see Figs. A.4.11).

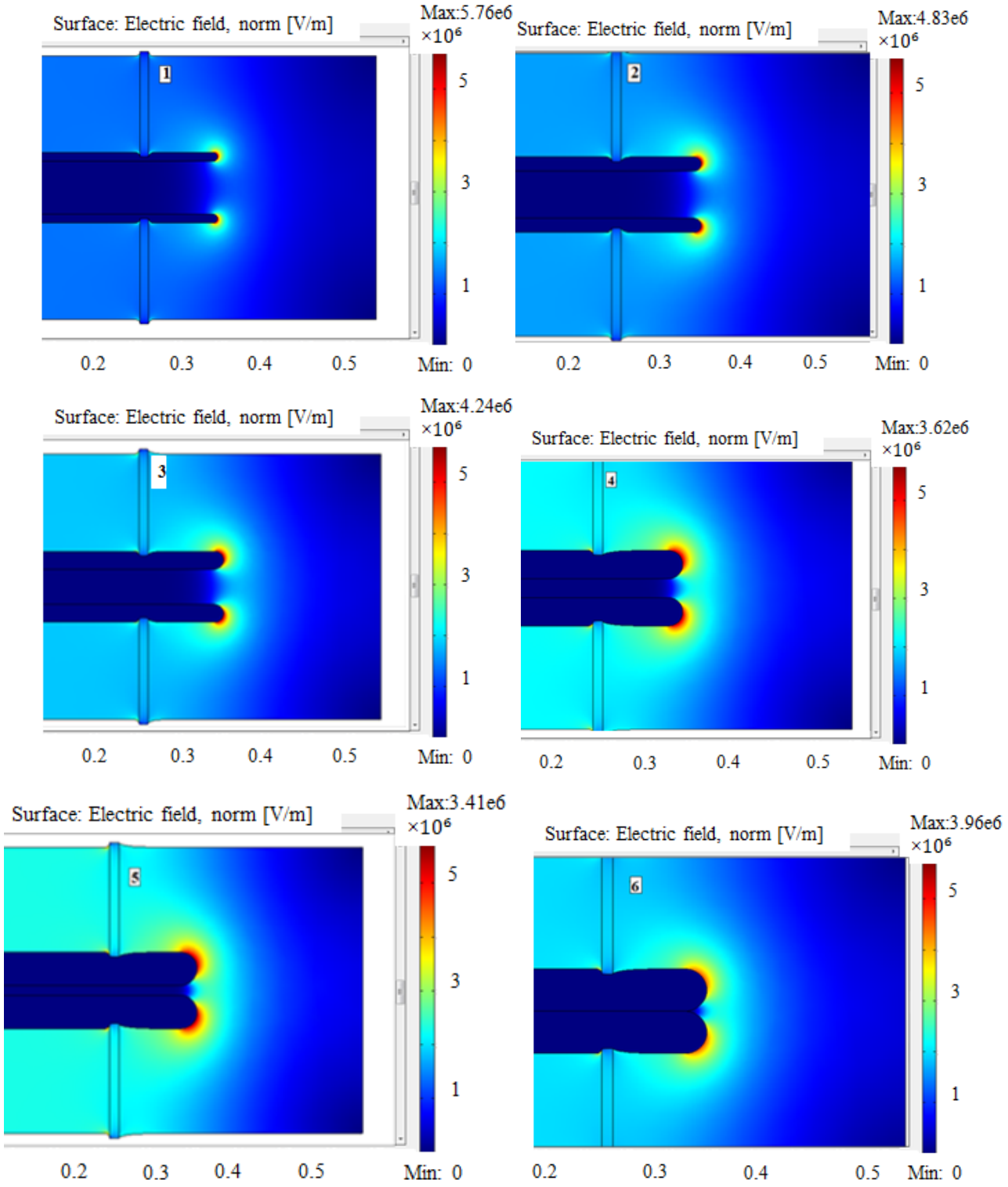

Figures A.4.11(1-6): COMSOL simulation of the electric field distribution for different thicknesses of the HV electrodes and their distance. Plots 1-6 demonstrate the electric field distortions outside the neutron chambers. The thickness (radius of edge rounding) changes from 10 mm to 40 mm, the distance between electrodes varies from 0 mm to 40 mm.

As we can see, the electric field strength increases on the narrow edges and become weaker on the thick ends of the electrode, but in inverse ratio varies the area of inhomogeneities. When we calculate the mean of the electric field in the vacuum chamber, we will see almost the same values (see Fig. A.4.12).

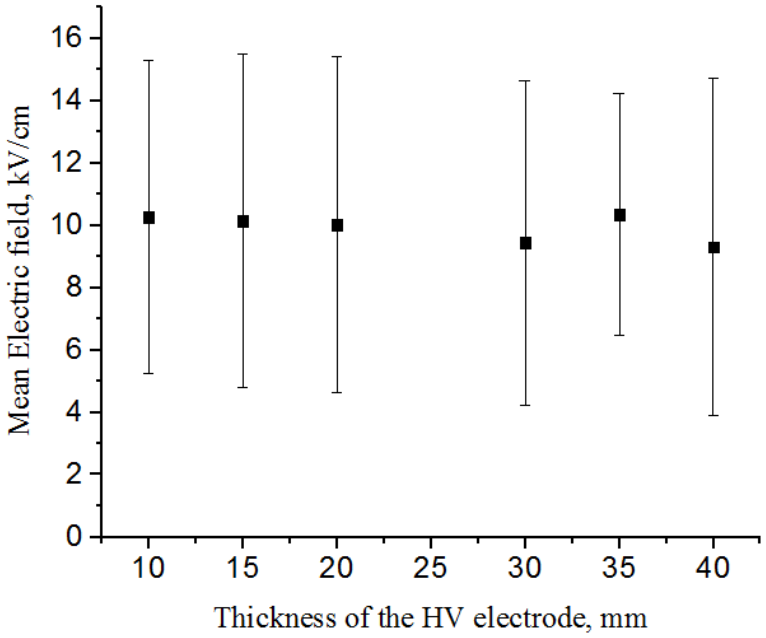

Figure A.4.12: The analysis of the electric field inhomogeneity depending on the thickness of the electrode edges.

5. Silicone gel instead of vacuum

One can see here the most interesting and demonstrating versions of the shapes of the simulated HV electrodes and groundings.

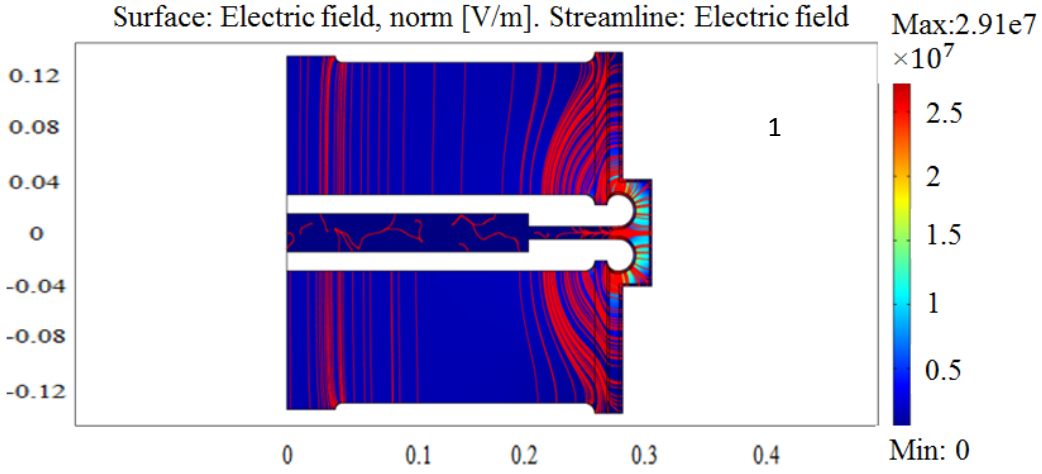

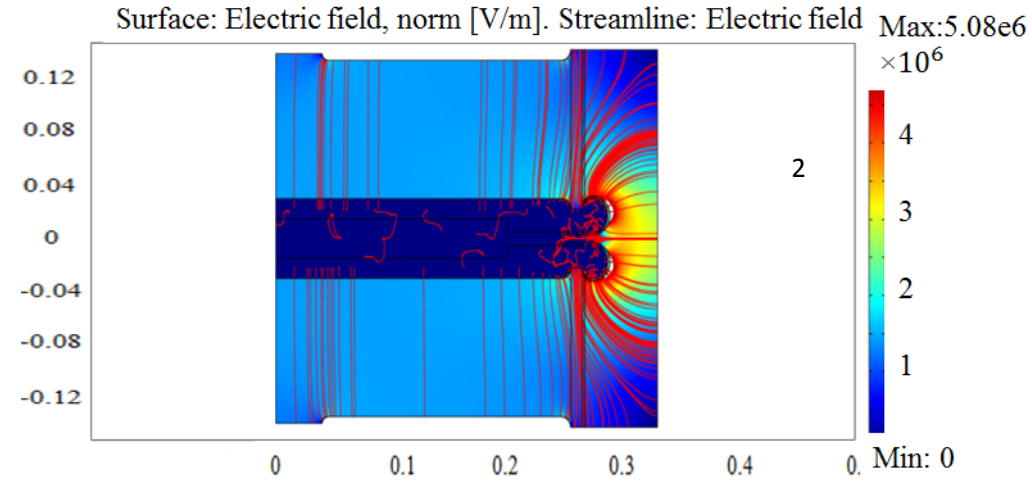

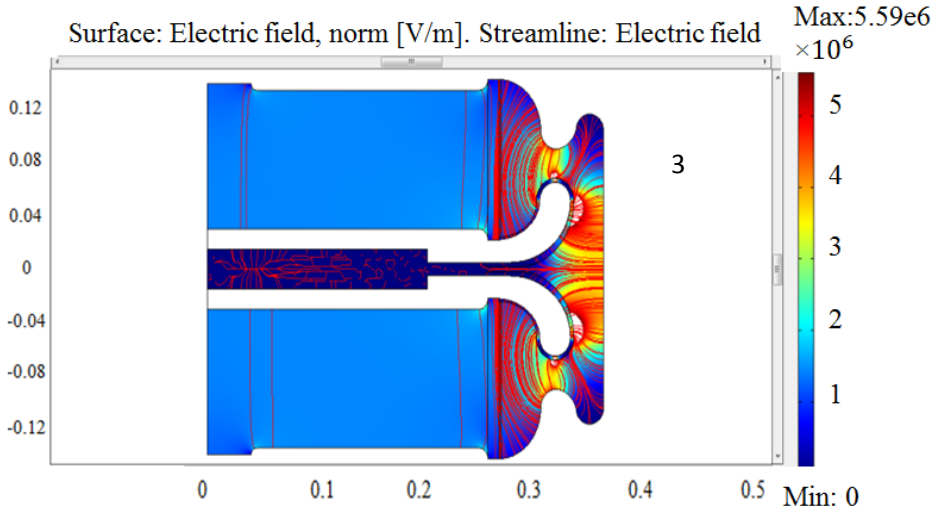

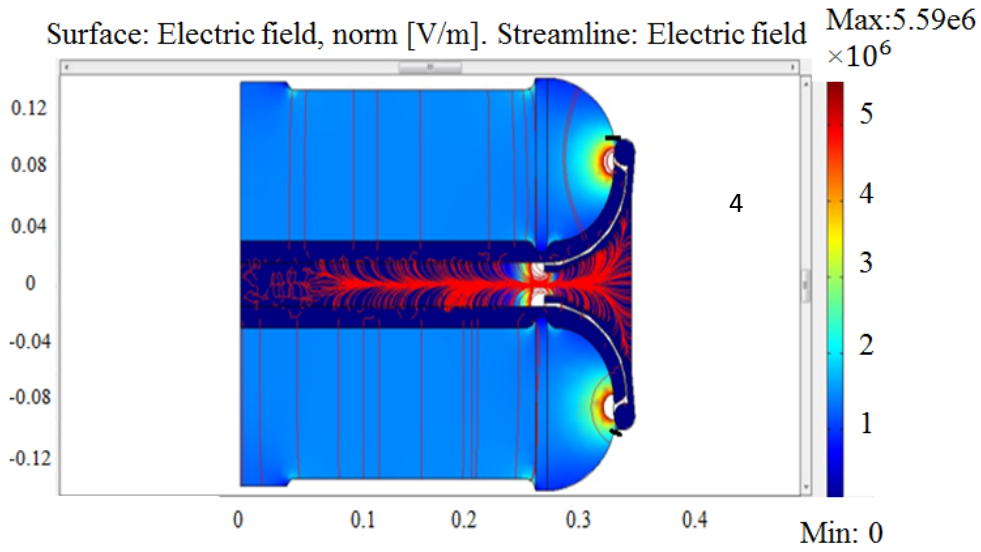

Figure A.(5.1-5.4): COMSOL simulation of the electric field distribution for the different shapes of the HV electrodes and groundings in case of using the silicone gel as insulator: 1. The worst and the simplest case. The electric field distribution is not uniform near the insulator ring due to the short HV electrode and grounding; 2. The ground electrode is a bit larger, the HV electrode is short. The electric field uniformity in this case is much better than in the case 1; 3) Additional shape of the outer part of the HV electrode, the ground electrode is respectively curved. In this case we can provide an uniform electric field inside the experiment. The electric field in the outer part is about 45 kV/cm. The HV breakdowns are avoided, because the silicone gel has dielectric strength of 23 kV/mm; 4) "Special" grounding. In this case, the additional ground electrode is installed around the outer part of the high voltage electrode. It allows us to avoid problems with the huge electric field in the narrow region between the HV electrode and grounding electrode and to divert leakage currents from high voltage electrode concentrically through the insulating layer of silicone gel. The grounding will be separated (black scratches).

6. Design of a high-voltage electrode.

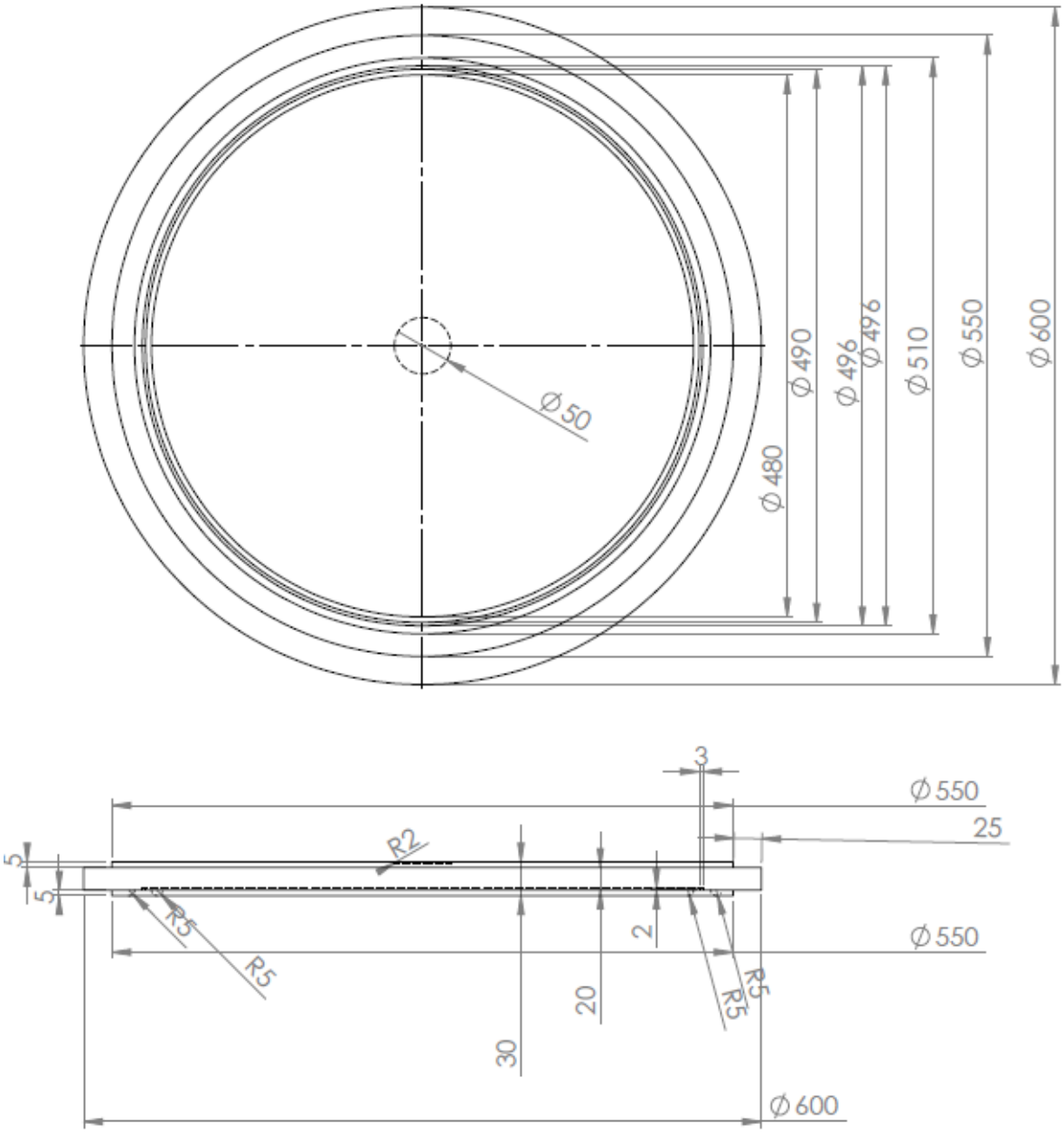

Figure A.6.1: Drawing of the high-voltage electrode.

7. DEPOL

7.1. Wall collisions rate

The rate of collisions of UCN per unit area of the wall for a gas in equilibrium is given by the formula of standard kinetic theory [112]

$$J = \frac{1}{4} n \bar{v}, \tag{A.10}$$

where n is the local gas density, $\bar{v}$ is the local gas average particle velocity.

The velocity of UCNs with total energy E_0 at height h_0 is

$$v(E_0, h_0) = \sqrt{\frac{2E_0}{m}}. \tag{A.11}$$

Then at an arbitrary height the velocity will be

$$v(E_0, h) = v(E_0, h_0) \sqrt{\frac{\left(E_0 - E_{pot}(h)\right)}{E_0}}. \tag{A.12}$$

The same we can write for the density

$$n(E_0, h) = n(E_0, h_0) \sqrt{\frac{\left(E_0 - E_{pot}(h)\right)}{E_0}}. \tag{A.13}$$

And finally

$$J(E_0, h) = J(E_0, h_0) \frac{\left(E_0 - E_{pot}(h)\right)}{E_0}. \tag{A.14}$$

If the storage volume is a cylinder of radius R, then the differential wall collision rate is

$$\frac{d\nu}{dh} = S(h)\cdot J(E_0,h) = 2\pi R\cdot J(E_0,h), \tag{A.15}$$

where $S(h)dh$ is the surface area at height h.

We start the calculation of the neutron density for the one-neutron case. Let's A(h) be a cross-sectional area at height h. The neutron moves between the bottom and the top of the cylinder, then the integral

$$\int_{h_{bottom}}^{h_{top}} n(E_0,h)\cdot A(h)dh = \pi R^2 n(E_0,h_0)\int_{h_{bottom}}^{h_{top}}\sqrt{\frac{\left(E_0-E_{pot}(h)\right)}{E_0}}dh = 1. \tag{A.16}$$

$$n(E_0,h_0) = \frac{\sqrt{E_0}}{\pi R^2\left([\frac{-2}{3a_1}\sqrt{\left(E_0-E_{pot}(h)\right)^3}]_{h_{bottom}}^{h_0}+[\frac{-2}{3a_2}\sqrt{\left(E_0-E_{pot}(h)\right)^3}]_{h_0}^{h_{top}}\right)}, \tag{A.17}$$

where a_1 and a_2 are the slopes, i.e. coefficients in the Eq. (5.1). We know that $V(h_0)=0$ and $V(h_{top})= V(h_{bottom})= E_0$. Then we have

$$n(E_0,h_0) = \frac{3}{2\pi R^2 E_0(\frac{1}{a_2}-\frac{1}{a_1})} = \frac{3}{2\pi R^2 E_0}\cdot 1.14\frac{neV}{cm} = \frac{1.71}{\pi R^2 E_0}\frac{neV}{cm}. \tag{A.18}$$

Then we can determine the wall collision rate for one UCN with total energy E_0 between the heights h and h+Δh as:

$$\frac{d\nu}{dh}\Delta\text{h} = S(h)\cdot J(E_0,h)\Delta h = \frac{\pi R}{2}\sqrt{\frac{2E_0}{m}}\frac{1.71}{\pi R^2 E_0}\frac{neV}{cm}\frac{\left(E_0-E_{pot}(h)\right)}{E_0}\Delta h = 0.86\frac{neV}{cm}\cdot\sqrt{\frac{2E_0}{m}}\cdot\frac{1}{R}\cdot\frac{\left(E_0-E_{pot}(h)\right)}{E_0^2}\Delta h =$$

$$= 0.86\frac{neV}{cm}\cdot\sqrt{\frac{E_0}{neV}}\cdot 0.44\frac{m}{s}\cdot\frac{1}{0.035\ m}\frac{\left(E_0-E_{pot}(h)\right)}{E_0^2}\Delta h = 10.76\frac{neV}{cm\cdot s}\cdot\sqrt{\frac{E_0}{neV}}\cdot\frac{\left(E_0-E_{pot}(h)\right)}{E_0^2}\Delta h, \tag{A.19}$$

Where the inner diameter of the sample is 0.07 m and a neutron velocity is 0.44 m/s per neV.

7.2. Depolarization probability

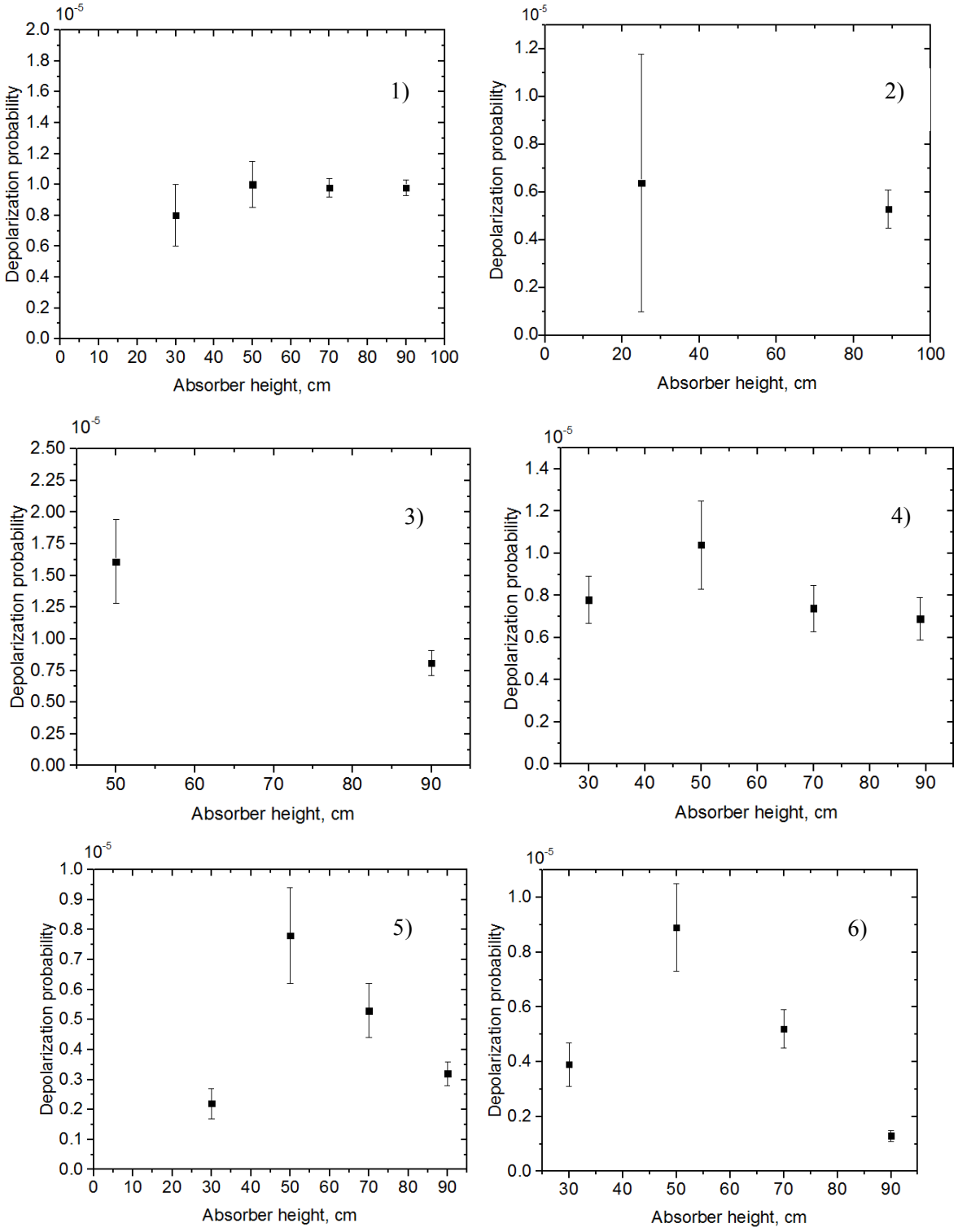

Figures A.7.4: Depolarization probability for different heights of absorber for: 1) Ni/Mo-82/18; 2) Ni/Mo-85/15 (glass); 3) Ni/Mo-85/15 (aluminum); 4) Ni/Mo-88/12; 5) Cu; 6) dPS.

7.3. Energy loss parameters

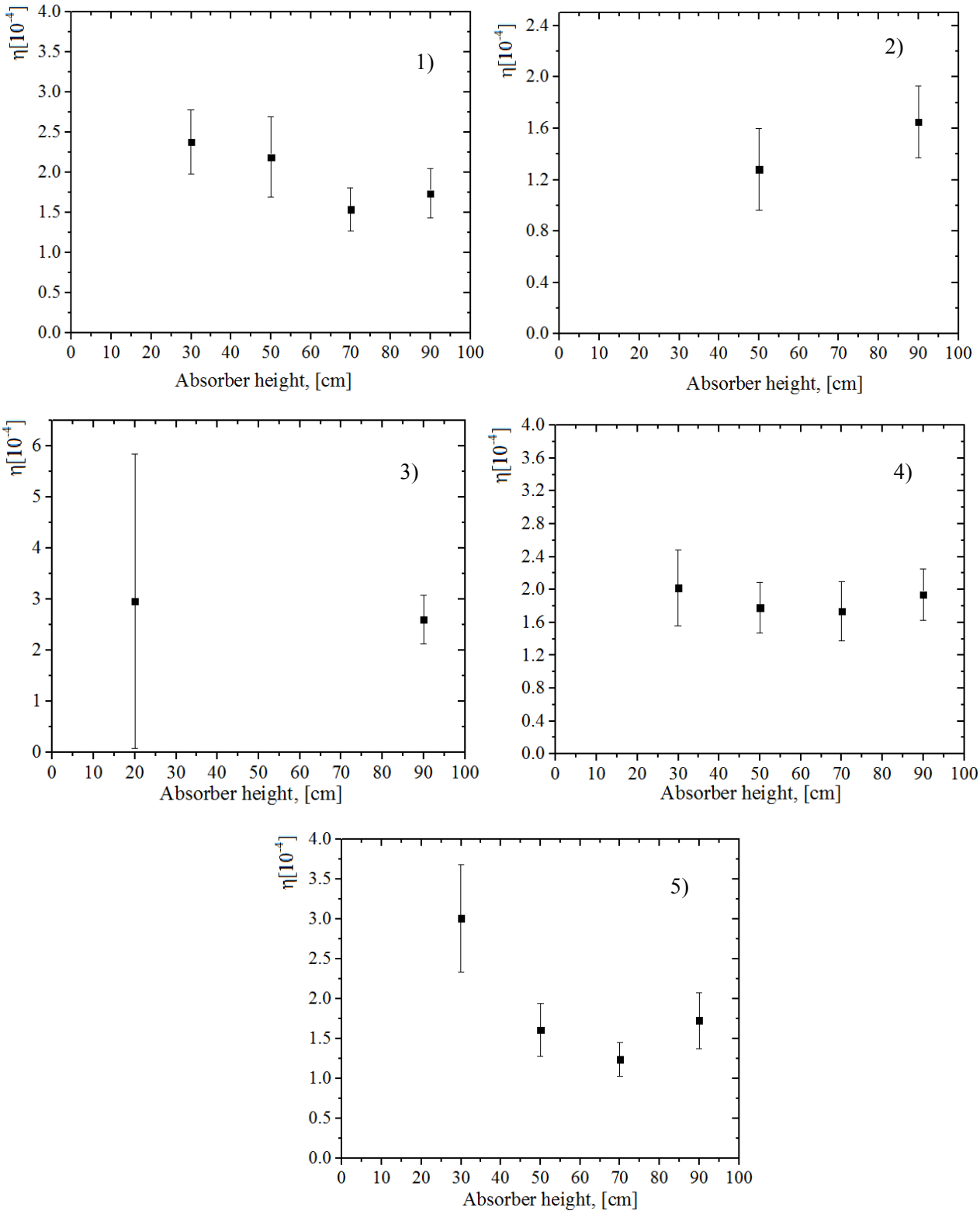

Figures A.7.5: Energy loss parameter η as a function over absorber height for: 1) Ni/Mo-88/12; 2) Ni/Mo-85/15 (aluminum); 3) Ni/Mo-85/15 (glass); 4) Cu; 5) dPS.

Acknowledgements

I would like to express gratitude to my supervisors, Prof. Dr. Stephan Paul, Prof. Dr. Peter Fierlinger and Dr. Erwin Gutsmiedl, for the opportunity to work in the UCN group at TUM, Excellence Cluster Universe. Also I am very grateful to the member of our group, Dr. Igor Altarev, for useful discussions and support of my work. I would like to thank Dr. Thorsten Lauer for fair corrections and comments. I wish to thank Dr. Manfred Daum for a strong and friendly support, guidance and assistance. In addition, I want to thank the guys from my group for a very warm and friendly atmosphere, for our joint discussions, celebrations, for a coziness of human relations.

Bibliography:

[1] T. D. Lee and C. N. Yang. Physical Review, 104:254, 1956.

[2] C. S. Wu et al. Physical Review, 105:1413, 1957.

[3] R. L. Garwin, L. M. Lederman and M. Weinrich. Physical Review, 105:1415, 1957.

[4] Jerome I. Friedman and V. L. Telegdi. Physical Review, 105:1681, 1957.

[5] J. H. Christenson et al. Physical Review Letters, 13:138, 1964.

[6] Zhi Zhong Xing. arXiv:hep-ph/9606422v2, 1996.

[7] K. Abe et al. http://arxiv.org/abs/hep-ex/0202027, 2002.

[8] B. Aubert et al. http://arxiv.org/abs/hep-ex/0203007, 2002.

[9] J. Schwinger. Phys. Rev., 82:914, 1951

[10] J. Schwinger. Phys. Rev., 91:713, 1953.

[11] J. Ellis and Mary K. Gaillard. FERMILAB-Pub-78/66-THY, 1978.

[12] M. Kobayashi and T. Maskawa. Progress of Theoretical Physics, 49:652, 1973.

[13] F. Halzen, Alan D. Martin. QUARKS AND LEPTONS: An Introductory Course in Modern Particle Physics. John Wiley & Sons, Inc., 1984.

[14] S. Weinberg, The Quantum Theory of Fields. Cambridge University Press, 2000.

[15] C. G. Callan and et al. Physics Letters B, 63:334, 1976,

[16] A. A. Belavin and et al. Physics Letters B, 59:85, 1975.

[17] R. J. Crewther et al. Phys. Lett., 88B:123, 1979.

[18] M. Pospelov and A. Ritz. Phys. Rev. Lett., 83(13):2526-2529, Sep 1999.

[19] C.A. Baker et al. Phys. Rev. Lett., 97:131801, 2006.

[20] M.S.Sozzi. Discrete symmetries and CP-violation. Oxford University Press, 2008.

[21] I.B.Khriplovich and S.K.Lamoreaux. CP-violation without Strangeness, Springer, 2004.

[22] I.B.Khriplovich and A.R.Zhitnitsky. Phys. Lett. 109B:490, 1982.

[23] E. M. Purcell and N. F. Ramsey. Phys. Rev., 78(6):807, Jun 1950.

[24] W. W. Havens and et al. Phys. Rev., 72:634, 1947.

[25] N. F. Ramsey. Phys. Rev., 84:506, 1951.

[26] I. S. Altarev et al., JETP, Lett. 44, 1986.

[27] K. F. Smith et al., Phys. Lett. B234, 1990.

[28] J.H. Smith et al., Phys. Rev. 108, 1957.
[29] Y.B. Zeldovich, Zh. Eksp. Teor. Fiz. 36, 1959.
[30] F. L. Shapiro, Usp. Fiz. Nauk. 95, 1968.
[31] N. F. Ramsey, A Molecular Beam Resonance Method with Separated Oscillating Fields, Phys. Rev. 78, no. 6, 695, 1950.
[32] P. G. Harris, The Neutron EDM Experiment, arXiv:0709.3100v2 , 2007.
[33] Philip R. Bevington and D. Keith Robinson. Data Reduction and Error Analysis for the Physical Sciences. McGraw-Hill Inc., US; 3rd edition, 2002.
[34] J. M. Pendlebury and E.A. Hinds. Nuclear Instruments and Methods in Physics Research A, 440:471, 2000.
[35] B. McKellar, S. Choudhury, X. G. He, and S. Pakvasa. Phys. Lett. B, 197:556, 1987.
[36] C. A. Baker, D. D. Doyle, P. Geltenbort, K. Green et al., Phys. Rev. Lett. 97, 13180, 2006.
[37] S. N. Balashov, K. Green et al., A Proposal for a Cryogenic Experiment to Measure the Neutron Electric Dipole Moment, 2003.
[38] T. Ito, J. Phys. Conf. Series 69 (2007) 012037.
[39] I.S. Altarev, Yu. Borisov, N.V. Borovikova et. al., Phys. At. Nucl. 59, 1996.
[40] I. Altarev et al., Nucl. Phys. A 844, 2010.
[41] W. C. Griffith, M. D. Swallows, T. H. Loftus, M. V. Romalis, B. R. Heckel, E. N. Fortson, Phys. Rev. Lett. 102, 101601, 2009.
[42] W.-M. Yao et al., J. Phys. G 33, 2006.
[43] K. Green et al., Nucl. Instr. Meth. A 404, 1998.
[44] http://www.frm2.tum.de/en/technik/brief-description/index.html
[45] P. Fierlinger, I. Altarev, et al., A magnetically shielded room with ultra-low residual field and gradient, Rev. Sci. Instrum., 2014,85(7), doi: 10.1063/1.4886146.
[46] Annual EDM discussion, Excellence Cluster Universe-TUM, November 2014.
[47] Jacobs J. P., Klipstein W. M., Lamoreaux S. K., Heckel B. R. *et al.*, *Phys. Rev. A*, 52, 1995.
[48] I. Altarev, D. H. Beck, S. Chesnevskaya et al., A next generation measurement of the electric dipole moment of the neutron at the FRM II, IL NUOVO CIMENTO, doi: 10.1393/ncc/i2012-11271-0.
[49] I.S. Altarev, Yu. Borisov, N.V. Borovikova et. Al., Phys. At. Nucl. **59** (1996), 1152.
[50] J. M. Pendelbury et al., Geometric-phase-induced false electric dipole moment signals for particles in traps, Phys. Rev. A **70**, 032102 (2004).
[51] M. V. Berry. Proceedings of the Royal Society of London A, 392:45, 1984.

[52] P. G. Harris and J. M. Pendelbury, Dipole-field contributions to geometric phase-induced false electric-dipole-moment signals for particles in traps, Phys.Rev. A **73**, 014101 (2006).
[53] P. G. Harris et al. Phys. Rev. Lett., 82:904, 1999.
[54] F. Bloh and A. Siegert, Magnetic Resonance for Nonrotating Fields, Phys. Rev. **57**, no. 6, 522, 1940.
[55] N. F. Ramsey, Resonance Transitions Induced by Perturbations at Two or More Different Frequencies, Phys. Rev. **100**, no. 4, 1191 (1955)
[56] I. I. Rabi, N. F. Ramsey & J. Schwinger, Use of Rotating Coordinates in Magnetic Resonance Problems, Rev.Mod. Phys. **26**, no. 2, 167, 1954.
[57] A. Knecht, Towards a new measurement of the neutron electric dipole moment, 2009.
[58] Zenner J., Thesis "The search for the neutron electric dipole moment", 2013.
[59] M. B. Horras, A highly sensitive 199Hg magnetometer for the nEDM experiment, DISS. ETH NR. 20558.
[60] http://www.zemiceurope.com/Products-Miniature-Sensors/product-q70x5x9-h.html
[61] Altarev I., privat communication.
[62] Berne F., Kardone Zh.,Vodoochistka. Ochistka stochnyh vod neftepererabotki.: Himiya, 1997.
[63] M. Born, E. Wolf, Principles of Optics (4th.ed.), Pergamon Press, 1970.
[64] A. Yariv, Quantum Electronics (3-rd edition), 1975.
[65] G.S. Landsberg, Optics. Moscow, Nauka, 1976.
[66] M. Born and E. Wolf, Principles of Optics. Moscow: Nauka, 1970.
[67] Slivkov I.N., Elektroizolyaciya I razryad v vakuume, Moskva, Atomizdat, 1972.
[68] De La Rue W., Muller H.W., Experimental Researches on the Electric Discharge with the Chloride of Silver Battery, Phil. Trans. Roy. Soc.– London 171 (1), 1880.
[69] Friedrich Paschen, Ueber die zum Funkenübergang in Luft, Wasserstoff und Kohlensäure bei verschiedenen Drucken erforderliche Potentialdifferenz, Annalen der Physik und Chemie 273 (5), 1889.
[70] Townsend J. S.; MacCallum S. P., Electrical properties of neon, Philosophical Magazine 6, 1928.
[71] McCallum S. P., Klatzow L., Deviations from Paschen's Law, Philosophical Magazine 17, 1934.
[72] B. Lee Roberts, W. J. Marciano, Lepton dipole moments, ISBN: 978-981-4271-83-7, 2009.
[73] E. Aleksandrov et al., A new Precision Measurement of the Neutron Electric Dipole Moment (nEDM), 2005.
[74] G.I. Skanavi, Fizika dielektrikov, Moskva, 1958.

[75] Rogowski R. W., Arch. f. El. 12/1, 1923.
[76] Schilling , Arch. f. El. 22, 337, 1929.
[77] L. Landau, Sov. Phys. JETP 5, 1957.
[78] N.F.Ramsey, Phys. Rev. 109, 1958.
[79] A. Sakharov, JETP Lett. 5, 1967.
[80] I. Altarev, G. Ban, G. Bison, K. Bodek et al., Nucl. Instr. and Meth. in Phys. Res. A 611, 2009.
[81] I. Altarev, D. H. Beck, S. Chesnevskaya, T. Chupp, et al., II Nuovo Cimento, Vol. 35 C, N4, 122, 2012.
[82] U.Trinks, F. J.Hartmann, S.Paul, W. Schott, Nucl. Instr. and Meth. in Phys. Res. A 440, 2000.
[83] A.Anghel, F.Atchison, B.Blau, B. van den Brandt et al., Nucl. Instr. and Meth.in Phys. Res. A 611, 2009.
[84] R.Golub and K.Boning, Z. Physik B 51, 1983.
[85] A. Serebrov, V.Mityukhlaev, A. Zakharov, A.Kharitonov et al., Nucl. Instr. and Meth. in Phys. Res. A 440, 2000.
[86] C.-Y. Liu, A.R.Young, S.K. Lamoreaux, Phys. Rev. B 62, 2000.
[87] A.P. Serebrov, E.A.Kolomenski, M. S. Lasakov, V.A.Mityukhlaev et al., JETP Lett. 74, 2001.
[88] C. L.Morris, J.M.Anaya, T. J.Bowles, B.W.Filippone et al., Phys. Rev. Lett. 89, 2002.
[89] A. Saunders, J.M.Anaya, T. J.Bowles, B.W.Filippone et al., Phys. Lett. B 593, 2004.
[90] F.Atchison, B. van den Brandt, T.Bryś, M.Daum et al., Phys. Rev. C 71, 2005.
[91] F.Atchison, B. van den Brandt, T.Bryś, M.Daum et al., Phys. Rev. Lett. 94, 2005.
[92] F.Atchison, B. van den Brandt, T.Bryś, M.Daum et al., Phys. Rev. Lett. 95, 2005.
[93] F.Atchison, B.Blau, K.Bodek, B. van den Brandt et al., Phys. Rev. Lett. 99, 2007.
[94] I.Altarev, F.Atchison, M.Daum, A.Frei et al., Phys. Rev. Lett. 100, 2008.
[95] F.Atchison, B.Blau, K.Bodek, B. van den Brandt et al., Phys. Rev. Lett. 101, 2008.
[96] I.Altarev, M.Daum, A.Frei, E.Gutsmiedl et al., Eur. Phys. J. A 37, 2008.
[97] F.Atchison, B.Blau, K.Bodek, B. van den Brandt et al., Nucl. Instr. and Meth. in Phys. Res. A 611, 2009.
[98] M.Daum, B.Franke, P.Geltenbort, E.Gutsmiedl et al., Nucl. Instr. and Meth. in Phys. Res. A 741, 2014.
[99] K. Bodek, M. Daum, R. Henneck, S. Heule et al., Nucl. Instr. and Meth. in Phys. Res. A 597, 2008.
[100] F.Atchison, T.Bryś, M.Daum, P.Fierlinger et al., Phys. Lett. B 625, 2005.

[101] R. Kovacs-Mezei, Th. Krist, Zs. Révay, Nucl. Instr. and Meth. in Phys. Res. A 586, 2008.
[102] A. Schebetov, A. Kovalev, B. Peskov, N. Pleshanov et al., Nucl. Instr. and Meth. in Phys. Res. A 432, 1999.
[103] S. Ghosh, N. Das and A. Mookerjee, J. Phys.: Condens. Matter 10, 1998.
[104] M.Wohlmuther and G. Heidenreich, Nucl. Instr. and Meth. in Phys. Res. A 564, 2006.
[105] M. G. D. van der Grinten, J. M. Pendlebury, D. Shiers, C. A. Baker et al., Nucl. Instr. and Meth. in Phys. Res. A 423, 1999.
[106] F. Atchison, T. Bryś, M. Daum, P. Fierlinger, et al., Phys. Rev. C 76, 2007.
[107] F. Atchison, B. Blau, M. Daum, P. Fierlinger et al., Phys. Lett. B 642, 2006.
[108] F. Atchison, T. Bryś, M. Daum, P. Fierlinger, et al., Diamond and Related Materials 16, 2007.
[109] F. Atchison, B. Blau, M. Daum, P. Fierlinger et al., Phys. Rev. C 74, 2006.
[110] F. Atchison, B. Blau, M. Daum, P. Fierlinger et al., Nucl. Instr. and Meth. in Phys. Res. B 260, 2007.
[111] V.K. Ignatovich, The Physics of Ultracold Neutrons, Oxford Ser. Neutron Scatt.Condens. Matter, vol. 5, Clarendon Press, Oxford, 1990.
[112] R. Golub, D.J. Richardson, S.K. Lamoureaux, Ultra-cold neutrons, Adam Hilger, Bristol, Philadelphia, and New York, ISBN 0-7503-0115-5, 1991.
[113] A. Serebrov, A. Vasiliev, M. Lasakov, Yu. Rudnev et al., Nucl. Instr. and Meth. in Phys. Res. A 440, 2000.
[114] Yu. Pokotilovski, JETP Lett. 76, 2002.
[115] T.Bryś, M.Daum, P.Fierlinger, P.Geltenbort et al., Nucl. Instr. and Meth. in Phys. Res. A 550, 2005.
[116] V.V.Vladimirski, JETP Letters 12, 1960.
[117] Yu.G.Abov et al., JETP Letters 44, 1986.
[118] ILL YellowBook, www.ill.fr/YellowBook/PF2/
[119] W.Drexel, Neutron News 1, 1990.
[120] A. Steyerl et al., Phys. Lett. A116, 1986.
[121] F.Atchison, T.Bryś, M.Daum, P.Fierlinger, Nucl. Instr. Meth. in Phys. Res. A 552, 2005.
[122] M.Daum, P.Fierlinger, B.Franke, P.Geltenbort, et al., to be published.
[123] R. Holsinger and K. Halbach, POISSON SUPERFISH code, copyright 1985- 2004 by the Regents of the University of California (unpublished).

[124] The Particle Data Group, K. A. Olive, K. Agashe, C. Amsler, M. Antonelli et al., Chinese Physics C 38, 2014.
[125] S.Arzumanov, L.Bondarenko, S.Chernyavsky, W.Drexel et al., Phys. Lett. B 483, 2000.
[126] A. Serebrov, V.Varlamov, A.Kharitonov, A.Fomin et al., Phys. Lett. B 605, 2005.
[127] A.Pichlmaier, V.Varlamov, K. Schreckenbach, P.Geltenbort, Phys. Lett. B 693, 2010.
[128] E. Korobkina, R. Golub, B. W. Wehring, and A. R. Young, Phys. Rev. B 70, 2004.
[129] T.Bryś, M.Daum, P.Fierlinger, A.Fomin et al., Nucl. Instr. and Meth. in Phys. Res. A 551, 2005.
[130] F.Atchison, A.Bergmaier, M.Daum, M.Dobeli et al., Nucl. Instr. and Meth. in Phys. Res. A 587, 2008.